Technology developments for the Alkali Metal Thermal to Electric Converter (AMTEC) Test Facility

Zur Erlangung des akademischen Grades
Doktorin der Ingenieurwissenschaften (Dr.-Ing.)
der KIT-Fakultät für Maschinenbau
Karlsruher Institut für Technologie (KIT)

genehmigte

Dissertation

von

Dipl.-Ing. Rocío Nerea Díez de los Ríos Ramos

Tag der mündlichen Prüfung: 16.07.2018

Hauptreferent: Prof. Dr.-Ing. Robert Stieglitz

Korreferent: apl. Prof. Dr. rer. Nat. Sven Ulrich

Acknowledgments

Abstract

The Alkali Metal Thermal-to-Electric Converter (AMTEC) is an electrochemical cell that requires a high temperature heat source to generate electricity with a theoretical efficiency close to that of the Carnot cycle ($\sim 45\,\%$ at $> 800\,°C$ [1]). An essential interest arises when coupled to a concentrating solar power (CSP) plant by connecting AMTEC to a solar receiver on its hot side and to a thermal energy storage tank on its cold side. The present work deals with the research of an AMTEC cell, which is tested in the AMTEC Test Facility (ATEFA). The work validates the developed ATEFA and AMTEC test cell designs and demonstrates that the test cell is able to generate electric power. The cell behavior has been analyzed attending to the AMTEC system: temperature, pressure, electrode and current collector.

For the AMTEC converter, the main issues are identified and summarized. Here, a conventional cell design is taken based on [2] and characterized by a sodium liquid anode and a single ß"-alumina solid electrolyte (BASE) tube. Considerations regarding the material selection, thermal stresses, heat losses, instrumentation and electrical insulation of the cell have been incorporated into the design and optimization phases of the ATEFA facility. Moreover, to fulfill actual safety requirements, dedicated safety measures are included for the handling of sodium, the operation-phase and the control system. Design optimizations are supported by numerical (e.g. thermo-mechanical analysis of the cell structure) and experimental analysis (e.g. current collector structure).

Two main technological developments have been addressed: the development of a stable electrode coating layer on the BASE surface utilizing the magnetron sputtering technique and the development of a high-temperature ceramic to metal brazing (up to 700 °C). Mo, TiN and TiC have been considered for the coating of the BASE elements. A microstructural and elemental analysis of several sputtered samples have been performed using the Scanning Electron Microscopy (SEM) and the Energy-Dispersive X-ray Spectroscopy (EDX). The morphology of the Mo and TiC sputtered layers show a homogeneous grain distribution and the presence of porous channels between grains. A partial detachment of the TiC coating is also observed. The analysis of the detachment process suggests to be caused by the vaporization of gases (e.g. water or CO_2) from the ceramic surface, driven by high local temperatures ($> 200\,°C$) provided during the magnetron sputtering process.

ATEFA and the AMTEC test cell have been operated in a temperature range of 400 - 700 °C and up to 0.05 MPa. To exclude the influence of the electrode magnetron sputtering on the BASE properties (e.g. increased brittleness), the current collector has been mechanically pressed directly to the BASE. The current production of the cell (up

to 52 mA at 700 °C) agrees with the small effective contact surface of the current collector to BASE. The maximum measured power of the cell without electrode sputtered layer rises to ~ 7 mW at 700 °C. An open circuit voltage (OCV) of 1037 mV at 700 °C has been measured. The agreement between theoretical and measured OCV varied strongly with the wettability of the ceramic. A wetted BASE tube showed a deviation of the OCV to the theory of less than 3.5 %. The exposure time to liquid sodium required in the tests to obtain a good wetting of the ceramic is in reasonable agreement with the literature (~ 5 h at ~ 300 °C) and can be accelerated by i) increasing the temperature beyond 300 °C and ii) driving a current (electrowetting) by closing the electric circuit of the cell.

The structure of the current collector (CC) and its assembly on top of the cylindrical BASE surface have a great influence on the cell power (up to > 70 % power difference). During the assembly of the CC an inefficient pressing force of the CC-corset towards the BASE outer surface can reduce significantly the cell power. Moreover, the electric contact between the BASE-cathode-CC is also influenced by the different thermal expansion coefficients, leading to changes in the cell performance. This issue is emphasized by the cylindrical form of the BASE, used historically in AMTEC cells. A planar configuration of the BASE can minimize this effect, since a planar surface favors an improved electric contact. As result, the cell losses can be significantly reduced.

Kurzfassung

Der Alkali-Metall thermoelektrischer Konverter (AMTEC) ist eine elektrochemische Zelle, die eine Hochtemperatur-Wärmequelle benötigt, um Strom mit einem theoretischen Wirkungsgrad ($\sim 45\,\%$ bei $> 800\,°C$ [1]) nahe dem Carnot Zyklus zu erzeugen. Seine Flexibilität in Bezug auf die Wärmequelle macht diesen Energiewandler vielversprechend. Eine Option ist die Kopplung mit einer konzentrierenden thermischen Solaranlage (CSP). Die heiße Seite der Zelle wird daher mit dem Solarempfänger verbunden und die kalte Seite mit dem Wärmespeicher der Solaranlage. Die vorliegende Arbeit beschäftigt sich mit der Entwicklung eines AMTEC-Konverters, der zunächst in der AMTEC Testanlage (ATEFA) getestet wird. In dieser Arbeit konnten die Designs der ATEFA und AMTEC Testzelle validiert- und der Beweis einer funktionierenden AMTEC Zelle erbracht werden. Das Verhalten der Zelle wird unter Berücksichtigung des AMTEC-Systems analysiert: Temperatur, Druck, Elektrode und Stromsammler.

Die Arbeit fasst die wichtigsten technologischen Fragenstellungen der AMTEC Technologie zusammen, die Gegenstand der Untersuchung sind. Ein neues Zellendesign wurde entwickelt, dass auf dem getesteten Prototyps von [2] basiert. Dieses Design zeichnet sich durch eine flüssige Anode aus Natrium und ein einzelnes ß"-Aluminiumoxid Festelektrolyt (BASE) -Rohr aus.

Überlegungen zur Materialauswahl, thermischen Belastung, Wärmeverlusten, Instrumentierung und elektrische Isolierung der Zelle sind während der Betriebsphase der ATEFA Anlage einbezogen worden. Um die Sicherheitsanforderungen zu erfüllen, sind spezielle Sicherheitsmaßnahmen für einen sicheren Umgang mit Natrium entwickelt worden. Diese sind in die Betriebsphase und das Kontrollsystem integriert worden. Die entsprechenden Designoptimierungen werden durch numerische (z.B. thermomechanische Analyse der Zellstruktur) und experimentelle Analysen (z.B. Stromsammlerstruktur) ergänzt.

Zwei wesentliche technologische Entwicklungen sind vor dem Zusammenbau der Zelle untersucht worden: i) die Entwicklung einer Elektrodenbeschichtung auf der BASE-Oberfläche unter Verwendung der Magnetron-Sputtertechnik und ii) die Entwicklung einer Keramik-Metall Lötung für hohe Temperaturen (bis zu 700 °C). Hierbei sind Mo, TiN und TiC für die Elektrodenbeschichtung der BASE-Elemente berücksichtigt worden. Eine mikrostrukturelle und Elementanalyse mehrerer gesputterter Proben wurden mithilfe der Rasterelektronenmikroskopie (SEM) und der energiedispersiven Röntgenspektroskopie (EDX) durchgeführt. Die Ergebnisse zeigen eine homogene Kornverteilung in den Mo- und TiC-Sputterschichten sowie die Anwesenheit von porösen Kanälen zwischen den Körnern. Es wurde zudem eine unvollständige Ablösung der TiC-Beschichtung festgestellt. Die Analyse des Ablösungsprozesses deutet darauf hin,

dass die TiC-Beschichtung durch die Verdampfung von Gasen an der keramischen Oberfläche (z.B. Wasserdampf oder CO_2) abgelöst wurde. Ein Grund für die Verdampfung von Gasen können die hohen lokalen Temperaturen ($> 200\,°C$) im Sputterverfahren sein.

Die AMTEC Testanlage (ATEFA) und die AMTEC Testzelle sind in Betrieb genommen worden. Die ATEFA ist im Temperaturbereich von 400 - 700 $°C$ und bis zu 0.05 MPa betrieben- und die Leistung der AMTEC Zelle bei verschiedenen Betriebsbedingungen analysiert worden. Um die Auswirkung des Elektrode-Sputterverfahrens auf die BASE-Eigenschaften auszuschließen (z.B. erhöhte Sprödigkeit), wird der Stromsammler direkt auf die Oberfläche der BASE gedrückt. Die Stromerzeugung der Zelle (bis zu 52 mA bei 700 $°C$) stimmt mit der kleinen effektiven Kontaktfläche des Stromsammlers zur BASE überein. Die gemessene maximale Leistung der Zelle (ohne Elektrodensputterschicht) lag bei $\sim$7 mW, bezogen auf einer Temperatur von 700 $°C$. Eine Leerlaufspannung (OCV) von 1037 mV bei 700 $°C$ wurde gemessen. Der Vergleich der theoretischen und der gemessenen Leerlaufspannung (OCV) zeigt, dass die Benetzbarkeit der Keramik entscheidend ist. Eine benetzte BASE zeigt lediglich eine Abweichung des OCV von der Theorie von weniger als 3.5 %. Die während des Experiments ermittelte Zeit zur Benetzung der Keramik ($\sim$ 5 h bei $\sim$ 300 $°C$) ist in einer guten Übereinstimmung mit der Literatur. Der Benetzungsprozess kann durch i) das Erhöhen der Temperatur über 300 $°C$ und ii) durch einen elektrischen Stromfluss (Elektrobenetzung) beschleunigt werden.

Die Struktur des Stromsammlers und sein Zusammenbau auf der zylindrischen BASE haben einen großen Einfluss auf die Leistung der Zelle (bis zu 70 % Leistungsunterschied). Bei dem Zusammenbau des Stromsammlers kann eine nicht ausreichende Presskraft vom Korsett die Ursache für die Leistungsreduzierung sein. Der elektrische Kontakt zwischen BASE und Kathode wird ebenfalls durch die unterschiedlichen Wärmeausdehnungskoeffizienten negativ beeinflusst. Dieser Zustand wird durch die zylindrische Form der BASE verstärkt, welche historisch in den AMTEC Zellen verwendet wird. Dieses kann durch eine flache Konfiguration der BASE verbessert werden, da der elektrische Kontakt zu einer flachen Oberfläche vorteilhafter ist. Aus diesem Grund reduzieren sich die gesamten Verluste der Zelle.

Publications related to this thesis

N. Diez de los Rios Ramos, W. Hering, A. Weisenburger, M. Stüber, A. Onea, M. Lux, S. Ulrich, and R. Stieglitz. Design and construction of the ATEFA facility for experimental investigations of AMTEC test modules. *IOP Conference Series: Material Science and Engineering*, 228 (012014), 2017.

N. Diez de los Rios Ramos, A. Weisenburger, A. Onea, W. Hering, M. Stüber, S. Ulrich and R. Stieglitz. Technological developments in ATEFA for AMTEC research, *Proceedings of the 10th PAMIR International Conference - Fundamental and Applied MHD*, pages 653 - 658, 2016.

N. Diez de los Rios Ramos, A. Onea, S. Scherrer, A. Weisenburger and W. Hering. Direct energy conversion of heat to electricity using AMTEC. *Proceedings of 5th International Youth Conference on Energy (IYCE)*, ISBN 978-1-4673-7171-1, 2015. A. Onea, N. Diez de los Rios Ramos, W. Hering, J. L. Palacios, and R. Stieglitz. AMTEC clusters for power generation in a concentrated solar power plant. *Magnetohydrodynamics*, 51 (3): 249 – 261, 2015.

A. Onea, N. Diez de los Rios Ramos, W. Hering, R. Stieglitz and P. Moster. Direct Energy Conversion using liquid metals. *EPJ Web of Conferences,* 79: 03010, 2014.

J. L. Palacios, A. Onea, N. Diez de los Rios Ramos, W. Hering and R. Stieglitz. Structural and thermal analysis of an AMTEC experimental cell with the finite element method. *EPN Journal*, 33 (1): 1 - 7, 2013.

Nomenclature

Roman Symbols

$\dot{m}$ mass flow rate $[kg/s]$

$\dot{m}_f$ mass flux $[kg/m^2 s]$

A surface $[m^2]$

a activity coefficient $[-]$

a_{cc} accommodation coefficient $[-]$

B magnetic field $[T]$

B_{ex} temperature-independent charge-exchange coefficient $[AK^{1/2}/Pam^2]$

C concentration at the electrode surface $[kg/m]$

c_v flow coefficient value $[-]$

c_p specific heat capacity $[J/molK]$

CTE thermal expansion coefficient $[K^{-1}]$

D diffusion coefficient $[m^2/s]$

d_m molecular diameter $[m]$

D_{out} outer diameter $[m]$

E cell potential. Potential difference between the electrodes. $[V]$

e measurement error $[^o/_o]$

F Faraday constant: 96485.33 $[As/mol]$

f force $[N]$

G Gibb's free energy $[J]$

G_p electrode pressure loss factor $[-]$

G'_p total geometry factor of cathode and current collector $[-]$

h specific enthalpy $[J/kg]$

h_P Planck constant 6.62×10^{-34} $[Js]$

H_{Na} fill level of sodium $[m]$

J electric current $[A]$

j electric current density $[A/m^2]$

j_0 exchange current density at equilibrim conditions $[A/m^2]$

J_f flux of species $[mol/m^2 s]$

k thermal conductivity $[W/mK]$

k^r rate constant of an electrochemical reaction $[cm/s]$

K_e coefficient of pressure loss at the cathode - current collector $[Pa\,cm^2/A]$

K_f coefficient of pressure drop through the electrode $[-]$

K_t Tafel slope $[-]$

K_{eq} temperature-dependent equilibrium constant $[-]$

Kn Knudsen diffusion coefficient $[-]$

L heat of vaporization $[J/mol]$

M molecular weight $[kg/mol]$

n number of electrons transferred in a chemical reaction $[-]$

P power $[W/cm^2]$

p pressure $[Pa]$

p^T vapor pressure of sodium at electrode surface due to evaporation at the condenser $[Pa]$

p_j pressure due to sodium leaving the electrode surface $[Pa]$

$p_\triangle$ sodium pressure drop from the interface to the surface of the electrode through a long cylindrical pore $[Pa]$

Q heat $[J]$

q electric charge $[C]$

R electrical resistance $[\Omega]$

r radius $[m]$

R_g	universal gas constant, 8.3144598 $[J/molK]$
S	entropy $[J/K]$
s	specific entropy $[J/Kkg]$
S_e	Seebeck coefficient $[V/K]$
T	temperature $[K]$
t	thickness $[m]$
U	inner energy $[J]$
u	uncertainty [units of the variable]
V	cell voltage, equivalent to cell potential E
v	velocity $[m/s]$
Vol	volume $[m^3]$
W	work $[J]$
W_{cc}	pressure factor of vapor transport through the current collector $[-]$
Z	geometric factor of the Stefan-Boltzmann equation $[-]$
ZT	figure of merit $[-]$

Abbreviations

ABB	Asea Brown Bovery
AFC	Alkaline Fuel Cell
AMPS	Advanced Modular Power Systems
AMTEC	Alkali Metal Thermal to Electric Converter
ARPS	Advanced Radioisotope Power System
ATEFA	AMTEC Test Facility
BASE	ß"-Alumina Solid Electrolyte
CC	Current Collector
CSP	Concentrating Solar Power

EDX	Energy-Dispersive X-ray Spectroscopy
HEMCP	Helmholtz Energy Material Characterization Platform
IAM-AWP	Institute for Applied Materials – Applied Materials Physics
IHM	Institute for Pulsed Power and Microwave Technology
INR	Institute for Neutron physics and Reactor technology
JPL	Jet Propulsion Laboratory
KASOLA	Karlsruhe Sodium Laboratory
KIT	Karlsruhe Institute of Technology
LCOE	Levelized Cost of Energy
LIMTECH	Liquid Metal Technology
LSM	Strontium-doped Lanthanum Manganite
MC	Measurement Campaign
MCFC	Molten Carbonate Fuel Cell
MHD	Magnetohydrodynamics
MIEC	Mixed Ionic and Electronic Conductor
NaS	Sodium Sulfur Battery
NRC	Nichols Research Corporation
OCV	Open Circuit Voltage
OHP	Outer Helmholz Plane
OSC	Orbital Sciences Corporation
PAFC	Phosphoric-Acid Fuel Cell
PandID	Piping and Instrumentation Diagram
PCVD	Photolytic Chemical Vapor Deposition
PEFC	Polymer Electrolyte Fuel Cell

PETE   Photon-Enhanced Thermionic Emission

PID   Proportional-Integral-Derivative controller

PV   Photovoltaic

PVD   Physical Vapor Deposition

PX   Pluto Express mission

SEM   Scanning Electron Microscopy

SOFC   Solid Oxide Fuel Cell

SS   Stainless Steel

TE   Thermoelectric

TEC   Termionic Energy Converter

TES   Thermal Energy Storage

TPB   Triple Phase Boundary

VTM   Very Thin Molybdenum electrode

XRD   X-Ray Diffraction analysis

YSZ   Yttrium-Doped Zirconia

ZEBRA   Zero Emission Battery Research Activities

Greek Symbols

α electrochemical transfer coefficient $[-]$

$\bar{\mu}$ electrochemical potential $[J/mol]$

δ diffusion layer thickness $[m]$

η process efficiency [-]

κ Boltzmann constant, 1.38×10^{-23} $[J/K]$

μ chemical potential $[J/mol]$

ϕ_e volume porosity of the cathode electrode $[-]$

ρ	electrical resistivity $[\Omega\ m]$
σ	electrical conductivity $[S/m]$
σ_k	Stefan-Boltzmann constant, 5.670373×10^{-8} $[W/m^2K^4]$
ε	thermal emissivity $[-]$
Φ	inner electric potential of the phase (electrode) referred to as the Galvani potential $[V]$
ϱ	specific density $[kg/m^3]$
ξ	charge-exchange polarization overpotential $[V]$

Superscripts/Subscripts

a	anode
B	BASE
b	backward reaction (oxidation)
c	cathode
cc	closed electrical circuit
cd	condenser
con	electrical contact
$cond$	heat conduction
e	electrode or BASE/electrode interface
el	electrical
eq	equilibrium conditions
ev	evaporation
f	forward reaction (reduction)
hyd	hydrostatic pressure
ic	current collector
in	input

vi

ion	ionic
K	Knudsen flow regime
l	lead
max	maximum value
O	oxidation reaction
oc	open electrical circuit
p	pore
R	reduction reaction
r	electrical resistance
rad	heat radiation
s	standard conditions
sat	saturated conditions
st	structure
th	thermal
vis	viscous flow regime

Contents

1 Introduction

In this chapter the motivation of the work is presented, which focuses on the combination of two technologies: concentrating solar power (CSP) and the Alkali Metal Thermal to Electric Converter (AMTEC). Furthermore, the state-of-the-art concerning the application of concentrating solar power as heat source of AMTEC is addressed. Third, a review on direct energy conversion technologies is given and finally the aim of the work is presented.

1.1 Motivation: AMTEC & Concentrating Solar Power 2.0

Concentrating solar power (CSP) is a promising technology that can provide dispatchable electricity generation if integrated with a thermal storage device that allows the plant a continuous operation 24h/7d. However, efforts need to be focused on reducing the levelized cost of energy (LCOE) to increase its competitiveness. One favorable development consists of increasing the overall efficiency of the power plant by combining a CSP tower plant with a solar driven thermal to electrochemical electricity generation, the Alkali Metal Thermal to Electric Converter. AMTEC is a clean technology that transforms heat directly to electricity avoiding any emission of exhaust gases and operates with sodium at temperatures between 600 - 1000 °C . A second consideration to increase the overall efficiency of the plant deals with expanding the operational temperature range. Liquid metals, in particular liquid sodium, have excellent properties as heat transfer fluid: low melting point, high heat conductivity and a good chemical stability at high temperatures. Thus, they are excellent candidates as heat transfer fluid in CSP plants. The proposed concept of *Concentrating Solar Power 2.0 Plant* at the Institute for Neutron Physics and Reactor Technology (INR) combines the advantages of the AMTEC converter with those of liquid metal technology in a CSP plant [3]. A schematic representation of the system is summarized in figure 1.1.

The *CSP 2.0* concept consists of advanced AMTEC cells acting as topping system of a sodium-cooled solar tower plant. The hot side of AMTEC is connected to a solar receiver and the colder side to a thermal storage tank. The peaks of solar energy that appear for instance at mid-day are directly transformed by AMTEC in electricity for the grid (peak load). A thermal storage tank allows a continuous operation of the facility during night and compensates short term heat fluctuations occurring during daily operation (base load). This solution can be considered as a complementary system of existing solar tower power plants to enhance their applicability and efficiency.

As first step towards the present concept, a Demonstrator of the system will be integrated in the KArlsruhe SOdium LAboratory (KASOLA). KASOLA is a medium-sized sodium loop constructed at the Institute for Neutron physics and Reactor technology

(INR) for research activities on thermal-hydraulics in sodium operated systems. A small scale solar collector system has been designed by M. Strotjohann [4] and will be built on the top of the KASOLA as depicted in figure 1.2. Moreover, the effect of the non-uniform distribution of the solar irradiation on the thermal stresses appearing on the receiver tube of a parabolic through CSP plant has been analyzed [5].
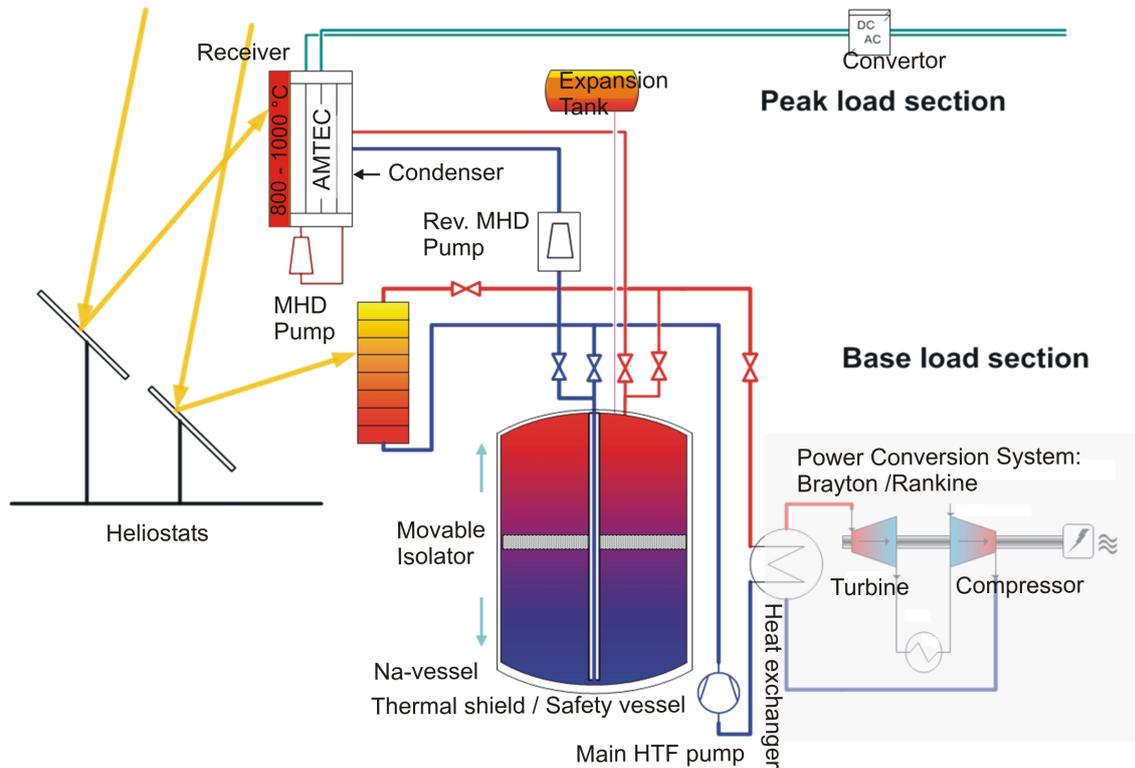
Figure 1.1: Sketch of a Concentrating Solar Power 2.0 Plant integrating AMTEC as topping system of the thermal utilization (modified according to [3]).

The present work deals with the research on an AMTEC converter, which is first tested in the AMTEC Test Facility (ATEFA), developed in this work and represented in figure 1.3. ATEFA has been designed for short term experiments on AMTEC, focusing the research on cell characteristics, performance evaluation and process optimization. A future mature and optimized design of the cell will be integrated in KASOLA in order to test the viability of the Demonstrator for *CSP 2.0*.
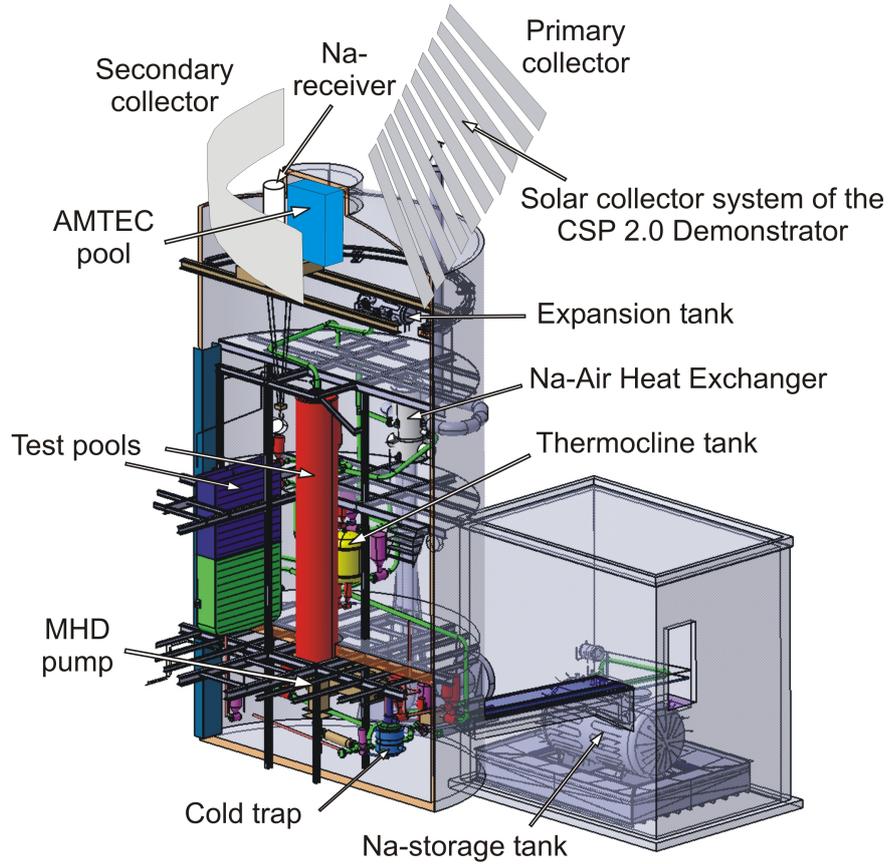
Figure 1.2: Scheme of the KASOLA with integrated solar collector system for the realization of the CSP 2.0 Demonstrator (modified according to [4, 6]).
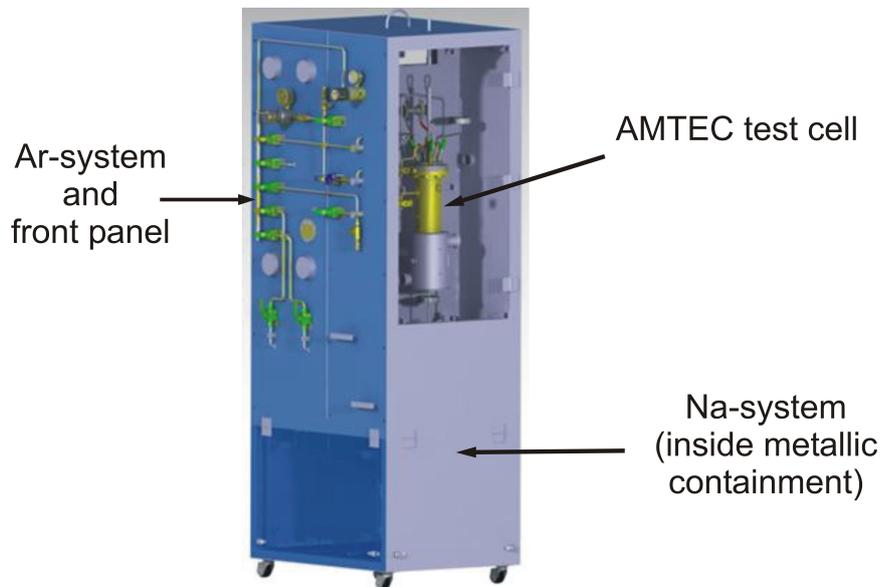

Figure 1.3: 3D-view of ATEFA [7].

1.2 State-of-the-art direct energy conversion technologies

Direct energy conversion can be defined as the transformation of energy in one form (thermal, kinetic, chemical...) into another form (such as electrical) without passing through an intermediate stage. One can identify the most common direct energy conversion processes as i) thermionics, ii) thermoelectricity, iii) electrochemistry, iv) photovoltaics, and v) magnetohydrodynamics. A review on state-of-the-art of various direct energy conversion technologies is given in this chapter.

Thermionic energy converters (TEC) contain a hot conductive anode, whose electrons located on the surface stripe away due to the high thermal energy and jump to another metallic surface with a lower temperature and energy. In this process, electrons pass through a potential difference, which produces electric current when anode and cathode are connected. The energy required to remove an electron away from its nucleus is known as the work-function and the Fermi-level is the energy level at which the valence electrons of an atom vibrate about the nucleus; both parameters are material properties of the anode/cathode [8]. A good thermionic converter needs a cathode with a low Fermi-level and a high work function and in contrast an anode with a high Fermi-level and a low work function [8]. The main challenges are to optimize the space charge barrier in the inter-electrode gap and to develop an anode with a low work function that withstands high operating temperatures >1000 °C [9]. Typical TEC conversion efficiencies are 10 - 15 % [10].

Yuan et al. [9] (2017) demonstrated that using a back-gated graphene anode, barium dispenser cathode and a inter-electrode gap reduced to 17 μm the overall efficiency is 6.7 times higher compared with that of a TEC with a tungsten anode and same inter-electrode gap. The TEC prototype was tested in an ultra-high vacuum system in the laboratory. Further optimizations need to be performed to decrease heat radiation losses, which amounts to 70 % of the total losses.

Schwede et al. [11] (2010) presented a new concept of thermionic conversion: the photon-enhanced thermionic emission (PETE). This technology combines photovoltaic and thermionic effects in a single process, thus taking advantage of the energy of photons and the available thermal energy simultaneously. It is a promising technology that can provide high efficiency solar thermionic converters in temperature ranges out of reach for solar cells. PETE could reach theoretically conversion efficiencies above 50 % [11].

Thermoelectric generators (TE) work based on Seebeck, Peltier and Thomson effects. A quantitative measure of the performance ability is defined by the maximum value of the figure of merit ZT [8, 12]:

$$ZT = \frac{S_e^2 \sigma}{k} T \qquad , \tag{1.1}$$

where S_e denotes Seebeck coefficient, σ represents the specific electrical conductivity, T is the temperature and k the thermal conductivity. Attending to equation (1.1), a good thermoelectric converter requires thermoelectric materials with a low thermal conductivity and high electrical conductivity. To find a material that accomplishes both conditions at high temperature is one of the main issues of TE. Progress in the research field has led to significant ZT increased values of > 7, however typical values of commercial TEs remain as low as $ZT = 1$ - 2 [13].

TEs have a rather low conversion efficiency $< 10\,\%$ [13]. The maximum efficiency and power of a thermoelectric cell is strongly dependent on the temperature of the hot junction; for higher temperatures the efficiency and the power increase rapidly [8]. Performance improvements have been mainly contributed by improved TE material research, geometrical optimizations and the development of advanced TE mathematical models [13]. The key issues remain in finding an optimum balance between ZT and power factor of TEs as well as finding an optimum assembly of TE generator devices [13]. The nanoscale tailoring technique has been considered to enhance the TE performance of the materials [14].

Solid Oxide Fuel cells (SOFC) transform chemical energy directly to electricity by means of converting hydrogen and oxygen to water, electricity and heat. The overall reaction is:

$$2H_2 + O_2 \rightarrow 2H_2O + energy \qquad . \tag{1.2}$$

The family of fuel cells can be divided into low temperature cells: AFC (Alkaline Fuel Cell), PEFC (Polymer Electrolyte Fuel Cell), PAFC (Phosphoric-Acid Fuel Cell); and high temperature cells: SOFC and MCFC (Molten Carbonate Fuel Cell).

Typical efficiencies of SOFC systems are: 50 - 55 % [15]. Due to the high operating temperatures $\sim 900\,°C$, fast degradation and high costs appear as main issues [15]. Therefore, a first step is to reduce the cell temperature under 800 °C by means of finding materials for electrolytes, electrodes and interconnectors that lead to same high power output than at higher temperatures. To this aim, proton-conducting oxides have been developed as electrolyte materials, which mostly belong to the class of perovskite-based materials [15]. Also costs on interconnection materials have been reduced using ceramic conductive materials as thin protective layers deposited on metallic interconnections [15].

Improving the three-phase boundary leads to a direct increment of the power output.

Optimizations can be performed employing metal and ceramic composites or ionic and electronic mixed conductors (MIEC) [15]: at the cathode, strontium-doped lanthanum manganite (LSM) is generally combined with an ionic conductor such as yttria-stabilized zirconia (YSZ).

Further improvement is still needed for increasing the lifetime, decreasing the costs as well as addressing the difficulties with the production, transportation and storage of hydrogen.

Alkali Metal Thermal to Electric Converter (AMTEC) has been very often defined as a thermoelectric device even if the conversion process of AMTEC and a thermoelectric converter are not the same. In fact, the conversion process of an AMTEC device can be analyzed from two parallel points of view. Thermoelectric converters transform thermal energy into electrical energy. However, heat energy absorbed by the system in AMTEC is combined with a pressure difference across the solid electrolyte to generate an electrochemical potential, enabling as a result the direct transformation of electrochemical energy to electricity. Therefore, the conversion process happening in AMTEC can be described through the same electrochemistry principles as in a galvanic cell. AMTEC has a theoretical efficiency close to that of the Carnot cycle, namely a value of $\sim 45\,\%$ can be theoretically obtained at 800 °C [1]. Previous investigations of AMTEC devices performed at FZK (today KIT) by the group of Heinzel et al. [1] reported efficiencies as high as 25 %, however typical efficiency values given by the literature are $\sim 15\,\%$. Some of the main challenges of AMTEC requiring further investigation are the power loss occurring during long time operation, and the low real efficiency compared to the theoretical value. To deal with these two issues material research is needed for electrolyte, electrode and current collector.

Photovoltaic solar cells (PV) transform the energy from the photons to electricity by means of releasing free electrons coming by a reaction from a p-n junction between two semiconductors (p-type and n-type semiconductors). Earlier photovoltaic solar cells are based on the silicon wafer technology (single crystal, multi-cristalline) and have relative high efficiencies of 12 - 18 % [16], however the production costs are significantly high. In contrast thin film solar cells are 50 % less expensive than conventional silicon cells but their efficiencies are slightly lower (9 - 12 % for Cadmium Telluride (CdT) and Copper Indium Gallium Di-Selenide (CIGS) solar cells) [16]. New promising technologies like concentrated solar cells have been developed that can reach efficiencies as high as 40 % [16], however they are still not commercially attractive mainly due to their high costs. Other PV cells are thin-film solar cells and tandem cells. PVs still have various issues that need to be further optimized: lowering the cost of production, eliminating or

reducing toxic and rare elements and increasing the efficiency of commercial systems [17].

Magnetohydrodynamics (MHD) convert kinetic energy in electricity based on the Faraday's induction law. In an electrically conducting fluid, moving at a velocity $\vec{v}$ in a magnetic field $\vec{B}$, an electromotive force $(\vec{v} \times \vec{B})$ is induced perpendicular to the magnetic field and the direction of the movement of the fluid. If the system is connected to an external load, a current density $\vec{j}$ is induced following Ohm´s law:

$$\vec{j} = \sigma \left(\vec{v} \times \vec{B} \right) \qquad , \qquad (1.3)$$

where σ is the electrical conductivity of the fluid. Finally a force $\vec{f}$ is induced on the fluid in the perpendicular direction to the current density and magnetic field given by the Lorentz law:

$$\vec{f} = \vec{j} \times \vec{B} \qquad . \qquad (1.4)$$

Theoretically high efficiency rates up to $\sim 60\,\%$ should be achievable with MHD generators, however, real values stay underneath at $\sim 20\,\%$ [18]. The main limitation is the required extreme high temperature of the medium of $\sim 1500\,°C$ [18].

All mentioned direct energy conversion systems require further development, despite significant research progress. Table 1.1 summarizes the characteristics of the direct energy conversion systems mentioned above.

Fuel cells and solar cells have reached an optimized technological level, with advanced industrial production. In the field of renewable energies, AMTEC technology has the potential to be an important contributor, especially when coupled to a clean heat source, thanks to the high theoretical efficiency and the regenerative process that allows to reuse the working fluid (sodium) in a closed cycle. Issues concerning AMTEC technology have much to do with the issues of SOFC since both work with a solid electrolyte at high temperatures. Technology improvements in SOFC could be transferred to AMTEC systems to obtain improved cells.

Energy conversion system	T_{max} [℃]	η [%]	Issues
Thermionic converter	$> 1000 - 1500$	10 - 15	Very high operating temperature, material research required
Thermoelectric converter	< 800	< 10	Low conversion efficiencies, material research required, complex assembly
AMTEC	1000	~ 15	Conversion efficiency, lifetime, material research required
SOFC	~ 900	50 - 55	Fuel storage, fuel generation, lifetime, high costs material research required
Solar cell	60	9 - 12	High costs, "environmentally" expensive, low conversion efficiencies
MHD generator	~ 1500 ℃	~ 20	Very high operating temperature

Table 1.1: Comparison of temperature, efficiency and most significant issues of various direct energy conversion technologies.

1.3   State-of-the-art AMTEC and solar thermal energy

One of the most significant advantages of the AMTEC technology is related to its flexibility regarding the heat source. In the field of solar thermal energy AMTEC has aroused interest since the nineties. The main prerequisite for this coupling is the need of concentrating the solar energy with a high concentration ratio, enough to reach high temperatures ≥ 800 °C and thus high efficiencies. The main challenges to design an AMTEC-solar receiver loop are to obtain a stable temperature and to define a liquid return line. Three concept designs of a sodium solar receiver for application in AMTEC have been found in the literature and are presented next; one of them has been tested experimentally.

Tanaka et al. [19] (1990) designed a cylindrical cavity receiver where sodium is heated up by solar concentrated rays in 20 different receiver tubes; each of the receiver tubes contained 4 BASE tubes. The hot sodium vapor carries thermal energy to a latent thermal energy storage (TES) and generation section as represented in figure 1.4, where the BASE tubes and a thermal energy storage are. The temperature of generation section remains almost constant due to the latent thermal energy storage system. The colder vapor reaches a condenser and using an electromagnetic pump it is directed back to the receiver. The calculated total electrical output of the system was 24 % of the total energy coming in through the receiver, however, assuming a relative high AMTEC efficiency of 30 %.

Heinzel et al. [1] (1991) equally considered concentrating solar power for application in AMTEC. They planned a common project with the Plataforma Solar de Almería to use the sodium-cooled solar tower plant for tests on AMTEC cells. Unfortunately after the Almería accident [20], the work stopped.

Tanaka [21] (2010) optimized the former design of the combined system and deleted the section for thermal storage from the system. The combined system was divided in a cylindrical receiver (same as former), a power generating part (containing 20 cell-tubes), condenser and an electromagnetic pump (see figure 1.4). The calculated maximum overall efficiency was 19 % for a 27 % AMTEC system efficiency at 727 °C hot temperature and an electrical power output of 10.3 kW. A power peak of 19.1 kW was calculated at an AMTEC efficiency of 20 % and an overall receiver system efficiency of 17 % at 727 °C.

Wu et al. [22] (2010) designed as well a cylindrical solar receiver for a dish/AMTEC solar thermal power system (see figure 1.5). The design had a concentration ratio of more than 2000 in order to reach temperatures as high as 627 - 1027 °C. The evaporator of the system is placed at the solar absorber and is adjustable to the dish rotation. Two different concepts were developed: i) a combined dish/AMTEC system with an electromagnetic pump and ii) a combined system with capillary pumped loop. In both
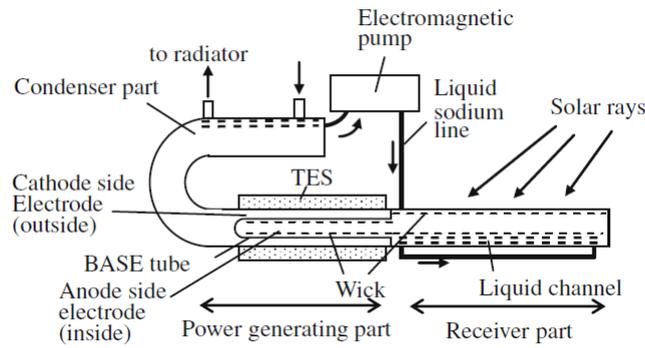
Figure 1.4: Optimized design of a vapor-anode AMTEC cell and solar receiver combination by Tanaka et al. [21].
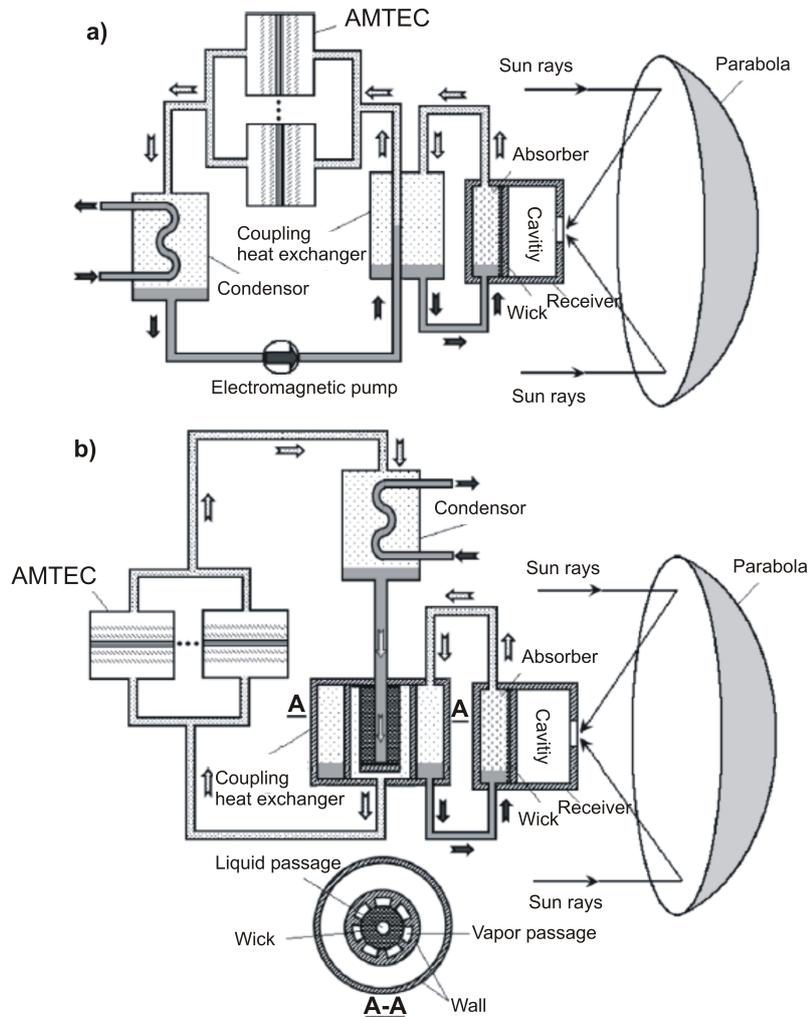

Figure 1.5: Combined system of a dish/AMTEC solar thermal power system; (a) with an electromagnetic pump; (b) with a capillary pumped loop [22].

cases the system consists of two separated sodium loops; one at the receiver and the other one in the AMTEC system loop. The design includes a heat exchanger to transfer the heat from one loop to the other one. The peak system efficiency was calculated to be 20.6 % at an operating temperature of 1007 °C for an AMTEC efficiency of $\sim$ 26 % and a power output of 18.54 kW.

In 2015 Boo et al. [23] designed and constructed a small sodium solar receiver system (800 - 1100 W thermal energy) for AMTEC applications (see Figure 1.6) that is provided with an evaporator and a condenser connected by a sodium loop. The evaporator is located on the side of the solar reflectors to collect the solar thermal energy and give it to the AMTEC system through the condenser. The sodium loop of the receiver system works independently from the AMTEC system and consists of two separated lines for vapor and liquid sodium. This configuration allows the use of a loop-type thermosyphon if the condenser of the receiver loop is located higher than the evaporator, eliminating the return line problem. For the experimental tests, however, a capillary structure in the liquid line was used to avoid formation of a solid plug in the liquid line. Operating under natural convection conditions, steady state was reached after 1.5 to 2 hours. This design had some problems by obtaining an uniform distribution of temperature in the condenser side of the receiver (temperature differences of 80 °C at 1100 W thermal). The heat losses were relative high; a temperature drop between evaporator and condenser of 90 - 180 °C was measured.
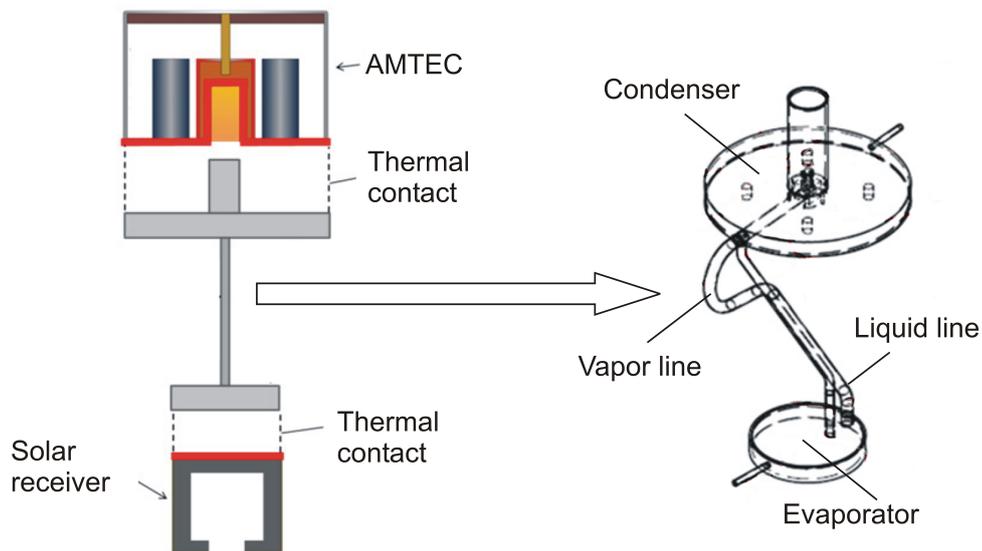

Figure 1.6: Sketch of a sodium solar receiver system for AMTEC application provided with a Na-loop with separated lines for liquid and vapor sodium [23].

1.4   Aim and structure of the work

At the Karlsruhe Institute of Technology (KIT), Institute for Neutron physics and Reactor technology (INR), research on AMTEC technology has been resumed focusing on the use of concentrating solar energy as heat source of an electrochemical converter. This work serves as primary step towards the visionary *AMTEC & CSP 2.0* concept. The aim is to develop a layout and engineering solutions for the construction, set into operation and first operation of an AMTEC Test Facility (ATEFA) and an AMTEC test cell by using state-of-art technologies within the Helmholtz AMTEC Center (HAC) that is funded by the HEMCP (Helmholtz Energy Material Characterization Platform) and supported by the LIMTECH Alliance (LIquid MEtal TECHnology). For this purpose a data acquisition and control system has been developed for a safe operation of the facility. An experimental procedure has also been developed taking into consideration handling solutions for high-temperature liquid sodium. ATEFA is designed for short term experiments on AMTEC cells and focuses on the proof of concept of the AMTEC technology and on the analysis of the cell behavior at different operating conditions of temperature and pressure.

Assuming the main developments reported in the literature on AMTEC cells and the still existing challenges, a basic cell design has been elaborated based on the work of Heinzel et al. [2]. A detailed characterization of AMTEC technology is first given in section 2 and solutions for performance improvement are proposed. Section 3 provides a detailed overview of the main developments presented in the AMTEC literature. The main challenges regarding the development of AMTEC test cells are connected to the development of: i) porous cathode coating of the solid electrolyte, ii) high-temperature ceramic-metal joint and iii) the chemical stability of the ceramic electrolyte. Section 4 summarizes the main numerical models that describe the pressure loss and the electro-chemical processes occurring in the cell. Section 5 deals with the experimental setup of the work and sections 6 and 7 present the experimental results on AMTEC components and AMTEC performance respectively. In section 8 the major achievements are summarized and an outlook on research and development (R&D) challenges is formulated.

2 Alkali Metal Thermal to Electric Converter (AMTEC)

This section focuses on the fundamentals of electrochemical cells, which are further specified for AMTEC cells and finishes with a description of the AMTEC components. The fundamentals of electrochemical cells are given based on thermodynamics, electrochemistry, kinetics and mass transport. The operating principle of AMTEC is explained and the losses appearing in the process are discussed. Subsequently, the main components of AMTEC cells are presented (BASE, porous electrode, current collector and fluid conditioning), and their functionality in the AMTEC process is addressed. The possibilities of a modular connection are as well discussed. The chapter finishes with the description of the main fields of application of the technology.

2.1 Fundamentals of electrochemical cell

2.1.1 Thermodynamics

According to the first law of thermodynamics and the conservation of energy, in a closed system any change in the internal energy of the system ΔU has to be balanced by the exchange of heat ΔQ and work ΔW

$$\Delta U = \Delta Q + \Delta W \qquad . \tag{2.1}$$

The second law of thermodynamics says that the heat in a reversible processes at constant temperature can be calculated in terms of entropy ΔS and temperature T:

$$\Delta Q = T \Delta S \qquad . \tag{2.2}$$

The work done in an electrochemical system, which undergoes a reversible process at constant temperature T and pressure p, is composed of a mechanical part and an electrical part:

$$\Delta W = \Delta W_{mech} + \Delta W_{elec} = -p \Delta Vol + \Delta W_{elec} \qquad , \tag{2.3}$$

where ΔVol represents the volume change involved in the mechanical work.

The change in enthalpy ΔH and Gibb's free energy ΔG of the system at constant pressure and temperature can be expressed as follows:

$$\Delta H = \Delta U + p \Delta Vol \qquad , \tag{2.4}$$

$$\Delta G = \Delta H - T \Delta S \qquad . \tag{2.5}$$

The Gibbs free energy represents the maximum reversible work performed by a thermodynamic system at constant pressure and temperature. Combining equations (2.1) to (2.5), the Gibb's free energy is simplified to:

$$\Delta G = \Delta W_{elec} \qquad , \tag{2.6}$$

which means that in an electrochemical system, ΔW_{elec} is the maximum reversible energy dissipated through a load resistance. Thus referring to equation (2.5), the maximum amount of electrical energy available in the system is ΔG, the total thermal energy available is ΔH and the amount of heat produced by the electrochemical cell in a reversible process is $T\Delta S$. The electrical energy of the system can be expressed as:

$$\Delta G = -q\Delta E = -nFE \qquad , \tag{2.7}$$

where q is the electric charge, n is the number of moles of electrons transferred in the overall chemical reaction, $F = 9.64 \cdot 10^4$ As/mol represents the Faraday constant and E the potential of the electrochemical cell. When the cell is under standard conditions ($T = 25\,°C$, $p = 1$ atm) and all the components are at unit activity, then the standard Gibb's free energy ΔG^0 is:

$$\Delta G^0 = -nFE^0 \qquad . \tag{2.8}$$

According to the second law of thermodynamics, $\Delta G < 0$ if the chemical process is spontaneous and $\Delta G > 0$ if non-spontaneous. At equilibrium $\Delta G = 0$. The Gibb's free energy is also related to the chemical potential μ of a system with constant temperature and pressure [24]:

$$\mu_i = \left(\frac{\partial G}{\partial l_i}\right)_{T,P} \qquad , \tag{2.9}$$

where l is the particle number of species i in the reaction. If the system includes charged species, an electrochemical potential $\bar{\mu}$ can be defined as [24]:

$$\bar{\mu}_i = \mu_i + z_i F\Phi = \mu_i^0 + R_g T ln a_i + n_i F\Phi \qquad , \tag{2.10}$$

here Φ is the inner electric potential of the phase, a the activity coefficient of the species, R_g the universal gas constant and n the number of electrons transferred in the overall chemical reaction.

Nernst equation. According to chemical thermodynamics, the change in the Gibbs free energy of a chemical reaction $\alpha A + \beta B \longleftrightarrow \gamma C + \delta D$ is:

$$\Delta G = \Delta G^0 + R_g T \, ln \frac{\sum a_{Products}}{\sum a_{Reactants}} = \Delta G^0 + R_g T \, ln \frac{(a_C)^\gamma \, (a_D)^\delta}{(a_A)^\alpha \, (a_B)^\beta} \qquad , \qquad (2.11)$$

where T is the absolute temperature in Kelvin [K] and a represents the activity coefficient of the species (A, B, C and D). At equilibrium $\Delta G = 0$ equation (2.11) reduces to:

$$\Delta G^0 = -R_g T \, ln K_{eq} \qquad , \qquad (2.12)$$

being K_{eq} the equilibrium constant of the reaction. Substituting equations (2.7) and (2.8) in equation (2.11), then the Nernst equation is derived:

$$E = E^0 - \frac{R_g T}{nF} \, ln \frac{(a_C)^\gamma \, (a_D)^\delta}{(a_A)^\alpha \, (a_B)^\beta} \qquad , \qquad (2.13)$$

more commonly expressed with inverted sign of the logarithmic term:

$$E = E^0 + \frac{R_g T}{nF} \, ln \frac{(a_A)^\alpha \, (a_B)^\beta}{(a_C)^\gamma \, (a_D)^\delta} \qquad . \qquad (2.14)$$

2.1.2 The double layer

In the previous subchapter the bulk electrode-electrolyte system was contemplated as a system without the consideration of the interfacial region between the phases. However the structure of the interfacial region influences the chemical reaction processes in the system. Assuming a solid-solution electrochemical system, a charged solid surface in contact with a solution will attract ions of opposite charge and repeal ions of equal charge, thus establishing a potential gradient at the electrode-electrolyte interface that shows a capacitor behavior. The interfacial region in the solution is known as the *electrolyte double layer* and the interfacial region in the solid, the *space-charge region*, both represented in figure 2.1.

The *space-charge region* in solid metals is very thin, owing to the high polarizability of metals. Electrons from the solid penetrate a very small distance into the solution [25] and therefore the electrostatic potential in the metal decreases gradually at the surface of the solid as shown in figure 2.2 (b). However, since the solution side of the interfacial region has been historically more of interest than the solid side, the space-charge region has been neglected in the models described below, which consider an ideally polarizable solid with a constant electrostatic potential as depicted in figure 2.2 (a).
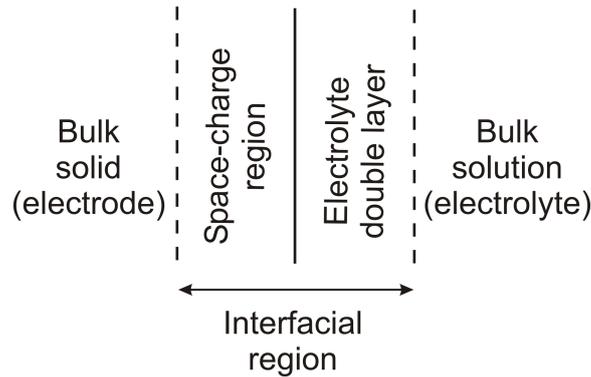
Figure 2.1: Schematic illustration of the solid-solution interface (modified according to [25]).
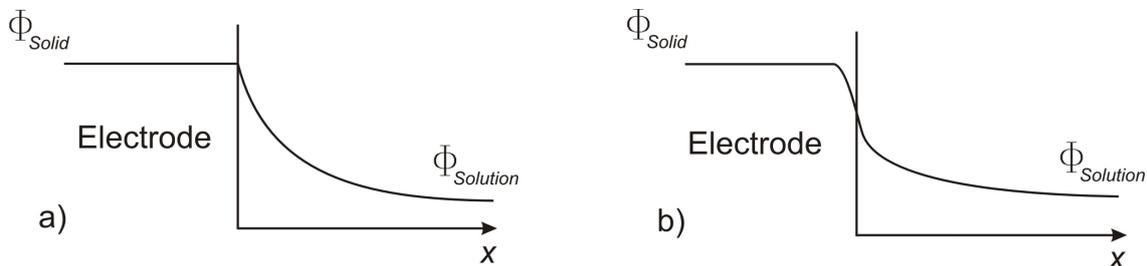
Figure 2.2: Variation in the interfacial region of the inner electric potential at the electrode with distance *x*. a) ideally polarizable solid, b) solid with space-charge region (modified according to [25]).

The following three basic models of the electrolyte double layer are described below: the Helmholtz model, the Gouy-Chapman model and the Stern model. A schematic representation of the models is provided in figure 2.3.

Helmholtz model   assumes that the excess charge in the solid is located at the surface and that the solution side exactly neutralizes this excess charge by generating an opposite charge located in a parallel plane very close to the solid surface (comparable to a parallel-plane capacitor). This plane is known as the *Outer Helmholz Plane* (OHP). As depicted in figure 2.3 (left), the Helmholtz model assumes a linear decrease of the electric potential over the thickness of the OHP, from its surface value to the bulk value in the solution. The main advantage of this model is its simplicity, however, it assumes a constant capacity, neglecting thereby the dependency of the double-layer capacitance on the potential and the solution composition [24].

Gouy-Chapman model   assumes that ions are subjected to random thermal motion and, therefore, are not immobilized on the surface as predicted by Helmholtz. The neutralization of the excess charge is thus given by ions spread out into the solution,
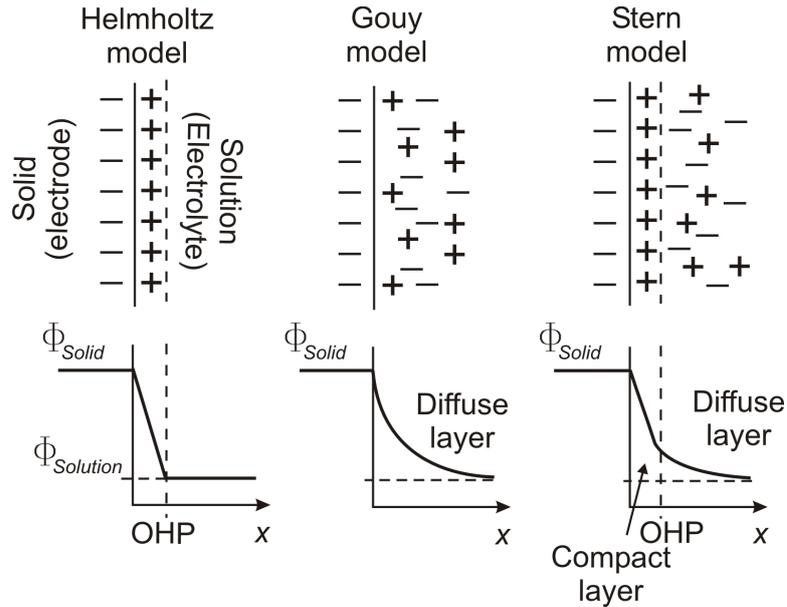
Figure 2.3: Schematic representation of the three main models of the double layer in a solid-solution system and the distribution of the electric potential within the interfacial region assuming an ideally polarizable solid (modified according to [26]).

creating the so called *diffuse double layer*. The potential in the interfacial region at the solution side falls slower than in the Helmholtz model, as shown in figure 2.3 (middle). The Gouy-Chapman model predicts well the dependency of the double-layer capacitance on the applied potential and on the ionic concentrations; however, limited to very dilute solutions [24].

Stern model   combines the last two models and their advantages. The ions located at the OHP form a *compact double layer* (Helmholtz layer), and the potential falls linearly and rapidly. These ions are usually not enough to completely neutralize the charge; the rest of the charge is neutralized by a *diffuse layer* (Gouy layer) that extends out into the solution. At high ionic concentration, the diffuse double layer can be neglected [24].

In an AMTEC cell, both electrodes are metals and are therefore highly polarizable. However, the solid electrolyte is considered a solid semiconductor and the space-charge region is, therefore, larger than in metals. *"It is suggested that the structure of the metal-solid electrolyte interface is similar to that of the metal-liquid electrolyte interface [...]. However [...] there are a number of situations at the metal electrolyte interface which are unique to that interface, e.g.: 1. Whereas in a liquid electrolyte ions can take up any position outside the distance of closest approach, in a solid the possible positions are quantised; 2. The Debye length in the electrolyte may be comparable with a lattice spacing; 3. The absence of solvent molecules in a solid; 4. The region of*

17

electrolyte closest to the metal may be atypical" [27]. In the literature, several models for the metal-solid electrolyte interface are presented: e.g. [27, 28]; moreover, latest presented mathematical models characterize the metal-electrolyte interface based on the computed differential capacitance e.g. [29].

2.1.3 Basic electrode kinetics

An electrochemical reaction is characterized by an electrode potential E_e (half-cell potential), which is responsible for the exchange of electrical current across the electrode interface in opposite directions. Considering that in the electrode the reduction is the forward (cathodic) reaction, subscript f, and the oxidation the backward (anodic) reaction, subscript b, the following reaction takes place:

$$Ox + e \rightleftharpoons Red \qquad . \tag{2.15}$$

At equilibrium, both partial currents are equal to the exchange current: $j_0 = j_f = j_b$, but opposite in direction. Therefore, the net current is: $j = j_f - j_b = 0$. The *exchange current* j_0 represents the charge transfer that appears due to the continuous reaction activity in the cell that balances an equilibrium state.

If the electrode potential is moved from equilibrium: $E_e \neq E_{eq}$, a net current j will flow across the electrochemical cell. The *overpotential* ξ is defined as the deviation of the electrode potential from the equilibrium value:

$$\xi = E_a - E_{eq} \qquad , \tag{2.16}$$

and measures the amount of electrical energy dissipated to overcome the reaction resistances.

Electron transfer to and from the electrode occurs at the highest occupied energy level (*Fermi level*). Electrons are transferred between the Fermi level E_F and the energy level of the redox reaction E_{Redox} in the electrolyte [25]. By applying a potential to the electrode, the highest occupied electronic level (E_F) is altered as shown schematically in figure 2.4. E_F represents the electrochemical potential of the electrons in the metal electrode phase.

Butler-Volmer equation.   The reaction rate constant k^r of an electrochemical reaction follows the Arrhenius equation:

$$k_f^r = \frac{\kappa T}{h_P} exp\left(-\frac{\triangle G^c}{RT}\right) \qquad , \qquad k_b^r = \frac{\kappa T}{h_P} exp\left(-\frac{\triangle G^a}{RT}\right) \qquad , \tag{2.17}$$
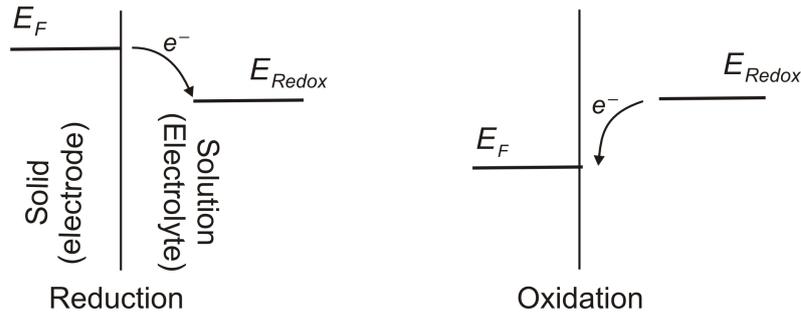
Figure 2.4: Schematic representation of electron transfer process at an inert metallic electrode. The highest occupied electronic level E_F changes with the applied electrode potential: reduction (negative electrode potential) or oxidation (positive electrode potential). (Modified according to [25])

where superscripts a and c represent respectively the cathode and anode, $\kappa = 1.38 \cdot 10^{-23}$ J/K is the Boltzmann constant, h_P the Planck constant and $\triangle G$ is the standard electrochemical free energy of activation. The potential dependence of $\triangle G$ is shown schematically in Figure 2.5. When applying a potential $E = \Delta\Phi$ to the cathode, the free energy of activation for the forward reaction $\triangle G^c$ decreases, while increases the free energy of activation for the backward reaction $\triangle G^a$. For the transfer of one electron $n = 1$, the free energy changes as follows:

$$\triangle G^c = \triangle G^{0c} - \alpha F E \qquad , \qquad \triangle G^a = \triangle G^{0a} + (1-\alpha)F E \qquad , \qquad (2.18)$$

in which α is the electrochemical transfer coefficient.
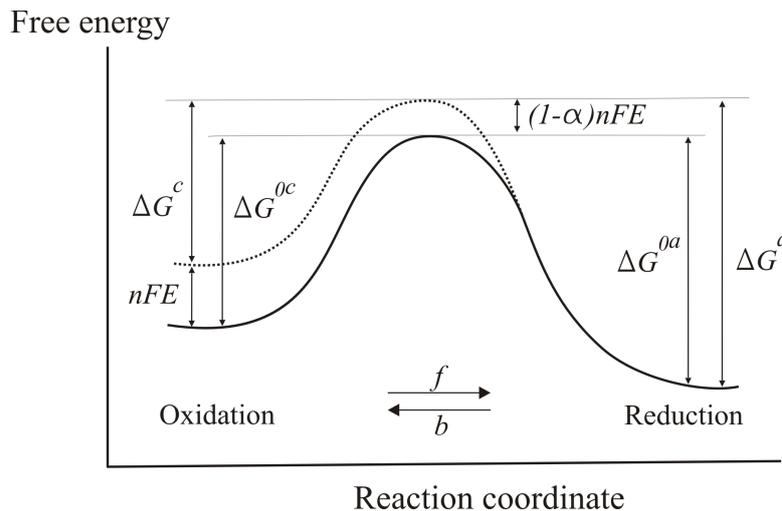
Figure 2.5: Free energy - reaction coordinate diagram for an electron-transfer process. Representation of the dependence of the electrochemical energy of activation on the applied potential E.

As a result, the rate constants can be expressed as:

$$k_f^r = \frac{\kappa T}{h_P} exp\left(-\frac{\triangle G^{0c}}{RT}\right) exp\left(\frac{\alpha EF}{RT}\right) = k_f^{r0} exp\left(\frac{\alpha EF}{RT}\right) \quad , \quad (2.19)$$

$$k_b^r = \frac{\kappa T}{h_P} exp\left(-\frac{\triangle G^{0a}}{RT}\right) exp\left(-\frac{(1-\alpha)EF}{RT}\right) = k_b^{r0} exp\left(-\frac{(1-\alpha)EF}{RT}\right) \quad , \quad (2.20)$$

where k^{r0} represents the two first factors of the expression, which are independent of the potential. The partial forward and backward current densities can be calculated through:

$$j_f = -Fk_f^r C_O \quad , \quad j_b = Fk_b^r C_R \quad . \quad (2.21)$$

C_O and C_R denote the concentrations of reduction and oxidation at the electrode surface. At equilibrium, the concentrations are equal to the bulk concentrations C_O^0, C_R^0. Assuming $C_O^0 = C_R^0$ and considering the Nernst equation, the applied potential becomes $E = E^0$, which is the standard potential of the electrode reaction. Under these conditions the net current density is zero, therefore $k_f^r = k_b^r$.

$$k_f^{r0} exp\left(\frac{\alpha E^0 F}{RT}\right) = k_b^{r0} exp\left(-\frac{(1-\alpha)E^0 F}{RT}\right) = k_s^r \quad , \quad (2.22)$$

where k_s^r is the standard heterogeneous rate constant of the electrode reaction. j is given by:

$$j = j_b + j_f = F\left(k_b^r C_R - k_f^r C_O\right) \quad , \quad (2.23)$$

$$j = Fk_s^r \left\{ C_R\, exp\left(\frac{\alpha(E-E^0)F}{RT}\right) - C_O\, exp\left(-\frac{(1-\alpha)(E-E^0)F}{RT}\right)\right\} \quad . \quad (2.24)$$

At equilibrium $j = 0$. Substituting concentrations for activities, the Nernst equation yields:

$$\frac{C_O^0}{C_R^0} = exp\left(\frac{\left(E_{eq} - E^0\right) F}{RT}\right) \quad . \quad (2.25)$$

At the given conditions, and after performing some tedious algebra, the exchange current can be represented by [25]:

$$j_0 = FAk_s^r \left[C_R^0\right]_\infty^{(1-\alpha)} \left[C_O^0\right]_\infty^\alpha \quad . \quad (2.26)$$

Assuming that $[C_O^0]_\infty = [C_R^0]_\infty$, the net current is obtained dividing equations (2.24) and

(2.26), expressed in terms of the overpotential ξ:

$$j = j_0 \left\{ \frac{C_R}{C_R^0} exp\left(\frac{\alpha F\xi}{RT}\right) - \frac{C_O}{C_O^0} exp\left(-\frac{(1-\alpha)F\xi}{RT}\right) \right\} \qquad . \qquad (2.27)$$

This is called the Butler-Volmer equation. The first term represents the effect of the anode (backward), while the second term reflects the cathode effect (forward). If the mass-transport limitation is neglected, $C_O = C_O^0$ and $C_R = C_R^0$, then:

$$j = j_0 \left\{ exp\left(\frac{\alpha F\xi}{RT}\right) - exp\left(-\frac{(1-\alpha)F\xi}{RT}\right) \right\} \qquad . \qquad (2.28)$$

A schematic representation of the current-overpotential relationship is given in figure 2.6 for $\alpha = 0.5$. In equilibrium both absolute values j_f and j_b are equal to j_0 and the net current is zero.
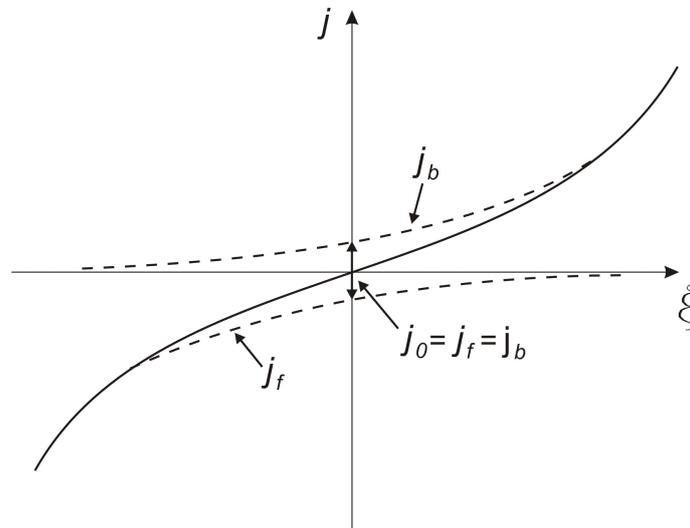

Figure 2.6: Current-overpotential diagram (j, ξ) for an electrode reaction with $\alpha = 0.5$. j_f and j_b are, respectively, the forward and the backward partial currents. j_0 is the exchange current in equilibrium.

Tafel equation.   At high overpotentials ξ, one of the terms in equation (2.28) becomes negligible:

$$\text{if} \quad | \alpha F\xi/RT | \gg 1 : \qquad j = j_0\, exp\left(\frac{\alpha F\xi}{RT}\right) = j_b \qquad , \qquad (2.29)$$

$$\text{if} \quad | -(1-\alpha)\, F\xi/RT | \gg 1 : \qquad j = -j_0\, exp\left(-\frac{(1-\alpha)F\xi}{RT}\right) = j_f \qquad . \qquad (2.30)$$

These are the *Tafel equations* for the electrode reaction. The logarithmic current-potential relationship of equation (2.29) is:

$$ln\,j = ln\,j_0 + \frac{\alpha F \xi}{RT} \qquad .$$

(2.31)

A representation of equation (2.31) is shown in figure 2.7. There is a linear relationship that starts from a minimum current density, the exchange current density j_0. The Tafel plot represents the correlation between the exchange current and the overpotential and suggests that the current increases exponentially with the overpotential. The slopes of the lines $K_t = -(1-\alpha)\,nF/RT$ and $K_t = \alpha nF/RT$ intercept at $\xi = 0$ as shown in figure 2.7, where $j = j_0$, and the plotted lines deviate due to the double direction of the reaction. The Tafel slope is high for those chemical reactions that are slower. A high Tafel slope involves a small change in overpotential (voltage drop) with a large change in current. This results in higher cell performance and lower slope of the characteristic current-voltage (I-V) curve. The larger the exchange current density j_0, the larger is the cathalysis effect of the porous cathode.
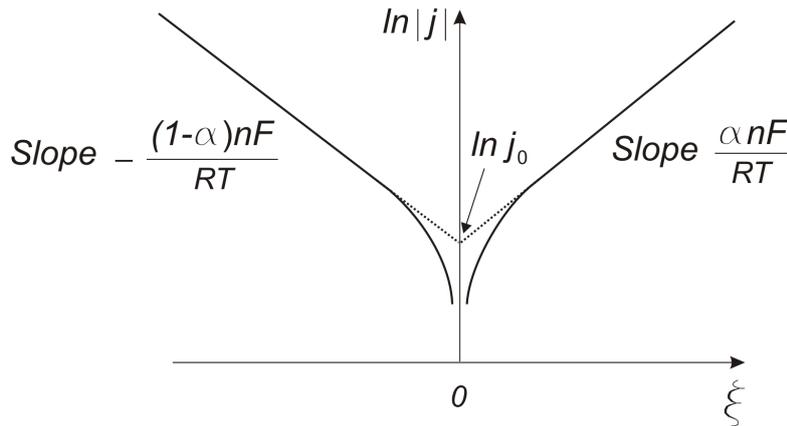

Figure 2.7: Plot of the Tafel equation showing how to obtain j_0 and α from the slopes.

2.1.4 Mass transport limitations in electrode reactions

The mass transport in the electrode is affected by the following processes [24]: a) diffusion, the stochastic transport of species originated through concentration gradients, b) migration, the transport of charged species driven by the electric field, and c) convection (natural or forced), the transport of species caused by hydro-dynamic motion of the liquid.

During the electron reaction process, reactants are consumed and products accumulated near the electrode surface. Since mass transfer processes are in most cases more slowly than interfacial charge transfer processes, the global rate of the electrode reaction is limited by diffusion [30]. In such cases, the concentration of the

reactants/products at the reaction site differ from their respective bulk concentrations. Figure 2.8 shows a sketch of the change in the concentration of a reactant along the thickness δ of the double layer. In case 1 no net current flows and thus the concentration remains constant. An increasing current flow through the system yields a rising concentration gradient (cases 2 and 3).
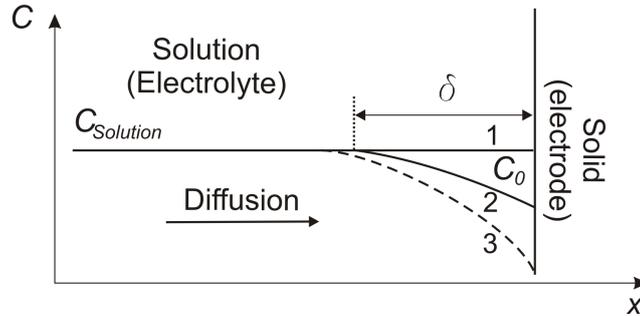

Figure 2.8: Scheme of the change in the concentration of a reactant along the thickness δ of the double layer under diffusion limitation process. Case 1 is in equilibrium $j_1 = 0 \, \text{A/m}^2$, while cases 2 and 3 $j_3 > j_2 \neq 0$ (Figure modified according to [30]).

The rate of diffusion depends on the concentration gradients according to the *Fick's first law*:

$$J_f = -D\frac{\partial C}{\partial x} \qquad , \tag{2.32}$$

where J_f is the flux of species (the amount of species that flows through a unit area during a unit time interval, [mol/m^{2}s]), D is the diffusion coefficient [m^2/s] and $\partial C/\partial x$ is the concentration gradient in direction x of a plane surface.

The variation of the concentration in time in a one-dimensional system is given by *Fick's second law*, which reads to:

$$\frac{\partial C}{\partial t} = D\frac{\partial^2 C}{\partial x^2} \qquad . \tag{2.33}$$

Solving the solution of Fick's second law gives the diffusion-limited current. For a planar electrode, the electric current is:

$$J = nFAJ_f = nFAD\left(\frac{\partial C}{\partial x}\right)_{x\to 0} \qquad , \tag{2.34}$$

at x distance from the electrode. To solve the Fick's second law, we define the following boundary conditions:

$$t = 0, \qquad C_0 = C_\infty \qquad \text{(no electrode reaction, homogeneous solution)} \qquad , \tag{2.35}$$

$$t \geq 0, \qquad \lim_{x \to \infty} C_0 = C_\infty \qquad \text{(stable bulk solution)} \qquad , \qquad (2.36)$$

$$t > 0, \ x = 0 \qquad C_0 = C_0 \, (x = 0) \qquad \text{(diffusion-limited current)} \qquad , \qquad (2.37)$$

in which C_0 represents the concentration at the electrode and C_∞ the concentration in the bulk solution. Considering the diffusion-layer thickness δ by a linear extrapolation of $\left(\frac{\partial C}{\partial x}\right)_{x \to 0}$, the current is given by:

$$J = nFAD \frac{[C_\infty - C_0 \, (x = 0)]}{\delta} \sim t^{-1/2} \qquad . \qquad (2.38)$$

Assuming that δ is given by the Einstein-Smoluchowski equation:

$$\delta = \sqrt{\pi D t} \qquad , \qquad (2.39)$$

where t is the time. The diffusion-controlled electric current J is given by:

$$J = \frac{nFAD^{1/2} \, [C_\infty - C_0 \, (x = 0)]}{\sqrt{\pi t}} \qquad . \qquad (2.40)$$

The current decreases with $t^{1/2}$. The maximum limiting current J_L is reached at large overpotentials, when $C_0 = 0$, which results in the Cottrell equation:

$$J_L = \frac{nFAD^{1/2} C_\infty}{\sqrt{\pi t}} \qquad . \qquad (2.41)$$

The diffusion layer thickness δ can be defined as:

$$\delta = (\pi D t)^{1/2} \qquad , \qquad (2.42)$$

which also increases with $t^{1/2}$. The increment of the diffusion layer thickness is represented in figure 2.9 for equation (2.41), when $C_0 = 0$ (Cottrell conditions).

If in a one-dimensional system, the fluid is subjected to both, convection and diffusion processes; then the flux J of species is defined as:

$$J = Cv - D \frac{\partial C}{\partial x} \qquad , \qquad (2.43)$$

in which v is the velocity of the species. This modifies Fick's second law to:

$$\frac{\partial C}{\partial t} = -v \frac{\partial C}{\partial x} + D \frac{\partial^2 C}{\partial x^2} \qquad . \qquad (2.44)$$

Referring to the AMTEC conditions, the cathode electrode is a porous body. In
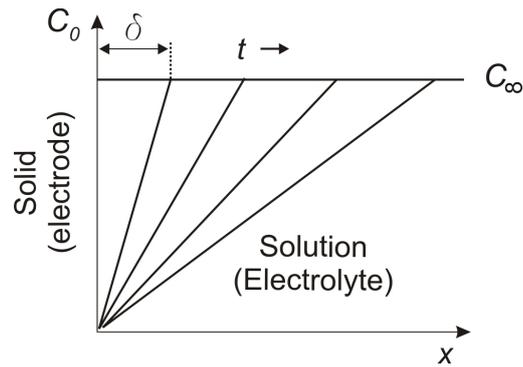
Figure 2.9: Schematic representation of the change in the electrode concentration and diffusion layer thickness with time at Cottrell conditions, $C_0 \left(x = 0 \right) = 0$ (Figure modified according to [24]).

case of relevant cathode porosities, the flow velocity is low and also the concentration gradient, hence the diffusive part in equation (2.44) dominates.

2.2   Fundamentals of AMTEC cell

2.2.1   General operating characteristics

The Alkali Metal Thermo-electric Converter is a concentration cell that uses a heat source to derive the conversion of electrochemical energy to electricity. The electrical transfer is divided into an electronic and an ionic charge transfer. As a result, the electron transfer can be utilized to feed an external load with electric current while the ionic transport is done within the ATMEC system. To separate the electron from the ionic charge transfer, a material is required satisfying the following conditions: electrically insulating, conductive for ions and impermeable to fluids (gas or liquid). The component that performs these functions is called electrolyte.

The interfaces at which the electronic/ionic separation/recombination occurs are the electrodes. At the cathode the transferred electrons combine with a positively charged ion (half-cell equation (2.45)) and the reduction reaction occurs, thus the cathode is positively charged. At the anode the oxidation reaction takes place (half-cell equation (2.46)) and the net charge is negative. Since the oxidation and reduction products in AMTEC are the same, an alkali metal, AMTEC cells can be considered a zero net fuel consumption technology if the obtained sodium at the cathode is further redirected to the anode. In this work the chosen alkali metal is sodium as it is the most commonly used metal in this kind of converter; therefore, the following explanations are made for the specific case of a Na-AMTEC cell. A brief introduction to the different alkali metals for the AMTEC technology is given in subchapter 2.3.4.

$$\text{cathode side (reduction)} \qquad Na^+ + e^- \rightarrow Na \qquad , \qquad (2.45)$$

$$\text{anode side (oxidation)} \qquad Na \rightarrow Na^+ + e^- \qquad . \qquad (2.46)$$
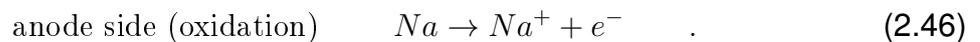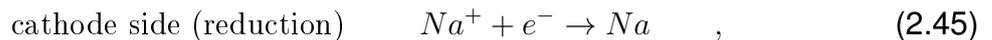
According to the electrolyte temperature, AMTEC cells are categorized in liquid-anode or vapor-anode cells. At temperatures lower than the boiling point of sodium ($<$ 880 °C), liquid-anode cells use molten sodium as electrically conductive anode. Due to the high process temperatures, liquid sodium, that is in direct contact with the BASE surface, provides a good wetting of the electrolyte surface and therefore, from an electrochemical point of view, liquid-anode cells exhibit negligible polarisation losses. Above the boiling point of sodium, vapor-anode cells need an additional porous and electrically conducting anode due to the poor electric conductivity of sodium vapor. This porous material acts as interface for the oxidation reaction. Here, a liquid-anode AMTEC cell is selected to reduce polarisation losses at the anode and to implement a more simplified cell construction. At the cathode sodium is reduced and appears in vapor form,

therefore a porous and electrically conducting material is required.

Figure 2.10 shows the schematic setup of an AMTEC cell. The anode is separated from the cathode by a ceramic electrolyte called ß"-Alumina Solid Electrolyte (BASE). The anode side is filled with sodium and heated up to 600 - 1000 °C at relative high pressure (~ 0.1 MPa). High temperatures > 600 °C are needed to increase the ionic conductivity of the electrolyte. The cathode side is confined with sodium vapor at vacuum conditions and is cooled down at the condenser to < 400 °C. The colder liquid sodium is then collected and redirected back to the hot side of the cell for instance using an electromagnetic pump or a wick that applies capillary forces.
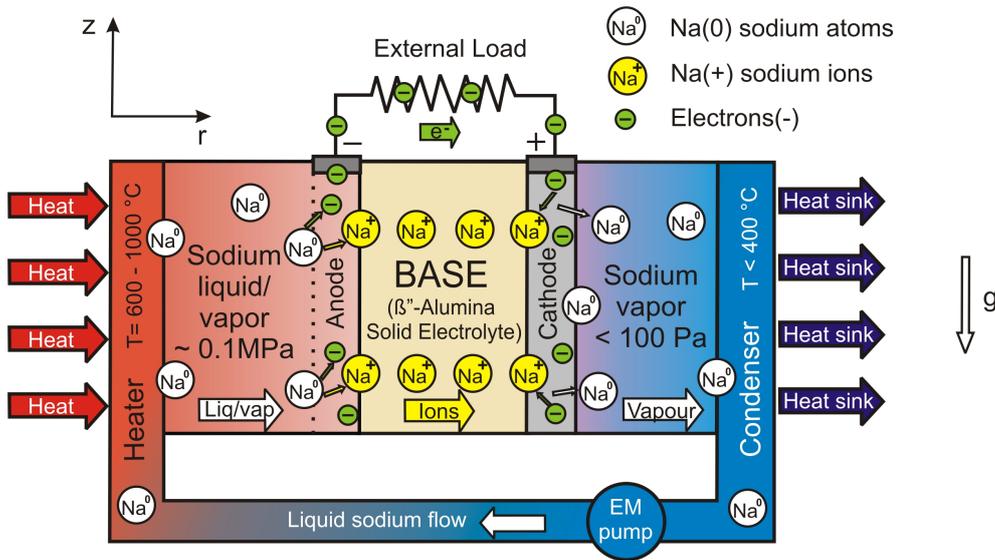
Figure 2.10: Functional principle of AMTEC (modified according to [31]).

A pressure difference is applied across the electrolyte that generates an electrochemical imbalance. Consequently, the system tends to balance it by oxidizing sodium atoms at the anode side and further diffusion of ions through the electrolyte to the cathode side. Connecting electrically both electrodes of the cell through an external load leads to the travel of the electrons released in the sodium reduction (at the anode) to the cathode generating thereby electricity. At the inner cathode surface, electrons recombine with sodium ions to generate sodium vapor. When the transferred electrical charge exchange between electrodes is blocked, the system generates an open circuit voltage (OCV) at electrochemical equilibrium. The Nernst equation (2.47) represents the theoretical OCV for an AMTEC cell in terms of the sodium vapor pressure at the anode and cathode, p_a^{oc}, p_c^{oc}:

$$E_{cell} = V^{oc} = \frac{R_g T_B}{F} ln \left[p_a^{oc}/p_c^{oc} \right] \qquad , \qquad (2.47)$$

where T_B represents the mean temperature of the BASE in Kelvin [K], $R_g = 8.314$ J/mol K

the universal gas constant and $F = 9.64 \cdot 10^4$ As/mol the Faraday constant. Typical experimentally obtained values in AMTEC cells are $V^{oc} = 0.6$ - 1.2 V.

The technical realization of the AMTEC cell is based on the form of ceramic electrolyte, which is tubular. Figure 2.11 depicts a scheme of an AMTEC test cell. The BASE is the central part of the cell and is closed at the lower end to retain the liquid sodium anode, which is pressurized with argon and heated up through a heater (electrical resistance) wrapped in a spiral form. The outer side of the BASE tube is coated with three porous cathodes and covered with a current collector structure. The current collector is electrically connected to a current lead that drives the electric current to an external load. The cathode-side of the cell contains sodium vapor at a very low pressure, which is cooled and condensed at the condenser surface. The latter is cooled by air. The ceramic electrolyte is held by a niobium transition part (Nb-brazing) coupled to the ascending metallic pipe located at the central flange, which prevents high thermal stresses at the BASE due to the similar thermal expansion coefficient than that of the BASE.


Figure 2.11: Scheme of the AMTEC test cell with a coaxial design.

2.2.2   Basic thermodynamics

Thermodynamic laws are applied in steady state or equilibrium. A transition from one state to another is therefore calculated in several steps, which are individually assumed to be in equilibrium. In an electrochemical process, the net change in U before and after the reaction is therefore $\Delta U = \triangle Q + \triangle W$. Considering AMTEC a closed control volume (represented in figure 2.10 and excluding the heat source/sink and the external load), then $\triangle U = 0$. Consequently the thermal efficiency η_{th} of a thermodynamic system that converts heat to work, can be expressed as the ratio between the total work output W_{out} and the total heat input Q_{in}

$$\eta_{th} = \frac{W_{out}}{Q_{in}} \qquad . \tag{2.48}$$

The Carnot cycle is the reference thermodynamic system described by isothermal and isentropic state changes and represents the most efficient thermal machine. Its ideal maximum thermal efficiency can be calculated for given inlet and outlet temperatures as follows:

$$\eta_{th} = 1 - \frac{T_{out}}{T_{in}} \qquad . \tag{2.49}$$

From equation (2.49) can be concluded that in order to maximize the Carnot efficiency the outlet temperature T_{out} has to be decreased and the inlet temperature T_{in} increased. A Carnot cycle with equivalent temperatures to those of the AMTEC system has a maximum efficiency referred to the temperature of the BASE (T_{in}) and to the temperature at the condenser (T_{out}).

During the AMTEC process sodium passes through five different thermodynamic states. Figure 2.12 shows a diagram of the thermodynamic process of AMTEC in terms of temperature versus entropy. First, the fluid is heated at constant pressure p_B up to the operating converter temperature T_B, reaching thereby state 2. The electrochemical process takes place between $2 - 3$; it includes the vaporization of liquid sodium at the anode surface ($2 - 2'$) and the isothermal expansion of sodium vapor at T_B ($2' - 3$) at the cathode. Once the steam has passed through the electrode and the chamber between the electrode and condenser, it is cooled down to T_{cd} ($3 - 4$) and condenses at the condenser surface ($4 - 5$). By using for instance a pump, liqiud sodium can be returned to its initial state 1.

The total work output corresponds to the work obtained in the isothermal process W_{23}, minus the work used to pump the liquid sodium W_{51},

$$W_{out} = W_{23} - W_{51} \qquad . \tag{2.50}$$
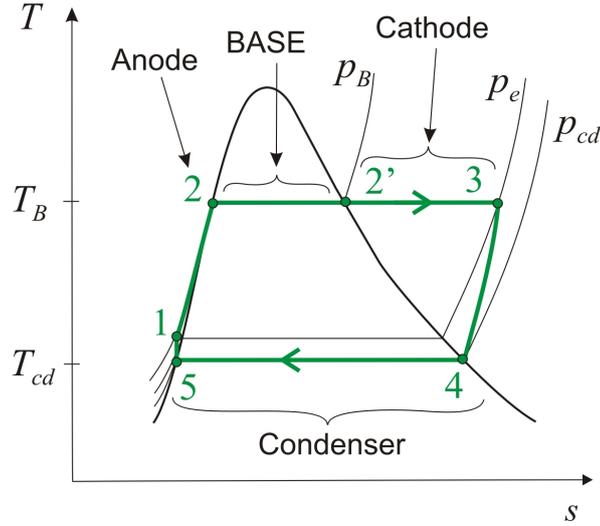
Figure 2.12: T-s Diagram of the AMTEC process.

From the thermodynamics point of view W_{23} can be expressed as:

$$W_{23} = \dot{m} \left[(h_3 - h_2) - T_B (s_3 - s_2) \right] \qquad , \tag{2.51}$$

where $\dot{m}$ is the mass flow rate, h represents the specific enthalpy and s the specific entropy. Considering $5 - 1$ an isochoric process, liquid sodium as incompressible fluid, negligible kinetic and potential energy gradients and a constant specific density, the work required to pump sodium can be calculated as:

$$W_{51} = \dot{m} \int_1^5 \frac{dp}{\varrho_1} = \dot{m} \left(\frac{p_B - p_{cd}}{\varrho_1} \right) \qquad , \tag{2.52}$$

where ϱ is the specific density. The power required to recirculate sodium can be neglected compared to the work output $W_{51} \ll W_{23}$ [32].

On the other hand, the total heat supplied to the system is the sum of thermal power provided in the isochoric heating, Q_{12}, plus the thermal power given for the isothermal process, Q_{23},

$$Q_{in} = Q_{12} + Q_{23} \qquad . \tag{2.53}$$

The heat supplied from 1 to 2 is:

$$Q_{12} = \dot{m} (h_2 - h_1) \qquad , \tag{2.54}$$

and for the assumed isothermal process between 2 to 3 (anode-electrolyte-cathode porous layer) is:

$$Q_{23} = \dot{m} T_B (s_3 - s_2) \qquad . \tag{2.55}$$

31

Thus the ideal maximum thermal efficiency achievable by AMTEC is:

$$\eta_{th} = \frac{W_{23}}{Q_{12} + Q_{23}} = \frac{(h_3 - h_2) - T_B (s_3 - s_2)}{(h_2 - h_1) + T_B (s_3 - s_2)} \qquad . \tag{2.56}$$

2.2.3 Basic electrochemistry

The equilibrium of a chemical reaction implies that the forward and backward reactions are balanced. In AMTEC, the oxidation and reduction of sodium atoms are balanced (see equations (2.45) and (2.46)). This chemical equilibrium is temperature dependent. The temperature-dependent equilibrium constant K_{eq} is calculated using the activities or concentration of the single reactants and products.

$$K_{eq}^c (T) = \frac{[Na_c^+]}{[Na_c^0]} \qquad , \qquad K_{eq}^a (T) = \frac{[Na_a^+]}{[Na_a^0]} \qquad , \tag{2.57}$$

where the subscripts c and a represent cathode and anode conditions respectively.

For the AMTEC conditions the following assumptions have been considered:

– The concentration of sodium atoms is at constant temperature proportional to the pressure at gaseous state.

– The concentration of sodium at the liquid anode is equal at standard and interfacial conditions.

– Interfacial and bulk sodium ion concentrations are equal.

– The coefficient of electrochemical transfer of sodium is $\alpha = 0.5$.

– The overpotential at the anode can be neglected $\xi_a = 0$.

– The pressure at the interface BASE-cathode can be expressed at constant temperature as a current-dependent pressure.

$$p_j + p_\triangle = K_f \, j + p^T \qquad , \tag{2.58}$$

in which p_j is the pressure due to sodium leaving the electrode surface, $p_\triangle$ is the sodium pressure drop from the interface to the surface of the electrode through a long cylindrical pore. The coefficient K_f contains G_p, the dimensionless geometric parameter which characterizes the electrode morphology (explained in detail in chapter 4). p^T represents the vapor pressure of sodium at the electrode surface due to evaporation at the condenser and depends on the temperature difference between electrode and condenser.

– The temperature in the anode-BASE-cathode system is constant (isothermal process), therefore it can be assumed that the temperature at the cathode/anode is equal to the temperature of the BASE.

For an ideal gas, the concentration of sodium at anode and cathode is equal to:

$$\left[Na_c^0\right] = \frac{p_c}{R_g T_B} \qquad , \qquad \left[Na_a^0\right] = \frac{p_a}{R_g T_B} = \frac{p_{sat}\left(T_B\right)}{R_g T_B} \qquad . \tag{2.59}$$

Nernst equation. The maximum electric potential of an electrochemical cell is the open circuit voltage given by the Nernst equation for the electrode potential (half-cell potential):

$$E_e = E_e^0 + \frac{RT}{Fn} ln\left(\frac{[Ox]}{[Red]}\right) \qquad , \tag{2.60}$$

where the subscript e stands for electrode (anode a, cathode c) and n denotes the number of electrons transferred in the reaction. For the AMTEC system both half-reactions are combined and the final open circuit voltage obtained is:

$$E = E_c + E_a = E^0 + \frac{RT_B}{F}\left[ln\left(\frac{[Na_c^+]}{[Na_c^0]}\right) - ln\left(\frac{[Na_a^+]}{[Na_a^0]}\right)\right] \qquad . \tag{2.61}$$

Since in an AMTEC cell the reactant and product is the same, namely sodium, $E^0 = 0$. Therefore the cell voltage is expressed as:

$$E = \frac{RT_B}{F} ln\left(\frac{[Na_c^+][Na_a^0]}{[Na_c^0][Na_a^+]}\right) \qquad . \tag{2.62}$$

Considering that the concentration of sodium ions at cathode and anode is equal $[Na_c^+] = [Na_a^+]$, then equation (2.62) reduces to:

$$E = \frac{RT_B}{F} ln\left(\frac{p_{sat}\left(T_B\right)}{p_c}\right) \qquad . \tag{2.63}$$

For $T_B = 800\,°C$ and $p_c = 10\,Pa$ the obtained cell voltage at open circuit conditions is $E = V^{oc} = 0.77\,V$. The higher the temperature and the lower the pressure at the cathode, the higher is the obtained potential. At open circuit conditions, the vapor pressure at the cathode p_c^{oc} is controlled by molecular effusive flow (thermal transpiration) due to the microscopic pores of the cathode electrode [33, 34]:

$$p_c = p_c^{oc} = p_{cd}\sqrt{\frac{T_B}{T_{cd}}} = p_{sat}\left(T_{cd}\right)\sqrt{\frac{T_B}{T_{cd}}} \qquad . \tag{2.64}$$

Introducing equation (2.64) in (2.63) the cell potential is reduced to:

$$E = \frac{RT_B}{F} ln \left(\frac{p_{sat}\left(T_B\right)}{p_{sat}\left(T_{cd}\right)} \sqrt{\frac{T_{cd}}{T_B}} \right) \qquad . \tag{2.65}$$

Increasing the temperature difference between the electrolyte T_B and the condenser T_{cd} has a positive impact on the voltage of the cell E. This is due to the large impact of the temperature on the saturated pressure ratio $p_{sat}\left(T_B\right)/p_{sat}\left(T_{cd}\right)$. As illustrated in figure 2.13 the pressure increment of saturated sodium vapor between temperatures 200 - 400 °C is $\sim 50\,\mathrm{Pa}$, which is considerably smaller than the pressure increment between 600 - 800 °C, $\sim 40000\,\mathrm{Pa}$.
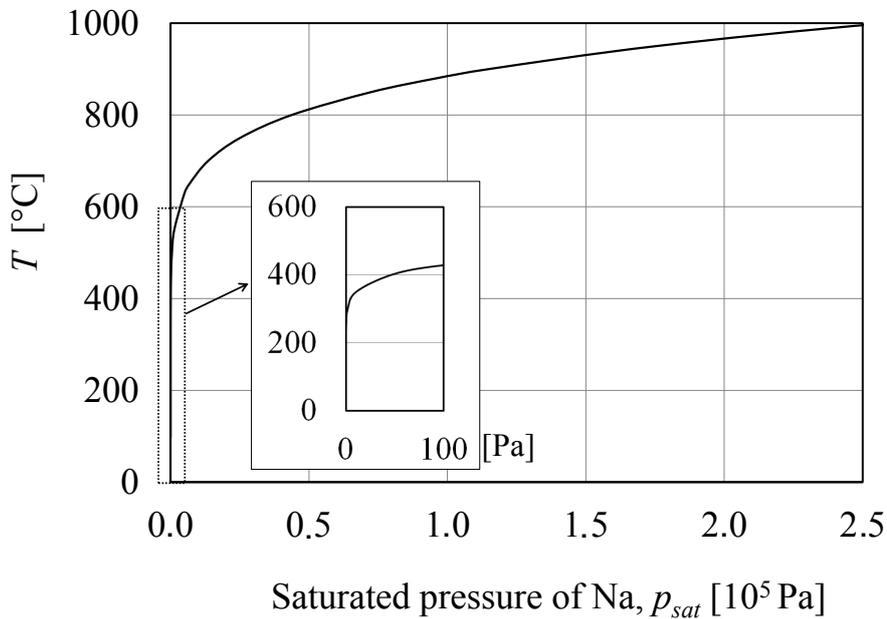
Figure 2.13: Saturated vapor pressure of sodium as function of temperature.

Therefore, the effect of the T_B is significantly larger than the effect of the T_{cd} on the cell voltage, since at lower temperatures the saturation vapor pressure of sodium $p_{sat}\left(T_{cd}\right)$ does not change significantly.

Butler-Volmer equation. Applying the same mentioned assumptions to the Butler-Volmer equation one obtains that for an AMTEC cell [35]:

$$j_i = j_{0i} \left\{ exp\left(-\frac{F\xi_i}{2RT} \right) - \frac{K_{fi}\,j_i + p^T}{p^T} exp\left(\frac{F\xi_i}{2RT} \right) \right\} \qquad . \tag{2.66}$$

being $i = a,\ c$ for the anode or cathode respectively and $\alpha = 0.5$. At the anode $j_a \leq 0$ and $\xi_a \geq 0$, while at the cathode $j_c \geq 0$ and $\xi_c \leq 0$.

2.2.4 Cell efficiency

The efficiency of the AMTEC cell has been obtained in thermodynamic terms in sub-chapter 2.2.2, equation (2.56). A second useful reference for indicating a cell performance includes the electrical point of view. Equation (2.67) determines the thermal energy equal to the electrical power output generated plus the heat required for the sodium vaporization.

$$Q_{23} = W_{23} = JE + \frac{JM}{F}L \qquad , \qquad (2.67)$$

where J represents the electric current of the cell, M is the molecular weight of sodium, F the Faraday constant and L the heat of vaporization. Q_{12} can be expressed based on the specific heat:

$$Q_{12} = \frac{JM}{F}c_p \left(T_B - T_{cd}\right) \qquad , \qquad (2.68)$$

here c_p is the specific heat capacity. Thus the efficiency of AMTEC can be expressed as:

$$\eta = \frac{E}{E + M\left[L + c_p\left(T_B - T_{cd}\right)\right]F^{-1}} \qquad . \qquad (2.69)$$

Based on equations (2.65) and (2.69) an increasing temperature difference between electrolyte and condenser has a positive impact on the thermal efficiency of the system. Equations (2.56) and (2.69) consider an ideal AMTEC thermal cycle without parasitic losses, which can reduce the system efficiency as much as 50 % [1] and are discussed later in section 2.2.5. Taking into account the heat and electric losses, the operating efficiency of an AMTEC cell can be written as follows [32]:

$$\eta = \frac{E - JR_{lead}}{E + M\left[L + c_p\left(T_B - T_{cd}\right)\right]F^{-1} + J^{-1}Q_{loss} - JR_{lead}} \qquad , \qquad (2.70)$$

where $Q_{loss} = Q_{rad} + Q_{cond}$ represent the heat losses in the cell and R_{lead} is the total electrical resistance of the current leads, or in other words, the electrical losses outside the cell. Heat losses are composed of two main terms, heat conduction Q_{cond} and Q_{rad} radiation losses from the hot regions (e.g. BASE) to the cold regions of the cell structure (e.g. condenser). Referring to figure 2.11, heat conduction occurs from the BASE through the current collector and current leads and through the connecting Nb-brazing and further steel tube to the upper flange and condenser outer tube (cold regions). Radiation losses are mainly generated due to the coaxial configuration of the cell: from the BASE tube (hot region) to the condenser tube (cold region). The latter represent the main parasitic heat losses in AMTEC.

The thermal model presented in this work is based on the model from Tournier et al.

(1997) [33]. Assuming an uniform and equal temperature at BASE and electrode, the radiation losses are expressed as:

$$Q_{rad} = \frac{\sigma_k A}{Z} \left(T_B^4 - T_{cd}^4 \right) \qquad . \qquad (2.71)$$

Here $\sigma_k = 5.67 \cdot 10^{-8}$ W/m²K⁴ is the Stefan-Boltzmann radiation constant, and A the outer surface of the current collector (see figure 2.11) involved in the heat transfer process. It is assumed that the BASE surface has a negligible emissivity. In a coaxial cell, the geometric factor, Z is given as [33]:

$$Z = \frac{1}{\varepsilon_{ic}} + \frac{1}{\varepsilon_{cd}} - 1 \qquad . \qquad (2.72)$$

The BASE is covered with the porous cathode and the current collector. The latter acts as a gray body due to its rough surface and porosity, hence the emissivity can be assumed to be $\varepsilon_{ic} = 0.9$ at 800 °C. Previous experiments have shown that the condenser surface is only partially coated with liquid sodium and therefore, the emissivity factor corresponds almost to that of the condenser surface [33]. In the present work the emissivity of the condenser is equal to that of polished stainless steel 1.4571, $\varepsilon_{cd} \sim 0.62$ at 600 °C [36]. In comparison liquid sodium has an emissivity of $\varepsilon_{Na} \sim 0.041$ at 600 °C [36, 37]. Therefore, Z has a value of ~ 1.7, in contrast to 24.5 of a complete coated condenser with liquid sodium. A good possibility to reduce the heat losses is to use additional radiation shields between BASE and condenser made of molybdenum $\varepsilon_{Nb1Zr} \sim 0.110$ at 600 °C [38], or to use a grid to form a film of liquid sodium on the surface of the condenser due to the capillary forces. Here, the focus is not on heat loss reduction. Literature studies show that using a remote condenser improves the cell efficiency, however the mass transport losses increase considerably [39].

Parasitic losses through heat conduction and Joule heating are small compared to radiation losses. Stainless steel is selected as cell structure material to reduce the heat losses through conduction. Losses in current leads can also be reduced by decreasing their cross-sectional area. However, it should be considered that too small cross-sections lead to high Joule heating losses. Heat losses through conduction in the cell can be expressed as:

$$Q_{cond} = Q_{la} + Q_{lc} + Q_{st} \qquad , \qquad (2.73)$$

where Q_{la} accounts for conduction losses through the anodic current lead, Q_{lc} through the cathodic current leads and Q_{st} for the supporting structure of the BASE (Nb-steel tube). The conduction losses in the radial direction within the BASE are neglected, since a constant temperature between anode-BASE-cathode is considered according to fig-

ure 2.12.

Adding equations (2.71) and (2.73) to (2.70) the overall efficiency of AMTEC can be obtained. The efficiency of AMTEC cycle is close to that of the Carnot cycle, for given $T_B = 800\,°C$ and $T_{cd} = 250\,°C$, the maximum efficiency of AMTEC is calculated to $\eta \sim 47\,\%$ and Carnot $\sim 52\,\%$ [1].

2.2.5 Cell losses

In contrast to the thermodynamics, which consider a system in steady state, the electrochemistry refers to any concentration cell as a system that is always operating off-equilibrium [15]. The cell continuously tries to balance the concentration difference between anode and cathode. Therefore chapters 2.2.2 and 2.2.4 are strictly speaking only valid at open circuit conditions, without the presence of an electric current. A cell without charge transfer (no losses) exhibits a constant voltage equal to the OCV. In a real system, losses are expressed as voltage drop. Figure 2.14 shows a typical characteristic curve of an AMTEC cell and reflects the relation between cell voltage, current density and voltage losses.
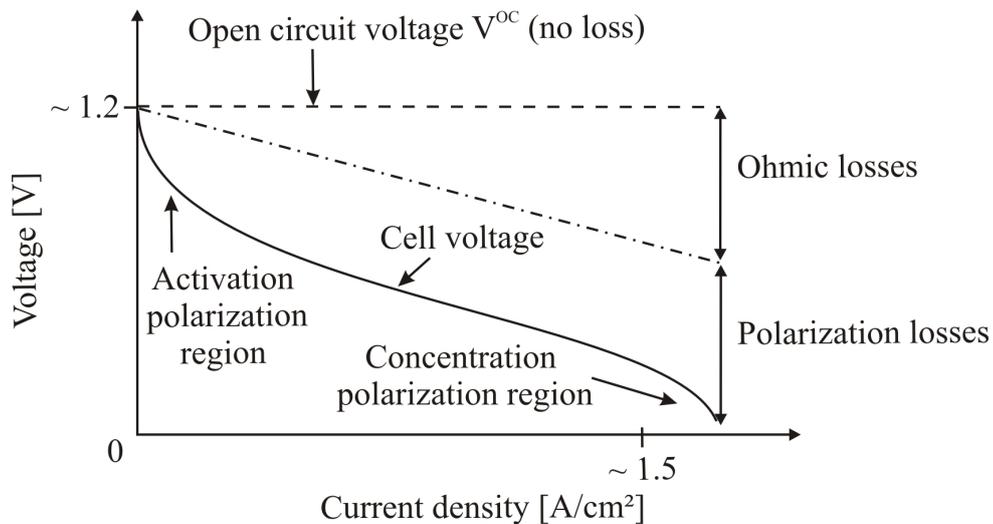
Figure 2.14: Representation of an AMTEC characteristic curve. The diagram shows the different losses that occur in AMTEC cells when connected to an electric load. At low current densities the activation polarisation losses predominate, while at high current densities the concentration polarisation losses become important.

The curve exhibits a rapid initial drop at low current densities. In this region the activation losses represent the main source of voltage drop, which appear due to the slow reaction kinetics on the surface of the electrodes. At the anode the wetting of the ceramic with liquid sodium plays an important role. The voltage decreases further after the activation polarisation region; however, at lower rate and with a linear slope. The latter is characteristic of a voltage drop due to ohmic losses. Ohmic losses represent the

resistance offered to the flow of electrons and ions in the electric circuit. An optimized AMTEC cell should have a cell resistance similar to that of the electrolyte.

At high current densities the concentration polarisation losses, originated mainly at the cathode, are responsible for a further increase in the voltage drop. This appears as a result of an increased sodium vapor concentration at the cathode inner surface, caused by a considerably lower diffusion process of sodium vapor compared to the reaction kinetics. Most of the reported AMTEC cells in the literature do not exhibit the concentration polarisation region, indicating a good sodium vapor transport of the cell. The linear voltage-drop region prevails even at current densities as high as 1.5 A/cm^2 [40].

Ohmic losses.   The ohmic losses appear due to the resistance to electron flow inbetween the electrodes, current collector and current lead; and the resistance to ion flow in the electrolyte (see figure 2.15). Their behavior is linear and current dependent. The overvoltage due to ohmic losses ξ_r is represented by Ohm's law:

$$\xi_r = j\, R_{cell} \qquad . \tag{2.74}$$

R_{cell} is the internal resistance of the cell. Assuming one active electrode R_{cell} is composed by the ionic resistance in BASE (B), electrical resistance in the anode and cathode $R_e = R_a + R_c$, where $R_c \gg R_a$; current collector (ic), current leads (la, lc) and the total contact resistance between the different parts (con).

$$R_{cell} = R_B + R_e + R_{ic} + R_{la} + R_{lc} + R_{con} \qquad . \tag{2.75}$$
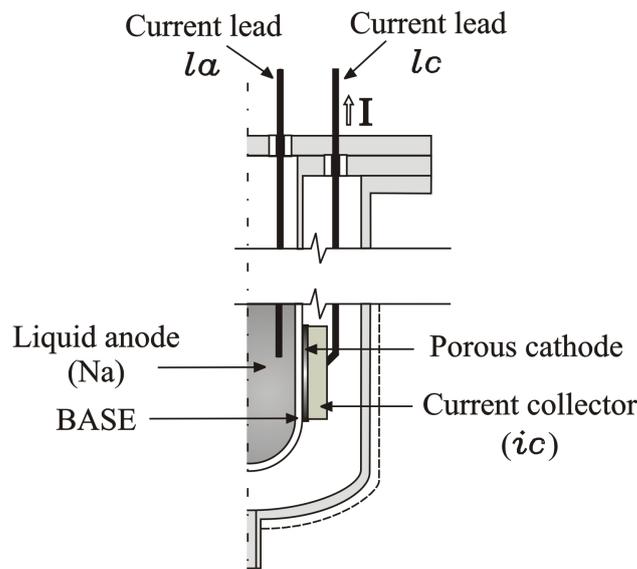
Figure 2.15: Scheme of the AMTEC cell components involved in the ohmic losses.

The ohmic polarisation can be reduced by decreasing the electrolyte thickness, choosing adequate materials with low electrical resistance and accounting for a good contact between electrodes and current collectors. At 600 °C the ionic resistivity of the BASE is $\rho_B = 2\,\Omega$cm [41] and thus assuming that the thickness of the BASE is negligible in comparison to the diameter of the BASE tube $t_B \ll D_B$, the resistance of the BASE can be calculated as

$$R_B = \rho_B\, t_B / A_e \qquad . \tag{2.76}$$

Given a BASE thickness of $t_B = 2\,$mm and a mean electrode area of $A_e = 45\,\mathrm{cm}^2$ the resistance of the BASE is $R_B = 9\,$mΩ. By reducing the thickness of the electrolyte, the resistance of the BASE is proportionally reduced.

Polarisation losses. Losses originated at electrodes through i) limitations in the electrochemical reaction (*activation losses*) and ii) the resistance to diffusion at the porous electrode of the cell (*concentration losses*) are denoted as polarisation losses and are responsible for a non-linear voltage drop of the cell.

Activation losses. Insufficient charge transfer accounts for the so called activation losses. Forcing the redox reaction to completion causes a voltage drop due to activation polarisation, which can be explained through the Buttler-Volmer equation. This occurs due to the limited catalysis performance in the cathode and uncompleted wetting of the anode. Liquid-anode AMTEC cells provided with a good wetting of the BASE surface exhibit negligible losses at the anode. In order to minimize the voltage drop due to activation losses at the electrodes, one can increase the operational temperature, improve the contact area at the BASE-cathode interface, rise the pressure at the anode and/or decrease the pressure at the cathode and to use a more effective electrode material for higher exchange current densities [15].

Concentration losses (diffusion polarisation). The resistance to vapor transport in electrodes is responsible for additional voltage loss. After the electrochemical process, the recombined sodium atoms need to travel through the porous cathode. If the resistance to vapor transport in the electrode is high, sodium vapor accumulates on the inner cathode surface and hence, the sodium concentration increases p_c. As a result cell voltage is reduced according to the Nernst equation. Mass transport losses are predominant at high current densities; one can assume a limiting current density over which the voltage drop is accelerated and the total electromotive voltage tends to zero.

Working fluid crossover / Internal current losses. The actual OCV of the cell is lower than what the theory predicts. This voltage loss is due to working fluid crossover and internal current losses. The liquid sodium from the anode side may diffuse through the electrolyte to the cathode side without experiencing an electrochemical state change; thus no electric current is generated. In AMTEC cells this effect has been mostly neglected due to the large current density of the cell compared to the internal current loss.

Heat losses. In subchapter 2.2.4 the heat losses have been identified and a simplified thermal model and solutions for reducing the heat losses in AMTEC have been presented. Summarizing, the temperature difference between BASE and condenser plays an important role in a coaxial configuration of the cell. Heat losses through radiation can reach $\sim 40\,\%$ of the total losses at high temperatures ($> 800\,°C$) as reflected in figure 2.16 [1].
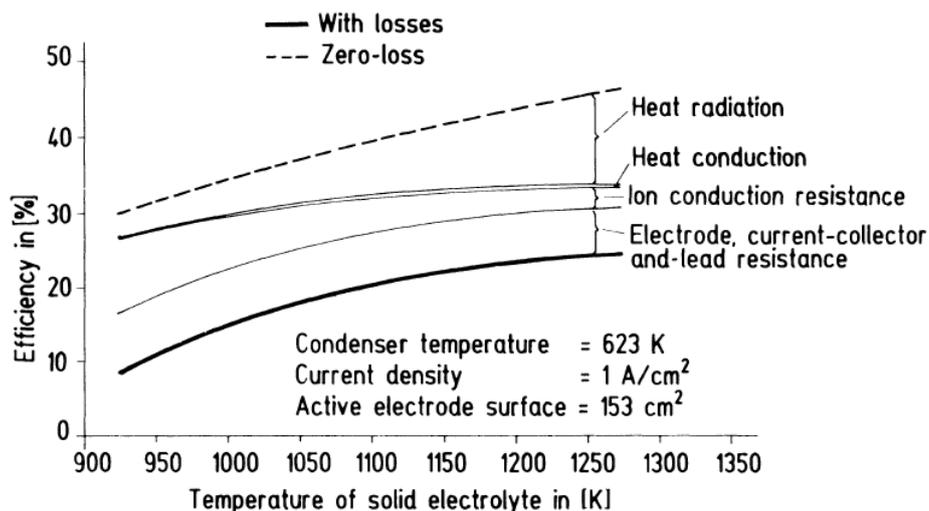
Figure 2.16: AMTEC efficiency versus electrolyte temperature for a coaxial configuration of the cell. Distribution of the main losses changes with the temperature [1].

2.3   Components of an AMTEC cell

The main aspects of the technical realization of AMTEC cells are presented in this chapter. An overview of the main characteristics of the BASE, electrodes and current collector is given first, then the effect of the different alkali metals as working medium in AMTEC is discussed and finally the concept of modular connection is introduced.

2.3.1 β"-alumina solid electrolyte (BASE)

The BASE emerged in the field of sodium batteries and is characterized by a high ionic conductivity and negligible electronic conductivity. It has a complex crystal structure (see figure 2.17) that consist of spinel-like close-packed blocks of Al^{3+} and O^{2-} ions, built with octahedral and tetrahedral prismas, and separated by loosely packed planes containing Na^+ and O^{2-} [42]. The large oxygen ions in the loosely packed planes guarantee enough space for the movement of the sodium ions between spinel blocks; these are known as conduction planes [42]. The conductivity is limited to these planes only, supported by the high resistance to ion movement along the c axis [42].

Two BASE polycrystalline structures that have been mainly used in AMTEC cells: ß-Al$_2$O$_3$ has a hexagonal form and two conduction planes that act simultaneously as mirror planes; and ß"-Al$_2$O$_3$ has a rhombohedral form and three conduction planes (not mirror planes) [42]. The stacking arrangement of the ß-structure is repeated every two spinel-type blocks, while ß"-Al$_2$O$_3$ has a three-block structure as depicted in figure 2.17.
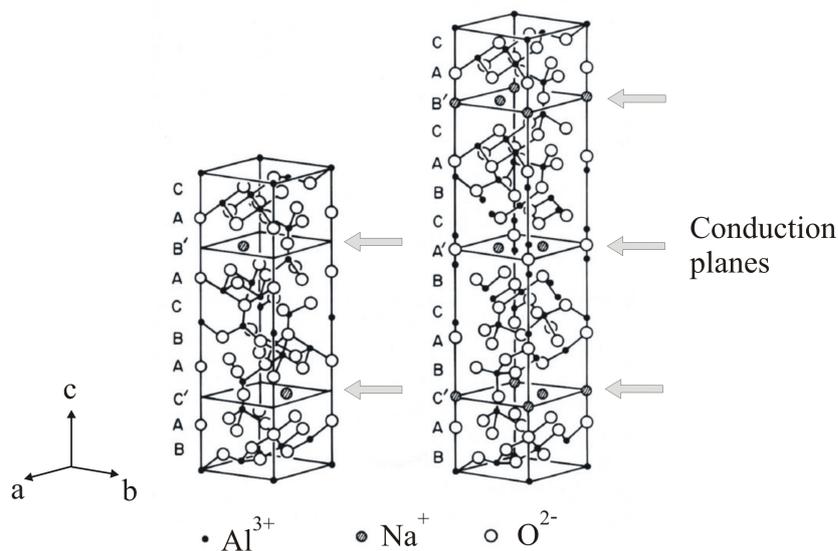
Figure 2.17: Structure of Na-ß-alumina (left) and Na-ß"-alumina (right). Spinel-like blocks of Al-O are separated by conduction planes in a direction [42].

The ß- and ß"-alumina are non-stoichiometric and an excess of sodium is always observed [43]. The non-stoichiometry influences positively the ionic conductivity of the

alumina and the cation excess, typically in the order of 12 - 20 % for ß"-Al_2O_3, and acts decreasing the activation energy for sodium transport in the electrolyte [44]. Moreover, the ß" structure is stable only in the presence of a M cation like Li_2O and MgO, giving the general formula of $Na_{1+x}M_xAl_{11-x}O_{17}$; where x represents the substitution of Al^{3+} with a divalent ion M in the structure (typical saturating values $x = 0.66 - 0.7$) [45, 43]. As result of the doping with cations, the conductivity of the BASE is increased [43].

Single crystal structures have also been proposed in the literature, owing to their lower ionic resistivity compared to polycrystalline structures [42]. Polycrystalline ceramics have a random orientation of the crystals that leads to an increased ionic resistivity. Nevertheless, the lower costs connected with synthesizing polycrystalline phases compared to single phases make them more competitive. Table 2.1 orders the different BASE structures based on their ionic resistivity ρ_{ion}. There is a dispersion of the results in the case of the polycrystalline structure, which reveals the relative influence of the composition e.g. by stabilizers and reinforcements. Adding a ZrO_2 content to the BASE was found to increase the fracture toughness and strength of the ceramic, however the ionic resistivity increased to $\sim 9\,\Omega$cm at 300 °C [46]. Lithium-stabilized BASE has been recommended for AMTEC cells due to its higher resistivity to structure-changes compared to the magnesium-stabilized BASE [47].

Type	ρ_{ion} [Ωcm]		Activation energy [eV]	Stabilizator / Reinforcement	Ref.
	$\sim$300 °C	$\sim$700 °C			
Single Crystal ß-Al_2O_3	4.76	-	0.13	-	[48]
Polycrystalline ß-Al_2O_3	15.38	-	0.27	-	
Single Crystal ß"-Al_2O_3	1	-	0.33	-	
Polycrystalline ß"-Al_2O_3	2.75 - - 4.68		0.18	Li_2O	[49]
	9	-	$\sim$0.3	MgO / ZrO_2	[46]
	7.24	2.14	-	-	[50]
	4.23	-	-	MgO / Li_2O / ZrO_2	[51]
	4.2	2 (600 °C)	-	Li_2O	[41]

Table 2.1: Overview on measured ionic resistivity and activation energy of single crystal and polycrystalline Na-ß/ß"-alumina solid electrolyte.

Usually BASE is synthesized using Al_2O_3, Na_2CO_3 and MgO or Li_2CO_3 powders by conventional solid-state reaction technique [48]. Process temperature involves a sintering treatment above 1600 °C [48]. Other chemical methods like the sol-gel technique have been tested [52], which give products with higher purity and sintering at lower temperatures, however it also leads to the formation of unfavorable ß"-ß mixture with a low conductivity [48]. The patented vapor phase method from Virkar et al. [53] (2000)

consists on employing Y_2O_3 stabilized Zirconia composites together with α-Al_2O_3 powder immersed in Na_2O vapor source and stabilizers. Advantages of the method include i) full conversion of α-Al_2O_3 to ß"-Al_2O_3, ii) elimination of sintering avoiding high temperatures and thus the formation of increased grain size too, iii) lowered activity of Na_2O in the process avoids the formation of water soluble sodium aluminates that makes the ceramic resistant to moisture and iv) Y_2O_3 increases the strength of the electrolyte. The main disadvantage is the obtained low ionic conductivity due to the Zirconia composite. The measured ionic resistivity at 300 °C was 38 Ωcm [53], which is still relative high in comparison with a conventional polycrystalline ß"-alumina.

The behavior of the ionic resistivity in Na-ß"-aluminas in terms of temperature is illustrated in figure 2.18. Above 300 °C the BASE shows a high ionic conductivity. Silent Power (former Ionotec) developed BASE ceramics special for AMTEC applications. The ionic conductivity of their BASE was significantly higher at temperatures exceeding 600 °C. Unfortunately the current developments in Ionotec are rather focused on the battery field with lower operating temperatures and optimized geometries for NaS-batteries (ceramic tube). The BASE available for this work from Ionotec exhibits a comparable low ionic resistivity at temperatures < 500 °C.
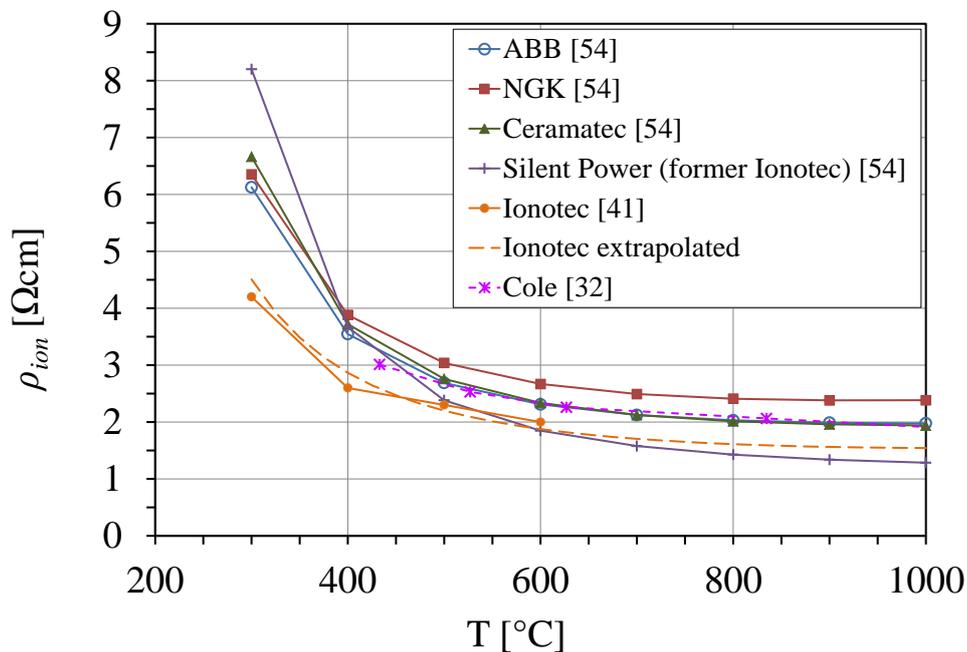
Figure 2.18: Ionic resistivity of different polycrystalline Na-ß"-alumina electrolytes as a function of temperature [32, 54, 41].

It is well known that BASE is very sensitive to moisture. There is a rapid physical adsorption of water by the surface micropores which causes saturation in less than 1 hour, followed by a slower diffusion of hydronium ions (H_3O^+), coming from the water,

into the crystal lattice leading to ion exchange with Na^+ [55, 56]. The hydroniThese effects require a careful handling of the BASE, which should be always stored in an inert atmosphere and cleaned through firing at $\sim 600\,°C$ in vacuum.

The BASE emerged in the field of liquid metal batteries and is nowadays mainly used in NaS and ZEBRA batteries. This gives the ceramic electrolyte its particular tubular configuration. When looking at power density in terms of volume and weight, AMTEC cells developed with the tube-ceramics have a rather poor profitable design; high sodium amount - electrode surface ratio, high BASE manufacturing costs, low power/volume and low power/weight ratios. A planar configuration should help to reduce the costs, volume and weight. Moreover, the interconnections of a modular design can be simplified by the planar configuration. Such a configuration was patented by R. K. Sievers in 1992 [57]. Already some very interesting work has been done in the field of planar Na-BASE ceramics, however, for battery applications at lower temperatures ($< 300\,°C$); a common project between EaglePicher Technologies and Pacific Northwest National Laboratory (PNNL) is running for the development of planar BASE ceramics applied to Na-Batteries [58] (see figure 2.19).
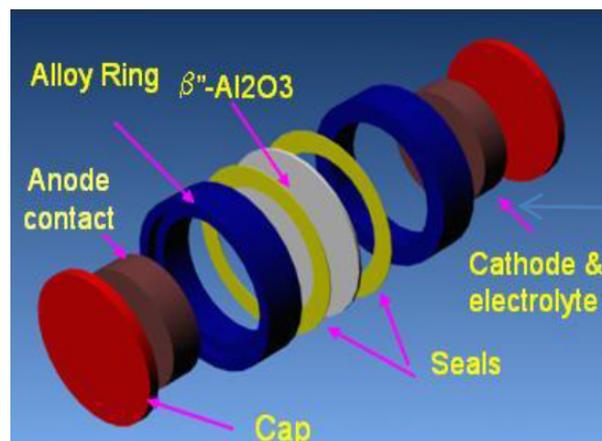
Figure 2.19: Sketch of a $3\,cm^2$ button Na-Air cell with a planar configuration of the BASE [58].

2.3.2   Electrode

Porous cathode.   The cathode in AMTEC is the part of the cell where the reduction of sodium takes place. The aim of the cathode is to act as a catalyzer of an electrochemical reaction and to provide:

i)   a proper transport of electrons through the current collectors,

ii)   a proper transport of sodium vapor through the cathode, current collector and to the condenser surface.

Moreover, the cathode must satisfy following properties:

iii)   good adhesion to BASE's surface,

iv)   similar thermal expansion coefficient as that of the BASE,

v)   good corrosion resistance to sodium vapor (this can bee achieved by reducing the operating temperature of AMTEC),

vi)   high temperature stability, translated into slow grain growth and material migration,

vii)   large triple phase boundary (TPB) to reduce polarisation losses.

At the cathode the TPB is the zone represented by the points where the electrode (electronic conductive phase), a pore (gas phase) and the electrolyte (ionic conductive phase) coincide, as sketched in figure 2.20. Maximizing its length is crucial for the optimization of the cell performance. In fuel cells this has been achieved by employing cermets (ceramic and metal composites), in which the metallic catalysts and an ionic conductor are mixed in the proper amount; or by using ionic and electronic mixed conductors [15]. In AMTEC cells refractory and ceramic electrode materials have been commonly used due to their suitable properties [59]; nevertheless their long-term stability at high temperatures is still to be further investigated. The main properties of electrode materials reported in the literature are summarized in tables 2.2 and 2.3; and will be further analyzed in chapter 3.
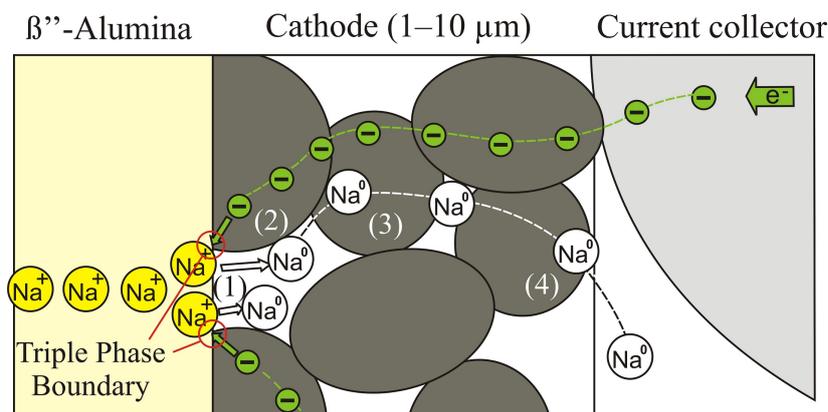
Figure 2.20: Representation of the transport processes in the cathode electrode. (1) Recombination of Na ions with electrons at the triple phase boundary (BASE-electrode-pore); (2) Surface diffusion of Na atoms on electrode grains; (3) Desorption of Na atoms from surface of electrode grains; and (4) Sodium vapor diffusion through the pores of the electrode. (Figure edited from [60])

The transport process occurring in the cathode is described in figure 2.20. Sodium ions coming out from the BASE recombine with the electrons transported by a porous cathode exclusively at the TPB. Therefore, the porosity of the cathode is essential to allow a low resistance to transport of sodium vapor. The morphology of an AMTEC electrode can be defined during the manufacturing process. For instance, by using the magnetron sputtering technique, changes in pressure and applied voltage of the process contribute to changes in the porosity and microstructure [61].

Electrode	ρ (20 ℃) [$10^{-8}\,\Omega$m]	ρ (800 ℃) [$10^{-8}\,\Omega$m]	Melting point [℃]	CTE (20 ℃) [$10^{-6}\,$K^{-1}]	CTE (800 ℃) [$10^{-6}\,$K^{-1}]	Ref.
Mo	5.5	26	2622	5.1	5.5 (1000 ℃)	[62, 63]
TiN	20	~37	2930	9.4		[64, 59] [65]
TiC	60		3140	7.4	8.31 (1000 ℃)	[66, 65] [67, 68]
TiB$_2$	~18	~94	2900	7.4	8.6 (1000 ℃)	[69, 65] [70]
PtW	Pt 10.3	Pt 3.75	Pt 1769	Pt 9.05	Pt 10.8	[71]
W	5.5	~25	3410	4.3		[72]
RhW	Rh ~5	Rh 2.25	Rh 1963	Rh 8.4	Rh ~11.8	[71]
NbN	137.5*		2575	10.1		[73, 65]
Ni	9	45	1445	13.3 (100 ℃)	16.2	[74]
Nb	15	~45	2468	7 (100 ℃)	7.7	[62, 63]
LaB$_6$ (75 % density)	26.3	94.7	2255		9 (1000 ℃)	[75, 76] [77]
Stainless steel 1.4571	74	118	1400	16	19.9	[78, 79] [80]

Table 2.2: Electrode bulk material properties for AMTEC cells. $CTE_{BASE} = 8.6 \cdot 10^{-6}\,$K^{-1} at $500 - 1000$ ℃ [81]. *Electrical resistivity given for a thin film.

Electrode	Remarks
Mo	Rapid grain growth > 827 ℃. Reaction $Na \rightarrow Na_2MoO_4$.
TiN	Reduced performance vs Mo. Large power loss.
TiC	Chemically stable. No long time experience.
TiB$_2$	Moderate performance. No long time experience.
NbN	Chemically stable vs Na, BASE. No long time experience.
RhW	Low power loss. Diffusion Rh→Ni. Chemically stable. Expensive.
PtW	Lifetime ~7 yr. Reaction with Mn from steel. Expensive.
LaB$_6$	Moderate performance. No long time experience.

Table 2.3: Main experimental observations on AMTEC electrode materials [59].

The morphological aspects of the cathode have great influence on the polarisation losses in AMTEC. The favored grain size, porosity and thickness tendencies of the cathode in order to decrease polarisation losses are indicated in table 2.4. The length of the TPB is connected with the grain size and the porosity of the cathode: the smaller the grain size (e.g. TiC $\leq 0.07\,\mu$m [40]) and the smaller the porosity, the longer is the TPB, which reduces the activation losses and increases the current density of the cell. A reduced porosity decreases the ohmic losses too, since the conductivity of the electrode is improved. However, the porosity also affects sodium vapor transport, being a small porosity responsible for increased diffusion losses. A similar effect has the electrode thickness; a thin electrode favors the diffusion of sodium vapor, nevertheless it also increases the ohmic losses. Optimum values for grain size, porosity (e.g. LaB$_6$ 55 % [82]) and thickness (e.g. LaB$_6$ 5 μm [82]) have to be determined experimentally, which depend strongly on electrode-material characteristics, operation conditions (T, p) and current collector structure (explained in subchapter 2.3.3).

Reduction of polarisation losses	Grain size	Porosity	Thickness
Activation	↓	↓	-
Ohmic	↑	↓	↑
Diffusion	-	↑	↓

Table 2.4: Favored cathode-morphology factors to reduce polarisation losses. ↓ and ↑ represent respectively a small and large size of grain size/porosity/thickness for reduced polarisation losses. The simultaneous reduction of all losses (activation/ohmic/diffusion) by adapting the morphology of the cathode is not possible due to the counteracting effect of the individual parameters.

The main electrode characteristics can be described through two main factors: i) the *coefficient of temperature-independent charge-exchange* B_{ex} [AK$^{1/2}$/Pa m^2]. Experimental investigations have shown that the saturated equilibrium exchange-current density j_0^{sat} is a function of the BASE temperature and of the type of electrodes (given by B_{ex}) [35, 83]:

$$j_0^{sat} = B_{ex}\,\frac{p_{sat}\,(T_B)}{\sqrt{T_B}} \qquad . \tag{2.77}$$

B_{ex} is related to the contact between electrode and electrolyte [84]. The second factor that describes the electrode properties is ii) the *electrode pressure loss factor* G_p [-], which denotes the pressure drop due to the diffusion process of vapor sodium through the porous cathode [84] (presented in chapter 4). An ideal perfect cathode should have an infinite long TPB: $B_{ex} \sim \infty$, and a negligible resistance to vapor transport: $G_p \sim 0$.

In the literature, both effects electrode morphology and materials have been extensively studied. Table 2.5 classifies so me of the most relevant literature results on

AMTEC cells attending to electrode materials. T_{Na} denotes the temperature of sodium in the anode, P_{cell} is the power output of the cell, t_e is the thickness of the cathode electrode and A_e the cathode area. According to table 2.5, materials with the highest power output seem to be Pt/W, Rh/W and TiC. However, an accurate comparison requires considering identical conditions of temperature, electrode surface, current collector structure, operating time, vapor pressure, etc. Therefore further experimental tests should be performed in this field to confirm this statement. In this work TiN and TiC electrodes have been selected for coating development. Despite the lower reported power density of TiN compared to TiC, TiN is one of the electrode materials with greater experience and wider documentation in the literature.

Several trends can be observed in table 2.5. The positive effect of small electrode surface is reflected on the molybdenum results. Higher power outputs are achieved by smaller electrode surfaces; this effect is directly connected with the current collector structure (see chapter 6.3).

A long operating time can lead to significant electrode sintering or corrosion effects depending on the material, and thus a decreased performance. Molybdenum for instance forms several Na-Mo-O compounds (e.g. Na_2MoO_4 and $Na_2Mo_3O_6$) during AMTEC operation [95]. These compounds may be responsible for an improved sodium ion transport in the electrodes during first operating hours but also lead to performance degradation due to their volatilization and decomposition at high temperatures and long operation [95]. While Mo electrodes should not be used for periods over one year due to the high power degradation, Pt/W and Rh/W are predicted to maintain power levels of $< 0.5\,\text{W/cm}^2$ for greater than 10 years [94]. Another trend observed from literature results is that each material has an optimum thickness; Mo for instance is known to achieve the best performance at a thickness of $\sim 1\,\mu$m (most of the reported results are therefore for $1\,\mu$m), however TiN performs better at larger thicknesses ($\sim 5\,\mu$m) in order to compensate its lower electric conductivity [89]. A similar effect can be observed in TiC and NbN cathodes. Lower thicknesses than $\sim 5\,\mu$m have a negative effect due to the increased sheet resistance, however larger thicknesses than ~ 5 - $6\,\mu$m have likewise a negative effect [40]. The difference is, that in the latter case, the limiting parameter is not the electrical resistance but the vapor transport resistance in the cathode, which has substantially increased.

An additional parameter which is not directly connected with the electrode but has a direct impact on cell performance is the pressure level in the cathode side. Table 2.5 shows the effect of the vacuum on the power output for TiC cathode. A good vacuum level increases the cell performance as seen in the Nernst equation (2.63) due to increased concentration gradient across the BASE; but it also contributes to an enhanced vapor transport and, therefore, to reduced diffusion polarisation losses.

Electrode	T_{Na} [°C]	t_e [μm]	A_e [cm^2]	P_{cell} [W/cm]	Operation [hours]	p in cathode side [Pa]	Ref.
Mo	800	1	0.5	0.5	few	-	[85]
	800	1	30	0.217	few	-	[86]
	927	$\sim$1	5	0.62	5	-	[87]
	927	$\sim$1	5	0.46	90	-	[87]
TiN	687	5	7	0.25	few	7×10^{-4} (without Na)	[87]
	746	-	60	0.315	-	-	[88]
	750	1	30	0.075	few	-	[89]
	750	5	30	0.16	few	-	[89]
	850	15...50	6	0.47	few	-	[90]
TiN/TiO$_2$	850	15...50	6	$\sim$0.38	few	-	[90]
TiC	800	3...5	0.5...1	0.11	-	130	[40]
	800	3...5	0.5...1	0.4	-	0.07	[40]
	800	5	0.5...1	0.75	-	0.5	[40]
TiB$_2$	800	-	30	0.24	10	-	[89]
W	927	50	-	0.35	-	-	[91]
PtW	827	-	5	0,25	475	1×10^{-5} (without Na)	[92]
	887	0.7...1	1...5	0.8	160	$7 - 8 \times 10^{4}$	[93]
RhW	817	1.2	<10	$\sim$0.53	150	-	[94]
	817	1.2	<10	0.5	500	-	[94]
	857	1.5...2.5	5	0.8	160	7×10^{-4} (without Na)	[87]
NbN	800	2...3	-	0.12	-	130	[40]
	800	6	-	0.36	-	0.5	[40]
LaB$_6$	800	-	-	0.54	-	40	[82]

Table 2.5: Investigated AMTEC electrode materials. Effect of the parameters: electrode thickness t_e, electrode surface A_e, operating hours and vacuum at the cathode chamber on the performance of the cell P_{cell}.

Liquid-anode. At the anode the oxidation of sodium takes place. A liquid sodium anode is able to provide a good and homogeneous electric contact to the BASE surface, facilitating the oxidation process. It simultaneously contributes to a fast transport of electrons released by the sodium oxidation due to the high specific electric conductivity of liquid sodium. Thus, polarisation losses in the liquid sodium anode are marginal compared to the porous cathode. Providing a good wetting of the BASE surface with liquid sodium is essential to reduce the interfacial polarisation losses. A review of the main achievements concerning the wetting of the ß"-alumina with liquid sodium is presented below. Most of the reported data is focused on NaS batteries, which operate at lower temperatures ($\sim$300 °C).

Virkar et al. [96] (1980) demonstrated that large current concentrations exist at the peripheries of blocked or unwetted BASE areas. This contributes to large local current densities, which can be several times larger than the average current density, leading to a possible premature failure of the ceramic. Therefore, a complete wetting of the BASE is mandatory to increase the lifetime of AMTEC cells. Non-wetted regions have a very high contact resistance, which blocks the sodium ion transport. The ß"-alumina is not easily wetted by sodium and several hours at high temperatures (~ 400 °C) are required to improve the wetting effect.

Viswanathan and Virkar [97] (1982) studied the effect of the moisture and temperature on the wettability of the BASE. They measured the contact angle of a sodium drop on a BASE disc at different treated BASE conditions: i) unbaked, ii) treated with moisture and iii) baked out in vacuum at 450 °C for 60 h. BASE discs treated with moisture showed an extremely high contact angle even at high temperatures (contact angle between the liquid and the solid surface of 103° at 360 °C). In contrast, the BASE specimens that were baked out in vacuum obtained a complete wetting of the disc with liquid sodium (0° at 360 °C). The unbaked BASE samples showed intermediate wettability: 90° at 360 °C. The surface roughness of the ceramic must be considered since a large roughness enhances the interfacial resistance and may affect the wettability negatively. An improvement of the wetting was observed with increasing operation time. Experiments also suggested some solubility of the BASE in liquid sodium, indicating a degradation of the ceramic.

Hu et al. [98] (2013) reported that the composition of the liquid sodium affects the wettability of the BASE: e.g. calcium impurities from the BASE may migrate to the Na/BASE interface and hinder the sodium ion transport. Moreover, they suggested that the polarization at the anode/BASE interface may be affected due to an incomplete wetting of the ß"-alumina by molten sodium, affecting the electrochemical performance of the cell.

Coating technologies for AMTEC electrodes.   There are several coating technologies that can be used to manufacture porous thin electrodes in AMTEC cells. The most used coating method in AMTEC cells has been the physical vapor deposition (PVD) through magnetron sputtering (described in chapter 6.2).

A liquid-based technology was presented by the group of Kato et al. [99, 100, 101] (1990) at the Kyushu University, Japan; the so called screen-printed method. An ultrafine metallic powder is mixed in a liquid solution of terpineol and ethyl-cellulose; the resulting paste is printed in a film on the substrate by a screen printing method. The

paste film is then leveled for more than 10 minutes and dried at 150 °C in air for 15 minutes. Finally the electrodes are fired at 800 - 1000 °C in an optional reactive atmosphere (nitridation) for 1 - 3 hours.

Photolytic chemical vapor deposition (PCVD) of molybdenum grids was reported by Ryan et al. [92] (1991); the substrate was heated to 120 °C and $Mo(CO)_6$ was placed in the metal carbonyl chamber. Metal carbonyl dissociates as result of absorption of UV light, the photoproduct (Mo) condenses on the substrate surface in the illuminated area. It was possible to write micrometer sized patterns on the substrate using the photodeposition technique. The PCVD process was also used to create RhW integral electrodes and current collecting grids [102] and showed an increased 25 - 50 % the overall performance of the cell due to the decreased electrode resistance

Mo/Na_xTiO_2 electrodes were made by Ryan et al. [103] (2001) by mixing a slurry of Mo metal and TiO_2 powders and letting the sintered electrode react with sodium vapor. Electrodes were further fired in vacuum for 2 hours at 1000 °C to remove the cement and sinter the electrode. The main purpose was to develop electrodes that contain Na-Ti-O compounds that are both electronically and ionically conducting. The mixed conducting electrodes had performed better: $G_p = 5$ - 10, $B \sim 100\,AK^{1/2}/Pa\,m^2$ than electrodes of Mo alone: $G_p = 20$ - 30, $B_{ex} \sim 80\,AK^{1/2}/Pa\,m^2$. Fletcher and Schwank [90] (2003) used the same technique to sinter TiN/TiO_2 electrodes. Sintered mixed electrodes exhibited a 39 % increase in power output over the sintered TiN electrode. However, sputtered TiN electrode showed still better results due to its excellent uniformity and adhesion to the BASE surface.

Using a sol-gel method Kim et al. [104] (2014) developed Mo/TiN composite electrodes. The motivation was to obtain electrodes that combine the properties of good conductive Mo and the high stability against grain growth from TiN. Results showed that after 10 times thermal cycling at elevated temperatures (800 °C) the grain growth was almost negligible ($0.62 \rightarrow 0.65\,\mu m$) compared to that of Mo electrodes ($0.24 \rightarrow 3.92\,\mu m$). The electrical conductivity, however, decreased rapidly with increasing temperature. At 700 °C the conductivity was $\sim 250\,S/cm$, significantly lower compared to the $\sim 750\,S/cm$ of Mo alone. The synthesis of the composite powder is a rather complicated process consisting of 6 steps and a total of $\sim 12\,h$, including a firing of the composite powder of 6 h at 900 °C.

Attending to the high chemical reactivity of the BASE, the coating process should be performed in vacuum or in an inert atmosphere or to be decontaminated during several hours at high temperatures > 600 °C. Ideally, the temperature applied during the process should be moderate in order to avoid additional not-desired chemical reaction products originated by the chemical activity of the BASE. Table 2.6 summarizes the different coating processes that can be applied to develop AMTEC electrodes.

Coating technology	Temp. [°C]	Deposit. rate [μm/h]	Vacuum [Pa]	Advantages	Disadvantages
Liquid-based technology (sol-gel, screen-printing)	800 -	-	-	Atmospheric pressure. Porous structure. Ability to combine materials (composite)	Elevated temperatures. Long sintering process (several hours). Low microstructural quality.
Physical Vapor Deposition (PVD)	100 - 1000	1 - 600	10^{-7} - 1	Columnar grain structures typical. Ability to control composition and morphology.	Moderate deposition rates. Difficulties of coating of elaborated shaped pieces.
a) Laser ablation (pulsed laser deposition) (at target)	≥ 700 - 600	~1 - 600	10^{-3} - 10^{-7}	Possible to vaporize high-melting metals (Mo, W, etc.). Very high deposition rates possible ($\sim 600\,\mu m$), however at the expense of quality.	High vacuum. Elevated temperatures.
b) Magnetron sputtering	100 - 250	< 5	10^{-1} - 1	High adhesion/bonding of the layer. Lower processing temperatures. Higher pressure. Ability to control composition and morphology of the layer	Impurities in the layer. Low deposition rates.
c) Ion Beam Sputtering	100 - 500	1.2 - 30	~1	No inclusion of gas molecules in the sputtered film. Low vacuum	Moderate deposition rates. Added expense and complexity. Difficulty to scale the process.
Vacuum plasma spray (VPS)	~100 - 800	< 10	~10 - 65	High deposition rate. Short fabrication time. Ability to be an automated production line (cost-effective). Control of the porosity.	High temperature process, nevertheless rapid solidification of melts. Low deposition rates. Thicker thicknesses.
Electrochemical Vapor Deposition	~1000	< 50	< 10^5	Fast deposition rate. Columnar structures typical.	Dense films. Metal halides needed. Elevated temperatures. Mostly used for production of electrolytes.
Chemical Vapor Deposition (CVD)	400 - 1000	3.6 - 36	0.13 - 10^5	Application to elaborately shaped pieces (holes). Extremely uniform layers. Possibility of Plasma-Enhanced process.	Precursors can be highly toxic, explosive or corrosive. Byproducts hazardous. Elevated temperatures. Film contamination. Low deposition rates.

Table 2.6: Review on coating technologies usable for AMTEC electrodes [61, 105, 106, 107, 108, 109, 110, 111].

For this work the reactive magnetron sputtering technique has been selected due to the possibility to control composition and morphology of the electrode, the typically high adhesion of the film due to the high energy of the particles reaching the substrate, the lower process temperature and the large reported experience in the AMTEC literature.

2.3.3   Current collector

The main function of the current collector (CC) is to electrically connect the current lead with the cathode electrode; the structure needs to allow a good transport of sodium vapor (same as the cathode), provide a low electrical resistance to reduce the ohmic losses and facilitate a fast electron transport to reduce the activation polarisation losses. A reduced attention has been paid in the literature to the current collector morphology. Though, it has been shown to have a great impact on the power output of the cell. Experimental results from Knödler et al. (1992) [86] showed that large electrode areas exhibit lower power densities than smaller ones. This was explained by an inefficient contact of the CC to the porous electrode and a non-uniform current distribution along the electrode surface. Experimental tests confirmed the large impact of the CC structure on the power density: a power output increase of 50 - 100 % was achieved through an optimized CC structure alone. This distinct increase of the power output can be explained by an enlargement of the active electrode area. A situation of poor or no contact between CC and electrode surface in some regions favors the deviation of the current to those regions where the contact is better due to the lower local electrical resistance. Therefore, the net active electrode surface is reduced.

This effect was also investigated in the nineteens at FZK [112, 113, 114, 115]. These authors tested an AMTEC cell at same temperature, electrode and inner CC structure and varied only the outer CC structure, the corset, and the electrode surface. Table 2.7 summarizes the most relevant results of the performed CC tests. The effect of the area is reflected comparing results AS11 and -22 with AS09, -17 and -20 (see figure 2.21). Although larger areas should give larger performances, results show the opposite. This is due to the better electric contact of configurations AS11 and -22, which is easier to obtain for smaller areas. Therefore if the electric contact obtained in configurations AS11 and -22 could be extrapolated to higher electrode surfaces, then the power output in AS09, -17 and -20 should be an order of magnitude higher. As shown in table 2.7, it is considerably difficult to obtain a good and homogeneous electric contact. Improving the contact quality can be achieved by using a proper corset. For instance, corset AS09 offers a poor radial compression in comparison to AS17 and -20. Even between AS17 and -20 a large difference in power output is observed. This is very likely due to the compression difference obtained through the screw connections, which can be gradually adapted to the desired compression. Here, special care is needed not to

tense the corset beyond the fracture toughness of the ceramic to prevent its fracture.

| AS09 | AS17, AS20 | AS11, AS22 |
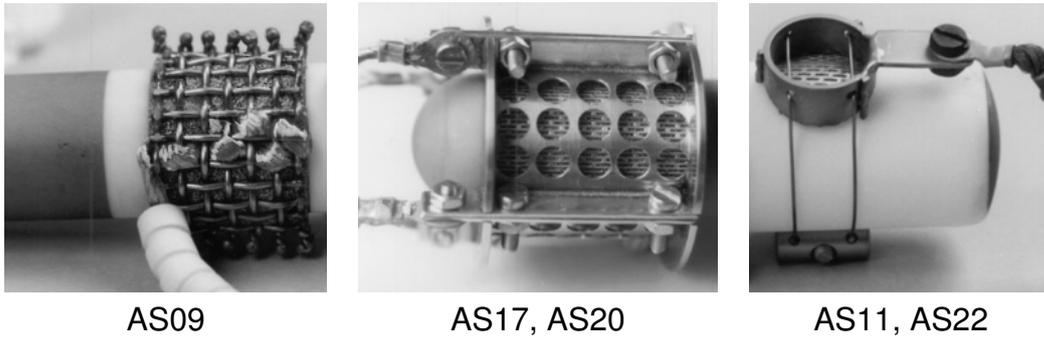
Figure 2.21: Photographs of different current collectors tested at FZK in the nineties [112, 113, 114, 115].

Test Nr.	Corset	A_e [cm^2]	P_{out} [W/cm^2]
AS09	Ni-mesh 4/1.2mm	26.4	0.147
AS11	Screening sheet (Ni)	1.65	0.405
AS17	4 pieces: 2x screening sheet (Ni) + + 2x perforated plate (SS)	26.7	0.249
AS20	4 pieces: 4x perforated plate (SS)	26.7	0.785
AS22	Screening sheet (Ni)	2.56	1.073

Table 2.7: Summary of current collector tests performed at FZK [112, 113, 114, 115]. Effect of current collector structure on the power output of the cell is presented for $T_{Na} = 800\,°C$, Mo electrode 1 - 2 μm, Ni foam (2.2 mm) inner current collector structure.

The losses due to sodium vapor transport in the cathode can be reduced through a decreased cathode thickness. This would, however, increase the sheet resistance of the electrode and thus the total cell resistance. The high electric sheet resistance of the electrode could be ideally compensated through a CC structure with an infinite number of contact points to the electrode as represented in figure 2.22. Moreover, a graded structure (increasing thickness of the wires and decreasing number of wires in the radial direction to the current lead) should reduce the ohmic losses. To further optimize the ohmic losses, the structure should be made of a single piece eliminating thus internal contact resistances. The configuration shown in figure 2.22 reduces additionally the concentration losses due to the enhanced porosity and reduced electrode thickness of the CC.

On the other hand a reduced electrode thickness has a positive effect on the mass transport in the cathode. Therefore, an optimum electrode morphology is directly dependent on the CC structure; meaning that literature data concerning the effect of the
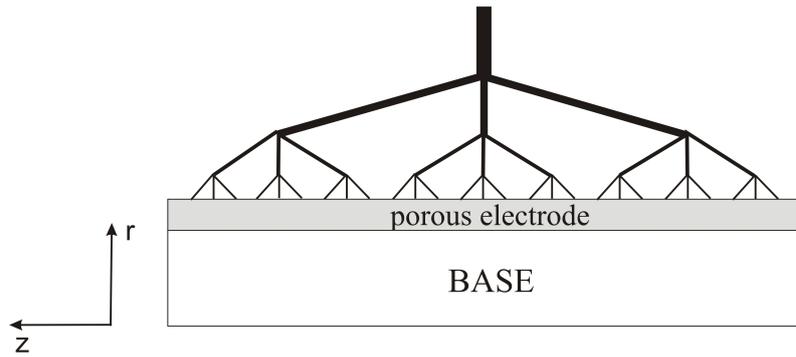
Figure 2.22: Sketch of an ideal current collector graded structure for an AMTEC cell.

cathode morphology needs to be interpreted together with the current collector. Unfortunately, most of the literature does not consider this aspect in a closed form.

Obtaining a good mechanical (and therefore electrical) contact of the CC to the electrode surface becomes a main issue due to the cylindrical geometry of the ceramic electrolyte. The contact resistance at the CC - cathode interface predominates among the electric losses of the cell and is significantly influenced by i) the geometrical tolerances in the radial direction and ii) the pressing force applied during the cell assembly to tighten the CC to the cathode surface. The large significance of the contact resistance in a cylindrical cell configuration is confirmed through the experimental study carried out by L. Biergans [116]. Here, different CC structures have been tested. Results are presented in chapter 6.3. In the case of the SOFC the importance of a good gas transport has also been confirmed experimentally by Kornely et al. (2011) [117]; a change in the flowfield design of the metallic interconnector (equivalent to CC) caused a performance decrease of up to 41 %.

2.3.4   Fluid conditioning

Sodium and potassium are the prime considered candidates working fluids in AMTEC cells due to their favorable thermo-physical properties, which are summarized in table 2.8. There is an extensive experience in AMTEC working with sodium in contrast to potassium, which has not been yet widely spread as working fluid especially owing to the difficulties in manufacturing K-BASE electrolyte with conventional techniques (very high vapor pressure of K_2O at very high sintering temperatures) and to the limited database on the large scale use of potassium [81]. Nevertheless a certain growing interest in K-AMTEC cells is observed since 2000 thanks to the vapor phase deposition method developed by Virkar et al. [53].

The most notable advantages of sodium compared to potassium are [84]: i) the higher surface tension in fluid state that supports the capillary process (used to form a "radiation shield" with liquid sodium due to its low emissivity), ii) a lower molecular

Properties	Sodium	Potassium
Melting point [°C]	97.82	63.2
Boiling point [°C]	881.4	756.5
Saturated vapor pressure [Pa]	~ 5	~ 38
Liquid density [kg/m^3]	805	696
Liquid surface tension [mN/m]	145.6	75.6
Latent heat of vaporization [kJ/kg]	4205	1983
Liquid specific heat capacity [J/kgK]	1251.7	788.7
Dynamic viscosity [10^{-4} Pa s]	2.01	1.51
Molecular weight [g/mol]	23	39.1
Elelectrical resistivity [$\mu\Omega$cm]	34.6	55
Ionic resistivity of BASE [Ωcm]	2	6

Table 2.8: Thermo-physical properties of sodium and potassium at 627 °C [84, 118, 119, 120].

weight that helps also the capillary process as well as decreases pressure losses on the cathode side, iii) a considerably lower electrical resistivity, and iv) a three times lower ionic resistivity of the Na-BASE. However, potassium has also several advantages like a higher vapor pressure (120 kPa at 1050 K versus 35 kPa for Na) that allows a higher anode vapor-pressure and a lower hot temperature, and a smaller latent heat of vaporization, which reduces the thermal heat input and lowers source temperature in vapor-anode cells, simplifying their design.

In this work sodium has been selected based on the following reasons: i) the advantages of sodium properties in AMTEC mentioned above, ii) the excellent properties of sodium as heat transfer fluid for CSP, iii) the background knowledge available in Na-technology at the institute and iv) the lower associated risks regarding the chemical reactivity compared to potassium.

2.3.5   Modular design integration

AMTEC cells can be connected in series for higher cell voltage and thus higher output power. Modular AMTEC cells are known as multi-tube AMTEC converters. Commonly only vapor-anode AMTEC cells have been connected in series due to the simplicity to insulate electrically the BASE tubes from each other and from the cell structure by using sodium vapor as insulator. Liquid-anode AMTEC cells showed difficulties in insulating the BASE tubes from each other because of the electrical conductive properties of liquid sodium. One example of a multi-tube AMTEC system is described in [121], a vapor-anode 7-tube AMTEC initially designed for the Pluto Express (PX) mission.
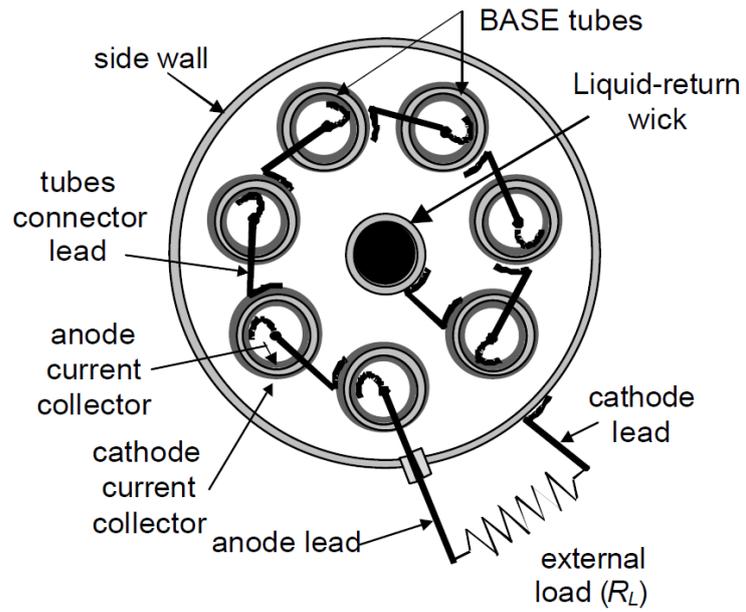
Figure 2.23: Schematic cross-section view of a vapor-anode multitube AMTEC for the Pluto/Express mission [121].

2.4   Fields of application

Since AMTEC allows any heat source able to reach high temperature, it can be coupled to different power conversion systems. During the history of AMTEC, many combinations were proposed for an AMTEC based power generation. The most widespread applications are for aerospace power generation: in the case of deep space applications like Pluto Express mission [121, 122, 123] the device is coupled with a radioisotope power system; on the other hand, for the use on midearth orbit satellites or for solar system exploration, concentrated solar energy can be used as the heat source. The main research on AMTEC-power generation for spacecraft operations has been carried out in the USA (Ford Motor Company, Jet Propulsion Laboratory (JPL), Advanced Modular Power Systems, Air Force Phillips Laboratory, Orbital Sciences Corporation).

Parallel, at the FZK (former KIT) developed AMTEC cells in cooperation with ABB for terrestrial concentrated solar power applications [1, 86]. The high working temperatures achievable in the AMTEC cell, make this converter a potential candidate in the concentrated solar thermal industry: e.g. the AMTEC & CSP 2.0 concept presented in this work. Also in Japan, China, Korea and USA the solar application of AMTEC has been proposed [21, 22, 124, 23]. Other applications are connected to the use of excess heat of industrial processes and other power conversion systems.

3 Literature review

This chapter resumes theoretical and experimental research on AMTEC devices. First, the history of AMTEC systems is summarized; then diverse experimental investigations on the main AMTEC components carried over the years are presented. At the end, various theoretical and modeling studies of AMTEC proposed by diverse authors are discussed.

3.1 History of AMTEC converter

AMTEC, originally called Sodium-Heat-Engine, arose as a spinoff of the NaS-battery research at the Ford Motor Company [125]. Jointly with the Jet Propulsion Laboratory (JPL), the Ford Motor Company followed the research focusing on electrical power generation for spacecraft operations. First AMTEC cells had a single-BASE tube configuration and a liquid sodium anode. Cole [32] showed in 1983 that at high temperatures the specific power output of the cell dropped in time. The effect of the power degradation increased with the electrolyte temperature and depended on the tested electrode.

The fast development on AMTEC technology in the 90s made it a promising power conversion device for space missions. Hunt reported in 1985 [126] a cell efficiency of 19 % and a stable cell performance of 0.4 - 0.5 W/cm^2 with TiN electrodes for 1600 hours at $\sim$ 800 °C. Underwood et al. [87] reported in 1988 power densities of 0.7 - 0.8 W/cm^2 with Rh/W electrodes during 160 hours and at 857 °C. The advantages of AMTEC technology in spacecraft were significant compared to the state-of-art of the technologies available in the nineties [127]: 20 % tested efficiency and expected efficiency of 30 %; static conversion system; d.c. output that allows modular connection in series; reduced platform/radiator area leading to significant savings in power system mass and cost; and a conversion technology that is compatible with many heat sources (solar, radioisotope reactor, combustion, etc.).

While the JPL focused its research efforts on space applications, the group of Heinzel [2] in the FZK, Germany, worked in cooperation with the Asea Brown Boveri (ABB) in different liquid-anode AMTEC experimental studies for CSP terrestrial applications. Elaborated tests were made from 1989 until 1993 to analyze different electrodes, current collectors and current leads [128, 1].

The concept of vapor-anode AMTEC cell appeared at the beginning of the 90es. This kind of AMTEC cells use vapor sodium and porous electrodes on both sides of the BASE tube and include a boiling heater for the vaporization. The disadvantages of vapor anode cells are a lower power density and lower maximum current density caused by higher polarisation losses in the anode and a complex design for the evaporator, which must avoid sodium to condense generating an electrical short circuit. The main advantage, however, is given by a simpler electrical isolation for serial stacking design.

Connecting the BASE tubes in series (modular design, see figure 2.23) increases the terminal voltage of AMTEC and thus the power output of the cell. The first liquid-anode AMTEC cell with series connected BASE tubes was tested in 1991 by Masuda et al. [129] at the Electrotechnical Laboratory in Japan, with two BASE tubes. The obtained terminal voltage was 2.73 V and power density 0.23 W/cm^2 remained low due to high electric losses in current collecting bus bar, however, heat losses could be reduced as a result of the optimized modular design. Nevertheless, the complexity for isolating electrically the BASE tubes in liquid-anode cells, led to further focus on vapor-anode multitube cells.

Some years later, the Air Force Philips Laboratory in in Albuquerque (USA) developed and tested different vapor-anode series-connected AMTEC cells for advanced radioisotope power systems (ARPS) in cooperation with Advanced Modular Power Systems (AMPS), Orbital Sciences Corporation (OSC), Nichols Research Corporation (NRC) and the Institute for Space and Nuclear Power Studies (ISNPS) [121, 130]. The development was focused on the Pluto Express (PX) mission. In 1997 Merril et al. [122] reported a fast power degradation of PX-cells in time by 20.7 % over $\sim$ 3000 hours. Subsequently, Lodhi et al. [131] from the Texas Technical University reported in 2001 also a power degradation of the PX-3A cell of up to $\sim$ 50 % after 2 years of operation.

A decrease on the BASE conductivity over the time has been observed by several authors, which influences significantly the power output. Consequently, different BASE degradation models have been developed [132, 133, 134, 135]. Authors reported the existence of a critical current density threshold, at which internal failure of the BASE is expected. In 2000 Lodhi et al. [136] simulated the degradation behavior of AMTEC and compared the results with empirical data. They found that during the first 7000 h of operation almost $\sim$ 70 % of the power loss was associated to a reduction of the ionic resistance of the BASE. Over 7000 h of operation, the degradation of other components, like electrodes, became relevant too. After 12000 h, the ionic resistance of the BASE increased, reaching 58 % of the total cell resistance.

In 1994 Ryan et al. [137] presented a model for the prediction of electrode lifetime based in the grain growth rate. Assuming that grain sizes $\geq 1\,\mu$m make AMTEC inefficient, they predicted that Mo electrodes would live ~ 6 years at 852 °C and Pt2.5W electrodes 60 years. Lodhi and Briggs [138] found in 2007 that the grain growth depends on different parameters: initial grain size, exponential growth, mobility, activation energy, electrolyte temperature and time of operation. They developed also an empirical relation to predict the power loss over time. Lodhi and Briggs were less conservative than Ryan et al. and predicted $\sim 30\,\%$ power degradation for Mo electrodes after 15 years at 877 °C and 32 % degradation for TiN electrodes.

Contrary to the disclosed results by several authors, Hunt and Rasmussen [139] reported in 2006 the long term constant performance of a small, multi-tube AMTEC converter over 5 years of continuous operation. The cell had an input temperature of ~ 642 °C and performed 0.5 to 0.6 W. This results show the first AMTEC cell operating over several years without power degradation. Although no explanation is given by the authors to these positive results, the statement may have been positively influenced by the relative low operation temperature, very low power output, and very low current $J_{max} \sim 1$ A.

Over the years, AMTEC converter has shown to have a large potential as direct energy converter. Still several issues remain, requiring further investigations, in particular losses in BASE and porous electrode.

3.2   Specific component research. Major developments

AMTEC cells have two main issues that have been investigated in detail in the literature:

High cell losses/low cell efficiency. Compared to the maximum theoretical efficiency ($\sim 45\,\%$ at $800\,°C$) the reported efficiency of a AMTEC cells remains low: the best AMTEC cell had a $25\,\%$ efficiency [1], however typical values are even lower: $\sim 15\,\%$. The main cell losses attributed to the low efficiency are distributed as: i) heat losses (heat radiation losses represent $\sim 40\,\%$ of the total cell losses at $800\,°C$ according to [1]), and ii) polarisation losses. As already mentioned in chapter 2, the morphology of the cathode and current collector structure are of vital importance to reduce polarisation losses. An optimum morphology of the cathode varies depending on the electrode material and is therefore individual for each material.

Fast power degradation. The output power of AMTEC cells has evidenced a fast power degradation (power output reduction of $\sim 50\,\%$ after 2 years of operation [122]). The reduced chemical stabillity of the BASE (e.g. sensitiviness to moisture absorpition), the high operation temperature and the corrosive medium (sodium) are the main responsibles for the power degadation of the cell. Referring to cell components, the degradation of the BASE is responible for the most power reduction (up to $\sim 70\,\%$ during first $7000\,h$ [136]), while the porous electrode degradation (cathode) begins to be relevant at temperatures $> 700\,°C$ [137] and more advaced operation time ($> 7000\,h$ [136]). The BASE experiences a decrease in the ionic conductivity as result of the degradation of the chemical structure. The main cause for cathode degradation is the grain growth. It occurs due to grain sintering at high temperature during long operation time and is strongly dependent on the electrode material [140]. As the grain grows, the length of the TPL decreases, which reduces the amount of sodium atom recombinations. Simultaneously, voids become larger, which can lead to a decreased grain-to-grain contact. The final effect is a drop in the cell current density.

Subchapter 3.2.1 deals with the major developments and investigations on AMTEC porous electrodes concerning the influence of electrode morphology, material and degradation behavior on the ouput power of the cell.

The transition of ceramic (BASE) to metal (cell structure) in AMTEC (see figure 2.11, Nb-brazing) remains a technological issue due to the chemical and thermo-mechanical challenges associated with the high operation temperatures and the thermal transients. An overview of the main developments on *ceramic-metal joint* is presented in subchapter 3.2.2.

Finally subchapter 3.2.3 summarizes the main investigations on BASE degradation mechanisms. The following literature is organized in a historical sequence.

3.2.1 Porous electrode

An extensive literature on AMTEC-porous electrodes exists that focus on overcoming the well-known challenges. This subchapter focuses on the main achievements of the porous cathode.

In 1986 Williams et al. [141] carried out voltammetry experiments with partially oxidized porous molybdenum (Mo) electrodes at different temperatures. Redox processes were detected involving sodium and MoO_2. The most important product of reaction was Na_2MoO_4. The ionic conductivity of Na_2MoO_4 was measured and revealed a sharp increase with the temperature. For temperatures higher than 427 °C the ionic conductivity was large enough to explain the enhanced results and to improve sodium transport in AMTEC electrodes below the melting point of Na_2MoO_4 (687 °C). In the same year, they developed a model for the chemical reactions that occur in porous Mo electrodes and achieved a regeneration of a degraded electrode by an O_2 treatment [95]. The regeneration treatment showed to recover up to $\sim 80\%$ of the initial current density.

1988 Underwood et al. [87] tested four different electrode compositions: very thin molybdenum (VTM), platinum/tungsten trilayer (Pt/W), rhodium/tungsten bilayer (Rh/W), and titanium nitride (TiN). The electrodes reached stable maximum power densities of 0.4 to $0.8\,\mathrm{W/cm^2}$ for temperatures between 827 and 977 °C during 90 to 160 hours.

1988 Wheeler et al. [91] tested porous Mo and W electrodes at different thicknesses. For thicknesses smaller than $0.4\,\mu\mathrm{m}$ the sheet resistance of the sputter film increased rapidly but the power degradation and the vapor flow resistance were reduced. In order to compensate sheet resistance, fine current collector grids with a higher density of contact points were required. Mo electrodes ($0.5\,\mu\mathrm{m}$) gave power densities of $0.4\,\mathrm{W/cm^2}$ at 927 °C and tungsten electrodes ($0.5\,\mu\mathrm{m}$) performed $0.35\,\mathrm{W/cm^2}$ at 907 °C both after 40 - 90 hours of operation.

1989 Williams et al. [93] studied the resistance and the power of the cell using WPt and WRh electrodes with different porosities and thicknesses. For the WPt electrode at 887 °C they obtained a final maximum power density of $\sim 0.8\,\mathrm{W/cm^2}$ and for the WRh electrode the maximum power density was 0.5 - $0.8\,\mathrm{W/cm^2}$ at 932 °C.

1991 the group of Boßmann [142] at the Asea Brown Bovery (ABB) tested two different liquid-anode AMTEC cells to examine the influence of the electrode thickness, operation temperature and the positioning of the condenser on the output power and

efficiency. They measured power densities, cell resistance and sheet resistance of the cell by TiN electrode thicknesses from 0.2 to 5 μm at a temperature of ~ 750 °C and a constant electrode area of 30 cm^2. The maximum power density of the cell increased continuously with the electrode thickness (from 0.02 to 0.12 W/cm^2 by respectively 0.2 to 5 μm thicknesses) [128]. In comparison with Mo, TiN has a much larger sheet resistance for the same electrode thickness due to the six times higher electrical resistivity of TiN. This explained the positive effect of increasing the thickness of the TiN layer on the resistance of the cell.

1991 Williams et al. [94] proved stable W/Rh electrodes with overlying molybdenum current collecting grids, mesh and leads during 800 hours at ~ 877 °C for an output power density of ~ 0.55 W/cm^2. A total of six electrodes with areas smaller than 10 cm^2 were tested with Ni and Mo current collector grids. Those with a Ni grid showed a significant metal migration of the Ni grid and the W/Rh electrodes, leaving about 40 % of the electrode area free of metal film. The performance of the electrodes with Mo grids was stable.

1992 Kato et al. [101] tested several ceramic electrodes: TiN, niobium nitride (NbN) and titanium carbide (TiC). They observed that the maximum power densities of the electrodes depended considerably on the degree of vacuum. For NbN electrodes a variation of the vacuum pressure from 130 to 0.037 Pa contributed to an increase in the power density from 0.12 to 0.27 W/cm^2 due to the enhanced diffusion process through the electrode. They also observed that at high current densities; the sodium diffusion process through the electrode became a power limiting factor. In contrast, the power limiting factor at low current densities was the charge transfer process. The transition between these two regions depends on the operating temperature. At temperatures < 750 °C for TiC electrodes, a limiting current region appears above a certain current density: < 1.1 A/cm^2. Due to the enhancement of the diffusion process by increasing the temperature, no limiting current density was observed at 800 °C.

1992 Fang and Knödler [89] published the test results of an AMTEC converter using titanium diboride (TiB$_2$) porous electrodes and compared them against AMTEC converters from the literature with Mo and TiN electrodes at 800 °C. TiB$_2$ is characterized by a good chemical stability, a low resistivity and a similar expansion coefficient to that of the ß"-alumina. The thickness of the TiB$_2$ electrode was varied between 0.5 and 4 μm and electrode area between 0.8 and 30 cm^2. A Mo mesh acted as current collector, wrapped with Mo wire to the sputter layer. For a maximum current density of about 1.3 A/cm^2 and an electrode area of 30 cm^2 they obtained a maximum power den-

sity of 0.24 W/cm^2 at 800 °C. The optimal thicknesses of the TiB$_2$ sputter layer at which the cell performed better, were between 1 and 2 μm. The tests exhibited a strong dependency of the power density on the electrode area: the maximum power density of $\sim$0.37 W/cm^2 was obtained for the smallest electrode area at 800 °C. Moreover, the stability of the TiB$_2$ electrodes was better than that of Mo, after more than 10 hours of operation at 750 °C the cell remained completely stable at 0.83 V and 0.5 A, which makes TiB$_2$ electrodes as a good candidate for AMTEC electrodes.

1992 Ryan et al. [143] proved the influence of the sintering rate of Pt and Rh in the lifetime of respectively PtW and RhW electrodes. The sintering process improves at the beginning the contact among the sputter grains and at the interface BASE/electrode. After a while, the larger coalescence between the grains reduces the operating area of the electrode and increases at the same time the grain volume. As a result opening voids in the electrode appear that increase the sheet resistance of the electrode. The authors showed that PtW electrodes deliver higher power densities than RhW electrodes ($\sim$20 % more). However, Pt sinters faster than PtW, meaning a shorter predicted operating lifetime. PtW electrodes would have a predicted lifetime up to 7 years, while RhW electrodes could achieve up to 40 years [143].

1993 Nakata et al. [144] examined TiN, TiC, TiC/TiN and Mo electrodes. A limiting current region was observed at $\sim$1 A/cm^2 and 750 °C, above which the power density decreased. For a vacuum pressure under 10 Pa the power density did not depend on the pressure, showing that there is a free molecular flow below such vacuum level. Above 10 Pa the power density decreased affected by the viscous flow. The obtained activation energies were lower for the ceramic electrodes (47 kJ/mol for TiN) than for the molybdenum electrodes (107 kJ/mol).

1993 Kato et al. [40] compared different electrode materials made of TiN, NbN, TiC, multilayered TiC/TiN, lanthanum hexaboride (LaB$_6$) and Mo. They observed that TiC/TiN porous electrode proportioned much lower current density compared to the others due to the larger grains in the electrode. Several TiC electrodes were studied for different grain sizes. The results of the TiC electrodes showed that smaller grain size ($\sim$0.07 μm) delivered the highest power density (up to 0.75 W/cm^2 at 800 °C and 5 μm electrode thickness).

1996 Fang and Wendt [145] tested a cell with liquid anode (Na) and two different liquid cathodes: Na-Sn and Na-Pb molten alloys. The purpose of using molten sodium alloys in the cathode side was to enhance the electrolyte-electrode and electrode-current

collector contact, since the contact resistances are eliminated. Furthermore, the liquid-cathode design does not require the vacuum system used in most AMTEC cells. A drawback of such a process, however, is the need of a sodium-metal distillation system in order to separate sodium vapor from the alloying metal. The theoretical efficiency of AMTEC cells with sodium alloy electrodes depend significantly on the sodium content, varying between 30 % for sodium concentration of 0.2 and a maximal value of 40 % for a concentration of 0.02. The measured cell resistance of AMTEC with molten electrodes was low (0.3 - 0.35 Ω/cm^2 at 700 °C), what denotes the important role of a good contact between electrolyte-electrode-current collector to enhance the power output of the cell. Fang and Wendt reported maximal power densities of 0.15 to 0.21 W/cm^2 at 700 °C for Na-Sn and 0.15 to 0.30 W/cm^2 for Na-Pb molten electrodes. The power densities obtained were rather low due to a low cell voltage of 0.3 V).

1997 Merril et al. [122] tested the AMTEC series cells PX-2C (6 BASE tubes) with TiN electrodes and a cathode area of 6 cm^2. A maximum power output of 0.12 W/cm^2 and an efficiency of $\sim$ 14 % were obtained during a continued operation of $\sim$ 500 hours. PX-3, PX-4 and PX-5 series were as well tested and gave similar power output and efficiencies [146].

1998 Tsuchida et al. [82] tested LaB$_6$ and TiB$_2$ electrodes and obtained optimum values for particle size, thickness, porosity and vacuum pressure for LaB$_6$ electrodes. Maximum power densities at 800 °C were 0.54 W/cm^2 and 0.24 W/cm^2 for LaB$_6$ and TiB$_2$ electrodes respectively. They observed that finer grain size allows a longer triple-phase boundary, thus enhancing the recombination rate of sodium ions with the electrons. However, the pore size in electrode decreases for too small grain sizes ($<$ 0.6 μm for LaB$_6$), causing a large resistance for sodium vapor transport. The same effect had a low porosity: in the case of LaB$_6$ electrodes the optimum porosity of 55 % supplied the highest power density. Higher porosities than 55 % decreased the power density due to increased sheet resistance of the electrode. Variation of the thickness showed that LaB$_6$ electrodes performed best with 5 μm thickness. Smaller thicknesses decreased the power density due to increased sheet resistance and higher thicknesses decreased the power density too due to an increased resistance of the transport of sodium vapor. Vacuum affects also power output: a pressure below 10 Pa had insignificant effect on power output of LaB$_6$ electrodes because sodium vapor has a free molecular flow; higher pressures instead implicated a lower power output due to a viscous flow behavior of sodium vapor. They obtained the activation energy for different electrodes and obtained that ceramic electrodes (LaB$_6$, TiB$_2$) have a lower activation energy than Mo electrodes.

2001 Ryan et al. [103] observed that in some TiN preparations had a better performance than expected even at electrode thicknesses as large as 20 μm. In those cases titanium-oxygen compounds were present. They could demonstrate that TiO_2 in a vapor sodium atmosphere reacts at high temperature to form Na-Ti-O compounds which are not only electronically but also ionically conductive. Some tests made with Mo/TiO_2 mixed electrodes showed an advanced performance compared to Mo electrodes. It was proved that both exchange current and sodium transport were improved in the electrode. Furthermore Mo/TiO_2 electrodes did not show power degradation during 1500 hours of operation.

2003 Fletcher et al. [90] published in 2003 developments of TiN/TiO_2 sintered electrodes. Due to the TiO_2 compound conductivity, the power output of the sintered electrode ($\sim 0.38\,W/cm^2$ at 850 °C) was increased 39 % compared to a sintered TiN electrode ($\sim 0.27\,W/cm^2$ at 850 °C). However, sputtered TiN electrodes still outperformed by ~ 23 % ($\sim 0.47\,W/cm^2$) the sintered mixed electrode due to its much smaller grain size, more uniform structure and better adhesion to the BASE surface.

3.2.2   ß"-alumina to metal joint

Ceramic-metal components can be joined by different techniques: from the mechanical, through indirect to the direct joint. Taking into consideration the typically cylindrical form of the ceramic, its chemical stability, low thermal expansion coefficient, the very small thickness ($< 2\,mm$), the high operating temperature in AMTEC process (> 600 °C), and the required gas tightness of the joint ($< 1 \times 10^{-3}\,mbar\,l/s$), the selection of an appropriated technique becomes challenging. A mechanical joint is not the most adequate method to use due to the small thickness of the BASE, the high temperatures and the reduced space inside the cell. Other methods like direct joint, which can be achieved for example through laser welding, ultrasonic welding, electron beam welding or diffusion bonding, have not been tested yet with ß"-alumina ceramics at AMTEC operating temperature. Ultrasonic welding and electron beam welding have been tested to weld alumina ceramics to metal [147, 148]. Up to date, only indirect bonding has been reported to be used in AMTEC cells. The most relevant bondings in AMTEC are mentioned here. Due to the different thermal expansion coefficients between the BASE and stainless steel, most of the authors have used a Nb transition tube due to its similar thermal expansion coefficient to BASE. Therefore, the following literature review focuses rather on the indirect joint through a brazing filler metal between the BASE and the Nb tube.

TiCuNi brazing filler metal was tested by Williams et al. [94] in 1991 and Knödler et al. [86] in 1992. In both cases the brazing was not recommended for high temperature

AMTEC cells ($>$ 800 °C) due to the volatility and high solubility of Cu in Na. However, the braze performed well in tests up to 600 hours of operation, without failure [122].

In the nineties at FZK Cu from the brazing filler metal was substituted with Nb. The brazing filler metal with 50 % NiTi and 50 % Nb was tested for the joint between Nb and BASE tubes. Nb helped to reduce the thermal stresses due to a similar thermal expansion coefficient as BASE. Authors tested 12 joints with different gap dimensions [149]. The obtained tightness was in the range of 10^{-7} - 10^{-9} mbar l/s. Samples were subsequently subjected to compatibility tests in sodium at 1000 °C and obtained a tightness in the range of 10^{-2} - 10^{-3} mbar l/s after 1000 hours [150]. Due to the color changes observed after the compatibility tests, a follow-up examination of the diffusion processes was performed [150]. Ti oxidated in contact with BASE and reduced the aluminum oxide to metal aluminum (see equation (3.1)); the concentration of titanium oxide (TiO) in the ceramic was small ($<$ 3 %) and it penetrated relatively slowly ($<$ 150 μm). However the metal aluminum penetrated rapidly ($\sim$ 1 mm) into the brazing and the Nb tube; the concentration of aluminum in the Nb tube was very high ($\sim$ 65 %). Thus the joint bond disintegrated. Authors recommended not to use this 50NiTi-50Nb joint for operating AMTEC cells.

$$3Ti + Al_2O_3 \rightarrow 3TiO + 2Al \tag{3.1}$$

Williams et al. [151] tested in 2001 different electrode materials (Mo, W, Pt, Rh, TiN, Vanadium (V), Ti) in sodium vapor medium at temperatures up to 900 °C for periods of up to 6800 hours. They concluded some positive aspects for brazing filler metals. In their tests they observed that V was also an adherent metal with no tendency to react with BASE over short periods of time ($\sim$ 10 hours). On the other hand, they confirmed that Ti alloys cause BASE surface degradation and damage the electrolyte. They considered Ti as a potentially damaging metal for the BASE and proposed V as a good sealing between metals and BASE, due to its good adhesion and no apparent reaction with electrolyte in long term.

2013 Kim et al. [152] evaluated the bonding properties of a CaO-Al_2O_3 adhesive for ß"-alumina in AMTEC environment (in Na vapor and at $>$ 600 °C). It was proven that the adhesive provides a strong bonding in Na vapor environment at high temperatures. For a bonding temperature of 1420 °C the bonding shear strength was 35 MPa. Higher bonding temperatures implicated higher bonding strengths but it would involve an accelerated grain growth of the BASE, not desired.

3.2.3   Electrolyte. BASE degradation mechanisms

A long time study on the AMTEC behavior is not foreseen in this work; however, during the 7 day long measuring campaign some power decrease was observed. Also, an incorrect handling of the BASE may lead to BASE degradation, which should be likewise considered. The following content summarizes the main investigations on BASE degradation mechanisms made along the years, which can help understanding the behavior observed in the experiments.

1974 Armstrong et al. [132] proposed a BASE degradation model in which the formation of molten sodium dendrites occurred in preexisting pores/cracks in the ceramic and propagated due to the Poiseuille pressure causing the extension of the crack and the final breakdown of the ceramic. A mechanism of dendrite-propagation was suggested. This degradation model of the BASE was called Mode I.

1975 Richman and Tennenhouse [133] developed a model for the degradation of ß-alumina in Na-S batteries. The model shows a threshold current density below which no degradation occurs. Cracks in the ceramic are filled up with sodium, decreasing the resistance in comparison to the surrounding surface, thus ions will concentrate at the crack tip. If the critical current is exceeded, the fracture strength will decrease considerably with the current.

1981 De Jonghe et al. [134] proposed a mode of degradation in sodium ß-alumina. In their experiments a loss of oxygen from the electrolyte was detected that introduced some electronic conductivity. Once an electron coming from the sodium ionization goes inside the solid electrolyte, it will recombine in the bulk of the electrolyte to generate sodium molecules and a local internal microfracture. This is the so called Mode II of BASE degradation.

1982 De Jonghe [153] developed a formulation for the critical applied voltage or current density above the electrolyte would undergo a fracture caused by internally deposited material. Not only the presence of impurities in the electrolyte induce the degradation of the electrolyte with Mode II, but as well the internal sodium formation inside the electrolyte causes microcracks. Molten sodium in direct contact with electrolyte (anode-BASE interface) removes oxygen from the electrolyte structure, leaving oxygen vacancies compensated by electrons. This process can be found in BASE, observed through the darkening of the ceramic; and propagates through the electrolyte but at a slow rate. Na-ß"-Alumina was tested in contact with liquid sodium at 350 °C from 1

to 8 days. The sodium propagation in the BASE reached $\sim 350\,\mu$m after one day and $550\,\mu$m after 8 days. This Mode II of degradation appears to be unlikely in early stages of cell operation.

1983 Nicholson [135] proposed a new mechanism for the degradation of BASE that would dismiss the degradation Mode I through Poiseuille-pressure. The suggested model is based on the Na$^+$ ions supersaturation, which occurs when Na$^+$ ions arrive faster at conduction plane sites than they can diffuse out and discharged. In this case oxygen O(5) ions will oxide to sodium and electrons will trap at oxygen sites. The removal of the O(5) ions generates the collapse of the conduction planes since they do not maintain the space between the structural spinel blocks anymore. The reaction sequence can be described like follows:

$$ Na^+ + O(5) \rightarrow Na + O + V_{Na}^{'} + (e)_o \qquad , \qquad (3.2) $$
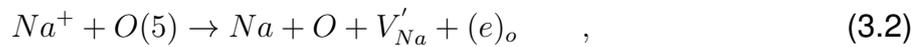
where $V_{Na}^{'}$ represents a vacant sodium site and $(e)_o$ is an electron trapped at an O(5) site. Nicholson suggested further, that the sodium atoms coalesce into colloids giving as result a dense microstructure which finish microcracking. The microcracks promote sodium precipitation ending with a sodium "dendrite" progressing through the electrolyte. The feasibility of this supersaturation concept is demonstrated for ß/ß"-alumina at 300 °C. According to the model the critical current density value requisite for the degradation mechanism suggested is 2.5 to 3 A/cm^2. On the other hand, the Poiseuille-pressure model is suggested not to be appropriate as the deterioration should decrease with the temperature according to the model, however, it was observed to increase.

1983 Kuribayshi and Nicholson [154] proved as well the unsuitability of Poiseuille pressure model, since the tested electrolytes suffered enhanced deterioration with applied tensile and as well compressive stresses during electrolysis. The work of Nicholson, showed that the dark coloration of the electrolyte happens without the need of a current flow. In addition it was observed that the surface flaws in the sodium liquid-anode/electrolyte interface play a very important role in degradation since they concentrate the current. For high polished surfaces (1 μm) lifetime was increased as found in [132].

1983 Singh and Lewis [155] proved in an experiment the mechanism of BASE degradation through the loss of oxygen ions from the electrolyte. They made optical observations in the sodium-electrolyte interface. Formation of needle-shaped sodium oxide

on the surface of Na-ß"-electrolyte appeared at 200 °C, meaning that liquid sodium re-acted with BASE to produce sodium oxide and thus degrading the electrolyte by means of loosing oxygen ions.

Following the findings of Kuribayshi and Nicholson [154],1986 Virkar [156] examined the role of externally applied stresses on solid electrolyte breakdown under electrolytic conditions. The results of the Poiseuille pressure model were consistent with their ex-perimental observations. For a BASE under compression of 150 MPa acting over a part of the length crack, the calculated critical current density was 2.23 A/cm^2, while for the case with no compression the value was significantly higher: 7.7 A/cm^2.

Most of the BASE degradation models obtained were based primarily on the assump-tion of a two dimensional crack. 1983 Virkar and Viswanathan [157] developed in con-trast a model for a three-dimensional crack, which extended in the width direction rather than along the length of the crack. Their results agreed well with experimental results: for a crack length of 200 μm and width 60 μm the critical current density was 18.8 A/cm^2; experiments showed values between 10 and 20 A/cm^2. Virkar criticizes the conclusions of Kuribayashi and Nicholson [154] as they did not take into account the role of the external stresses on the working fluid.

A typical issue related to AMTEC cells is the breakout of the BASE tube. For this rea-son, 1991 Hunt et al. [158] tested and analyzed the stresses induced in tube formed BASE of an AMTEC cell. The experiments showed that due to the poor reflectivity of the condenser or deficient radiation shielding, the radiation losses in the cell can be severe, causing significant temperature gradients across the BASE and thus, raising radial thermal ultimate stresses that could reach failure stress levels of the ceramic. Un-fortunately no specific value for this temperature gradient is mentioned by the authors. At high temperature, additional radial stresses in the exterior surface of the BASE tube can appear due to impurities infiltrating the BASE from the liquid sodium side. Further, internal stresses can appear when a significant amount of neutral sodium penetrates non-uniformly in the BASE or due to the residual stresses originated in the ceramic dur-ing its manufacture, sintering and cooling. A thermal shock is the most common failure of the BASE that takes place when liquid sodium is being introduced to the BASE at a different temperature. Temperature shocks of 200 °C could cause immediate electrolyte failure.

1993 Steinbrück et al. [159] tested four different ß"-alumina samples from four differ-ent manufacturers. Two of them were MgO stabilized and the other two Li$_2$O stabi-

lized. They observed that after exposure of the electrolyte to air, samples which were solely immersed in sodium were more reactive in humid atmosphere compared to virgin samples or samples used under AMTEC conditions. Electric conductivities of various BASE materials were measured at AMTEC conditions 650 - 800 °C and gave values between 1.1 - 2.8×10^{-4} Scm. Magnesia stabilized samples showed to have a two times higher electronic conductivities than the lithium stabilized ones. The values obtained in any cases were negligible concerning the efficiency of the AMTEC cell. However, it should be kept in mind regarding electrolyte degradation. XRD analysis revealed internal stresses within the ß"-alumina crystals, which may be caused by intracrystalline sodium penetration. Nuclear magnetic resonance showed a peak attributed to sodium metal inside the BASE only for the case of sodium exposed sample. Samples used in AMTEC were found not to have sodium metal (within the detection limit: $\sim$ 0.2 %). Other tests made in collaboration with Fritz et al. [160] (1993) revealed that at AMTEC open circuit conditions metallic sodium was formed at the condenser. This was not caused by leakage or diffusion of sodium through the BASE but by the simultaneous transport of sodium ions and electrodes through the ceramic. Increased electronic conductivity occurs at elevated temperatures due to a chemical interaction between the BASE and molten sodium or sodium vapor in AMTEC cells. The electrical conductivity becomes significant 3.4×10^{-4} Scm only at high temperatures $\geqslant$ 727 °C, for lower temperatures like in the Na/S batteries (T$\sim$ 357 °C) it can be neglected.

2001 Lodhi et al. [161] analyzed the test results from the PX-3A AMTEC cell and deduced the importance of the different mechanisms that take place in the cell and are responsible for power degradation. The degradation due to the BASE alone is originated by i) loss of sodium from the structure of the electrolyte as sodium oxide, thus decreasing the ionic conductivity and affecting negatively the stability of the BASE [155]. ii) Formation of sodium molten dendrites within the structure, which propagate through the structure and are able to cause an electrical short circuit. Third, iii) crack formation by conversion of sodium ions to metallic sodium inside the ceramic. This degradation mechanism was observed in an experiment. As the sodium ions convert to metallic sodium at the tips of the initial cracks, they spread and formed an opening between both sides of the cell, thus decreasing the power density. iv) Grain growth happens at high temperature during large periods of time. As grain size increases, the exchange current decreases due to the reduced contact between grains in BASE and electrodes. After a few 1000 hours of operation the grain size can increase so much that microscopic voids appear growing the ionic resistance of the electrolyte.

3.3 Key open questions. Conclusions

The following list summarizes the most relevant issues of each component addressed in the previous subchapter.

Electrolyte (BASE)

- Contamination. Several materials like Na and Ca account for the degradation of BASE performance. The exposure of the BASE to air has shown to have a negative impact not only in the ionic conductivity of the electrolyte but also on the chemical resistance to liquid sodium.

- Microcracks at the anode side. Initial microcracks appearing on the surface of the BASE account for BASE degradation Mode I. Formation of molten sodium dendrites are induced in the preexisting cracks and propagate into the bulk ceramic due to the Poiseuille pressure.

- Loss of oxygen from the BASE. Liquid sodium at the anode side reacts with the BASE by means of producing sodium oxide, decreasing thus the ionic conductivity and affecting negatively the stability of the BASE.

- Electrical conductivity. Even a very low electron conductivity produces that sodium ions recombine with electrons in the ceramic originating thereby a local internal microfracture. This is the degradation Mode II. The electrical conductivity becomes significant at $T > 700$ °C, 3.4×10^{-4} Scm [159].

- Electrolyte breakout. Thermal stresses originated through significant temperature gradients during operation (200 °C temperature shocks can cause immediate electrolyte failure [158]), internal stresses due to sodium intracrystalline penetration in the BASE or residual stresses appearing after the manufacturing, sintering and/or cooling of the ceramic, may be the main causes for electrolyte breakout.

Porous electrode (cathode)

- Grain size. Small grain sizes increase the power output of the cell (e.g. TiC $\leq$ 0.07 μm [40]) due to the increased length of the TPL. Optimum grain sizes depend on the electrode material.

- Porosity. A high porosity enhances the sodium transport through the electrode but increases the resistance for electron transport. Optimum porosity depends on the electrode material (e.g. LaB$_6$ 55 % [82]).

– Thickness. A large thickness allows a better electron transport but increases the resistance for sodium transport. The optimum value thickness varies depending on the electrode material: TiN $\geq 5\,\mu$m [142], TiB_2 $1 - 2\,\mu$m [89], LaB_6 $5\,\mu$m [82].

– Sintering rate vs. electrode lifetime. Under AMTEC operating conditions electrode´s grains tend to sinterize mainly due to the high temperatures (considerable electrode degradation usually at $T > 700\,$°C [137] for Mo electrodes). The faster the sintering rate, the faster the electrode degradation by means of reducing the TPB and electrical conductivity. The sintering rate and therefore the electrode lifetime is directly affected by the material properties: PtW electrodes have a predicted lifetime ~ 7 years, while RhW electrodes are predicted to withstand up to 40 years [143].

– Chemical stability. A good chemical stability in sodium is important to avoid power degradation mechanisms: e.g. Mo $\rightarrow$ MoO_2 (melting point 687 °C) [141].

– Current density. The higher the current density, the larger the pressure of sodium vapor at the porous cathode. A limiting current region appears at high current densities ($\sim 1\,$A/cm^2 for TiC electrodes at $< 750\,$°C [101]) above which there is a viscous flow of sodium vapor that increases the transport resistance and therefore decreases the cell power. Under the limiting current region sodium vapor undergoes a free molecular flow that provides for higher power densities. The limiting current increases with the operation temperature [101].

– Vapor pressure of sodium at the cathode. Connected to the current density is the vapor pressure of sodium, which dictates the flow properties and thus the losses due to transport in the porous electrode. At pressure $< 10\,$Pa sodium vapor is in free molecular flow regime and thus concentration/transport losses are smaller than at $> 10\,$Pa, where the flow regime is viscous [144].

– Deposition technique. The performance of the electrode depends strongly on the deposition technique. The best reported results are with magnetron sputtered electrodes. Sputtered TiN electrodes outperform $\sim 23\,\%$ (power output) compared to sintered TiN electrodes [90].

– Current collector structure. The transfer of electrons from current collector to the cathode depends on the number of contact points. The higher the number of contact points between current collector and cathode, the lower is the electrical resistance. A good current collector structure can increase the power output of the cell up to 50 %.

Ceramic to metal brazing

Adequate materials are needed for the brazing, which have a similar thermal expansion coefficient than BASE, withstand the high temperatures and do not react chemically with sodium and BASE. TiCuNi brazing filler metal is not recommended for high temperatures ($>$ 800 °C) due to the volatility and high solubility of Cu in Na [94]. A brazing filler metal composed of Ni-Ti-Nb may be promising, however an optimum proportion of Ti must be obtained in order to find a good adhesion of the brazing filler to the BASE without damaging the electrolyte due to the high reactivity of Ti with the BASE.

4 Evaluation method

In this chapter a pressure loss model and an electrochemical model are presented, which can be applied for the characterization of coaxial AMTEC cells.

4.1 Vapor pressure loss model

Pressure losses in the AMTEC cell occur due to sodium transport through the BASE, cathode, current collector, the annulus space to the condenser and at the condenser as illustrated in figure 4.1. Assuming a one-dimensional system as represented, steady-state compressible flow and Na vapor as an ideal gas, the total pressure drop can be described as the sum of the following contributors: i) pressure drop through the BASE $\triangle p_B$, ii) evaporation of sodium at the BASE outer surface $\triangle p_{ev}$, iii) vapor transport through the porous electrode and current collector $\triangle p_e$, iv) vapor flow in the annulus space between the current collector p_{ic} and the condenser p_{cd}, and v) condensation of sodium vapor at the condenser $\triangle p_{cd}$:

$$\triangle p_{Tot} = \triangle p_B + \triangle p_{ev} + \triangle p_e + (p_{cd} - p_{ic}) + \triangle p_{cd} \qquad . \tag{4.1}$$
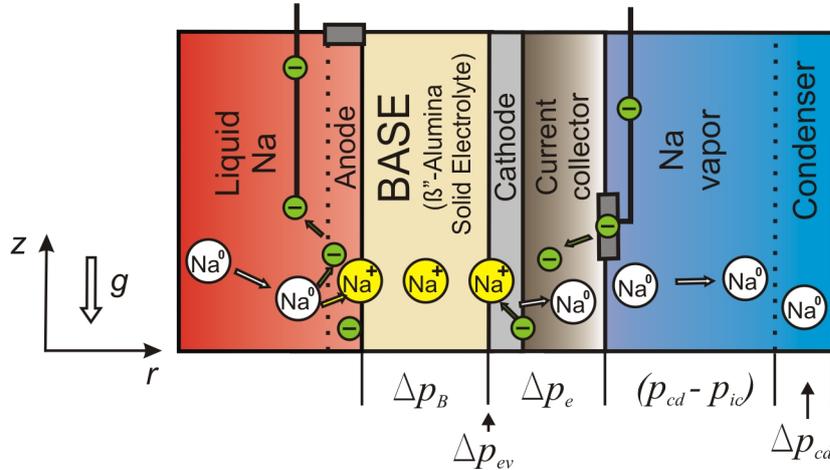
Figure 4.1: Scheme of the AMTEC one-dimensional system involved in the ATMEC pressure losses.

The pressure loss of sodium in the radial direction of the cell is represented roughly in figure 4.2. The largest pressure drop takes place across the BASE $\triangle p_B$ ($\sim 2\,\mathrm{mm}$ thickness). The pressure drop across the electrode porous layer/cathode ($\sim 5\,\mu\mathrm{m}$ thickness) and the current collector (CC) structure is considerably larger than the pressure drop across the annulus space between the CC and the condenser surface.

This chapter presents a vapor pressure loss model of a liquid-anode single tube AMTEC cell based on several models from Tournier and El-Genk [162, 33], Schock and
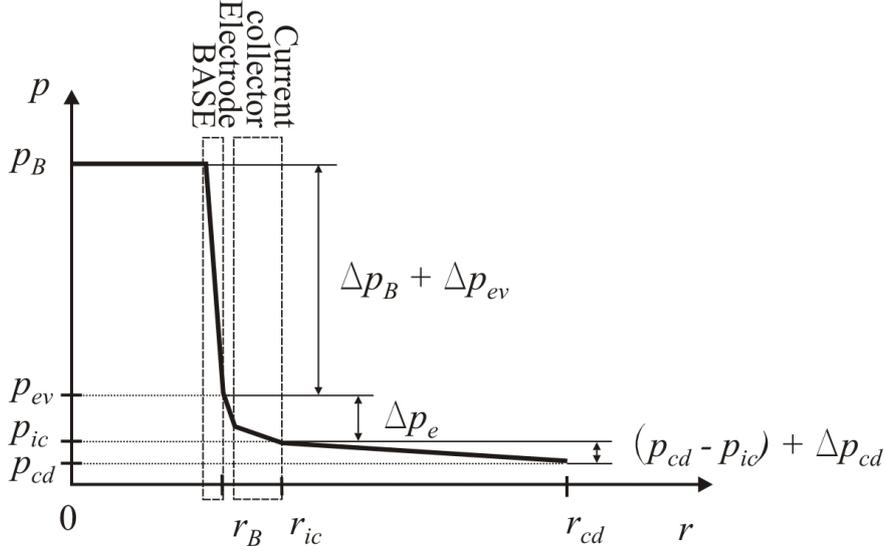
Figure 4.2: Pressure distribution of sodium in the radial direction of the cell. r_B represents the outer radius of the BASE tube, r_{ic} stands for the outer radius of the current collector, r_{cd} is the radius of the inner condenser-wall, p_B is the pressure in the anode side of the BASE and p_{ev} is the pressure of the evaporated sodium in the BASE-cathode interface.

Noravian [163, 164] and Schindler [165]. Three different concepts are presented for the modeling of vapor transport through the electrode and current collector.

1. Pressure drop across the BASE $\triangle p_B$. The pressure of sodium at the outer surface of the BASE (BASE/cathode interface) p_{ev} results due to the evaporation process that occurs during the recombination of sodium ions and electrons at the triple phase boundary. The pressure drop across the BASE is equal to the pressure of saturated sodium at the anode $p_B = p_{sat}(T_B)$ minus the pressure of sodium at the BASE/cathode interface after the evaporation p_{ev}, minus the pressure of evaporation of sodium $\triangle p_{ev}$:

$$\triangle p_B = p_B - p_{ev} - \triangle p_{ev} \qquad . \tag{4.2}$$

p_{ev} can be calculated adding to the pressure at the condenser $p_{cd} = p_{sat}(T_{cd})$ the total pressure loss in the cell $\triangle p_{Tot}$ minus the pressure drop across the BASE:

$$p_{ev} = p_{cd} + \triangle p_e + (p_{cd} - p_e) + \triangle p_{cd} \qquad . \tag{4.3}$$

Subsequently the required equations to calculate the different pressure drops (last 4 terms) of equation (4.3) are presented.

2. Evaporation of sodium at the outer surface of the BASE $\triangle p_{ev}$. The pressure drop through evaporation of sodium at BASE surface and BASE/cathode interface is given

by the kinetic gas theory [162], as:

$$\triangle p_{ev} = a_{cc} \left(\frac{2\pi R_g T}{M} \right)^{1/2} \dot{m}_f \qquad , \qquad (4.4)$$

where a_{cc} is the accommodation coefficient which for liquid metals is close to the unity in well evacuated and clean systems, M is the molecular weight and $\dot{m}_f$ is the vapor mass flux [kg/m^{2}s] in electrode pores, to be calculated through the following expression:

$$\dot{m}_f = \frac{M}{\phi_e F} j \qquad . \qquad (4.5)$$

j represents the electrode current density, while $\phi_e = Vol_{void}/Vol_{bulk}$ is the volume porosity of the cathode electrode, which can be assumed as 0.9. The higher the porosity the lower the vapor mass flux due to a longer TPB and thus a larger generation of sodium vapor at the BASE-cathode interface.

3. Vapor transport through the porous electrode and current collector $\triangle p_e$. Three different approaches from Williams et al. [166], Tournier and El-Genk [162] and Schindler [165] are presented for the modeling of vapor transport through the electrode and current collector. Williams et al. and Tournier and El-Genk neglected the effect of the current collector; only the model of Schindler incorporates the current collector.

At open circuit conditions, there is no mass flow rate of sodium between the cathode and the condenser:

$$\dot{m}_f = \left(\frac{M}{2\pi R_g} \right)^{1/2} \left[\frac{p_e^{oc}}{\sqrt{T_B}} - \frac{p_{cd}}{\sqrt{T_{cd}}} \right] = 0 \qquad , \qquad (4.6)$$

therefore the pressure at the cathode electrode/BASE interface p_e^{oc} (state 3) at open circuit conditions can be expressed with the following function [32]:

$$p_e^{oc} = p_{cd} \sqrt{\frac{T_B}{T_{cd}}} \qquad . \qquad (4.7)$$

Equation (4.7) assumes that the sodium temperature from the anode through the BASE until the porous electrode stays constant and is equal to T_B; and that the distance between the electrode and condenser is in the same order of magnitude than the mean free path [167]. In vacuum the main free path $\bar{l}$ is directly proportional to the temperature and inversely proportional to the pressure [168]

:

$$\bar{l} = \frac{\kappa_B T}{\sqrt{2}\pi p d_m^2} \qquad , \qquad (4.8)$$

where d_m is the molecular diameter. For a given distance between the electrode and

the condensed sodium film of 25 mm and $T_B = 800\,°C$, equation (4.7) can be used for pressures $p_e^{oc} < 13\,Pa$.

However, at closed circuit conditions the pressure at the BASE-porous electrode interface increases and sodium vapor diffuses through the porous electrode and the annulus space until it reaches the condenser. The pressure now is a function of the electric current density j and can can be calculated by adding the pressure at the cathode-BASE interface in open circuit conditions p_e^{oc} plus the pressure drop through the cathode and current collector $\triangle p_e$ [166]:

$$p_e^{cc} = p_e^{oc} + \triangle p_e \qquad . \tag{4.9}$$

The pressure drop through the cathode $\triangle p_e$ is caused by the transport of sodium vapor through the porous structure and can be differently calculated: i) assuming a linear pressure drop through the cathode[1]:

$$\triangle p_e^1 = K_e\, j \qquad , \tag{4.10}$$

where K_e represents the pressure loss coefficient of the porous electrode and j is the current density of the cell.

ii) Using the Dusty-Gas-Model. This model accounts for the effect of molecular collision of gas with walls or aerosols and the governing equations are derived from the kinetic gas theory. Assumed that the wall particles are uniformly distributed, and much larger and heavier than the gas molecules, the pressure drop in the porous cathode can be calculated as[2]:

$$\triangle p_e^2 = \frac{t_e}{D}\left(\frac{R_g T_B}{M}\right)\dot{m}_f \qquad , \tag{4.11}$$

in which t_e denotes the thickness of the cathode, F the Faraday constant, R_g the gas constant for sodium vapor, M the molecular weight of sodium ($M = 23\,g/mol$) and D the flow diffusion coefficient [m²/s]. D is given by a viscous (continuum) flow regime D^{vis} and the Knudsen flow regime D^K [162]:

$$D = D^{vis} + D^K\,\frac{1 + c_1^K\overline{p}}{1 + c_2^K\overline{p}} \qquad , \tag{4.12}$$

where $\overline{p}$ is the average vapor pressure in the pores of the cathode electrode and the coefficients of the Knudsen flow regime are described by [162]:

$$c_2^K = \frac{4r_p}{\mu}\cdot\left(\frac{M}{R_g T_B}\right) , \qquad c_1^K = 0.81 c_2^K \qquad , \tag{4.13}$$

---

[1]Pressure loss model from Williams et al. (1990) [166]
[2]Pressure loss model from Tournier and El-Genk (1999) [162]

where r_p represents the average hydraulic radius of the electrode pores.

In equation (4.12) the viscous D^{vis} and free-molecular D^K flow diffusion coefficients are given as [162]:

$$D^{vis} = a^K \overline{p} = \frac{r_p^2}{8\mu} \overline{p} \qquad \text{and} \tag{4.14}$$

$$D^K = \frac{20 + 8\,(t_e/r_p)}{20 + 19\,(t_e/r_p) + 3\,(t_e/r_p)^2} \cdot \frac{t_e}{4} \cdot \left(\frac{8R_g T}{\pi M}\right)^{1/2} \qquad , \tag{4.15}$$

in which r_p denotes the average hydraulic radius of the electrode pores.

At very low vapor pressure a free-molecular flow appears in the porous cathode, thus the Knudsen diffusion coefficient dominates the equation (4.12). However, at high pressure ($Kn < 0.02$) the Knudsen diffusivity can be neglected and a viscous flow takes place, becoming the viscous flow diffusion coefficient determining.

In some cases, the electrode does not have an apparent porosity and the sodium flow happens through molecular diffusion in the cathode. The pressure drop in the electrode is then expressed in terms of the geometrical factor G_p [-], as in [3]:

$$\triangle p_e^3 = \frac{3G_p}{8\pi} \left(\frac{2\pi R_g T_B}{M}\right)^{1/2} \cdot \frac{M}{F} j \qquad . \tag{4.16}$$

G_p coefficient accounts for pressure losses in the porous cathode and is determined experimentally.

Schindler [165] defined a model for vapor transport in electrode and also current collector $\triangle p_e$[4]. The total geometry factor G_p' of the cathode and current collector can be obtained through the equation[4]:

$$G_p' = K_e \frac{F}{\sqrt{2\pi M R_g T_B}} = \left(\frac{1}{\phi_e} + \frac{3}{8\pi} G_p + W_{cc}\right) \qquad , \tag{4.17}$$

where G_p is the geometry factor of the pores in the cathode and W_{cc} is the factor for vapor transport through the current collector.

4. *Vapor flow in the annulus space between BASE and condenser* $p_{cd} - p_{ic}$. The pressure loss from cathode to condenser depends on the properties of the AMTEC cell: geometry, vacuum level, current density or temperature at the condenser. Equations 4.10 and 4.16 assume a vapor flow in the molecular-flow regime; however Schock et al. [163] (1997) demonstrated that the vapor flow occurs in the transitional slip-flow regime. Tournier et al. [162] (1999) proposed the above mentioned model for all three regimes:

---

[3]Pressure loss model from Tournier and El-Genk (1997) [33]
[4]Pressure loss model from Schindler (1993) [165]

free-molecular, transition and continuum flow regimes (equation (4.11)).

5. Condensation of sodium $\triangle p_{cd}$. The pressure loss caused by condensation of sodium was obtained from the kinetic gas theory [162], and assuming an accommodation coefficient a_{cc} of unity and is reflected in equation (4.18). In this work, the condenser surface is much larger than the cathode surface, leading to very small mass flow rates at the condenser $\dot{m}_{cd}$ and thus to values of pressure drop tending to zero.

$$\triangle p_{cd} = a_{cc} \left(\frac{2\pi R_g T_{cd}}{M} \right)^{1/2} \dot{m}_{cd} \qquad . \qquad (4.18)$$

Summarizing, the pressure losses in the low pressure region of the cell (between the outer surface of the BASE and the condenser surface) depend mainly: on the temperature (T_B and T_{cd}), on the mass flow of sodium vapor which is dependent on the current density of the cell; and on several geometry factors: electrode and current collector morphology (thickness, porosity, pore size), as well as the space between the current collector and the condenser. Lower temperatures, larger electrode/current collector porosity, smaller electrode thickness and lower current density decrease the pressure drop in the cell. However, as shown in chapter 2 the mentioned parameters affect also the polarization losses through ohmic resistance (lower porosity, larger thickness favorable) and activation polarization (higher temperatures beneficial) and need to be considered for an optimum operation of the cell.

4.2 Electrochemical model

The electrochemical model calculates the current-voltage characteristics of an AMTEC cell, as a function of the BASE and condenser temperatures and sodium pressure difference across the BASE. Assuming a constant temperature distribution in the radial direction across the BASE (Seebeck voltage negligible), the effective electromotive force of the cell V_o^{cc} can be calculated as the open-circuit voltage V^{oc} minus the voltage loss originated through the charge-exchange polarization overpotentials at anode ξ_a and cathode ξ_c, and the ohmic losses ξ_r generated by the internal resistance of the cell:

$$V_o^{cc} = V^{oc} - (\xi_a - \xi_c) - \xi_r \qquad . \qquad\qquad (4.19)$$

For liquid-anode AMTEC cells the voltage loss through the anode ξ_a can be neglected if a good wetting of the BASE by the liquid sodium is ensured (at temperatures $> 400\,°C$ [96]). The Nernst equation (2.47) will be used to calculate the open-circuit voltage.

After an elaborated derivation of the Butler-Volmer equation and assuming that interfacial and bulk sodium and sodium-ion concentrations are equal, the current density at the cathode interface j can be calculated as follows [166]:

$$\frac{j}{j_0} = exp\left[-\alpha f_B \xi_c\right] - \frac{(K_f j + p_e^{oc})}{p_e^{oc}} exp\left[(1 - \alpha) f_B \xi_c\right] \qquad , \qquad (4.20)$$

in which $f_B = F/RT_B$ and j_0 represents the exchange current density at the actual equilibrium potential of the cell and can be interpreted as a measure of the effective local conductance at the TPB (BASE/electrode/sodium vapor) [169]. The current density at the interface j depends on the exchange current density at equilibrium j_0, the overpotential at the cathode ξ_c and sodium pressure at the interface at open circuit conditions p_e^{oc}.

Defining j_0^{sat} as the exchange current density of the cell at an equilibrium potential obtained with saturated sodium vapor in contact with the electrode and assuming that the electrochemical transfer coefficient is $\alpha = ½$, the exchange current is related to the saturated equilibrium current as follows [166]:

$$j_0 = j_0^{sat} \left[\frac{p_e^{oc}}{p_{sat}(T_B)}\right]^{1/2} \qquad . \qquad\qquad (4.21)$$

Rearranging equations (4.20) and (4.21) to clear the current density j on the right side [166]:

$$j = j_0^{sat} \frac{\left(p_a e^{-\alpha V^{CC} f_B} - p_e^{oc} e^{(1-\alpha)V^{CC} f_B} \right)}{p_a + K_f J_0^{sat} e^{(1-\alpha)V^{CC} f_B}} \qquad . \tag{4.22}$$

Underwood et al. [35] (1992) obtained experimentally a correlation for the saturated equilibrium exchange current density as a function of BASE temperature and type of electrodes:

$$j_0^{sat} = B_{ex} \frac{p_{sat}(T_B)}{\sqrt{T_B}} \qquad , \tag{4.23}$$

in which B_{ex} is characteristic for the type of electrodes and is determined experimentally. Combining equations (4.21) and (4.23), the exchange current density at the cathode can be calculated by:

$$j_0 = B_{ex} \left[\frac{p_e^{oc} p_{sat}(T_B)}{T_B} \right]^{1/2} \qquad . \tag{4.24}$$

Clearing the cell potential V^{cc} from equation (4.22) [166] at $\alpha = \frac{1}{2}$:

$$V^{cc} = \frac{2}{f_B} ln \left\{ \frac{p_a}{2\left(K_f\,j + p_e^{oc}\right)} \left[\frac{-j}{j_0^{sat}} + \left(\left(\frac{-j}{j_0^{sat}} \right)^2 + \frac{4\left(K_f\,j + p_e^{oc}\right)}{p_a} \right)^{1/2} \right] \right\} \qquad . \tag{4.25}$$

This equation, however, does not consider the overvoltage losses at the cathode through the internal resistance R_{cell} of the cell. The actual potential of the cell is therefore modified to:

$$V^{cc} = \frac{2}{f_B} ln \left\{ \frac{p_a}{2\left(K_f\,j + p_e^{oc}\right)} \left[\frac{-j}{j_0^{sat}} + \left(\left(\frac{-j}{j_0^{sat}} \right)^2 + \frac{4\left(K_f\,j + p_e^{oc}\right)}{p_a} \right)^{1/2} \right] \right\} - R_{cell}\,A_e j \qquad , \tag{4.26}$$

which reduces to the Nernst equation for $j = 0$. The right term of the equation (4.26) corresponds to the ohmic losses ξ_r and the left term encloses the rest of the equation (4.19): $V^{oc} + \xi_c$. The polarization overpotential at the cathode is caused by the accumulation of sodium ions at the BASE/cathode interface, and can be obtained combining equations (4.19) and (4.26):

$$\xi_c = \frac{2}{f_B} ln \left\{ \frac{p_a}{2\left(K_f\,j + p_e^{oc}\right)} \left[\frac{-j}{j_0^{sat}} + \left(\left(\frac{-j}{j_0^{sat}} \right)^2 + \frac{4\left(K_f\,j + p_e^{oc}\right)}{p_a} \right)^{1/2} \right] \right\} - \frac{1}{f_B} ln \frac{p_a}{p_e^{oc}} \qquad . \tag{4.27}$$

Assuming negligible charge-exchange polarization losses (which means that B_{ex} is

infinite), equation (4.26) reduces to the Nernst equation. In that case, the overvoltage is reduced to the effect of concentration losses:

$$\xi_c = \frac{2}{f_B} ln \left\{ \frac{p_a}{2\left(K_f\, j + p_e^{oc}\right)} \left[\left(\frac{4\left(K_f\, j + p_e^{oc}\right)}{p_a}\right)^{1/2} \right] \right\} - \frac{1}{f_B} ln \frac{p_a}{p_e^{oc}} \qquad . \qquad (4.28)$$

4.3   Validation of the model

Former measurement data from [165] has been used to validate the evaluation method. The authors tested a single-tube AMTEC cell with a liquid-anode and two sputtered cathodes. One of the cathodes was used to measure the current density of the cell while the other cathode was used to measure the open circuit voltage. The characteristics of the reference AMTEC cell are described in table 4.1.

Parameter	Value
A_e	42 cm^2
T_B	800 ℃
T_{cd}	280 - 380 ℃
Electrode	Mo
Current collector	Ni-foam + Ni-mesh

Table 4.1: Main characteristics of the AMTEC prototype and the testing temperature in [165].

To evaluate the measurement data a software was developed in Matlab, that included the equations presented in the pressure and electrochemical models. Figure (4.3) shows the characteristic curve of the AMTEC cell at $T_B = 800$ ℃ and $T_{cd} = 310$ ℃.
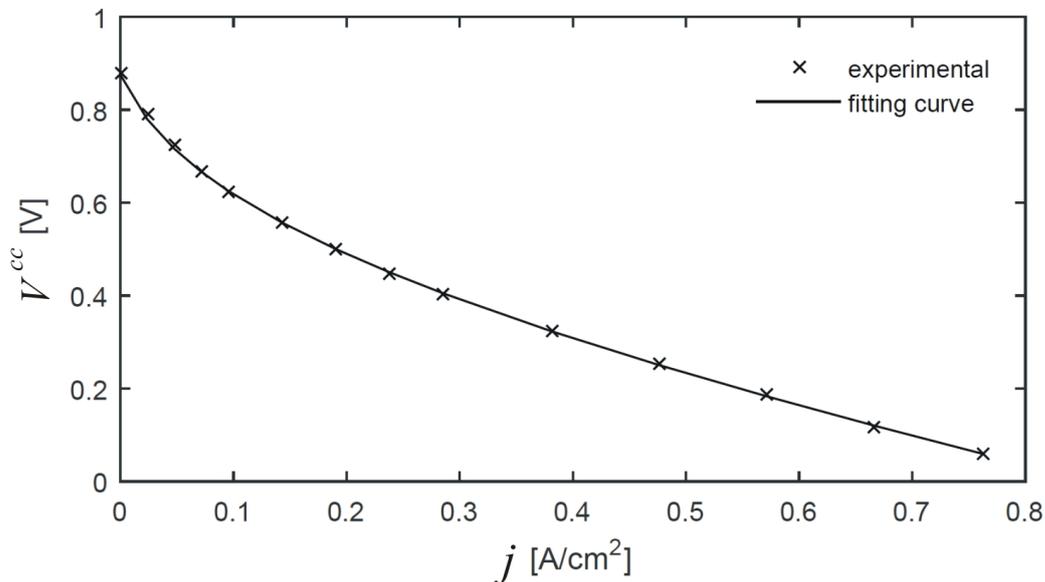
Figure 4.3: Comparison of computed and measured cell voltage V^{cc} as a function of the current density j of the in [165] tested AMTEC cell at $T_B = 800$ ℃ and $T_{cd} = 310$ ℃ (configured as in table 4.1).

The fitting curve has been obtained using equation (4.26). The obtained fitting parameters were the coefficient of pressure loss at the cathode and current collector $K_f =$

25.86 Pa cm^2/A, the exchange current density at saturated conditions $j_{sat}^{ex} = 6.35$ A/cm^2 and the resistance of the cell $R_{cell} = 9.45$ mΩ.

Based on the open circuit voltage measurements at the secondary cathode, the vapor pressure of sodium at the cathode side p_e^{cc} was obtained using the Nernst equation (2.63). Figure 4.4 shows that the tested AMTEC cell under the present conditions has a linear pressure increment K_f at the cathode side, which is directly proportional to the current of the cell. The fitting curve to the measurements was obtained using equations (4.7), (4.9) and (4.10). The obtained coefficient of pressure loss K_f at the cathode and current collector were 26.93, 25.86 and 23.15 Pa cm^2/A for $T_{cd} = 280$, 310 and 380 °C, respectively.
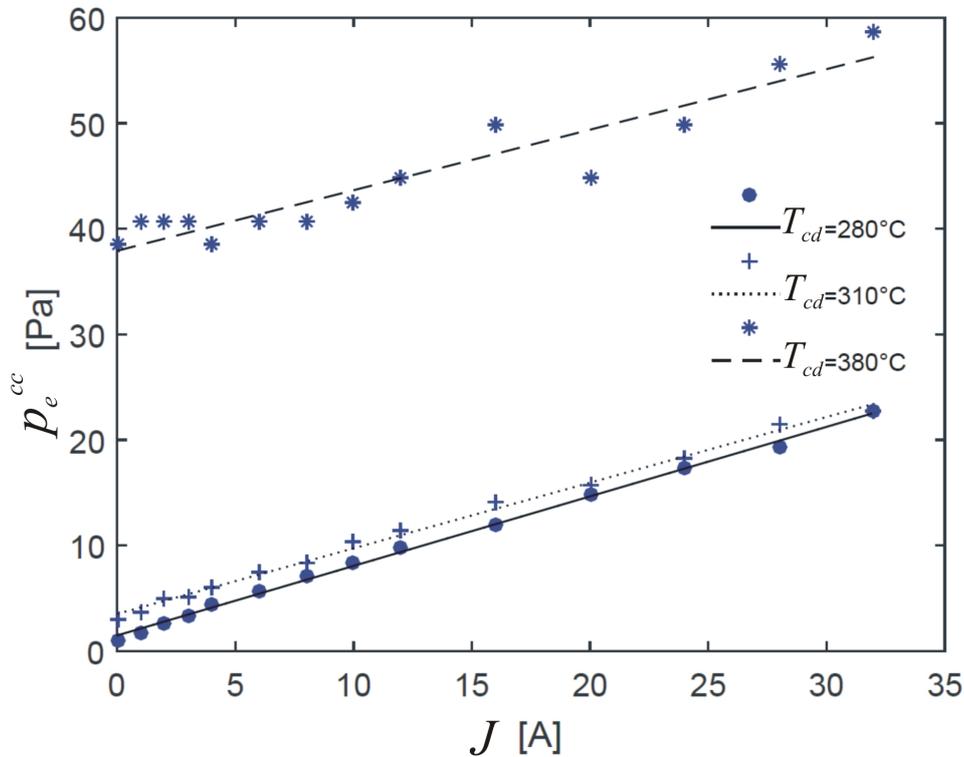
Figure 4.4: Comparison of computed and measured sodium vapor pressure at the cathode side p_e^{cc} as function of the cell current J at $T_B = 800$ °C and $T_{cd} = 280 - 380$ °C (configured as in table 4.1).

The polarization overpotential at the cathode ξ_c was obtained applying equation (4.27) and is represented in figure 4.5 for three different cathode temperatures. As expected, the polarization losses at the cathode increase with the current density, which indicates an increasing resistance of the cathode to vapor transport with rising current density. Moreover, the overpotential decreases with rising condenser temperature at the same current, this is due to the decreased activation losses favored by the higher temperature at the BASE-cathode.

The equations applied for the characterization of a single tube AMTEC cell have

shown to fit properly to the measurement data ($e < 5\%$). The assumption of a linear pressure increase has been confirmed for this particular experimental test, however this behavior may vary depending on the structure of the electrode-current collector and on the operation conditions. Therefore, a further validation of this model should follow this analysis focused on varying the parameters: temperature of the BASE, pressure, electrode and current collector.
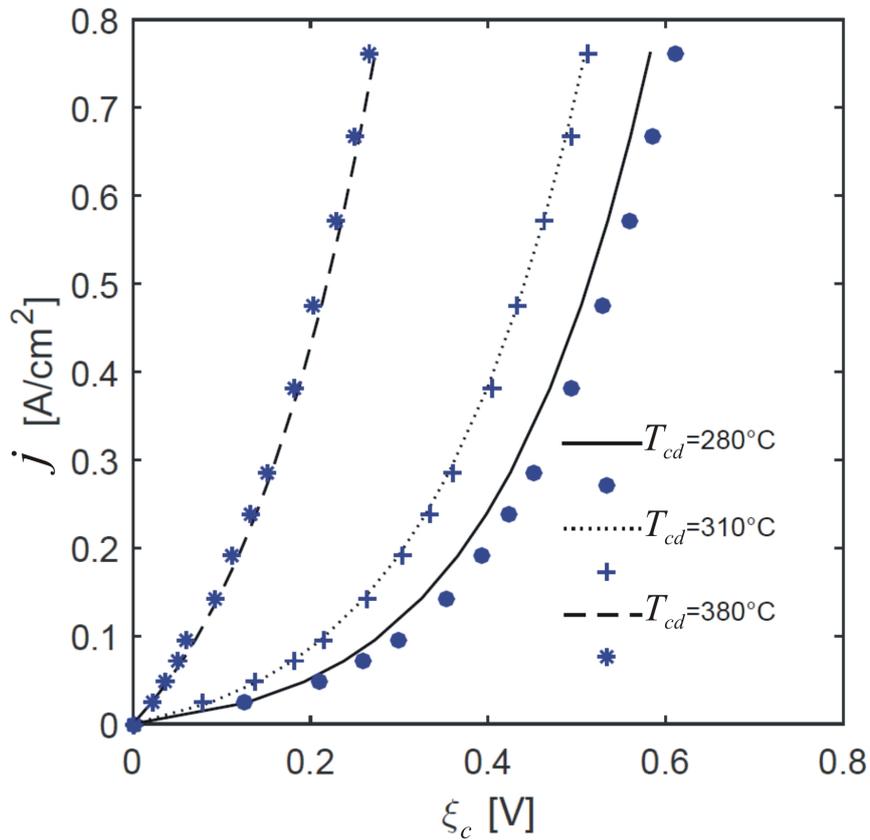
Figure 4.5: Comparison of computed and measured current density j as a function of the cathodic overpotential ξ_c of an AMTEC cell at $T_B = 800$ °C and $T_{cd} = 280 - 380$ °C (configured as in table 4.1).

5 Experimental setup

This chapter gives a description of the AMTEC TEst FAcility (ATEFA) and the test section. It provides the data of the AMTEC test cell and gives an overview of the main facility components. Finally, the data acquisition and control system of the facility are described.

5.1 AMTEC TEst FAcility (ATEFA)

ATEFA is a liquid sodium facility developed for the experimental investigations on AMTEC technology. It has been built for short term experiments, limited to a maximum sodium consumption of 3 liters. The facility is characterized by a compact structure, which is enclosed in a box of 1.8 m height and 0.8 m width (see figure 5.1). The key component of the facility is the AMTEC test cell that is located inside the box and coupled to the sodium system.

Double metallic walls isolate the sodium system and separate it thermally from the operators and the argon system. The latter monitors pressure and mass flow rate of the sodium system. All manual valves and displays of the sensors are located on a panel for an easy handling as illustrated in figure 5.1, left side. Cell and tanks can be disconnected from the facility during maintenance for examination or refill.

Figure 5.2 shows the piping and instrumentation diagram (P&ID) of the facility. The sodium open loop represented by the blue lines in figure 5.2 includes the AMTEC test cell, the condenser and the two sodium storage tanks. Fresh sodium is pumped, using pressurized argon, from a first tank (NA-ST-01) into the AMTEC cell; where it is heated up from 250 to 600 - 800 °C inside the ceramic. After the diffusion through the ceramic and electrode, sodium condenses on the condenser surface (air cooled loop) and is collected in a secondary tank (NA-ST-02). Purification of sodium takes place at the cold trap located in the KASOLA at INR-KIT.

Under operation, the facility can be divided in three pressure regimes, indicated by triangles in the P&ID diagram. Division 1 covers the high pressure side of the cell. Here, the maximum pressure permitted by the security valve AR-VS-04 is 0.17 MPa. Division 2 (AR-VI-05 closed) covers the low pressure side of the cell (1 - 500 Pa), including the secondary tank. Division 3 (AR-VI-04 closed) has a slightly higher pressure than division 1 to ensure the pump process of sodium from the tank to the cell.

As mentioned in chapter 2 a low pressure in the cathodic side of the cell is important to reduce the losses. A direct bypass (through valve AR-VI-09) between vacuum pump and AMTEC cell has been provided to allow a continuous monitoring of the vacuum pressure.
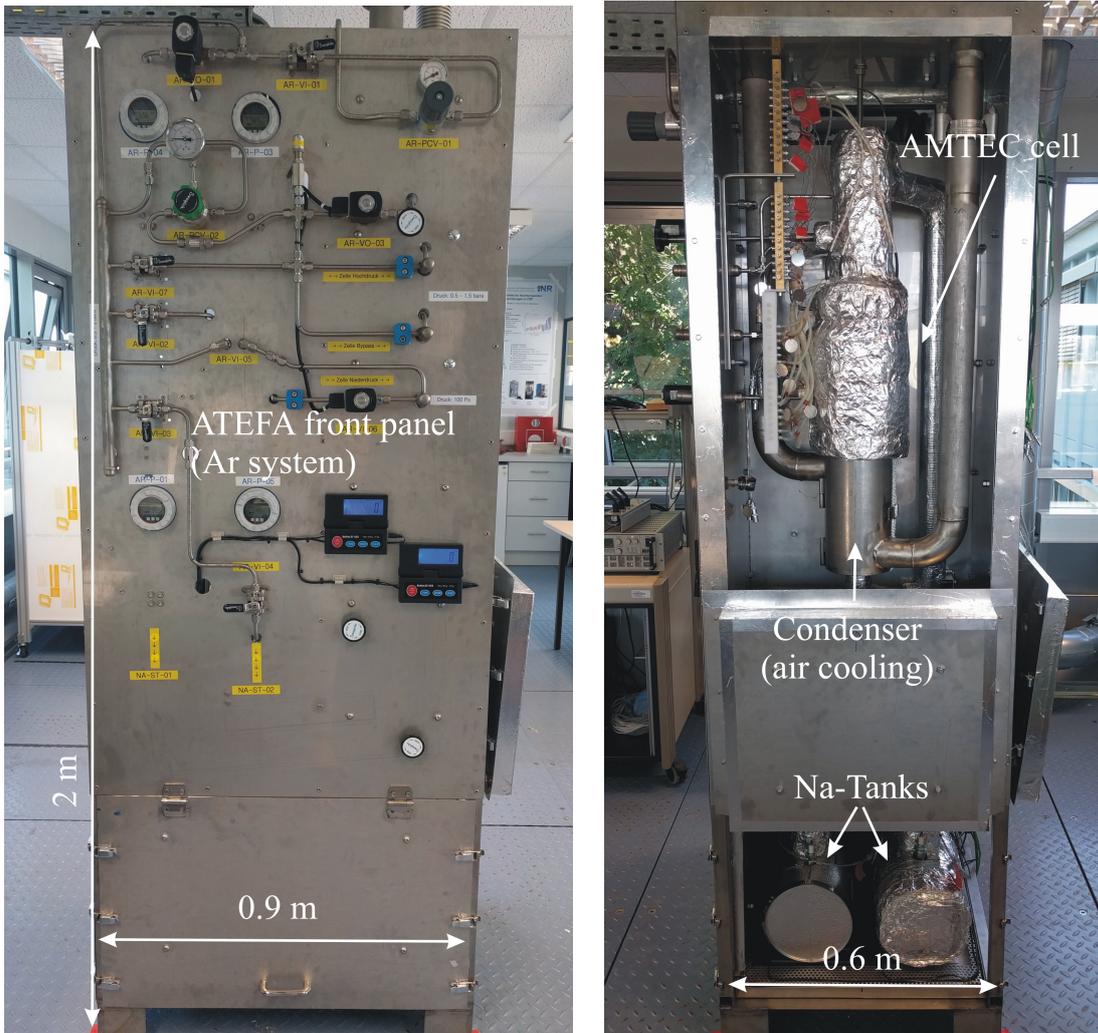
Figure 5.1: AMTEC TEst FAcility (ATEFA). Argon system is located outside the containment for thermal separation (left) and sodium system is enclosed through several metallic doors (right) for safety reasons.
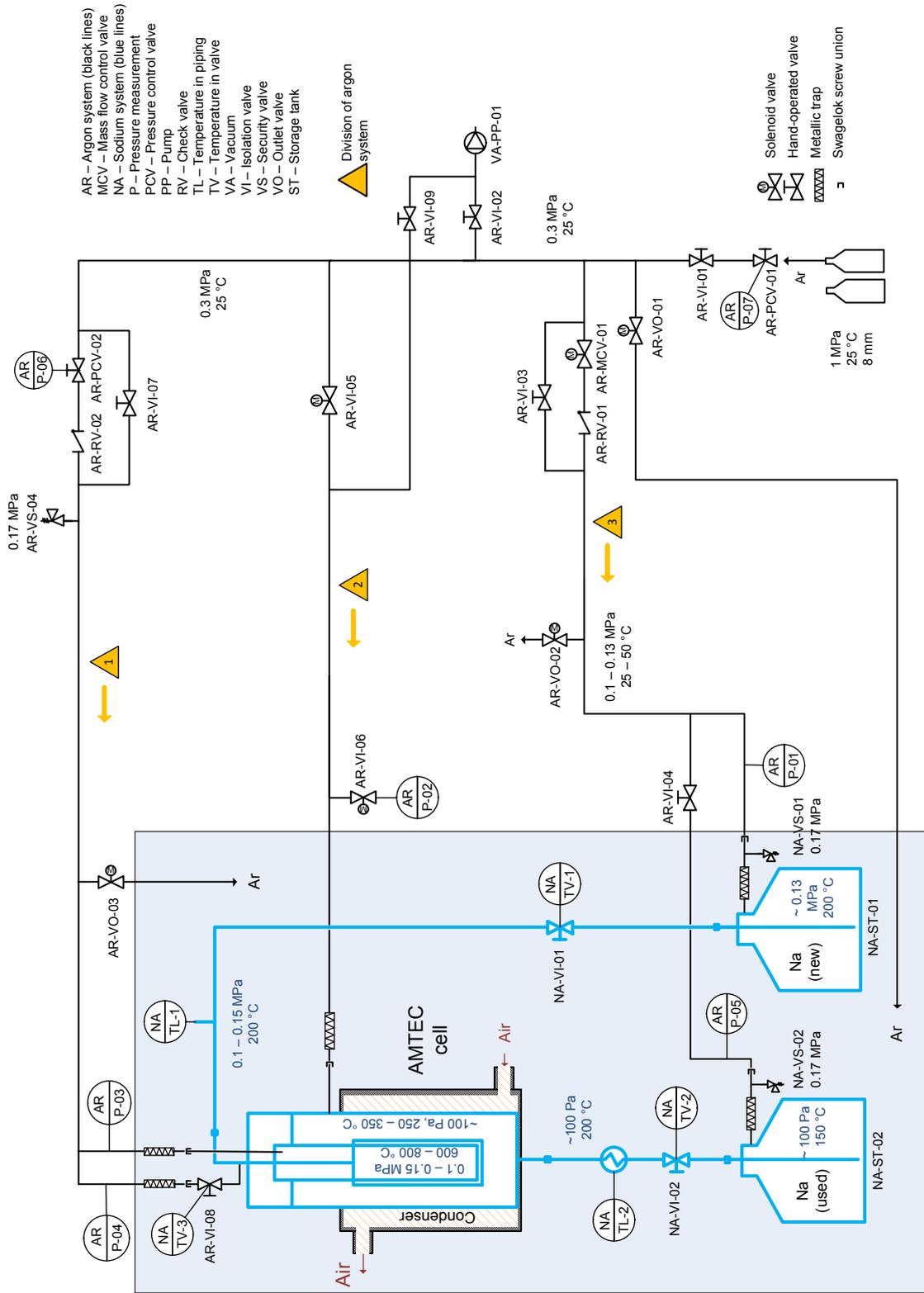
Figure 5.2: Piping and instrumentation diagram (PID) of ATEFA.

5.1.1 AMTEC test cell

The design of the AMTEC test cell is based on the previous work at KIT from Heinzel et al. [2]. An analysis of this design has lead to several optimizations: i) improvement of the electrical isolation of the cell structure, ii) enhanced instrumentation and iii) optimized cell design allowing for a draining of the BASE tube after a measurement campaign and preventing thus the break of the BASE tube while cooling down the cell. Moreover, specific component research has been performed to improve i) the ceramic to metal joint, ii) electrode sputtering of the BASE and iii) current collector structure.

Figure 5.3 (left) illustrates schematically the AMTEC test cell. The central part of the cell is the BASE, which has tube form ($D_{out} \sim 32\,\text{mm}$, $2\,\text{mm}$ thickness) and is closed at the lower end. The BASE tube divides the AMTEC cell in two regions: the inner side of the tube is filled with liquid sodium and pressurized with argon; and the outer side of the tube contains sodium vapor at a very low pressure (vacuum).
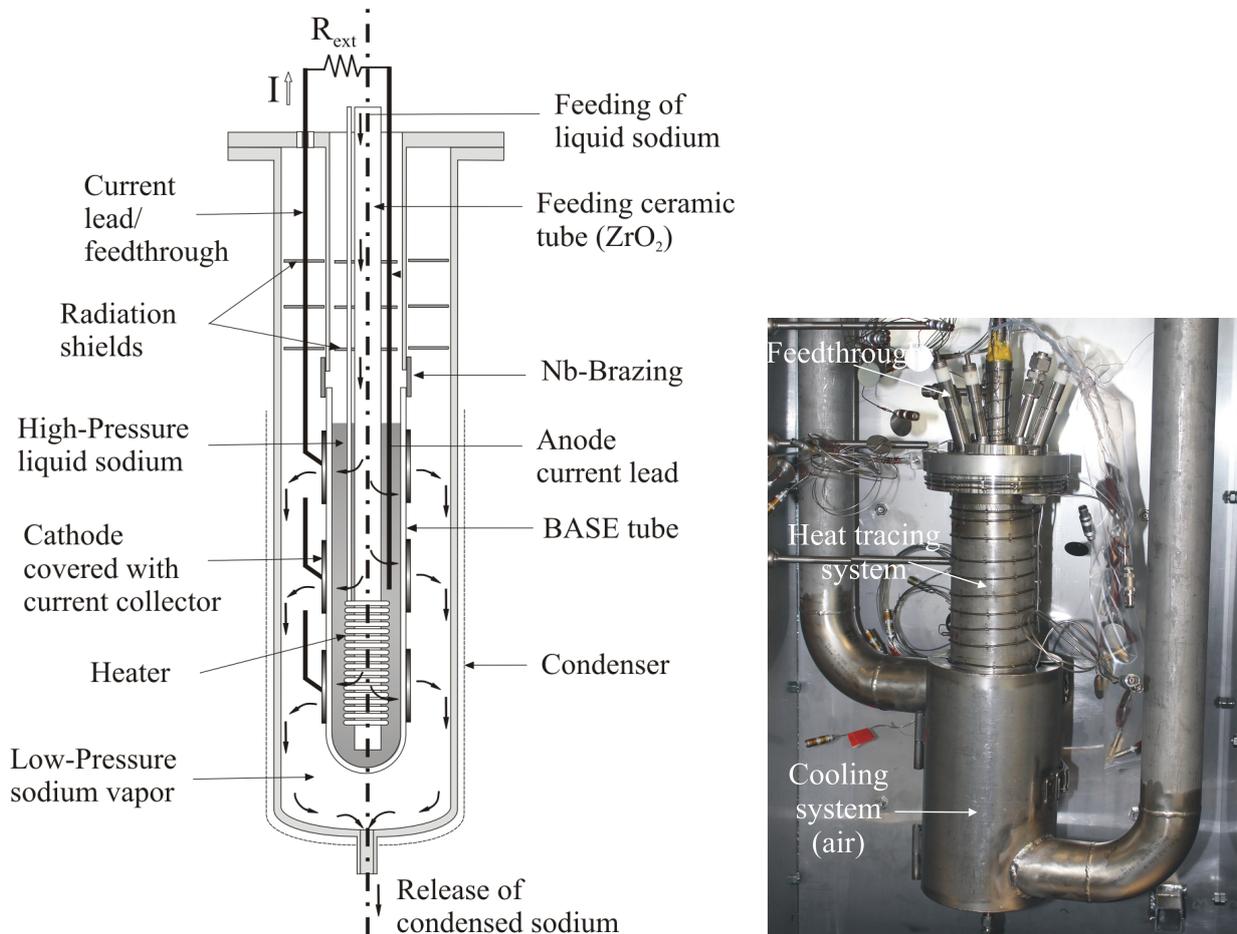
Figure 5.3: Schematic setup of the AMTEC test cell (left) and picture of the AMTEC test cell and the cooling system (right) integrated in ATEFA without thermal isolation .

Three porous cathodes of $\sim 45\,\text{cm}^2$ ($45\,\text{mm}$ high, $t_e \sim 5\,\mu\text{m}$) are placed on the outer surface of the BASE by reactive d.c. magnetron sputtering. The latter are covered

by three current collectors, which are connected to the current feedthroughs made of stainless steel. The outer cell steel-containment acts as condenser and is cooled by air at the outer surface as shown in figure 5.3 (right). The ceramic electrolyte is held by a niobium transition part coupled to the ascending metallic pipe located at the central flange. The cell ceramic is heated up through a heater (electrical resistance) wrapped in a spiral form and situated concentric in side the BASE (installation immersed in the liquid sodium). Special attention has been paid to the form of the wrapped heater, in order to avoid Lorentz forces appearing through the interaction of the magnetic field generated by the helical electric heater interacting with the current flow of the liquid anode. A current lead made of inconel is submerged in molten sodium and collects the electrons from the anode. A ceramic ZrO_2 feeding tube is introduced inside the BASE tube to allow a filling of the cell without splashing the inner upper walls of the test cell with sodium. This tube allows additionally the drain of the BASE tube preventing thus its break while cooling down the cell.

The cell assembly is divided in three main flanges (see figure 5.4) that allows a simple assembly and disassembly of all parts and defines a favorable handling of each component of the cell.

a) upper flange   b) central flange   c) lower flange
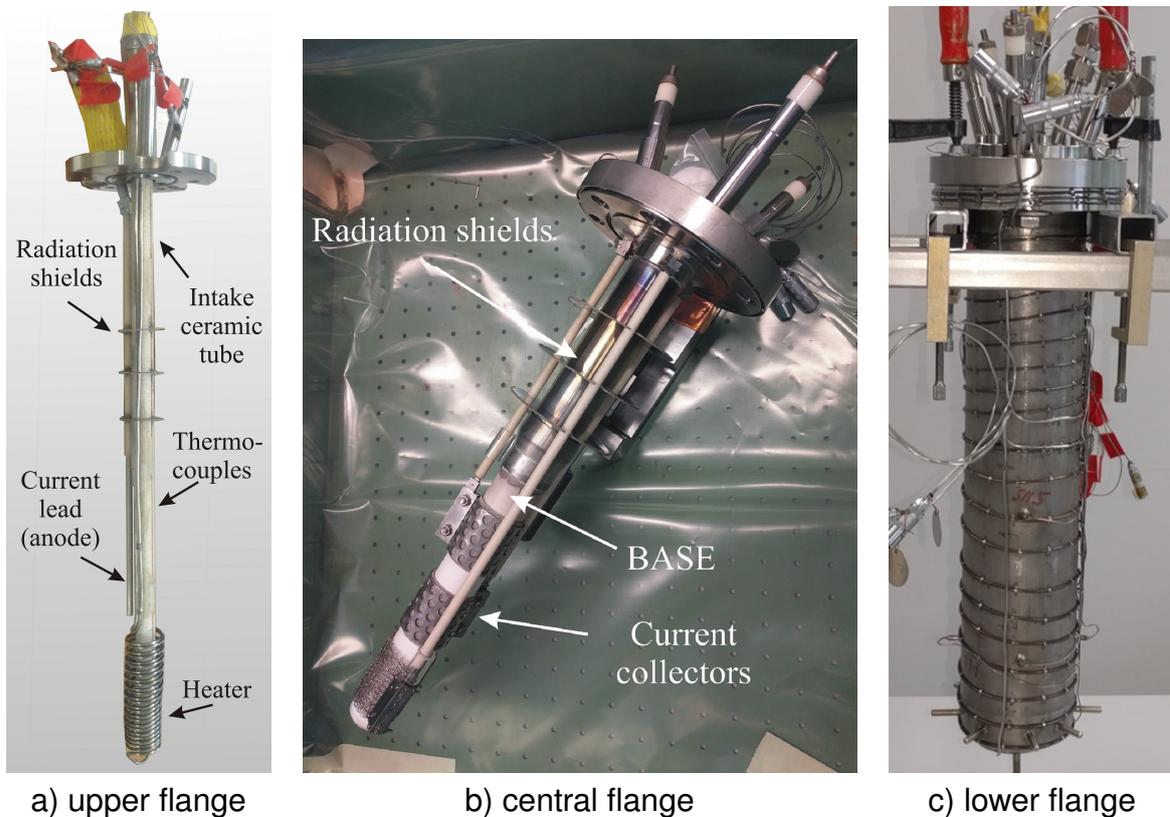
Figure 5.4: AMTEC test cell divided in three main flanges. The upper flange a) is assembled inside the central flange b), which is concurrently assembled inside the lower flange c).

a) the upper flange contains the ceramic ZrO_2 feeding tube, several radiation shields, the anode current lead/feedthrough, the main heater and several thermocouples, which are used to measure the temperature in the anode side of the cell and also to measure the level of liquid sodium in the BASE tube (detailed description of the level sensor is given in subchapter 5.2); b) the central flange is connected to the ensemble stainless steel tube-Nb transition tube-BASE tube, three cathodes, three current collectors, three current leads/feedthroughs and several radiation shields; and c) the lower flange includes the containment tube for the condenser and several thermocouples that are used to measure the temperature of condensed sodium.

A transition tube made of niobium was selected as a bridge structure for the ceramic to metal joint. This material was adopted because of the similar thermal expansion coefficient ($CTE_{Nb} = 7.47 \times 10^{-6}\,\mathrm{K}^{-1}$) with that of the ß"-alumina ($CTE_{BASE} = 7.9 \times 10^{-6}\,\mathrm{K}^{-1}$). Information about tested ceramic to metal brazing alloys in AMTEC can be found in chapter 3.2.2. A high-temperature ceramic to metal brazing alloy for AMTEC was developed at the Institute for Pulsed Power and Microwave Technology (IHM) at KIT by A. Weisenburger. The main achieved results are presented in chapter 6.1. The upper part of the niobium transition tube was brazed to the stainless steel tube of the central flange by using a nickel based brazing alloy Ni-650 from WLM.

The used BASE ceramic has been manufactured by Ionotec and has a lithium-stabilized structure. The standard composition is $Na_{1.7}Li_{0.3}Al_{10.7}O_{17}$. In the present prototype the BASE and the condenser are located coaxially. This configuration keeps losses due to vapor transport low. To reduce radiation losses radiation shields are placed axially on both sides of the cell and the inner wall of the condenser is polished. The AMTEC cell has been examined to short circuit before operation and the critical positions have been electrically isolated with a coating made of a ceramic adhesive. The observed critical positions are those where vapor sodium could solidify and act as an electrical bridge between different potentials; e.g. between radiation shields and inner wall of the condenser, current lead feedthroughs and upper/central flange.

Design verification. A thermal and stress evaluation of the assembly has been performed by J. L Palacios [170, 59] using the ANSYS V14.5 software. The main goals of the study have been: i) the verification of the cell design for the AMTEC operating conditions and ii) identification of pressure and temperature limits of the structure. Results indicate that no material failure occurs in the test cell, since all safety factors determined are sufficiently large above unity [59]. The weakest component in the cell is the upper brazing between the niobium transition part and the metallic tube, due to the stresses generated by the large difference in the thermal expansion of the materials ($CTE_{EN1.4571} > 2\,CTE_{Nb}$) [170].

The upper brazing between the niobium transition part and the metallic tube has been determined to be the weakest component in the cell, due to the stresses generated by the large difference in the thermal expansion of the materials ($CTE_{EN1.4571} > 2\,CTE_{Nb}$) [170].

Several simplifications of cell geometry have been considered in the numerical analysis: ceramic inlet pipe, electrodes and current collectors are eliminated from the model. A reduction of the computational time is achieved by applying symmetry conditions on the lateral sides of a 1/8th slice of the cell as illustrated in the left side of figure 5.2. Properties for both brazing alloys (stainless steel-Nb and Nb-ceramic) are assumed equal to nickel properties, considered as a conservative approach. The numerical model for the stationary state considers the thermal block for the determination of the temperature distribution and two structural blocks, one for the entire cell and a sub-model for a finer discretization of the steel-Nb-BASE region. The structural analysis in the stationary state has been performed for the nominal operating conditions planned, considering the relevant parameters at their extreme range. The sodium temperature on the inner side of the BASE is set to 1000 °C and the temperature of the condenser to 250 °C, while a pressure gradient of 0.2 MPa is considered across the BASE. As shown in figure 5.5 (left), the upper region of the cell is the coldest part with approximately 100 °C. To avoid such a low temperature a thermal insulation is provided in this area.
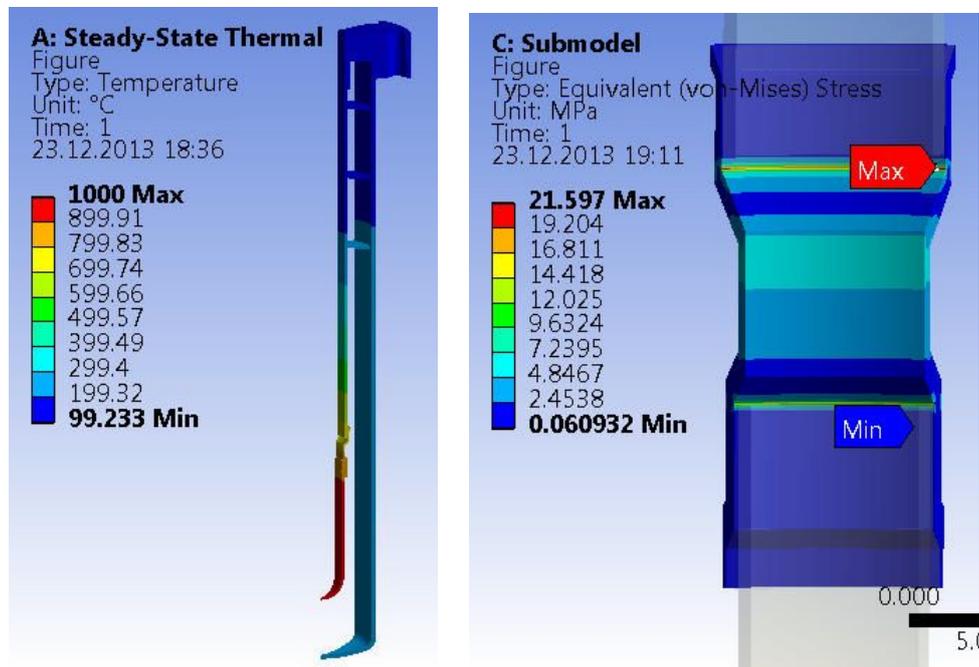
Figure 5.5: Calculated temperature distribution in 1/8 of cell (left) and von-Mises stress distribution in Nb-tube (right). Steady-state nominal operating conditions at the BASE are 1000 °C and 0.2 MPa [59].

To analyze the brazings at the stainless steel-Nb and Nb-BASE interfaces (see right

side of figure 5.5), the maximum shear stress theory has been considered. The maximum shear stress in the upper weld of the metal-Nb joint has yielded 9.1 MPa, corresponding to a safety factor of 4.3, while the maximum shear stress in the bottom weld (Nb-BASE interface) is computed to 4.8 MPa, corresponding to a safety factor of 8.2 [170]. The maximum von-Mises stress in the transition piece reached 21.6 MPa, which corresponds to a safety factor of 6.4, considering the von-Misses effective stress theory [170]. The maximum principal stress in the BASE is 1.83 MPa with a safety factor of 15, considering the Mohr-Coulomb theory for brittle materials [170]. Under these conditions, no material failure is expected in the test cell.

The development of the cathode coating of the BASE electrolyte has been elaborated at the (IAM-AWP) at KIT and is presented in chapter 6.2.1. A titanium carbide (TiC) cathode has been selected in this work due to the similar thermal expansion coefficient with that of the BASE and the good results reported in the literature [139]. Current collectors are used to compensate the high sheet resistance of the thin cathodes and spread the electrons homogeneously over the cathode surface. Two types of current collector have been considered for the tests; they consist of a nickel foam fastened to the cathode surface with i) stainless steel perforated plate (1 mm thickness, $\sim 37\,\%$ porosity) and ii) nickel knitted wire mesh from Drahtgestricke GmbH with a wire thickness of 0.2 mm and an estimated aperture of ~ 1.5 mm. A current bus made of stainless steel acts as an electrical bridge between the current collector and the current leads. An analysis of different current collector structures is presented in chapter 7.

Electrically isolated feedthroughs are provided to lead the current in and out of the cell. The thin cylindrical form of the BASE restricts the available space for the feedthroughs of the instrumentation. This can be observed at the upper flange in figure 5.4 c). Therefore miniature feedthroughs have been embedded for the 0.5 mm thermocouples and 2 mm heater at the upper flange. These are electrically isolated through ceramic capillary tubes to avoid or restrict the possibility of a short circuit in the cell. The sealing material for the miniature feedthroughs at the upper flange of the cell needs to be gas tight and electrically isolating at a temperature of ~ 250 °C. A gas tightness of the order 10^{-7} mbarl/s has been reached with a high temperature adhesive KYOWA type PI-32. Thermocouples are also placed at the condenser and were introduced through the outer cell containment. In this case however, a different approach has been followed for the sealing of the feedthroughs due to the very high temperatures at the condenser (up to 450 °C). First, thermocouples are laser welded to a metallic adapter, which later on has been tight welded to the feedthrough tube.

Different structural materials have been chosen according to the operating conditions to which they will be subjected. Stainless steel EN 1.4571 was selected due to its

suitability in corrosive mediums and high temperatures for the main cell structure and the radiation shields. For temperature regions up to 800 °C (like heater, thermocouples and current lead) a nickel based alloy, EN 2.4663, and ceramic materials are used.

5.1.2   Facility components.

Pressure and massflowrate of sodium are controlled in the argon system of ATEFA. A **gas-mass flow controller** (AR-MCV-01) has been installed for continuous feeding of sodium to the AMTEC cell. Due to the very small sodium mass flow rate, a special mass flow controller from Bürkert (type 8710) has been chosen, which works at $0 \dots 10 \, cm^3$/min regime with an inlet pressure of 0.3 MPa. Two **pressure controllers** are used in the argon system, one (AR-PCV-01) is located at the entrance of the argon supply-station ($> 10 \, bar$) to reduce the outlet pressure to 0.3 MPa for a proper operation of the mass flow controller AR-MCV-01; the second (AR-PCV-02) is directly connected with the anode side of the cell to adjust the pressure to 0.1 - 0.15 MPa.

The **valves** chosen for the sodium side (NA-VI-01, NA-VI-02) are manual bellows valves from Swagelok serie BW with welded bellows to the valve body. A fully metallic structure prevents corrosion up to temperatures of 480 °C. The isolation valves for the argon side are manual ball valves with PTFE sealing, from Swagelok series 60 and 40. Several solenoid valves from Bürkert (type 6027) have also been installed as outlet argon valves (AR-VO-01, -02, -03), which open in case of emergency (normally open configuration) and depressurize as result the facility as well as float the facility containment with argon simultaneously.

The **sodium piping system** has an inner diameter of 4 mm to minimize the amount of molten sodium in the facility and provide a low mass flow rate for a controlled filling of the cell. A ventilator from Helios (MV 125) with a maximum mass flow of $360 \, m^3$/h has been installed for the **cooling system** of the cell. Additional cooling is provided by the connecting pipe at the outlet of the cell, which has a length of ~ 1.4 m and is assembled with helical shape. Moreover, the helical shape helps to compensate the effect of the thermal expansion.

The **sodium tanks** have been designed (see figure 5.6) to serve as storage tank and sodium "pump" at the same time. The small size of the sodium inlet/outlet pipe (4 mm inner diameter) permits an easy drain of the tank ("pumping process") by pressurizing the tank with argon. The sodium pipe reaches the lowest part of the tank to allow a complete drain. The tank is provided with a security valve to avoid pressures higher than 0.17 MPa and a metallic feedthrough is placed as level sensor, indicating a full state (3 l). The argon inlet of the tanks has been designed as a hand grip for an easy transport of the tank. A metallic filter is located in the argon pipe for a safe separation of sodium and argon loops and an automatic-locking (or rapid coupling) mechanism is

used at the interface between Ar-system and Na-tank that closes them both tank and Ar-piping when separating them. This mechanism guarantees that no air enters in the sodium system and transport tanks.
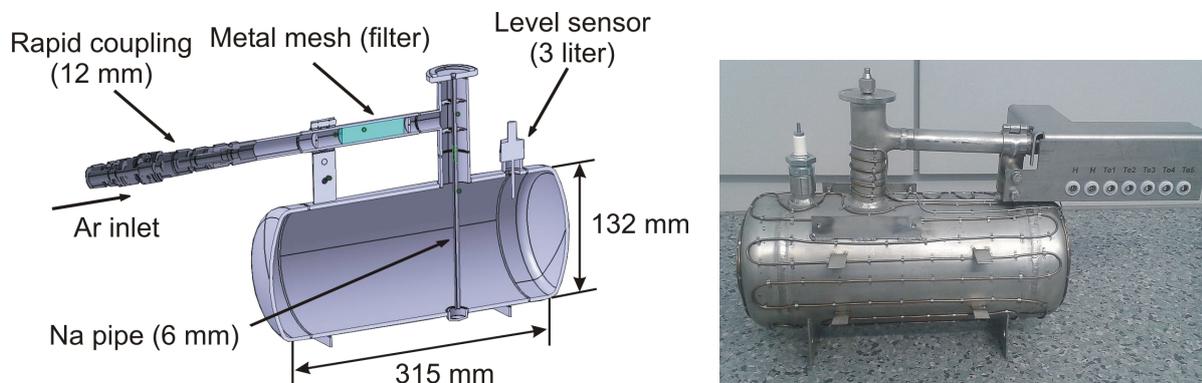
Figure 5.6: Cross section of the sodium transport tank (left), the level sensor signalizes a fill level of 3 l. Picture of the sodium tank with trace heating system (right).

Cleaning of the facility at the beginning of every test phase is essential to maintain a high purity of sodium during operation. Vacuum is generated in the facility during the cleaning process. The **vacuum pump** (VA-PP-01) used in ATEFA (HiCube$^{\mathrm{TM}}$ Eco from Pfeiffer-Vacuum) is able to generate vacuum up to $< 1 \times 10^{-7}$ mbar. Although divisions 1 and 3 from the facility (see figure 5.2) operate in overpressure, the cleaning process requires a gas-tight facility adapted for both under- and overpressure conditions. This has been specially taken into consideration for instrumentation, feedthroughs, valves and connectors. For instance relief or safety valves are usually not equipped to withstand high vacuum ranges, therefore isolation valves have been connected in series to the relief/safety valves that enhanced the gas tightness of the facility in case of operation in vacuum regime.

ATEFA was equipped with a **trace heating system** composed of: 15 heaters distributed all over the sodium system, 7 heaters located in the cell and 8 heaters in the sodium piping, valves and tanks. Each heating system is provided with miniature heaters of 1 - 2 mm diameter supplied by Thermocoax. They are made of stainless steel 1.4306 for a maximum operating temperature of 600 °C. The heater in the BASE tube however is made of inconel 600 for an increased operation temperature up to 1000 °C. The trace heating system prevents sodium from solidifying based on a previous exhaustive thermal analysis on the test facility and on the test cell (see subchapter 5.1.1): e.g. calculations have shown that the main heater of the cell can heat up the cell flanges only up to 100 °C, therefore additional trace heating system at the flanges is needed [170].

Further description of the ATEFA is given in Appendix B: ATEFA facility description, regarding the trace heating system, operation procedure and safety provisions. The

AMTEC **laboratory is** provided with **infrastructure** specific for handling with sodium. A glovebox has been installed in the laboratory that allows an easy and safe operation with liquid sodium at rather low temperatures < 300 °C while it permits direct optic observations. The glovebox has been used for several compatibility tests e.g. between molten sodium and high-temperature resistant polymer compounds [7] and for the filling of the sodium storage tanks. The sodium needs to be first cleaned and melted before it is filled in the tank. Therefore, a specific sodium melting device has been constructed for this purpose. Furthermore, a laboratory ventilation system has been constructed, which is activated in case of oxygen deficiency due to a large argon leakage or due to a sodium fire. A description of the laboratory infrastructure designed in the framework of this work is given in Appendix C: Laboratory infrastructure, as well as the **operation procedure.**

5.2 Data acquisition and control system

The performance of AMTEC is affected by temperature, pressure and material properties (e.g. ion conductivity of BASE). The thin cylindrical form of the BASE restricts the available space for the instrumentation. Therefore, miniature feedthroughs have been employed that allow a large amount of instrumentation in the cell. In the rest of the facility (along the sodium and argon systems), the amount of instrumentation aims to assist the trace heating system and the control of pressure and mass flow rate, as illustrated in figure 5.2. The measured quantities and the corresponding data acquisition system is summarized in table 5.1.

Measured variable	Range	Sensor type	Nr. of measuring points
Temp. T	0 - - 1000 °C	Thermocouple (type-K)	Cell: 28 Piping: 6 Tanks: 2x5
Absolute pressure p_{Ar}	0 - 4 bar	Capacitive transmitter	Cell : 2 Tanks: 2
	0 - 4 bar	Manometer	Piping: 1
	0 - 10 bar	Manometer	Piping: 1
Vacuum p_{Ar}	5×10^{-4} - - 100 mbar	Pirani transmitter p_{Ar}	Cell: 1
Saturated vapor $p_{Na}^{sat}(T_B)$	-	OCV (Nernst eq.)	Cell: 1 ... 3
Sodium level	0 - 1	Current feedthrough	Cell: 2
			Tanks: 2x1
Cell current	0 - 50 A	Shunt (electronic load)	Cell: 1
	0 - 10 A	digital multimeter	Cell: 1
Cell voltage	0 - 3 VDC	digital multimeter (Beckhoff, EL3681)	Cell: 3
		digital multimeter (electronic load)	Cell: 1
Argon massflowrate	0 - 10 Ncm^3/min	Massflow controller, anemometer principle	Piping: 1

Table 5.1: List of the measured physical quantities in ATEFA.

A safe handling of liquid sodium requires a continuous supervision of ATEFA by at least two operators during the high temperature tests. During the short term tests (< 1 day) in ATEFA the measurement data is recorded and the facility is controlled by a personal computer (PC) based software. The control system of the facility combines manual and automatic operation and the manual operation is always surveyed by the

control system software to limit possible mistakes of the operator. All manual valves and displays of the sensors are located on a panel for an easy handling. Key valves, e.g. to control the pressure in the facility (overpressure valves) or to protect the vacuum sensor from high pressures, are automatically monitored by the control software. Only during the commissioning process a partially manual operation is required. In steady state conditions the entire operation is controlled by the PC-based (automatic) software.

Instrumentation

Temperature.   28 thermocouples of type-K with isolated measuring point were assembled in the test cell (see figure 5.7). Thermocouples labeled with TCn are used to control the external heating system of the cell and thermocouples labeled with TCn-i or SNn measure the temperature of sodium inside the cell. TCn-i are connected to the upper flange of the cell and have a $D_{out} = 0.5$ mm; the small diameter allows a high number of temperature measuring points inside the ceramic. Due to the high temperatures in this region (up to 800 °C) the selected coating was Inconel 600. TCn and SNn thermocouples operate at temperatures < 450 °C and have, therefore, a stainless steel coating. Their diameter is $D_{out} = 1$ mm which makes them more resistant to fracture in comparison to the 0.5 mm thermocouples. TCn-i thermocouples measure the temperature of sodium in the anode domain. They were fixed on the surface of the ceramic inlet pipe in the axial direction using capillary ceramic tubes and high-temperature ceramic adhesive (Resbond 907 with mica basis) (see figure 5.8). SNn thermocouples measure the temperature of sodium at the inner wall of the condenser. The monitoring of the external heating system in the cell is performed using the TCn thermocouples placed at the outer surface of the cell structure and next to both o-rings. For a better evaluation of the temperature distribution in the cell, six different cross sectional planes were chosen to measure temperature difference in the radial direction, between anode and condenser. At the containment of the cell the sensors were located at the inner wall of the condenser, to measure directly the temperature of the condensed sodium. Two of them were placed 5 mm away from the inner wall of the condenser to record the temperature in vapor sodium. A strategic location of temperature measurement points was considered: critical positions in the cell and piping like indirectly heated areas or areas connected to a heat sink were selected to avoid solidification of sodium associated with a blockage of the sodium flow. Critical positions with a maximum temperature limitation (e.g. O-ring, feedthroughs) were also considered for temperature surveillance.

In the sodium system 5 thermocouples of tpye-K and $D_{out} = 1$ - 2 mm were used to control the trace heating system in the piping and valves (see figure 5.2). The TL-1 thermocouple was introduced inside the sodium piping by using a T-piece and a com-
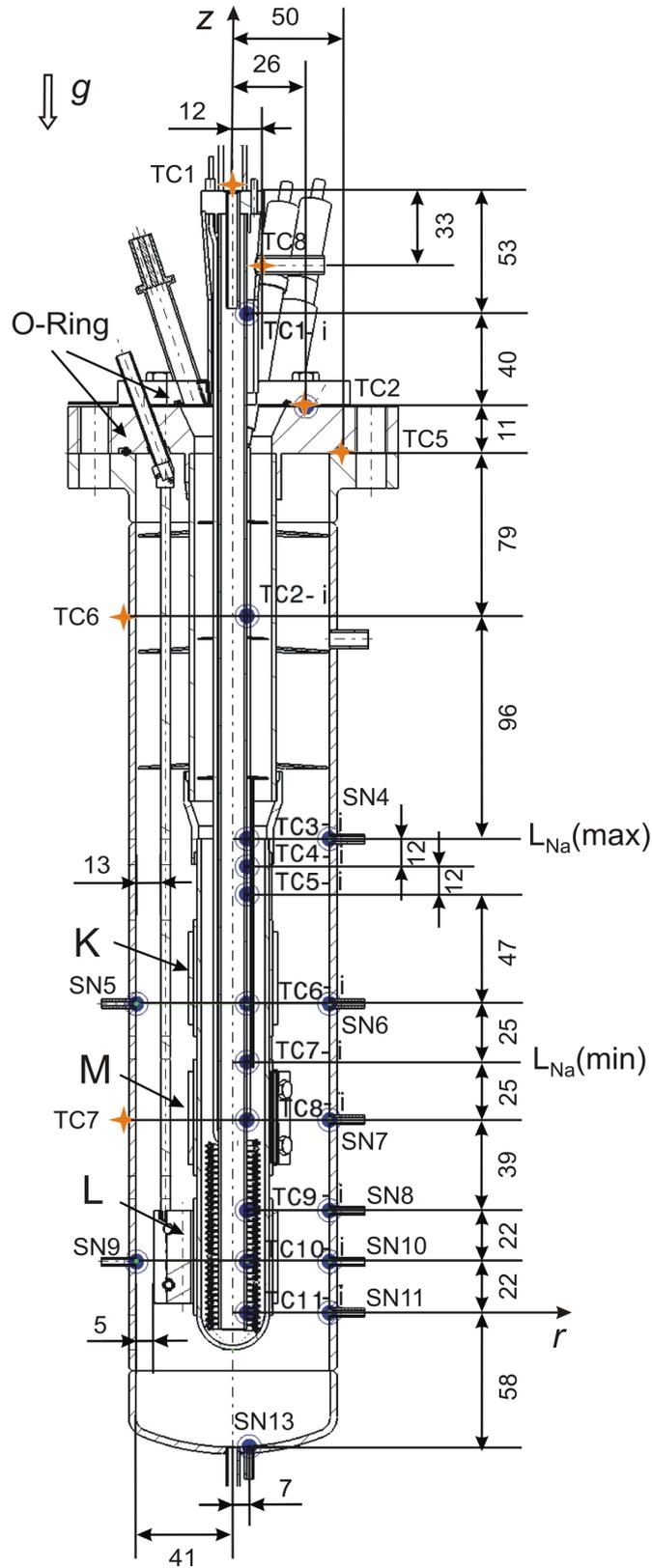
Figure 5.7: Instrumentation distribution in the AMTEC test cell at the perpendicular cross section with dimensions in mm. TCn, TCn-i and SNn represent thermocouples. K, M, L the cell cathodes and L_{Na}(max), L_{Na}(min) the Na-level measurements. Dimensions in [mm].

pletely metallic thermocouple-feedthrough from Swagelok. Each of the tanks has 5 thermocouples of type-K and $D_{out} = 1$ mm; the distribution is illustrated in figure 5.9.
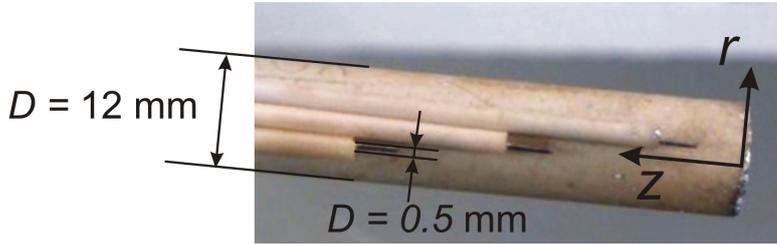
Figure 5.8: Assembly of 0.5 mm thermocouples on top of the ceramic intake pipe. Thermocouples are introduced inside capillary ceramic tubes in order to electrically isolate them for sodium level measurements.
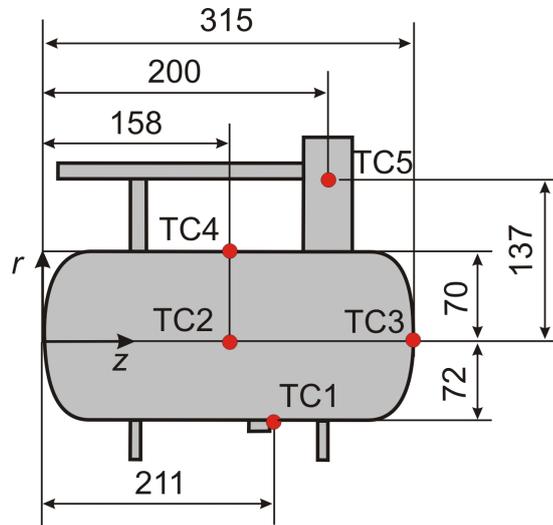
Figure 5.9: Distribution of thermocouples in sodium storage tank. Dimensions in [mm].

Pressure. Four absolute-pressure transmitters, a vacuum transmitter and two manometers were located in the experimental facility in the argon system (see figure 5.2). Two of them measure the absolute pressure in tanks (AR-P-01, -05) and the other two in the anode side of the cell (AR-P-03, -04), located at the main argon access and the bypass conduct respectively. To avoid damaging the pressure sensors by contact with sodium or aerosols, each transmitter was positioned after a metallic filter, which consisted of a metallic mesh rolled up covering the whole pipe cross section. This leads to a certain deviation of the measured pressure during transients. However, at steady state, they provide a real value. The sensors must be able to measure overpressure and vacuum, due to the AMTEC working regime and the handling with sodium. All four absolute-sensors are capacitive transmitters (Cerabar S sensor of type PMC71, from Endress and Hauser) with a ceramic membrane (Ceraphire: Al_2O_3), which allows a maximal operating temperature of 150 °C. They are suitable for vacuum.

A pirani transmitter from Pfeiffer-Vacuum (type TPR 280) measures the level of vacuum in the cathode side of the cell (AR-P-02). Relevant for the analysis of the cell performance is also the pressure at the interface between BASE and cathode. The lack of space and the high temperature at the BASE-cathode interface make the measurement of sodium vapor pressure with a pressure transmitter challenging. Assuming a homogeneous pressure distribution in all three electrodes the pressure of sodium vapor can be obtained by measuring the open voltage of one of the cathodes and using the Nernst equation (2.47) to obtain the sodium pressure.

Sodium level. In the cell, recording the level of sodium is essential to evidence that the required anode area (45 cm height per electrode) is completely covered with liquid sodium but also to indicate the rupture of the electrical isolation in case that the sodium level exceeds the maximum allowed height (total height of the BASE tube). The sodium level was measured recording the voltage drop V1 and V2 as illustrated in figure 5.10. Due to the reduced available space inside the ceramic no additional feedthroughs were used. Instead, the outer metallic coat of the thermocouples was employed to carry the electric current.
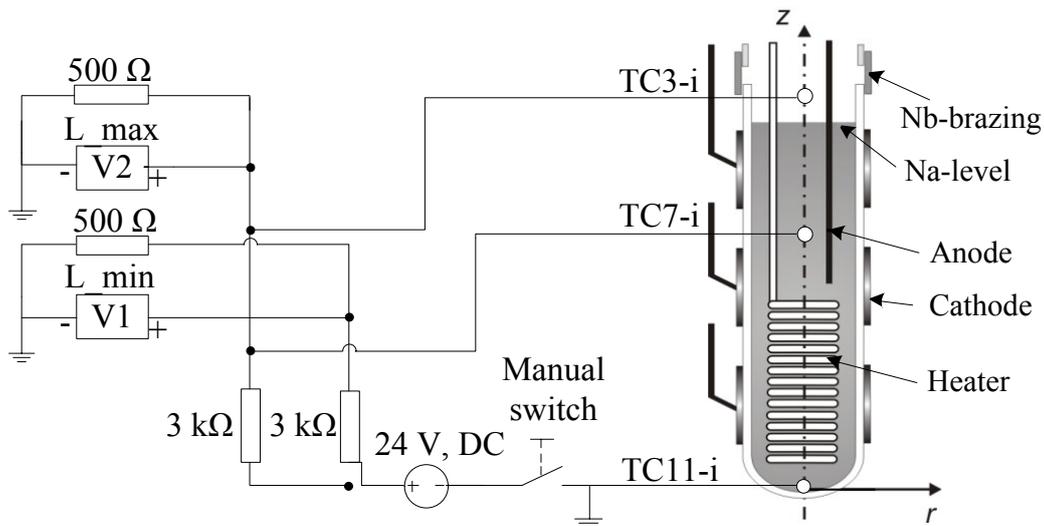
Figure 5.10: Sketch of the electrical circuit of the Na-level sensor in the AMTEC cell. V1 indicates the minimum level of sodium required and V2 the maximum level of sodium allowed in the BASE tube.

When liquid sodium contacts TC11-i and TC7-i, V1 goes to zero indicating that the minimum level of sodium required has been reached. If liquid sodium additionally contacts TC3-i, V2 goes to zero and the maximum allowed level of sodium in the BASE tube has been reached. Preliminary tests of this level sensor have been performed in the glovebox at 250 °C and show that the driven current through the thermocouple coat did not affect the temperature measurement and that the detection of the sodium level

was possible even with a moderate sodium oxide layer. The maximum current is set up to 8 mA, since at higher currents than 15 mA an electric lightning was observed that indicates the emergence of an electric bridge and a consequent disorted measurement signal.

Each of the tanks was supplied with a current feedthrough (see figure 5.6) positioned at the respective height of 3 liters of sodium. Measurements were performed by recording the presence of electric current flow between the current feedthrough and the metallic wall of the tank. The current feedthrough used is the ZE 18-12-1200 Al (Sonderzündkerze) from WS Weinmann & Schanz GmbH.

Argon massflowrate.   Sodium massflowrate in the cell can be controlled by a massflow-controller (AR-MCV-01) located in the argon system. This valve controls the massflow of pressurized argon that reaches the tank NA-ST-01. The tank is maintained at a constant temperature and the sodium is pumped into the cell. The massflow-controller has been installed to allow a continuous-operating of the cell for several days.

Cell current and voltage.   AMTEC is characterized by a high current and low voltage. The recording of the characteristic curve of the cell was done using an electronic load (ELP USBH-750 from Et-System Elektronik), which adapts the electrical resistance $0.04 \ldots 1.11\,\Omega$ for different currents. Besides, four digital multimeters EL3681 from Beckhoff were used to measure the voltage at the three electrodes (V_L, V_M, V_K) and currents up to 10 A. In total four electric switches from Kissling Elektrotechnik were used to control the electric circuit flow. They can break an electric circuit of up to 120 A; three of them are manually operated and the main switch is activated through a coil at normally open conditions. A representation of the electric circuit of the cell is in figure 5.11.

The external resistance of the electric circuit was measured from the current feedthrough of the anode at the cell passing through the electronic load, the electric switches and finishing at the current feedthrough of one of the three cathodes. The total external resistance is $R_L^{ext} = 231\,$mΩ, $R_M^{ext} = 216\,$mΩ and $R_K^{ext} = 218\,$mΩ for the electrodes L, M, K respectively. The main ohmic losses were at the contact transitions between parts.

Data acquisition and control system.   The LabVIEW system-design platform from National Instruments has been used for the development of the data acquisition and control system software of ATEFA. It is a personal computer (PC) based software that includes 41 programs-subroutines that are used for instance to control the temperature, pressure and massflowrate of the system as well as record continuously all process-relevant data in a database. The Front End of the software can be used to adjust the
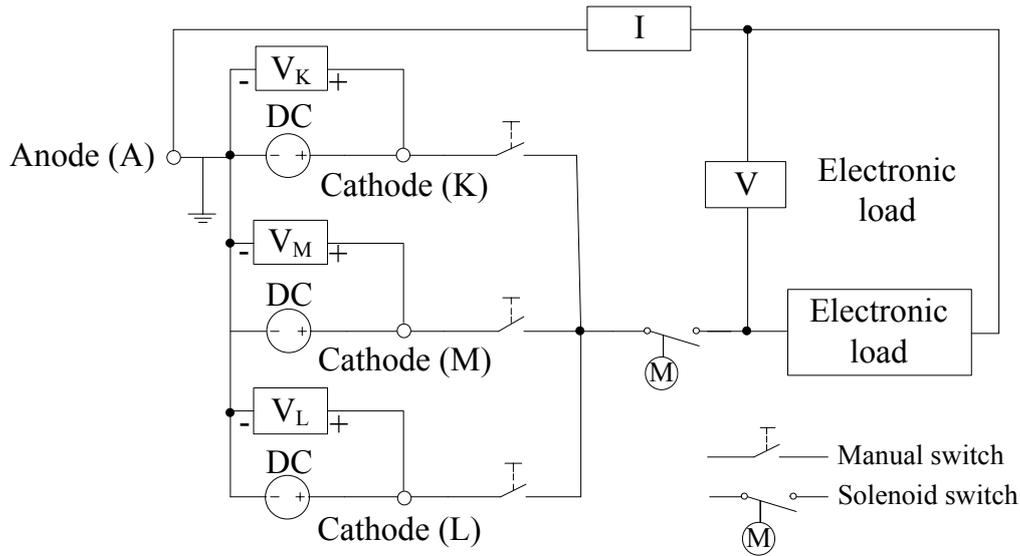
Figure 5.11: Electric circuit of the AMTEC test cell. The DC sources represent the AMTEC cell at the three anode-cathode combinations. The electronic load has integrated measurements of voltage and current. V_L, V_M, V_K are the measured voltages through the digital multimeters.

required physical parameters as well as to control several valves and the electric circuit of the cell. The software is able to simulate the flow direction and to consider the liquid or solid state of sodium.

The interface to the instruments, valves and system controllers (e.g. power regulator devices for the trace heating system, electrical switch) combines the I/O devices from Beckhoff and the TwinCAT 3 system manager. In TwinCAT the programmable logic controller (PLC) is conceived as a pure software that allows running user tasks in a virtual "PLC CPU", on a PC. The communication between LabVIEW and TwinCAT PLC was carried out through the Automation Device Specification (ADS) protocol. The ADS-system was developed in TwinCAT for data exchange between both different software modules. The resolution of the input Beckhoff devices for the data acquisition is listed in table 5.2. The module for thermocouples (EL3318) performs cold junction compensation through an internal temperature measurement at the terminals.

Module Type	Input signal	Resolution
EL3318	Thermocouple K [mV]	0.1 °C
EL3024	Pressure transducer 4 … 20 mA	12 Bit
EL3061	Vacuum pirani-gauge 0 … 10 V	12 Bit
EL3681	Multimeter	18 Bit
	Measurement range: 3 V, DC	1 μV
	Measurement range: 1 A, DC	1 μA

Table 5.2: Resolution the Beckhoff modules used for digitization of sensor signals.

To calculate the effective or propagated error of the measured quantities, the measurement accurancy, given by the sensor; and the conversion error, given by the digitalization (Beckhoff modules) and the calibration of the signal, need to be considered. A summary of the calculated propagated error is given in table 5.3.

In the case of the temperature, the Beckhoff module converts the thermocouple signal (mV) directly to grad Celsius (°C). Therefore, the propagated uncertainty, u_T, is the sum of both deviations, the measurement accuracy, u_{Tm}, and the conversion error during digitalization, u_{Tc}:

$$| u_T |= \sqrt{| u_{Tm} |^2 + | u_{Tc} |^2} \qquad . \tag{5.1}$$

The Beckhoff multimeter module (EL3681) measures voltage and current; and digitalizes simultaneously the signal converter. Therefore, the effective uncertainty is that given by the module. Pressure sensors send an analog signal as $4\ldots20$ mA (capacitive transmitter) and $2\ldots8.5$ V (pirani transmitter), which are further calibrated to Pascals (Pa) through the following equations given by the sensor data specification:

$$\text{Capacitive transmitter (4...20 mA):} \qquad p = 2 \cdot 10^5 \cdot \left(1 - \frac{20 - I}{16} \right) \qquad [\text{Pa}] \qquad , \tag{5.2}$$

in which I stands for the measured current in [mA] out of the sensor.

$$\text{Pirani transmitter (2...8.5V)}: \qquad p = K \cdot 10^{(V-3.5)} \qquad [\text{Pa}] \qquad , \tag{5.3}$$

where V denotes the measured voltage out of the sensor, and K is a konstant that varies depending on the pressure regime: $p < 1$ mbar $\Rightarrow K = 1.7$, $p \geq 1$ mbar $\Rightarrow K = 1$. Based on the previous equations, the calibration uncertainty for the pressure measurement u_{pc} is propagated and has been calculated as follows:

$$\text{Capacitive transmitter :} \qquad | u_{pc} |= \frac{\partial p}{\partial I} | u_I |= \left(\frac{2 \cdot 10^5}{16} \right) | u_I | \qquad , \tag{5.4}$$

$$\text{Pirani transmitter:.} \qquad | u_{pc} |= \frac{\partial p}{\partial V} | u_V |= \left(K\, 10^{(V-3.5)} ln10 \right) | u_V | \qquad , \tag{5.5}$$

where u_I and u_V represent the error in the analog/digital conversion given by the Beckhoff modules for the current and voltage signals respectively. Since u_I and u_V are given in different units as Pa, they are multiplied by the calibration coefficient $\frac{\partial p}{\partial x}$. The propagated error for the pressure is the sum of both, measurement accuracy and conversion erro:

Capacitive transmitter :
$$\mid u_p \mid = \sqrt{\mid u_{pm} \mid^2 + \left(\frac{\partial p}{\partial I} \mid u_I \mid\right)^2} = \sqrt{\mid u_{pm} \mid^2 + \mid u_{pc} \mid^2} \quad , \tag{5.6}$$

Pirani transmitter:.
$$\mid u_p \mid = \sqrt{\mid u_{pm} \mid^2 + \left(\frac{\partial p}{\partial V} \mid u_{Vi} \mid\right)^2} = \sqrt{\mid u_{pm} \mid^2 + \mid u_{pc} \mid^2} \quad . \tag{5.7}$$

Measured variable	Sensor type	Measured range	Measurement accuracy	Conversion error Analog/digital	Conversion error After calibration	Maximum propagated error
Temp.	Thermocouple (0.5 mm)	20 - 700 °C	BASE $|u_{Tm}|<2.8\,°C$	$|u_{Tc}|<2.1\,°C$	-	$|u_T|<3.5\,°C$
	Thermocouple (1 mm)	20 - 300 °C	Condenser $|u_{Tm}|<3\,°C$		-	$|u_T|<3.7\,°C$
Pressure anode-regime	Capacitive transmitter	0.03 - 2 bar	$|u_{pm}|<1.50\,mbar$	$|u_I|<0.06\,mA$	$|u_{pc}|<7.50\,mbar$	$|u_p|<7.65\,mbar$
		1 - 30 mbar	$|u_{pm}|<0.12\,mbar$			
		< 1 mbar	$|u_{pm}|<0.01\,mbar$			
Pressure cathode-regime	Pirani transmitter	$5\cdot10^{-4}$ - $1\cdot10^{-3}$ mbar	$|u_{pm}|<5\cdot10^{-4}\,mbar$	$|u_{Vi}|<0.03\,V$	$p<1\,mbar \Rightarrow K=1.7$	$p<1\,mbar$ $|u_p|<118.3\,mbar$
		$5\cdot10^{-4}$ - 100 mbar	$|u_{pm}|<15\,mbar$		$|u_{pc}|<117.4\,mbar$	
		100 - 1000 mbar	$|u_{pm}|<500\,mbar$		$p\geq1\,mbar \Rightarrow K=1$ $|u_{pc}|<69.1\,mbar$	$p\geq1\,mbar$ $|u_p|<504.7\,mbar$
Current	Digital multimeter	0 - 10 A	$|u_J|<2\,mA$	-*	-	$|u_J|<2\,mA$
Voltage	Digital multimeter	0 - 3 VDC	Beckhoff, EL3681: $|u_V|<0.3\,mV$ Electronic load: $|u_V|<4\,mV$	-*	-	$|u_V|<4\,mV$

Table 5.3: List of the measured physical quantities in ATEFA and the propagation of the measurement/conversion error. *The conversion error of the Beckhoff module for the digital multimeter (current and voltage measurements) is included in the measurement error.

6 Development and qualification of AMTEC components

This chapter deals with the experimental investigations regarding the main cell components: ceramic to metal joint, electrode sputtering of the ceramic electrolyte and the current collector structure.

6.1 Ceramic to metal joint

"Active brazing is a one-step process where a specifically designed brazing filler metal is placed between two main materials and then heated in vacuum [or in an inert atmosphere to avoid oxidation]. The filler metal contains a reactive metal that reacts with the ceramic and, therefore, guarantees a good wetting between the reaction layer of the ceramic and the base filler metal" [171]. Optimum brazing filler metals must have [172]: a low viscosity to ensure gap filling by capillary forces and provide thus a good distribution; low surface tension to provide a god wetting of the joint surfaces, elements such as P, Si or B reduce the surface tension significantly; and a low volatilisation of alloying elements of the brazing filler metals at brazing temperatures. Also an adequate surface preparation, a proper joint design and clearance and a concrete brazing time and temperature are fundamental for a good quality brazing [173].

The processes occurring during indirect brazing are still not completely understood and further analysis is required. The brazing presented in this work has been developed by A. Weisenburger at IHM [81]. The developed ceramic-metal joint has been directly tested under AMTEC conditions in the ATEFA facility up to 700 °C during the measuring campaign and showed a good performance, a detailed analysis of the brazing is presented in chapter 7. The BASE-Nb brazing effort is limited to the use of a commercial Ni base soldering paste (Ni 105 from WLM, Ni19Cr10Si) that is mixed with niobium (Nb) and titanium (Ti) or vanadium (V) powders. The Nb particles ($< 150\,\mu$m) are used as filler particles in the brazing process. For the required interaction between the brazing filler and the ceramic, Ti ($< 150\,\mu$m) and V ($< 150\,\mu$m) particles are foreseen as the active component. Preliminary tests revealed that the soldering paste containing V could not guarantee the targeted contact and strength of the BASE-Nb brazing. Finally, a composition of about 4 wt% Ti and 16 wt% Nb powder carefully mixed in the Ni-base soldering paste is used for all brazings. The mixed paste is applied directly to the areas to be joined as it is common in active ceramic wide gap brazing. Here, a rather large size of the gap of the order of 500 μm has been selected since the calculated shear stress at the joint is moderate. In order to melt the filler metal inductive heating process under inert gas (Argon) has been used. The crossed section of a brazed sample is illustrated in figure 6.1 and a detailed layout of the designed Niobium transition tube is displayed in 6.2. A gap of 2 mm has been provided between ceramic and niobium tube

on top of the brazing gap, where the soldering paste is situated (see Figure 6.2). The brazing has been performed by using induction heating, this permits treating only the targeted area covered with the heater and provides a non-invasive, fast, reliable and compact solution.
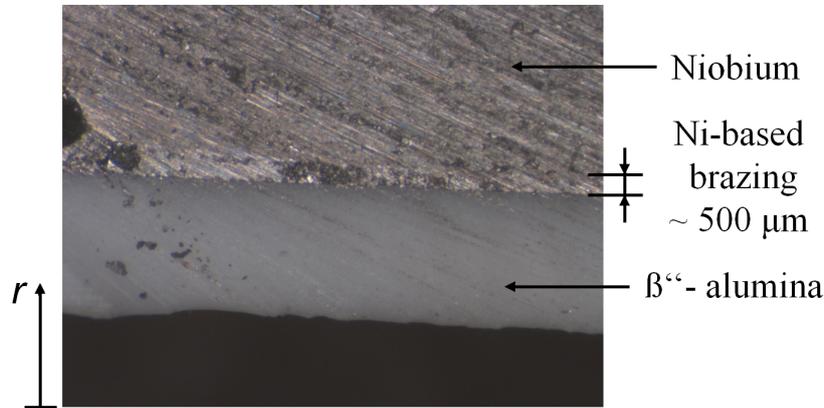
Figure 6.1: Cross sectional cut of a BASE - Niobium joint with a Ni-based brazing filler.

The design of the Nb-tube and the braze gap has been evaluated by J. L. Palacios using the ANSYS software [170]. Since the exact properties of the filler metal are not known, a conservative approach has been followed by using the properties of pure nickel. As mentioned in chapter 5 the calculated maximal shear stress able to face the Nb-BASE brazing is 4.8 MPa, cor responding to a safety factor of 8.2.

The 1st set of BASE tubes were not perfectly circular, they had an ovality of about 1 mm. This lead to cracking of the BASE tube after the joining process or to incomplete brazing contact. These problems have been overcame with enhanced BASE tubes that have a considerably improved circularity with tolerances $< 100\,\mu$m. The joining process has also been optimized by adapting the heating and cooling rates to the ceramic physical requirements. Using the above described brazing paste and dedicated brazing temperatures ($T_{max} = 1150\,°C$) and conditions (Ar plus 0.5 H$_2$ at 500 mbar) the BASE-Nb has been successfully joined. A He leak tightness of $< 10^{-5}$ mbarl/s has been achieved at the best ceramic-Nb joint. AMTEC cells are reported to work well with a tightness of $< 10^{-3}$ mbarl/s [86, 1], therefore, the requirements of tightness are fulfilled.

During the joining process, the ceramic has been covered with a metallic sheath to protect it from reacting with gases coming from the brazing. The ceramic area close to the brazing (~ 1 cm in the axial direction) changed the color to a dark gray-red after the brazing indicating that most probably a diffusion process had occurred (see figure 6.3). Titanium and Nickel from the brazing filler metal could have diffused in the BASE according to [174].
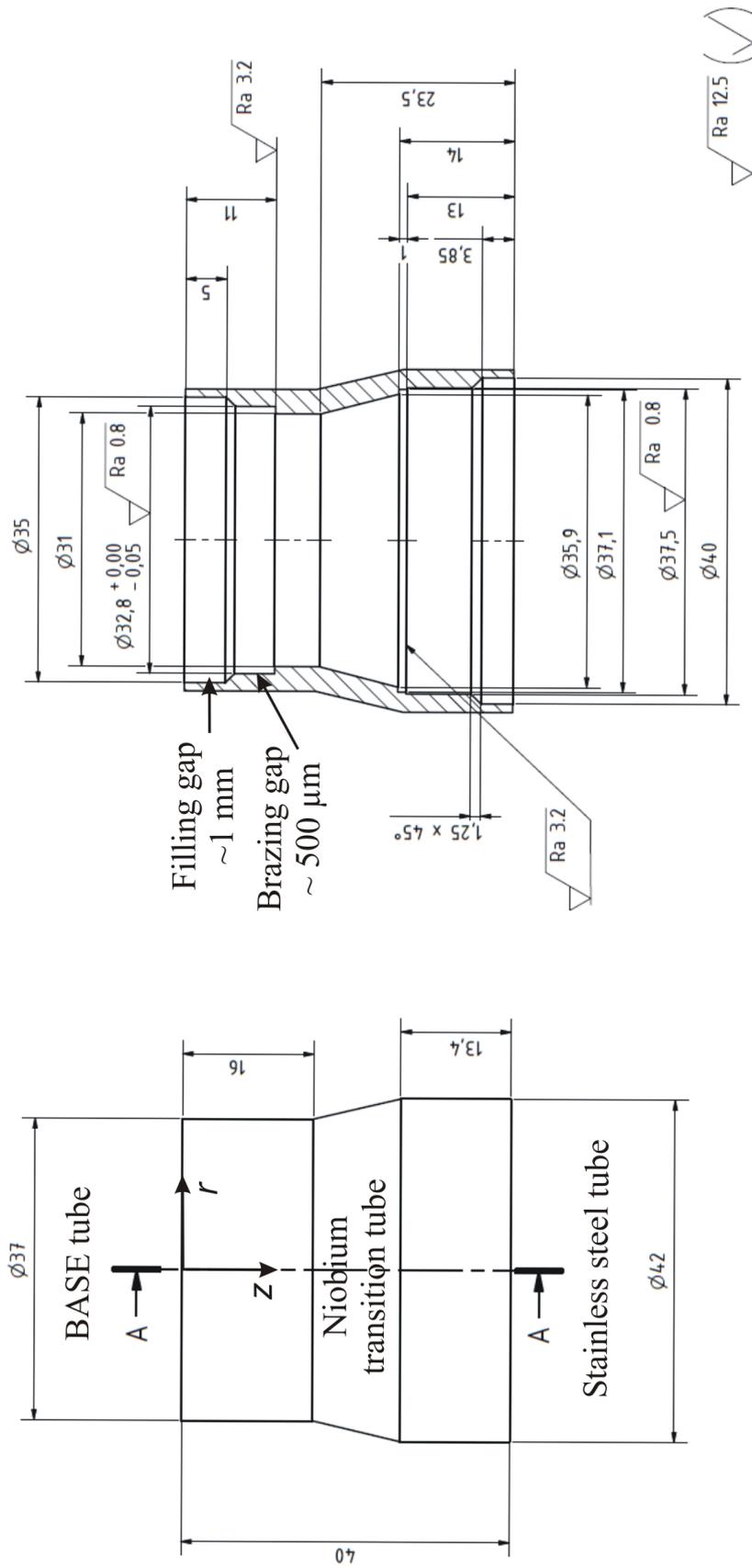
Figure 6.2: Dimensions of the Nb-transition tube showing the dimensions of brazing joint.

Figure 6.3: Change in the color of the BASE in the area close to the brazing.

6.2   Sputtered electrode

In this subchapter the experimental achievements regarding the electrode sputtering process are first presented and then the results of the experimental analysis of several BASE coated samples are described.

6.2.1   Electrode coating of the BASE

In chapter 2.3 a review on the coating technologies used in AMTEC was presented. Here the reactive magnetron sputtering technique has been selected due to the main advantages given by this technology: possibility to control composition and morphology of the electrode [106], a good adhesion of the film due to the high energy of the particles reaching the substrate [110].

Sputter deposition is a physical vapor deposition technique in which a material is vaporized in vacuum from the surface of a solid source (target) in the form of atoms, molecules or clusters by bombarding positively charged ions (e.g. Ar^+) to finally condense on the substrate surface [111]. The plasma (Ar^+) used in the sputtering system is generated through a diode; composed of an anode and a cathode inside a vacuum system and connected through a direct current (d.c.) power supply. Due to the low depositioning rates (0.5 - 5 μm/h [106]) the sputtering process is typically used to deposit thin films. Incorporating a magnetic field, the deposition rate and efficiency of the process can be increased [111], this is the so called magnetron-sputtering technique. The magnetic field directs the plasma concentrating it in the proximity of the target material [175].

Pictures of several successfully coated ceramics are presented in figure 6.4. The first sputtering tests were made at IHM, where BASE was coated with Molybdenum. The sputtered layer was stable under optic inspection. However, the thickness of the layer was not homogeneous, this effect was observed even at a macroscopic scale. In the second development phase, sputtering tests were performed at IAM-AWP with the coating facility HTC 625 from Hauzer. The advantages of this facility are in first place the larger size of the facility (the magnetron sputtering facility at IHM turned out to be too small for the BASE-Nb-Steel unit); the highest efficiency due to a confined plasma environment and the available rotating platform of the subtract, which allows a more homogeneous thickness of the coating. Figure 6.5 shows one of the coated BASE tubes after the deposition process in the magnetron sputtering facility. A reactive deposition process was used to deposit TiN and TiC compounds on the BASE substrate, in which the compound is formed either by the reaction of depositing material with the ambient gas environment such as nitrogen (e.g. TiN) or by the reaction through a co-deposition of different materials (e.g. TiC).

| a) Mo | b) TiN-a (left), TiN-b (right) | c) TiC | d) TiC-a |
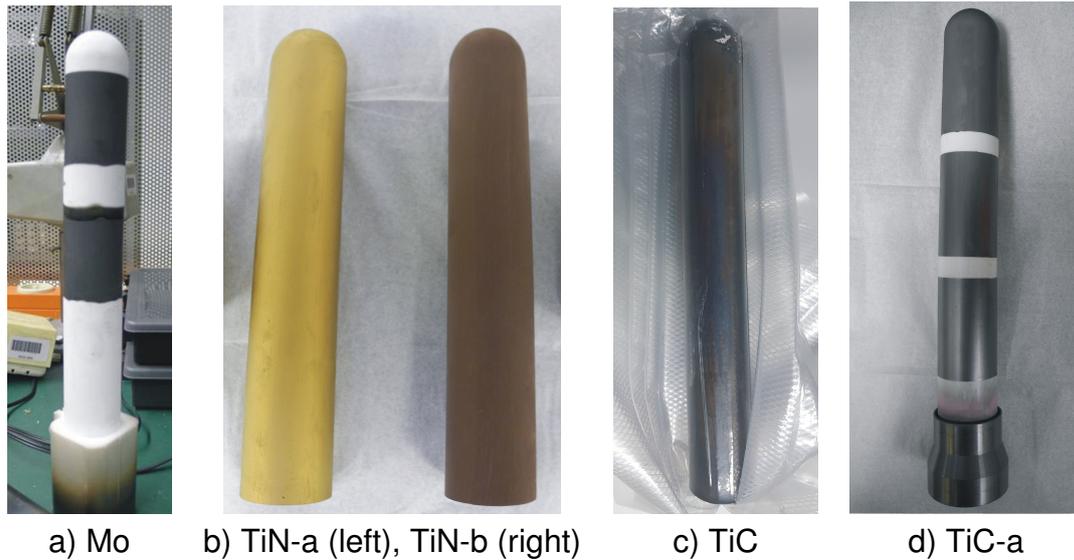
Figure 6.4: Main coating developments (IHM, IAM-AWP). Pictures made directly after the coating process.

Figure 6.5: Rotating platform of the magnetron sputtering facility at IAM-AWP with one BASE-Nb-Steel coated sample. A foil covers the areas not to be coated during the sputtering process (Nb transition tube, stainless steel tube and some parts of the ceramic).

The main challenge of the sputter deposition of AMTEC electrodes is given by the characteristics of the substrate, the BASE and its particular tubular geometry. Typically the magnetron sputtering process has been used to deposit metallic or aluminum oxide films on metallic substrates due to the excellent mechanical, abrasion and corrosion resistance properties or to serve as insulating or protection layer. However the magnetron

sputtering deposition of electron-conductive films on aluminum oxide substrates is not commercially widespread and documentation concerning such a process is rather limited. Moreover, the challenging properties of the ß"-alumina (high chemical reactivity) are added to the process of magnetron sputtering deposition of AMTEC electrodes.

During the sputtering process two main issues have been observed. Despite the carefully selected parameters, the continued d.c. magnetron sputtering damaged one of the samples as shown in figure 6.6. The ceramic dome was broken at one side and small molten holes were visible in this region. The latter suggest that a local microscopic to macroscopic overheating of the ceramic occurred at extreme high temperatures. During the sputtering process a large plasma concentration was observed in this damaged region and the coating process was interrupted for this reason. Therefore, the local overheating of the ceramic probably was caused by a large charge transfer through the ceramic.

Figure 6.6: Ceramic coated with continued d.c. magnetron sputtering. During the sputtering process a large plasma concentration appeared in the ceramic dome that damaged it.

The following tests have been performed with pulsed d.c. magnetron sputtering that showed not such damages at first instance (in a macroscopic scale); however, the adhesion of the TiC coating was insufficient. Two or three days after the coating process (in atmospheric environment) a considerable area of the coating detached as depicted in figure 6.7. Possible causes of the moderate adhesion are: i) the surface quality of the BASE, ii) pretreatment before the coating (cleaning, brazing, etc.) and/or iii) coating process. For a better understanding of the detachment process occurring at the coating, a microstructural and elemental analysis were performed and are presented next.
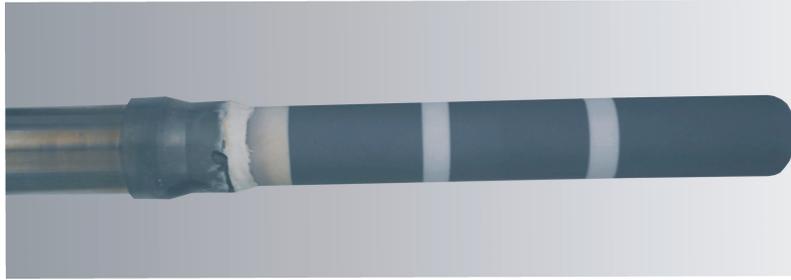
1st day after coating

2-3rd day after coating. Stored in air

Figure 6.7: Effect of coating detachment over time. BASE coated with TiC-b using the pulsed d.c. magnetron sputtering technique.

6.2.2 Experimental analysis of the TiC electrode layer

The microstructure and the elemental analysis of some of the TiC-coated BASE samples was analyzed by M. Bologa [176] using Scanning Electron Microscopy (SEM) and Energy-Dispersive X-ray Spectroscopy (EDX). The analysis presented in this subchapter is based on her previous work. The Mo-coated BASE was also analyzed through SEM. Finally, the quality of the layer concerning the sheet resistivity was analyzed using the 4 point probe technique.

Microstructural/elemental analysis. Several Mo and TiC sputtered electrodes were microscopically analyzed [176]. The selected TiC sample was a zirconium strengthened BASE (Ionotec) homogeneously coated using the pulsed d.c. magnetron sputtering technique. A picture of the samples has been presented in figure 6.4 a) and c). Before the sputtering process, the ceramic sample was heated up to 150 °C in a vacuum chamber and underwent during one hour a plasma etching process.

In the SEM the sample surface is scanned with a finely focused electron beam and different signals (secondary electrons, reflected or back-scattered electrons, etc.) are received and evaluated by suitable detectors (e.g. scintillator-photomultiplier system) to produce the microscopic image of the sample. Several samples have been gained from the ceramic tube and further sputtered with a nanometer layer of Au/Pd to increase the electric conductivity at the surface of the ceramic and thus, to obtain a higher accuracy in the SEM analysis. The main objectives of the microscopic analysis are to examine the microscopic structure of the BASE and the electrode sputtered layer and to investigate more in detail the detachment process visible already in macroscale (see figure 6.7).

As it can be seen in in figure 6.8 picture a), the BASE has a secondary phase located at its surface. The generation of this phase is connected to the exposure of the ceramic in air/humid environment. Moreover, the polishing of the ceramic is relatively coarse and even after the coating process perceptible (see figure 6.8 picture b)).

The morphology of the Mo sputtered layer is summarized in figure 6.9. A relatively homogeneous grain distribution is observed in picture a) of figure 6.9. The measured average grain size is $\sim 6\,\mu$m. The thickness of the Mo sputter layer is $\sim 6\,\mu$m as displayed in picture b). Between the grains porous channels are visible in picture c) that propagate until the ceramic surface (see picture b)). Moreover the grains have a columnar morphology as observed in pictures d) and b). Typical Mo electrodes used in AMTEC have a significantly smaller grain size and thickness of $\sim 1\,\mu$m. Therefore, efforts need to be done to reduce both parameters. The columnar grain growth and the observed porosity pattern are favorable for an enhanced operation of AMTEC due to a simplified vapor transport that reduces the pressure losses and an increased TPL that increases the sodium recombination density.
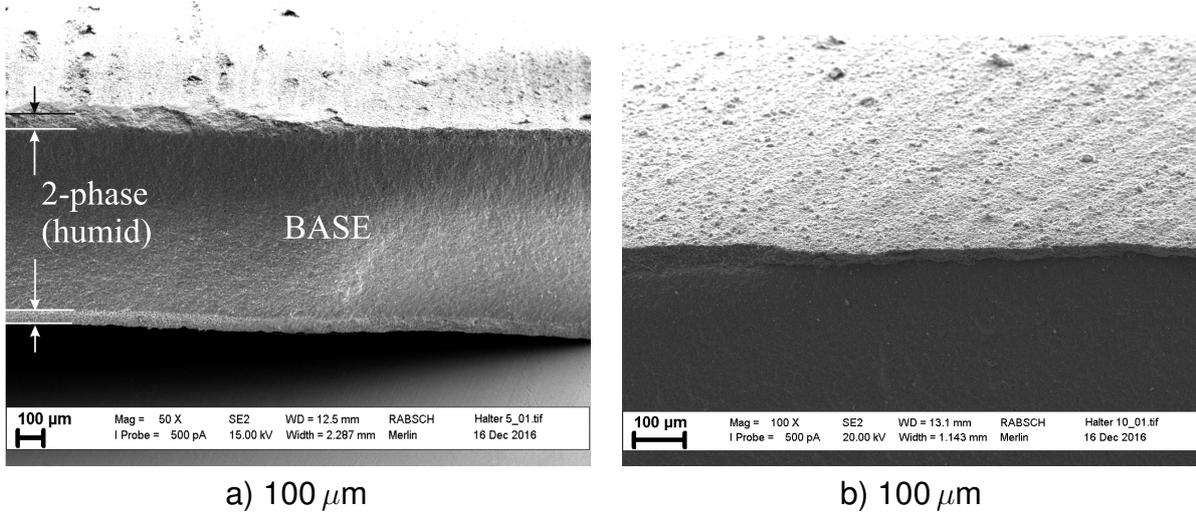
a) 100 μm

b) 100 μm

Figure 6.8: SEM pictures of the TiC-coated BASE (100 μm). a) A secondary phase appears on the surface of the ceramic. b) The polishing of the ceramic is still visible after the coating [176].

a) 30 μm. Mo coating

b) 10 μm. Porous Mo layer

c) 5 μm. Mo grains

d) 6 μm. Columnar Mo grains
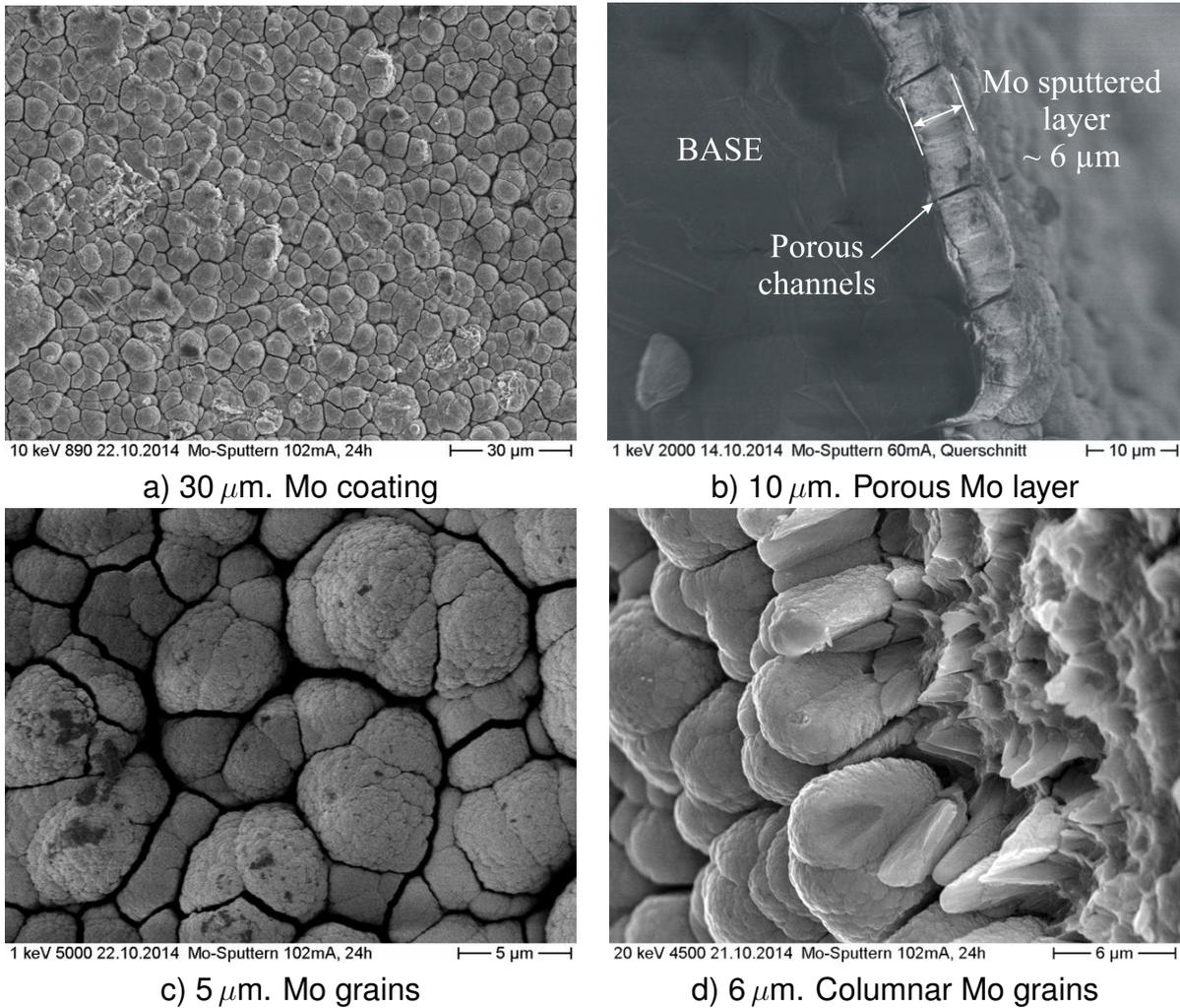
Figure 6.9: SEM pictures of the Mo electrode at different magnifications. a) and c) are top-views of the coating and b) and d) are side face-views.

The SEM analysis revealed that with increasing the sputtering electric current (from 60 to 102 mA) the sputtering rate increases, the grain size decreases and the porosity increases too (columnar configuration of the grains).

The detachment process of the TiC coating is illustrated in figure 6.10; it seems to start in the ceramic surface as a crater (illustrated in b) and c)) and propagates in circles in the direction of polishing (reflected in a) and d) at different sample areas). The observed craters could have been generated by an accumulation of gas in the ceramic surface. The morphology of the TiC sputtered layer is summarized in figure 6.11. Pictures a) and b) illustrate two different regions of the coated layer: a) shows a homogeneously deposited TiC layer that contains certain grain agglomerations and that has not been damaged or contains any detached areas, in contrast b) represents a zone affected by the detachment process, where the remains of a coating island are surrounded by the ceramic surface that appears after the detachment process.

a) 100 μm

b) 20 μm

c) 10 μm

d) 100 μm
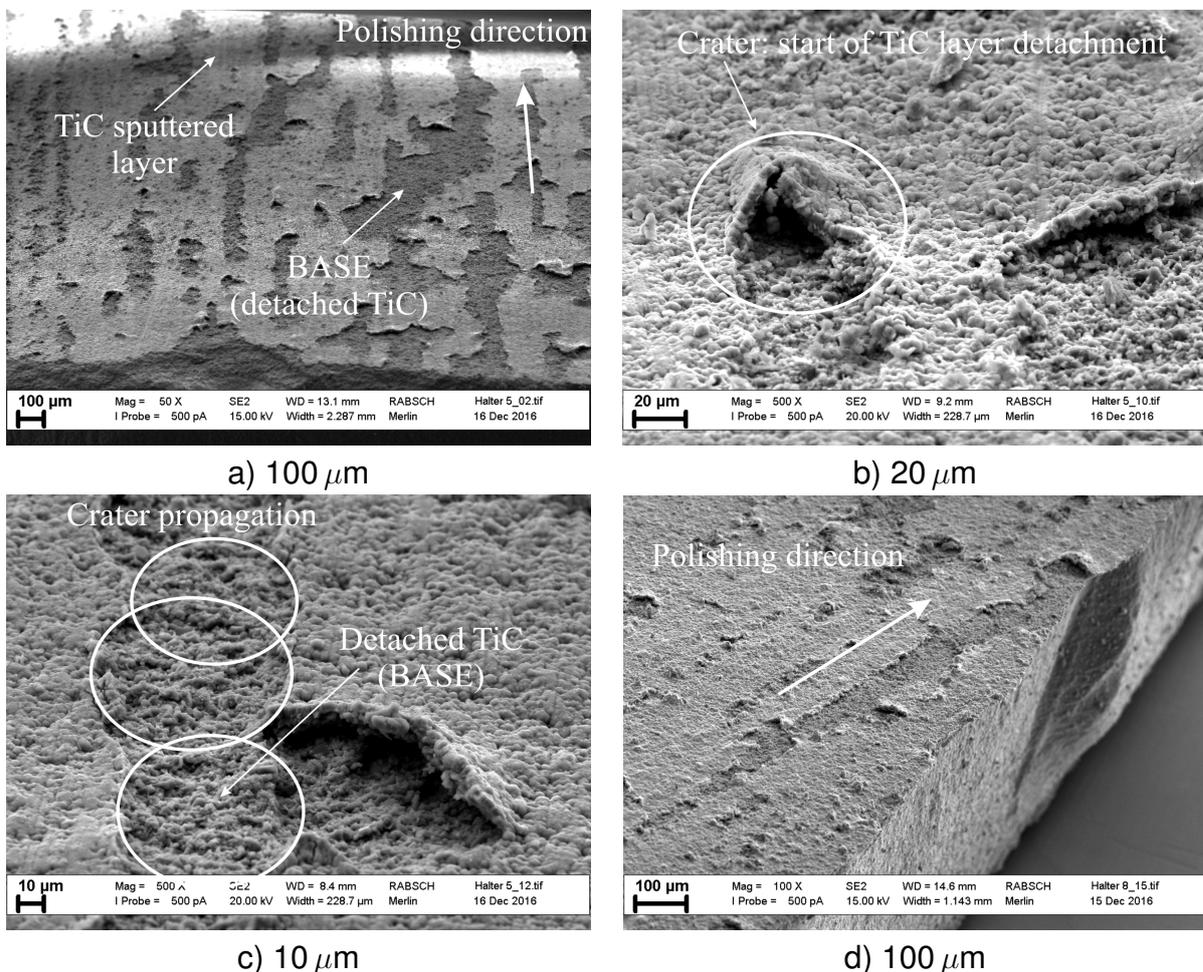
Figure 6.10: SEM pictures of the detachment process of the TiC sputtered electrode layer for different magnifications. The detachment of the electrode layer is originated by some kind of craters that appear in the ceramic surface and propagate in circles in the polishing direction [176].
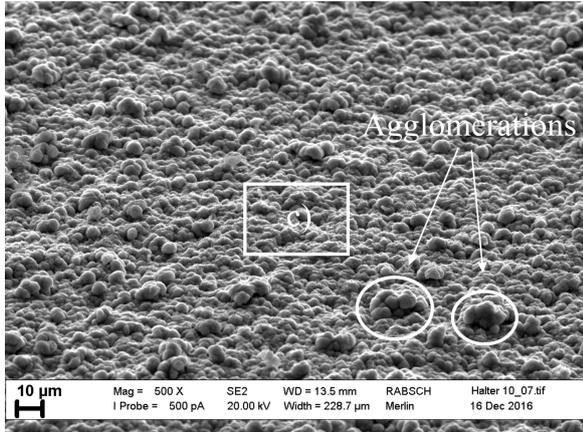
a) 10 μm. TiC coating
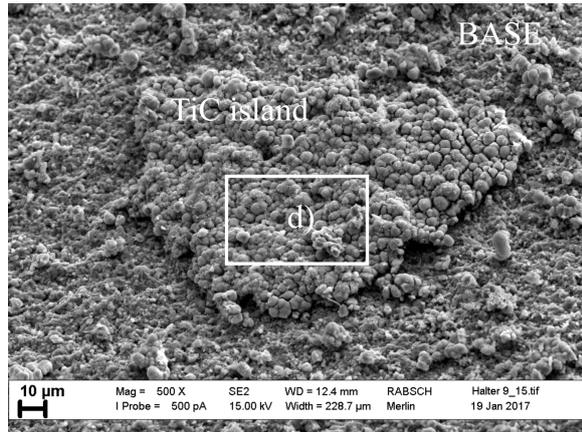
b) 10 μm. TiC island
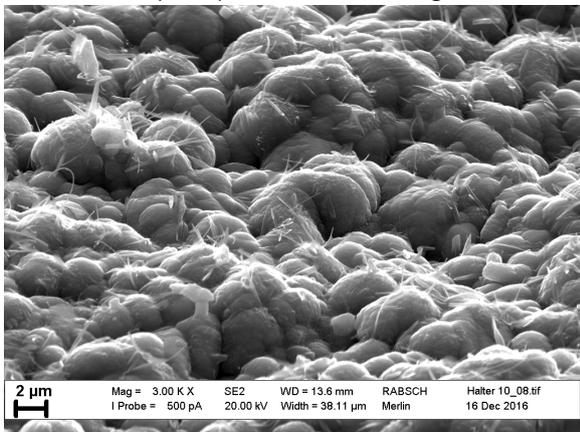
c) 2 μm. Magnification of a)
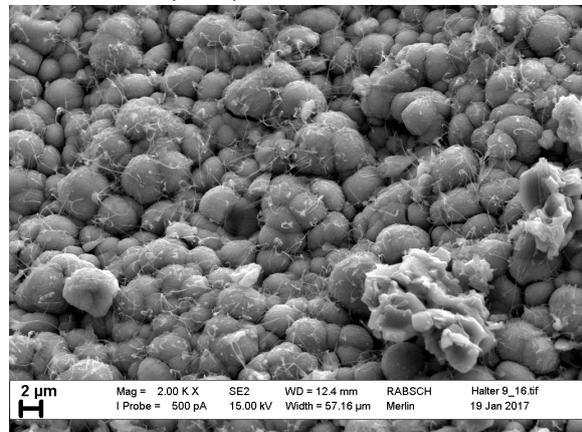
d) 2 μm. Magnification of b)
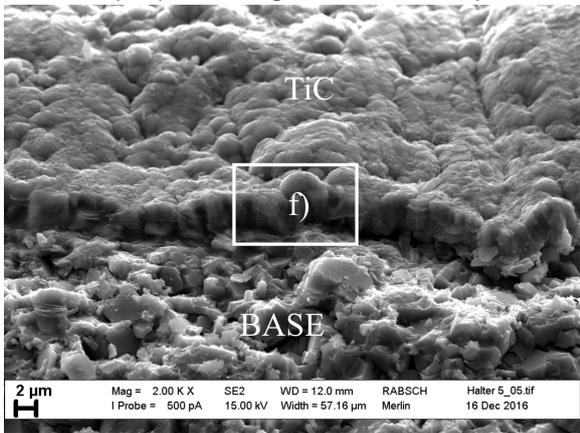
e) 2 μm. Reduced porosity of TiC
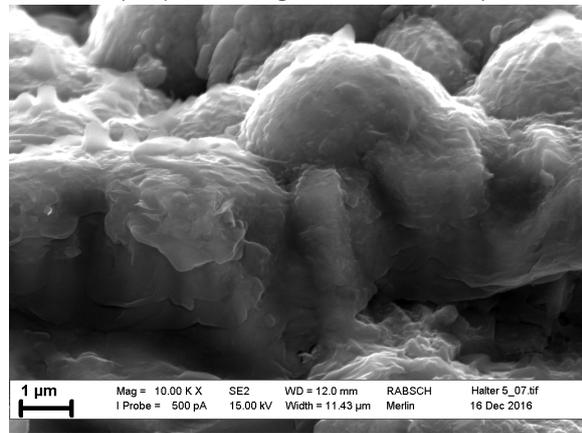
f) 1 μm. Magnification of e)

Figure 6.11: SEM pictures of the morphology of the TiC sputtered layer. a) The electrode layer has been homogeneously deposited on the ceramic surface, b) the remains of a TiC coated island surrounded by BASE are illustrated, c) and d) show the morphology of the TiC sputtered layer, e) and f) display a sputter layer region, where the porosity is reduced [176].

In b) is observed that the edges of the coating island have suffered intergranular fracture probably due to the gas accumulation underneath the layer, which has originated the final detachment. Pictures c) and d) are magnifications from samples a) and b) respectively. In both cases a certain intergranular porosity is observed and the grain size varies between 2 - 5 μm.

A certain porosity in the microstructure of the electrode layer is mandatory in an AMTEC cells to ensure the transport of sodium vapor. Pictures c) and d) of figure 6.11 exhibit in both cases small nanowires that grow fundamentally between grains and propagate further along the grain surface in different directions. The origin of these nanowires is unknown. Pictures e) and f) illustrate a third region of the coated layer. Here, the porosity between the grains is significantly reduced and the appearance of the coating surface resembles a coating that has been locally subjected to high temperatures forming a molten surface. An example of a molten spot was already presented in figure 6.6, where the ceramic suffered a local overheating, apparently originated through a electrically overcharged spot, and the sputtering process had to be interrupted. The electrode layer of this sample is 2 - 3 μm thick. Optimum values of thickness and porosity must be determined experimentally and depend on the material of the electrode, testing conditions and on the current collector morphology. Therefore, a quantitative assessment to the obtained thickness can only be given after an extended experimental analysis at the same AMTEC operational conditions.

The Energy-Dispersive X-ray Spectroscopy (EDX) has been used for the elemental analysis of the sample. The surface of the sample interacts with an electron beam source releasing energy in form of an X-ray, which can be detected by a semiconductor. The selected sample for a EDX-elemental mapping analysis is depicted in figure 6.12 and results are presented in figure 6.13 for carbon (C), titanium (Ti), zirconium (Zr), aluminum (Al), oxygen (O) and sodium (Na).

Carbon a) and Titanium b) are concentrated at the upper surface of the sample and are therefore well defined as coating of the ceramic. A minimal amount of carbon has diffused into the ceramic. The BASE has a certain amount of zirconium c) homogeneously distributed, and aluminum d) is situated also homogeneously in the ceramic structure.

Oxygen can be found overall in the sample e), especially the concentration of oxygen in the secondary phase of the ceramic is the highest ($\sim 70\,\mu$m thick region), which strongly suggests the presence of a hydrated surface region. According to Dunn [177] the hydrated area of a ß"-alumina is constrained to a surface region of $< 100\,\mu$m and decreases the ionic conductivity of the electrolyte. Finally, sodium f) is also situated everywhere in the sample; in particular the presence of sodium at the surface of the coating reveals that a diffusion of sodium from the ceramic has occurred and the ag-
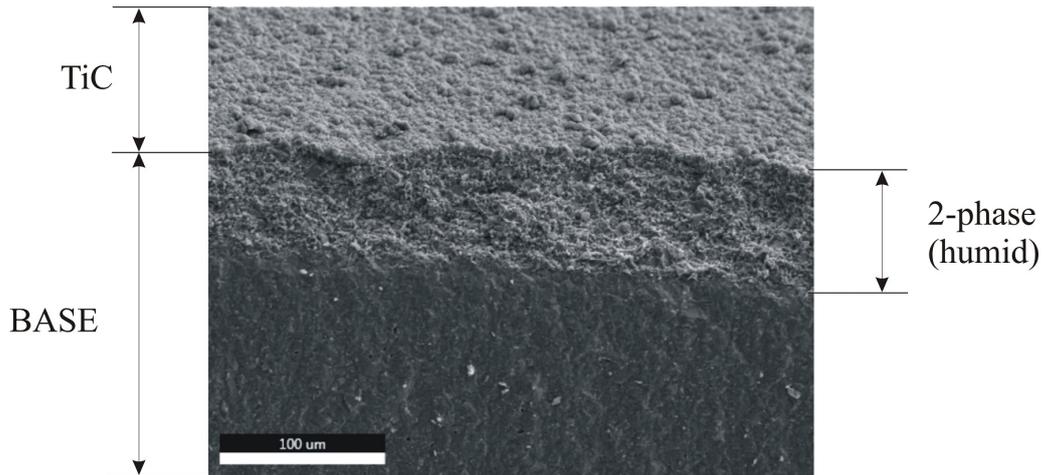
Figure 6.12: SEM capture used for the EDX elemental mapping analysis (100 μm). The sample lies on a specimen holder with a 60° surface inclination. The upper surface is the TiC coating, the middle and lower part of the sample represent both phases of the BASE [176].

glomerations mentioned in figure 6.11 a) are sodium agglomerations which have been further hydrated in air (e.g. NaOH) as indicated by the oxygen mapping e). Therefore it has been proven that the TiC layer is sodium permeable, which is essential for a proper function of the AMTEC cell. The high amount of sodium reported on the coating surface leads to the suspect that the observed nanowires on the coating surface (figure 6.11 pictures c) and d)) could be a kind of sodium nanowires.

The effect of air exposure of the BASE was explained by Dunn [177]. It consists mainly on the formation of a hydrated surface region, where both molecular water and hydronium ions H_3O^+ may enter the conduction planes. This would explain the high concentration of oxygen observed in figure 6.13 e). Hydronium ions replace the sodium ions, which migrate to the surface and react with the atmospheric moisture to generate sodium hydroxide. The latter effect agrees with the observed effect of sodium diffusion to the surface of the electrode in form of sodium agglomerations further hydrated in air. The position of the sodium agglomerations, appears as dark spots in the carbon a) and titanium b) mapping meaning that no chemical reaction occurred. Due to the catalytic effect of sodium hydroxide (NaOH) to attract CO_2, a consequent reaction produces CO_2 species (e.g. sodium carbonate Na_2CO_3 or sodium hydrogen carbonate $NaHCO_3$) on the surface [177]. In the Na mapping f) besides to the agglomerations at the outer surface of the electrode, also a homogeneous distributed smaller amount of Na is observed all over the electrode surface and coincides with the TiC layer (in contrast to the Na agglomerations). The same homogeneous distribution is observed in the O e) mapping at the electrode surface.

a) C

b) Ti

c) Zr

d) Al

e) O

f) Na
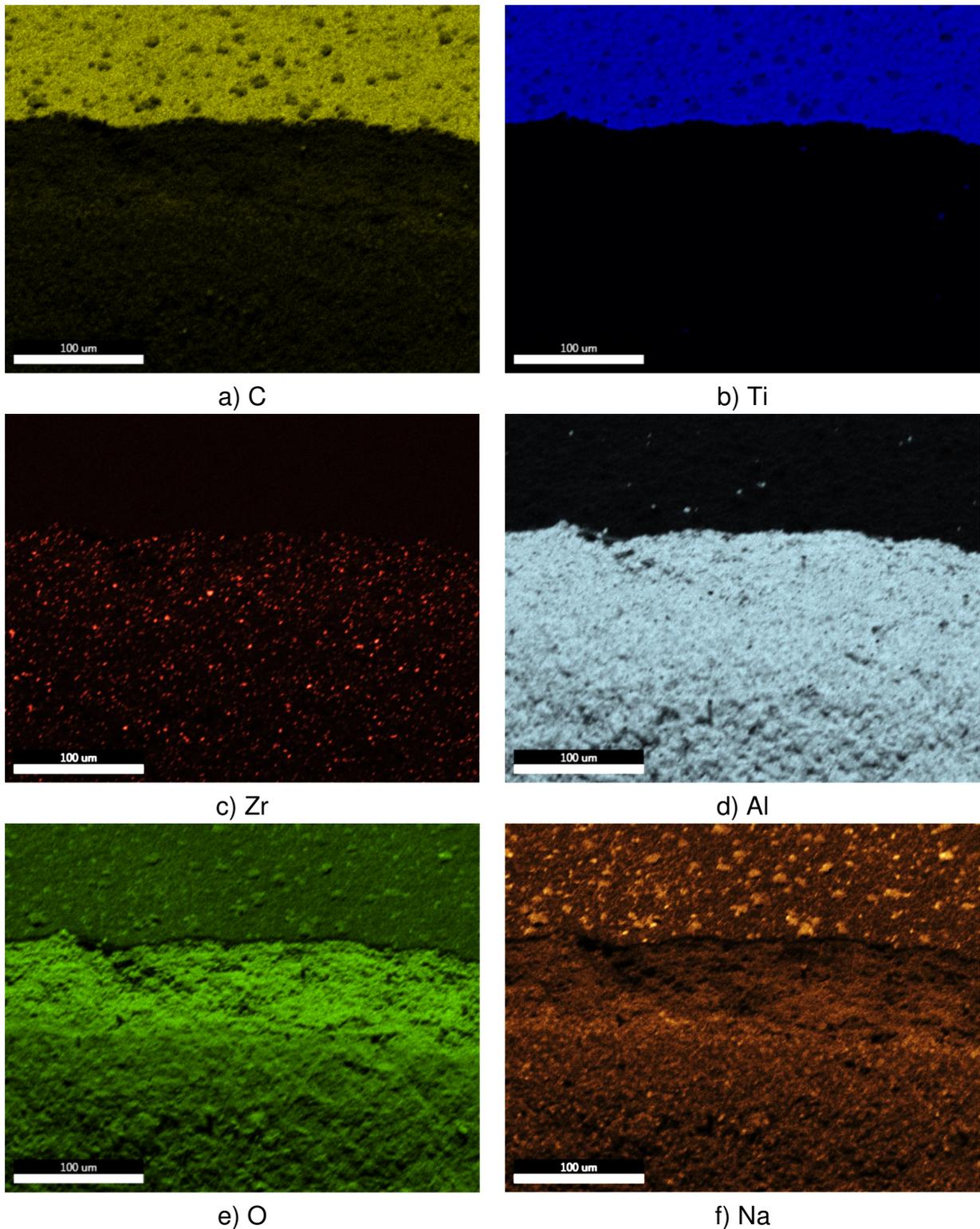
Figure 6.13: EDX elemental mapping (100 μm) of a BASE sample coated with a TiC sputter-layer. Analyzed elements are a) carbon, b) titanium, c) zirconium, d) aluminum, e) oxygen, f) sodium. [176]

Reaction products Na_2CO_3 or $NaHCO_3$ could have been involved in this effect, that may have occurred by the reaction of NaOH with CO_2 from air [177] and/or with C from the TiC sputter layer. The observed small amount of carbon in the ceramic a) may suggest that C from the electrode layer has diffused in the ceramic and further reacted with the hydrated BASE.

The microscopic analysis of the BASE-electrode system has served as first step towards the optimization of AMTEC electrode layers. However, many of the observations reported here are based on assumptions that must be corroborated by further and more detailed analysis of the magnetron sputtering process and the chemical stability of the ceramic electrolyte. As observed through the SEM analysis the adhesion of the TiC electrode layer is insufficient for a proper AMTEC operation. Moreover, it was observed that after the sputtering process the brittleness of the ceramic increased significantly, which complicated the assembly of the cell and increased considerably the risk of a ceramic rupture during the measurements. Hence, a BASE tube without electrode sputtered layer has been used for the AMTEC tests in this work. As a result, the effective electrode surface is given by the current collector, which has an electric surface contact to the BASE several orders of magnitude smaller than the contact surface provided by a sputter electrode layer. This leads to a current density of the AMTEC cell of several orders of magnitude smaller than conventional AMTEC cells. Therefore, the main focus of this work is devoted to the AMTEC proof of concept and open circuit voltage measurements.

In general, the EDX mapping analysis suggests to reduce the exposure time of the BASE in air during the handling process and to avoid or minimize the reduction of ion conductivity in the ceramic surface region as well as the loss of sodium ions from the BASE. The performed experimental analysis has evidenced the hydration of the ceramic surface and that the detachment process of the sputter layer starting at the ceramic surface in form of craters. The relative high temperatures that may have been reached during the sputtering process on the surface of the ceramic, could have promoted the dehydration process and, therefore, the emergence of water vapor and CO_2 out of the ceramic. The emergence of gases could have been as a result responsible for generating the cratered sputtered layer observed in the SEM analysis. According to Dunn [177] during the dehydration process all the water is removed from the BASE already at temperature of 200 °C, at higher temperatures the loss of CO_2 is predominant. Further analysis should focus on the validation of these statements and on a better understanding of the causes of the TiC electrode detachment process.

Sheet resistance measurement of electrode layer.   Several coated BASE samples were analyzed with the 4 point probe technique to measure the electrical sheet re-

sistance of the electrode surface. The measurement method consists of placing four probes along a line that contact the sample surface (see figure 6.14), the outer probes conduct electric current and the inner probes measure the potential drop. Assuming that the probe has been arranged symmetrically over the sample of dimensions (a, d), has a constant point linear spacing s, and the thickness of the layer is so small that the current passes along a two dimensional plane, then the sheet resistance is given as [178]:

$$\varrho_{sheet} = \frac{V}{I} C \left(\frac{a}{d}; \frac{d}{s} \right) \qquad , \qquad (6.1)$$

where $C \left(\frac{a}{d}; \frac{d}{s} \right)$ is a correction factor obtained experimentally and tabulated in [178] that depends on the coefficients between the dimensions of the sample surface and the spacing between the probes.
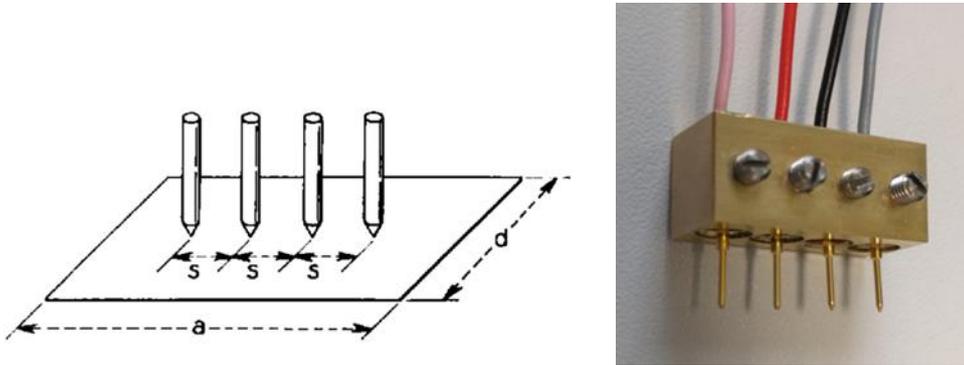
Figure 6.14: Setup scheme of the 4 point probe technique. 4 linear situated probes, separated at a spacing s are used to measure the sheet resisitivity of a thin conductive layer. The sample has a length a and a width d, the thickness is assumed to be infinitely small [178].

A comparison of the results obtained in this work and the literature can be found in table 6.1. The sheet resistance of the TiN samples (TiN-a and TiN-b of figure 6.4, picture b)) differ from each other due to the different TiN configurations, specially TiN-a shows a sputtering layer with a significant low resistance. The sheet resistance of the TiC-b coated sample (figure 6.7) has been reduced by a factor of 10 compared to the sample TiC-a (figure 6.4 sample d)) due to an increased layer thickness, which is one of the optimized parameters. However, the main difference between the coatings is given by the handling of the samples: sample TiC-a was subjected to a secondary brazing process at $T > 1000\,°C$ after sputtering, which damaged partially the sputtered layer. The homogeneity of the coating thickness distribution seems to play an essential role considering the large surface roughness of the ceramic. Despite the larger electrical resistivity of bulk TiC compared to other analyzed materials, it exhibits very good results in thin sputtered layer configuration.

A direct comparison of the sheet resistances between materials should be performed taking into consideration the layer thickness, porosity and temperature. However, these parameters may vary along the sample. Porosity is difficult to be experimentally determined, therefore it is rare to be found in the literature. In this work different measurements were performed at different locations and an average value is given in table 6.1.

Electrode	t_e [μm]	ρ_{bulk} (20 °C) [$10^{-8}\,\Omega$m]	ρ_{sheet} [Ω/sq.]	Ref.
Mo	-	5.5	11.1 ... 16.8 ($T \sim 770$ °C)	[87]
WPt	0.7 ... 1	W 5.5	18.8 ... 98.1 ($T \sim 900$ °C)	[93]
		Pt 10.3		
WRh	0.7 ... 1	W 5.5	40.9 ... 92.1 ($T \sim 900$ °C)	[93]
		Rh ~ 5		
NbN	2 ... 3	Nb 15	20 ... 100	[101]
TiN-1	1.1 ... 1.3	20	13.8 ... 19.1 ($T \sim 950$ °C)	[99]
TiN-2	0.9 ... 2		4.1 ... 17.7 ($T \sim 900$ °C)	
TiN-a	-	20	0.18 ... 0.70	This work ($T \sim 25$ °C)
TiN-b	-		0.31 ... 0.42	
TiC-a	TiC-1 < TiC-2	60	132 ... 351	
TiC-b	TiC-2 ≤ 5		21 ... 24	

Table 6.1: Measured sheet resistances of AMTEC electrodes for different materials [81].

6.3 Current collector structure

The important role of the current collector structure on the performance of the AMTEC cell was already discussed in chapter 2. In this section the results of an experimental study concerning the influence of the current collector structure on the contact resistance of the cell are first presented, which are based on the work of L. Biergans [116]. Then, the measured electrical resistance of the current collector/current lead of the cell is presented and commented.

6.3.1 Preliminary tests on current collector structures

A preliminary study of the current collector (CC) structure to be used in AMTEC cells was performed by L. Biergans [116] (2016). This subchapter presents the experimental setup of the work and summarizes the main results for further analysis of the impact on the power losses of AMTEC cells. The aim of the work was to obtain a CC with an improved CC electrode contact that homogenizes the current distribution over the surface and increases the active surface of the electrode. An ideal structure would be a homogeneous system composed of an electrode and CC of one piece. That would involve a three dimensional construction with increasing aperture in the radial direction the larger the distance to the BASE is (similar to figure 2.22). Since the sputtering deposition technique is rather used in a microscopic scale and the proposed structure goes to the macroscopic scale (millimeters), other technologies may be more suitable for this purpose: e.g. 3D direct laser sintering, thermal spraying or laser direct patterning; however these technologies should be first tested and analyzed for the particular AMTEC requirements, including the gain of experience with ß"-aluminumoxide ceramics.

In the first step an easy to handle and effective current collector consists of a combination of two or more layers organized from thin to wide aperture. The inner layer in direct contact with the electrode has a fine structure with a large contact surface in order to compensate the sheet resistance of the electrode. The outer layer has in contrast a rather robust structure and serves as a corset/holding structure of the inner layers; being responsible for a homogeneous electric contact of CC with electrode surface. This kind of modular current collector setup has been used until now by most authors due to its easy manufacture, assembly, and low cost. However, the main disadvantage of this setup is the low repeatability; considering the high influence of the geometry tolerances, the material properties and the mechanical forces on the contact surface of the current collector and electrode.

The layered configuration complicates also a numerical modeling of the electrical resistivity. First, the complex structure of the CC needs to be considered in the model. Further, the contact surface and contact resistance must be determined; the latter is

inversely proportional to the perpendicular force applied at the contact area. The high number of contact points in the layered structure of the CC lead to a high number of contact forces to be determined. Assuming however that the forces are equally distributed over the entire CC surface would involve a perfect geometry, which is not the case since the tolerances in the radial direction are not negligible [86]. This is in fact one of the main issues of the CC, to ensure homogeneous electric contact conditions over the cylindrical electrode surface. An electric model for several CC structures is given by Tournier et al. [169]. The model was used to estimate e.g. the contact resistance by fitting the calculated curves with measurement data of several PX-series cells. However, they assumed an ideal CC-electrode contact area and a homogeneous distribution of the current that tends to differ from the reality.

The present study focuses mainly on analyzing the impact of the CC structure on the active surface of the electrode. Therefore, several CC parts have been made of copper to minimize the influence of the material-dependent electrical resistivity on the result. However, at AMTEC conditions (700 °C, in sodium) materials with high melting point and good chemical stability are convenient, which normally are accompanied by a high stiffness. Therefore, the measured electrical resistance in this study serves as indicator of the quality of the CC structure rather than a representative value for AMTEC cells.

The experiment has been performed under standard ambient conditions (25 °C, 1 atm, air). A solid rod, (32 mm outer diameter) made of copper, is considered as an ideal electrode to mimic the radial electron flux. The studied electrode area is $\sim 50\,\text{cm}^2$. A d.c. current source is electrically connected to the system (Euro-test Elba-Modul) and generates up to 55 A. The voltage drop measurements are made between the copper rod (point A) and the end of the current collector structure (point B) as indicated in figure 6.15. The voltage is measured using a digital multimeter (DM3058E, Rigol) with an accuracy of $<|0.6|\ \mu\text{V}$ and the applied current is directly recorded from the current source device (Euro-test Elba-Modul) with an accuracy of $<|0.1|\,\text{A}$. Finally, the electrical resistance is calculated using Ohm's law for an electric conductor at an accuracy of $<|0.1|\ \Omega$. The resistance of the cable between the CC and the point B has been separately measured and subtracted from the total resistance. Furthermore, the copper rod has been polished before each test to keep the effect of the surface oxidation low.

Corsets have been first shaped to two half cylinders and then tightened at both sides with screwed copper bars, which act as electric bus collector. The copper bars are further connected to a cable. During the analysis following parameters have been considered: assembling complexity, adaptability, impact on electrode surface (e.g. scratches) and apparent active surface. The tested CCs have an inner structure (listed in table 6.2) fixed to the cylindrical tube with a corset. Foam and woven meshes have been typically
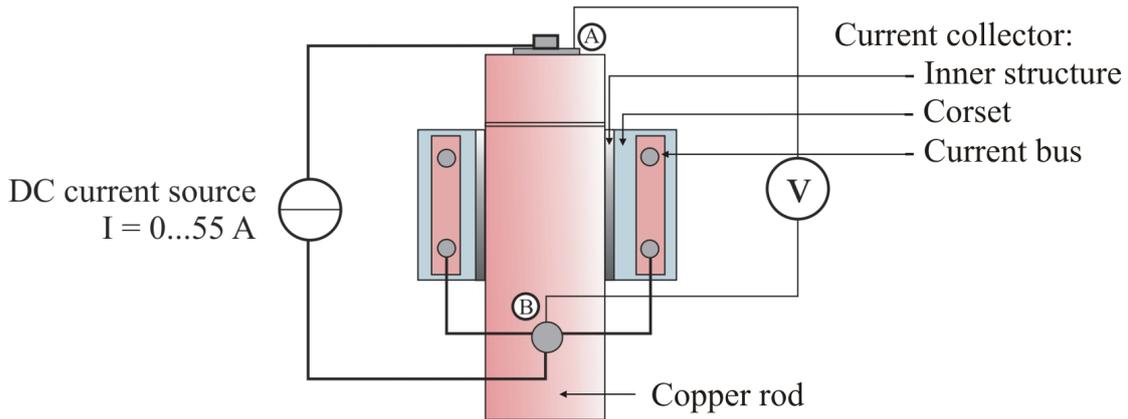
Figure 6.15: Scheme of the experimental setup for testing of different current collector structures. A d.c. current source was coupled to the electric circuit and the voltage drop between point A-B was measured. (Figure edited according to [116])

used in AMTEC cells [179, 86, 1, 91]. Considering the particular mechanical properties found in knitted meshes, they are proposed as a new AMTEC - CC structure in this work. The corset acts simultaneously as support for the electrical contact between the CC and the electrode and as secondary collector of the electric current derived from the inner structure. Therefore, the corset should be mechanically stable but also good electric conductor. For the presented analysis three different corsets have been used: i) a perforated stainless steel (SS) plate (1 mm thickness, $\sim 37\,\%$ porosity), ii) a SS mesh (wire thickness 1 mm, ~ 4.5 mm mesh aperture) with horizontal placed copper wires (wire thickness 0.4 mm, 1.5 mm aperture) and iii) a SS mesh with horizontal and vertical placed copper wires (wire thickness 0.4 mm, 0.5 mm aperture).

Mesh [mm]	I1 Cu woven mesh 1	I2 Cu woven mesh 2	I3 Mo woven mesh	I4 Copper knitted wire mesh
Wire thickness	0.2	0.056	0.056	0.1
Mesh aperture	0.63	0.2	0.2	~ 2

Foam [mm]	I5 Ni foam 1	I6 Ni foam 2	I7 Ni foam 3	I8 Ni foam 4	I9 Ni foam 5
Thickness	4.3	1.6	2.2	1.6	1.6
Pore size	~ 1	~ 1	~ 0.3	~ 0.1	~ 0.1

Table 6.2: Main geometry parameters of the tested inner-current collector-structures: meshes (upper table) and foams (lower table).

During the assembly of the current collectors, the inner structures showed different behaviors. Ni foams have a rather plastic deformation that facilitated the CC assembly; however, under thermal cycling this could be a disadvantage, since after operating at higher temperatures they do not recover their initial form at lower temperatures. The

sharp edges of the Ni foam could also damage the thin electrode layer during assembly. The deformation of the thin woven Cu and Mo meshes is fundamentally elastic; which complicated significantly the assembly. Regarding the impact on electrode surface the thin meshes have no apparent negative effect; in fact they tend to easily slide when tightening the corset creating open areas at the sides of the corsets like shown on the left side in figure 6.16.
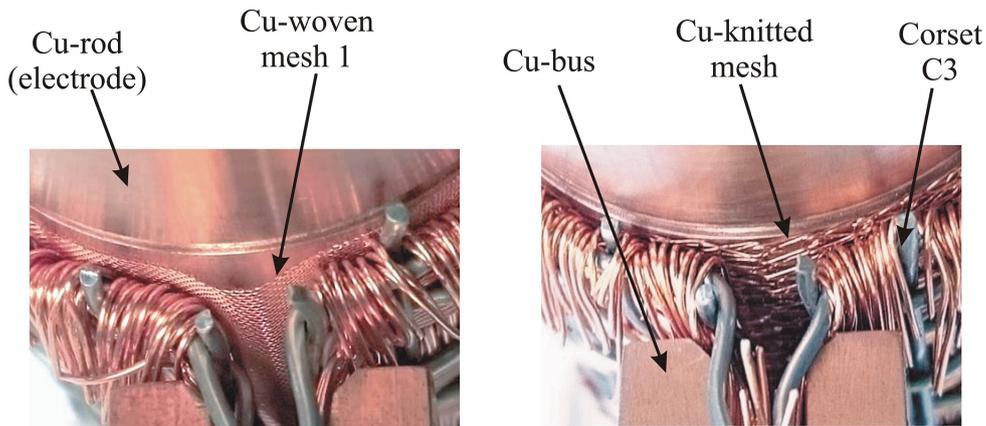
Figure 6.16: Left: assembly of the copper mesh after tightening the corset. Right: assembly of the copper knitted wire mesh after tightening the corset [116].

Knitted wire meshes have interlocking loops, which can move relative to each other in the same plane without distorting the mesh, allowing the structure to stretch or compress in two directions. This favorable characteristic for a cylindrical form is not given by woven meshes, as the wires are fixed to each other in both directions. Therefore knitted wire meshes show a very good conformability; no open areas have been observed (see right side of figure 6.16).

The perforated plate has an irregular contact to the fine inner structures during the assembly; only coarse nickel foams (I5, I7) could compensate to some extent the tolerances of the concentric corset. The other two tested corsets have copper wires which were placed underneath the stainless steel mesh in horizontal and vertical directions and are fixed only at the ends of the mesh to give the corset an additional elasticity. Copper gives the corset an improved electrical conductivity and structural adaptability; the stainless steel mesh is needed in order to give stability to the structure.

Horizontal and vertical placed copper wires perform the most homogeneous contact for all kinds of inner structures due to a higher density of copper wires. Table 6.3 shows the measured electrical resistance of all tested CC configurations. Assuming a good electrical contact between the different parts of the CC, the general tendency should be to see the effect of the electric conductivity in the first place, which depends on the materials used. On the other hand, structures with lower porosity should reach lower resistances due to an increased contact surface. However, if the contact resistances

are too high and/or the effective contact area is too small (e.g. no homogeneous contact along the electrode area), both effects the material dependent and porosity dependent, will be covered up by a poor electric contact.

Inner structure	Corset R_{el} [Ω]	C1 SS perforated plate	C2 SS mesh with horizontal Cu wires	C3 SS mesh with horizontal and vertical Cu wires		
I1	Cu woven mesh 1	-	0.10	0.03		
I2	Cu woven mesh 2	-	0.11	0.04		
I3	Mo woven mesh	-	0.31	0.26	Porosity ⇓ ⇓	El. conductivity ⇑
I4	Cu knitted mesh	-	0.08	0.05		
I5	Ni foam 1	0.56	0.32	0.23		
I6	Ni foam 2	1.09	0.11	0.10		
I7	Ni foam 3	0.40	0.15	0.14		
I8	Ni foam 4	1.54	0.11	0.08		⇑
I9	Ni foam 5	0.80	0.10	0.11		
		⇐ Porosity ⇐				
		⇒ El. conductivity ⇒				

Table 6.3: Measured electrical resistance R_{el} of the current collector for different corset - inner structure configurations [116].

Thinner inner structures could not be tested with the perforated corset C1 as it was bonded for larger thicknesses (C1-I1, -I2, -I3, -I4). Best results are achieved by larger thicknesses (C1-I5, -I7); the measured resistance for Ni thinner foams (1.6 mm) (C1-I6, -I8, -I9) is irregular. Since porosity of C1-I6 is larger than that of C1-I8 and C1-I9, the resistance of C1-I6 should be larger. However, measurements do not agree with this statement due to the irregular contact between corset and foam given by the geometrical tolerances. The CC with SS mesh and horizontal copper wires C2 performs considerably better than C1. Cu wires contribute mainly to this favorable low resistance according to its high specific electric conductivity and a malleable structure that improves an adjustment of the corset to the cylindrical form. Cu woven meshes, C2-I1 and -I2), and thin Ni foams, C2-I6, -I8 and -I9, show the same electrical resistance $\sim 0.11\,\Omega$, however the specific electrical resistance of Cu is four times smaller than that of Ni. This indicates that the effective contact surface of the corset C2 is not homogeneous enough when combined with very thin inner structures.

Best results have been achieved with C3 the SS mesh corset, horizontal and vertical Cu wires. A graphic representation of the measured voltage drop through the Cu rode-CC unit in terms of electric current applied is given in figure 6.17. The linear be-

havior of the curves agrees with the Ohm's law, meaning that the electrical resistance is practically constant during the tests. Therefore, secondary effects that can cause deviations are small. Deviations may be caused by: i) temperature changes, at low current the sample was at room temperature, however at 50 A the temperature increased ($< 200\,°C$) and, therefore, the electrical resistivity of the material varies as well as the thermal expansion (influence on the electric contact); and ii) a poor electric contact caused by a poor pressing of the corset may lead to unstable measurements. The repeatability of the results is strong influenced by the applied mechanical forces on the contact surface of the current collector and electrode, which depend on the assembly of the experimental setup. Geometry tolerances and mechanical properties of the materials used have also an important impact on the electric contact resistance of the assembly and therefore on the resistance measurements.
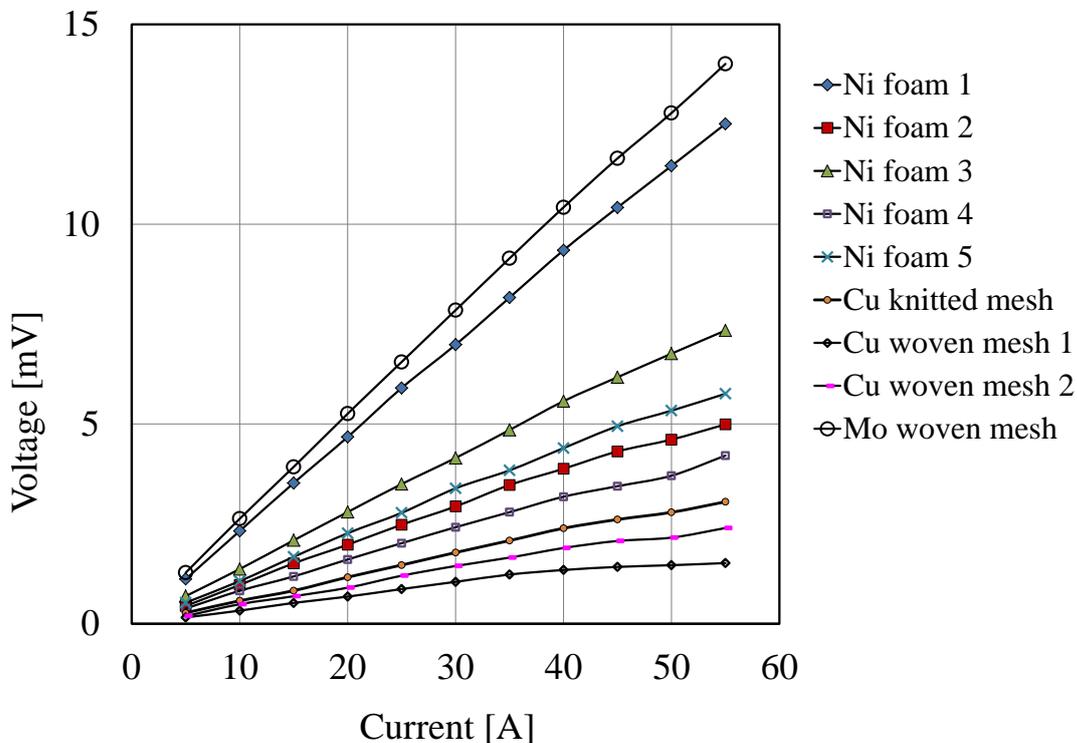
Figure 6.17: Measured voltage loss in the CC at different applied current ($5-55\,A$) for the SS mesh with horizontal and vertical placed Cu wires corset (C3) combined with different inner structures (I1..9) [116].

Results are arranged depending on the material of the inner structure (inner structures made of copper performed the best), meaning that a considerable reduced contact resistance and/or an improved active contact surface has been successfully achieved. In the case of molybdenum, however, the electrical resistance is too high considering the electric properties of the material. This is due to the stiffness of the mesh, which

hindered a good contact. Cu knitted mesh (C3-I4) and woven meshes (C3-I1, -I2) have almost the same electric conductivity although the knitted mesh has a four times larger mesh aperture; this confirms the good adaptability of the knitted structure.

Literature on AMTEC experiments have shown the importance of the CC structure on the cell performance. Available electrical models for AMTEC cells do not include the effect of the active electrode surface in the CC due to the complexity of the system. Experimental results on different CC structures have validated in this work the importance of the following parameters on the electrical resistance of the cell:

- Material. The selection of the material is determining regarding the electric conductivity, the thermal expansion and the stiffness of the CC. Besides, the ideal material should be high-temperature resistant, have a good chemical stability in sodium, a low electrical resistivity and favorably a low stiffness to improve the electric contact with the coated BASE. The reported materials for AMTEC CC up to date (e.g. Mo, Ni, Cu) did not match some of the above mentioned requirements (proper stiffness or long time chemical stability in sodium); therefore, further materials have to be analyzed and contrasted.

- Structure. Mostly high-temperature resistant materials have a large stiffness (e.g. Mo), an appropriate structure (e.g. knitted meshes) could compensate at some content the large stiffness of the structure. Moreover, the CC design should be three dimensional with a higher electric contact surface at the electrode-CC interface and therefore, a smaller porosity; and a decreasing electric contact and therefore, increasing porosity (for a better vapor transport) in the direction to the current bus.

- Temperature. The operation temperature can lead in a tubular configuration of the BASE-electrode-CC to different thermal expansion of the materials. This can directly affect the electric contact of the CC negatively. A final solution to optimize this effect can be found experimentally at the required operation temperatures. A numerical solution through computational efforts is not recommended, since assuming that the applied forces through the pressing are equally distributed over the entire CC surface would involve a perfect geometry, which is not the case since the tolerances in the radial direction are not negligible [86].

- Pressing. In the experiments was observed that the pressure applied to the corset has a large influence on the measured resistance. For instance the difference on the electrical resistance between a slightly pressed and stark pressed C1 corset was 2.5 to 0.4 mΩ respectively.

Tests under AMTEC conditions should be further performed to analyze the consequences of these results under the effect of the high temperatures (500 - 1000 °C), a corrosive environment (sodium) and the very thin porous electrode, which influence significantly the final electrical resistance of the cell. The main challenge to obtain a good electric contact is caused by the cylindrical form of the electrolyte. A planar BASE almost eliminates this issue and gives additionally a basis for a simple AMTEC stacking design. A planar cell design formulates the next step towards an optimized AMTEC 2.0 device.

6.3.2   Electrical resistance of the present current collector for AMTEC demonstration

The investigated AMTEC cell has no sputtered electrode layer. Hence, the electric contact area is significantly reduced and the internal resistance of the cell increases considerably. Therefore, the current collector selection has a rather small influence on the performance of the cell. For the AMTEC proof of concept a simple current collector has been selected. A combination between a nickel foam I6 for the direct contact with the BASE and a perforated plate of SS for the corset has been used in two of the three electrodes. For the third electrode the perforated SS corset is replaced with a nickel knitted mesh. Moreover, a single current bus and current feedthrough configuration per electrode is used due to the limited space in the condenser and the upper cell flange. The electrical resistance of the current collector and current feedthrough has been measured by applying a current of up to 50 A between points A and E represented in figure 6.18 and measuring the voltage drop between two intermediate points. Table 6.4 summarizes the results of the measured electrical resistance being performed at $\sim 200\,°C$. The main source of voltage drop is located between points B and C, that represents 75.4 % of the total voltage loss. This is due to the high resistivity of stainless steel. The resistance can be easily reduced by changing the material of the current lead to a better conductive one (e.g, nickel has almost 10 times higher electric conductivity than stainless steel). Transition parts in A'B and CD are improved to reduce the electric contact resistance by polishing both contact areas and ensuring a tight mechanical contact. During the operation of AMTEC the axial temperature gradient in the cell is large: the temperature in the BASE tube (and therefore CC) can go as high as 800 °C, while the temperature in the flange (points C to E) keeps a constant temperature of $\sim 250\,°C$. Also the liquid sodium anode is heated up inside the BASE tube by a heater that does not cover homogeneously the entire axial length of the BASE tube and CC, hence, the temperature gradient in the liquid sodium, BASE and CC is non-homogeneous ($\triangle T \sim 15\,°C$) that leads to an non uniform thermal expansion of the structure and thus changes in the electrical resistance occur. The data presented in table 6.4 has been taken for simplicity under an homogeneous temperature distribution to detect the components in the current collector-current feedthrough system with the largest ohmic losses and to serve as basis for design improvement. An equivalent test should be performed under AMTEC conditions to obtain resistance values that consider the real temperature gradient.
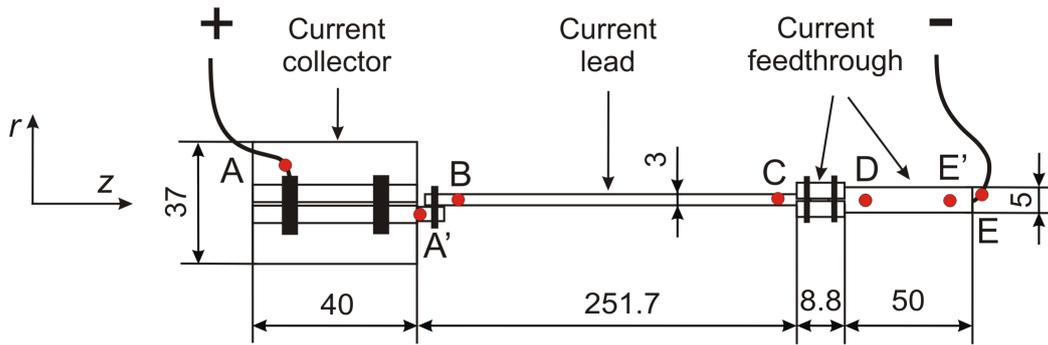
Figure 6.18: Scheme of the tested current collector-current feedthrough system. An electric current is driven between points A and E and the voltage drop is measured at different intermediate points. Dimensions in [mm].

Section	AB	BC	CD	DE	AA'	A'B	DE'	E'E	AE
R [mΩ]	2.13	14.16	0.60	1.78	1.45	0.68	0.19	1.59	18.77
[%]	11.3	75.4	3.2	9.5	7.7	3.6	1.0	8.5	100

Table 6.4: Distribution of the ohmic resistance along the current bus, current lead and current feedthrough at $\sim 200\,°C$.

7 Experimental results and discussion on AMTEC performance

Besides the AMTEC proof of concept, the AMTEC cell has been tested in ATEFA during continued 14 days up to temperatures as high as 700 °C. Unfortunately after 2 weeks, a damage in the main heater of the cell lead to the termination of the experimental campaign. The most important results are presented in this chapter including an analysis of the cell behavior at different temperatures and the comparison with the literature. Sampling rate of the measurements was performed by all the parameters (T, p, V and I) between $1 - 2$ Hz, which is lower than the response time of the instrumentation (~ 15 Hz thermocouples, $6 - 13$ Hz pressure sensors, 16 Hz multimeter) and the conversion time of the beckhoff modules ($16 - 1600$ Hz).

7.1 Design validation

This subsection comprises some of the pre-requisites necessary to understand the AMTEC cell and ATEFA characteristics as well as the achieved results.

Commissioning. Figure 7.1 illustrates the temporal evolution of the measured pressure, voltage and sodium level during the filling up process of the cell. A pressure gradient of ~ 0.1 MPa has been established between the cell p_B (AR-P-03 of figure 5.2) and the tank p_{tank} (AR-P-01 of figure 5.2) in the 9th minute. The sodium level in the ceramic tube is measured through a level sensor L_{Na}, which drops the signal from ~ 7.5 V to 0 V when molten sodium comes into contact. The filling valve situated between cell and tank (NA-VI-01, see figure 5.2) is opened in the 10th minute. Immediately, the level sensor indicates that the cell has been completely filled up with sodium as illustrated in figure 7.1. The sodium valve has been closed ~ 3 seconds afterwards. Directly after filling up the cell, the measured cell voltage V_{cell} increases to 2 V.

Figure 7.2 graph a) shows the temporal evolution of the measured temperature and sodium level in the cell during the filling up process. The level sensor has two measurement positions (see figure 5.8): $L_{Na}(min)$ which is located at the height of thermocouple TC7-i and indicates the minimum sodium required in the cell (see figure 5.7); and $L_{Na}(max)$ located at the height of thermocouple TC3-i indicating the maximum sodium level allowed in the cell. During the filling of the cell $L_{Na}(max)$ was reached in the 11th minute (see figure 7.2 graph a)); subsequently a small amount of sodium was drained (27 to 40th minute). Before the 11th minute the temperature oscillations, originated by the temperature controlling system, were slow, indicating that the cell is floated with argon. After filling up with sodium the temperature oscillations became smaller and faster,
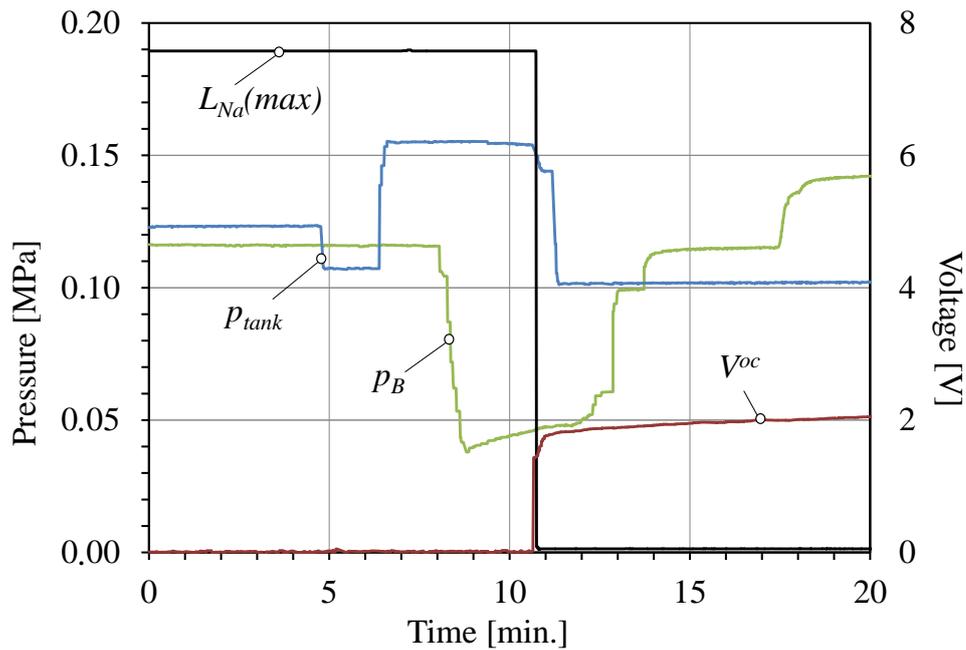
Figure 7.1: Temporal evolution of the measured pressure (p_B, p_{tank}), voltage (V^{oc}) and sodium level ($L_{Na}\,(max)$ in [V]) during the filling up process of the cell. $L_{Na}\,(max)$ measures changes in voltage and it goes to zero when contacting sodium. The cell has been filled up in the 11th minute.

due to the high thermal conductivity of sodium that reflects immediately the changes of the heater temperature. The draining process is also reflected in a temperature gradient between the thermocouples ($> 15\,°C$): TC3-i looses contact with sodium in the 27th minute and TC5-i in the 40th minute. The temperature distribution in the BASE tube has demonstrated to be a successful stepwise-indicator of the sodium level.

Temperature distribution in the cell. An adequate trace heating system of the cell allows a homogeneous temperature distribution, which is important to avoid the solidification of sodium. Figure 7.2 graph b) represents the temporal evolution of the measured temperature distribution in the cell under stable empty conditions (without sodium), showing a balanced thermal cell design. For the representation of this graph the reference thermocouples were chosen, which are located inside the ceramic tube (TCn-i) and at the condenser (SNn). The temperature gradient along the BASE in the axial direction (TC6-i/TC11-i) is $\sim 23\,°C$, while at the condenser the temperature gradient (SN6/SN11) is higher $\sim 39\,°C$ due to the not isolated condenser wall. In the radial direction, the maximum temperature gradient between the inner region of the BASE (anode) and the condenser wall (TC6-i/SN6) is $\sim 35\,°C$ at stable empty conditions.
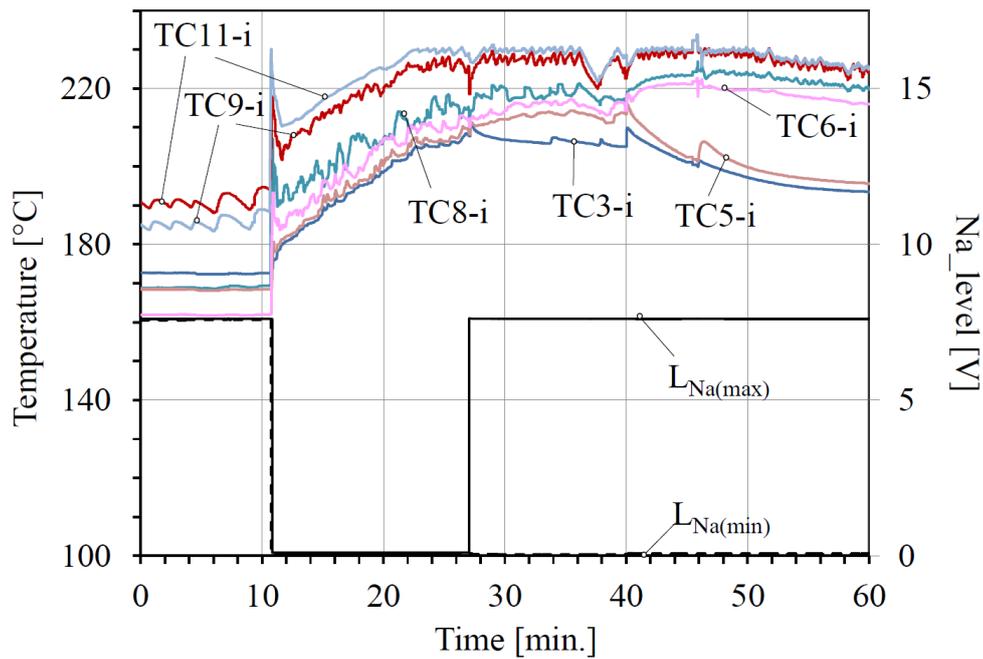
a) Filling up process of the cell. The temperature distribution in the ceramic tube changes depending on the fill level of sodium.
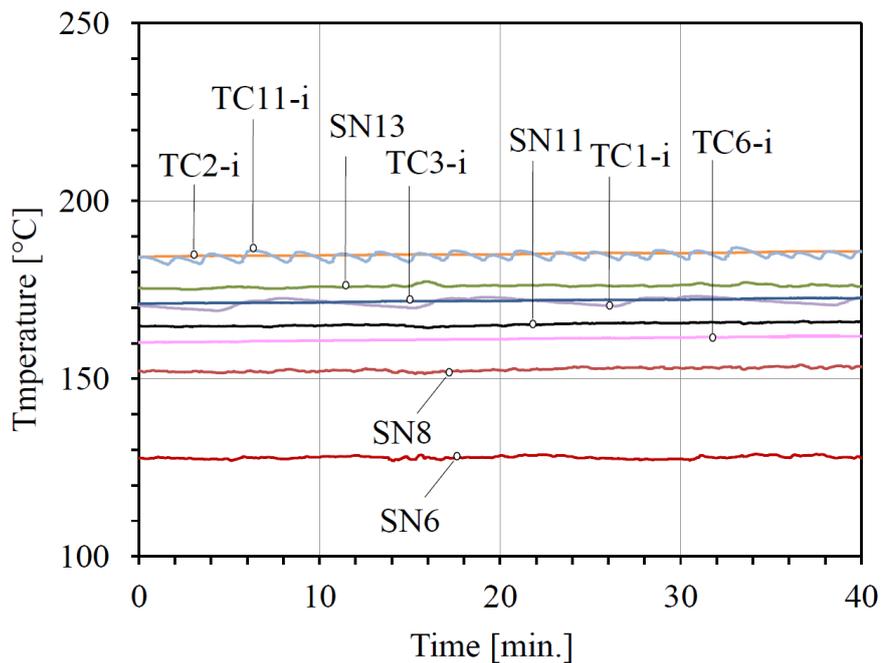
b) Temperature distribution in the cell under stable empty conditions.

Figure 7.2: Measured temperature distribution in the cell during a) filling up process of the cell and b) cell under stable empty conditions. Thermocouple distribution referred to figure 5.7.

The thermocouple SN6 is close to the metallic structure of the cooling system, which

acts as a heat sink source, giving thermocouple SN6 the lowest temperature in the cell. If the thermocouple SN6 is neglected, the maximum temperature gradient in the cell is as low as ~ 35 °C. Therefore, the risk of a BASE rupture through a thermal shock is eliminated.

Ceramic to metal joint.   Another pre-requisite for AMTEC operation is the development of a high-temperature ceramic to metal joint (see chapter 6.1). During the experimental tests of AMTEC the pressure of argon at the cathode side of the cell was constantly recorded in order to supervise any leakage or ceramic rupture during the operation. Since the gas tightness of the outer containment of the cell to the atmosphere is 1.2×10^{-7} mbarl/s, the main source of gas leak is the ceramic to metal joint. The present design of the ceramic to metal joint has been successfully tested under AMTEC conditions up to 650 °C and showed a good behavior during the 2 weeks of operation. It was observed that the pressure at the cathodic side p_c increased slightly with the temperature: the maximum pressure increment recorded was $\Delta \dot{p}_c \left(max \right) = 150$ Pa/min at 650 °C; while at lower temperatures < 550 °C the measured leak was $\Delta \dot{p}_c < 10$ Pa/min. During one of the experiments a large leak at 600 °C was observed at the joint, which disappeared by rising the temperature to 650 °C. The different thermal expansion coefficients of the joined materials make this region susceptible to gas tightness instabilities with the temperature. After repairing the cell heater, a post-experimental analysis of the cell should be performed to investigate the background of this leak more in detail.

7.2   Open circuit voltage

Understanding the different processes occurring in the cell is essential for a correct interpretation of the main AMTEC results. Therefore, the measured open circuit voltage (OCV) between the anode and the three cathodes (V_L, V_M, V_K) is compared with the theoretical open circuit voltage V_{Nernst}, the latter calculated using the Nernst equation (2.47). Furthermore, the effect of different parameters (temperature, pressure at the cathode, exposure time and CC structure and assembly) on the OCV is commented.

The saturated vapor pressure of sodium at the cathode p_c was calculated using equation (2.64), which depends on the pressure of saturated vapor at the condenser surface p_{cd} and on the temperature of the condenser T_{cd} and BASE T_B. For the saturated vapor pressure of sodium the correlation given by Browning and Potter [180] is taken:

$$p_{sat}\left(T\right) = exp\left[11.9463 - 12633.73/T - 0,4672 lnT\right] \qquad , \tag{7.1}$$

for a given temperature T in Kelvin [K].

Measured versus calculated OCV (V^{oc}, V_{Nernst}).   Figure 7.3 summarizes the evolution of one day-long measurement campaign. The temporal evolution of the measured OCV at cathode M, V_M, is represented and compared to the computed instantaneous Nernst voltage V_{Nernst} for different cell temperatures. During the measurement campaign several current measurements were performed at closed circuit conditions, represented in the graphic by voltage measurements of V_M towards zero.

V_{Nernst} was obtained after applying equations (2.63) and (2.64) using the measured temperature at the BASE/or anode T_B and at inner surface of the condenser T_{cd}, and the Browning and Potter correlation for the saturated vapor pressure of sodium. The error e or gradient between the theoretical and the measured voltage has been calculated using equation (7.2):

$$e = \frac{\mid V_M - V_{Nernst}\mid}{V_{Nernst}} \cdot 100 \qquad [\%]. \tag{7.2}$$

Table 7.1 summarizes the maximum error obtained in figure 7.3 graphic a), grouped in six main time zones. During the first 3 hours (until 200th minute) the measured cell voltage V_M was significantly higher than the theoretical value ($e > 100\,\%$). After 4 hours and at a temperature of 400 °C the OCV of the cell finally agreed with the theory. This effect is caused by a poor wetting of the ceramic, which requires several hours of exposure to liquid sodium at high temperatures ($\sim$ 400 °C) to complete [96]. The maximum deviation between the measured and calculated OCV after the 250th minute in figure 7.3 was $e < 20\,\%$ and the average deviation remained low $e \sim 10\,\%$.
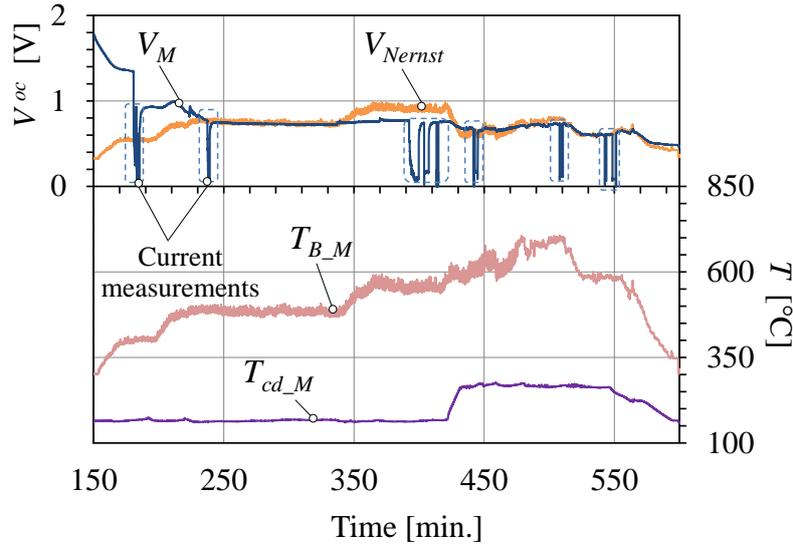
a) Representation of the OCV versus Nernst voltage.
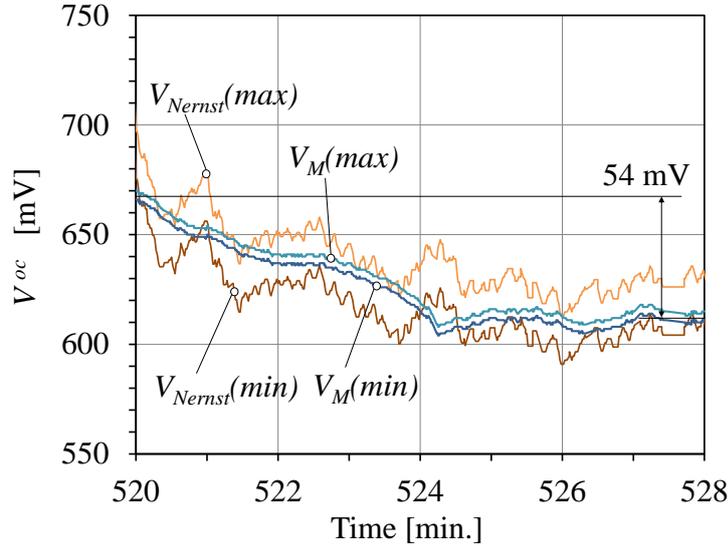
b) Scale amplification of a) between minutes $520 - 528$ showing the uncertainty regimes of the OCV V^{oc} for a temperature decrease at the BASE of $\Delta T_B = 36$ °C and a constant $T_{cd} = 267$ °C.

$$V_{Nernst}(max) = V_{Nernst} + u_{V_{Nernst}} \ , \ V_{Nernst}(min) = V_{Nernst} - u_{V_{Nernst}}$$
$$\text{and } V_M(max) = V_M + u_{V_M} \ , \ V_M(min) = V_M - u_{V_M} \ .$$

Figure 7.3: Temporal evolution of the measured (V_M) versus calculated (V_{Nernst}) OCV at cathode M during one day-long measurement campaign, for variable BASE and condenser temperatures (T_B, T_{cd}).

Minute	150 - 250	250 - 334	334 - 440	440 - 510	510 - 570	570 - 600
e [%]	> 100	< 3.5	< 20	< 10	< 5.5	< 15.5

Table 7.1: Distribution of the error e (measured vs Nernst voltage) along the OCV measurements displayed in graphic a) of figure 7.3.

Assuming a complete wetting of the ceramic after the 250th minute, the deviations observed are mainly due to:

– The theoretical assumption of an isothermal process in AMTEC, meaning that the temperature gradient across the ceramic electrolyte is neglected.

– The thermocouples are not exactly located at the BASE/anode interface but rather in the proximity to the heater of the ceramic, leading to a certain error in the temperature interpretation.

– The temperature distribution over the electrode surface is not perfectly homogeneous. For a $T_B \sim 500\,°C$ the temperature gradient in the axial direction of the electrode surface M was $\Delta T \sim 22\,°C$.

– Uncertainties of the correlation (7.1) (3 - 24 % see Appendix A: Uncertainty of Nernst equation) used to calculate the saturated vapor pressure of sodium.

– Uncertainties of the used instrumentation and data processing ($< 1\,\%$).

As already discussed in subchapter 2.3, the wettability of the ceramic with molten sodium affects the electrochemical performance and reliability of the cell. Also the polarization losses at the anode increase for an incomplete wetted ceramic [98]. The wettability depends mainly on:

– The sodium temperature.

– The composition of the liquid sodium affected by reaction in air and with moisture (Na_2O, NaOH) and by corrosion processes (e.g. with BASE). The physical properties of the melt are modified and can therefore influence the wetting process.

– The moisture content in the ceramic surface [97].

– The development time which is needed until the wetting is completed [96].

– The roughness of the BASE surface [157].

To reduce this effect, the tested BASE tube in the AMTEC cell was baked out in vacuum at 600 °C during one hour and was afterwards stored in argon atmosphere. Due to the long storage time (several months) the inclusion of moisture in the ceramic cannot be excluded.

In the $\sim 180^{\text{th}}$ minute at $\sim 400\,°C$ the electric circuit was closed during the development time ($V_M > V_{Nernst}$); subsequently V_M showed an enhanced approximation to the Nernst voltage. It can be therefore concluded that closing the electric circuit of the cell promotes also the wetting of the ceramic (by electrowetting).

The graphic b) of figure 7.3 illustrates an amplification of the graphic a) during minutes $520 - 528$. Here, the wetting of the ceramic is complete and therefore the measured OCV V_M ranges between the uncertainty regimes of the calculated V_{Nernst}, confirming a very good agreement. The uncertainty of the measurements is based on the propagated error through the instrumentation and conversion process as presented in table 5.3. The maximum uncertainty values are $| u_{V_M} | < 4 \, \text{mV} \, (\pm 0.25 \, \%)$, $| u_{T_B} | < 4.9 \, °\text{C}$ and $| u_{T_{cd}} | < 5.8 \, °\text{C}$. The uncertainty of the Nernst equation has been calculated considering the uncertainty of the measured temperature and the uncertainty of the correlation (7.1). A detailed explanation of the propagated uncertainty of the Nernst voltage is given in Appendix A: Uncertainty of Nernst equation. Between minutes $150 - 600$ the uncertainty of the Nernst voltage is $| u_{V_{Nernst}} | < 4 \, \text{mV} \, (\pm [1 \text{ - } 4] \, \%$ depending on the temperature range).

Effect of the temperatures (T_B, T_{cd}) on the OCV V^{oc}. During minutes $350 - 420$ in figure 7.3, the measured OCV is moderately lower than the Nernst voltage ($V_M < V_{Nernst}$) with a deviation of $e = 15 \text{ - } 20 \, \%$, showing the contrary effect to that observed during the development time ($V_M < V_{Nernst}$). This can be explained through a too high temperature gradient between the anode and the condenser wall ($T_B - T_{cd}) > 350 \, °\text{C}$, which leads to a not negligible temperature gradient across the anode/ceramic electrolyte/cathode. Therefore, the real temperature at the BASE and cathode is lower than the temperature measured by the thermocouples in liquid sodium (anode), meaning that the theoretical assumption of an isothermal process is not completely fulfilled. If the effective BASE temperature is lower than expected, then the cell voltage decreases too; leading to an overestimation of the cell voltage by the Nernst equation V_{Nernst}.

In the 450th minute however, the temperature at the condenser was increased and therefore, the temperature gradient in the cell decreased ($T_B - T_{cd}) \sim 310 \, °\text{C}$. As result, the measured open circuit voltage is in a good agreement with the literature, meaning that the temperature gradient across the anode/ceramic electrolyte/cathode is negligible.

Figure 7.4 illustrates the effect of a temperature change of $80 \, °\text{C}$ on the cell voltage V^{oc}: a) $V^{oc} = f(t)$ for variable T_B and $T_{cd} = \text{const.}$ and b) $V^{oc} = f(t)$ for $T_B = \text{const.}$ and variable T_{cd}. The measured cell voltage increases with rising T_B and $T_{cd} = \text{const.}$ and in contrast decreases with rising T_{cd} and $T_B = \text{const.}$ This agrees with the theory represented by equations (2.47) and (2.64) and is mainly explained due to the exponential behavior of the saturated vapor pressure of sodium with the temperature. Moreover, the effect of the ΔT_B on the $\Delta V^{oc} = 110 \, \text{mA}$ almost doubles the effect of the ΔT_{cd}, with $\Delta V^{oc} = 60 \, \text{mA}$. This is, again, connected with the exponential behavior of the saturated vapor pressure of sodium $p_{sat} \sim exp[T_{Na}]$. The same change in the temperature is

translated in a significantly higher change of the saturated vapor pressure of sodium at higher temperatures: $\Delta p_{sat}\left(T_B\right) \gg \Delta p_{sat}\left(T_{cd}\right)$.
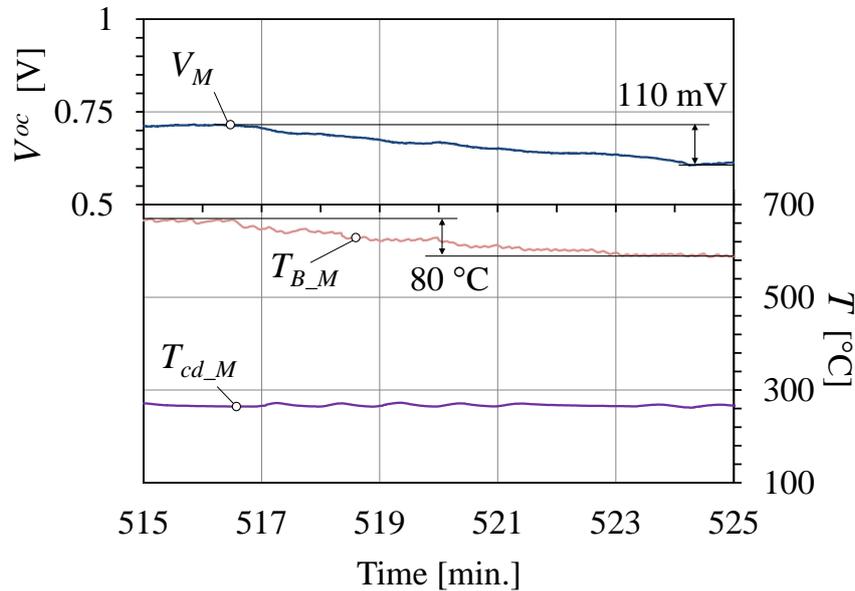
a) V^{oc} as a function of time for $\Delta T_B = 80\ ℃$ and $T_{cd} = 260\ ℃ = \text{const.}$
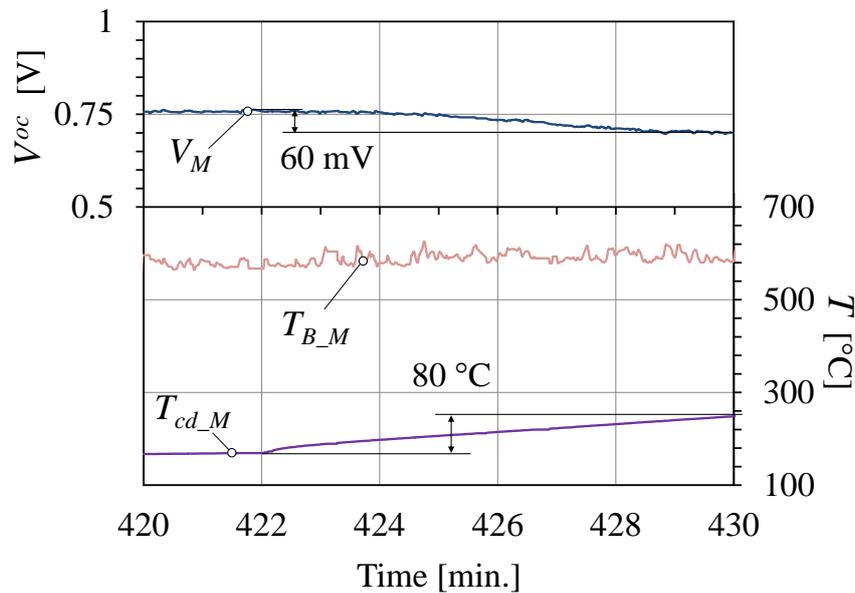
b) V^{oc} as a function of time for $T_B = 600\ ℃ = \text{const.}$ and $\Delta T_{cd} = 80\ ℃$.

Figure 7.4: Temporal evolution of the measured OCV V^{oc} at cathode M (V_M) for a temperature gradient of 80 ℃ at the BASE T_B (a) and at the condenser T_{cd} (b).

Effect of the exposure time to hot liquid sodium on the OCV V^{oc}.   Figure 7.5 graphics a) and b) show the measured OCV at electrodes L and M (V_L, V_M) for increasing cell temperature at a constant argon pressure at the cathode side of the cell $p_c\left(Ar\right)$

(AR-P-02 in the flow chart, figure 5.2) during $0 - 360^{\text{th}}$ minutes and for decreasing argon pressure $p_c\,(Ar)$ and at a quasi constant cell temperature between the $365 - 420^{\text{th}}$ minutes. The case illustrated here exhibits an AMTEC cell that has a higher temperature at the condenser than at the BASE ($T_B < T_{cd}$). In such a case, the Nernst equation provides a negative cell voltage V_{Nernst} as represented in the graphic. However, in the tested AMTEC cell it is not possible to obtain a negative cell voltage since that would mean that sodium would diffuse from the outside of the ceramic tube to the inside (reverted process). Outside of the ceramic there is no sodium at open circuit conditions and therefore the cell voltage should tend to zero. As it can be observed during the first 2.5 hours the measured cell voltage remains as high as ~ 1 V. In the 170th minute the electrode L reduces drastically the voltage to ~ 150 mV at a BASE temperature of $T_B \sim 270$ °C. Electrode M reaches more than 1.5 hours later (290th minute) the same voltage, at $T_B \sim 300$ °C. At this temperature and after a total exposure time of 5 hours, both electrodes reach the same voltage. It is, hence, confirmed that an initial exposure time of several hours and an increased temperature $T_B > 300$ °C (300th minute) are required for an optimal wetting of the ceramic, and thus, a reliable cell performance ($e < 10\,\%$). The development time can also be reduced by driving a current (electrowetting) as observed already in figure 7.3.

Effect of the current collector on the OCV V^{oc}. Although the temperature at both electrodes is practically the same ($T_{B-L} = T_{B-M}$), electrode voltages V_L and V_M develop differently with the time, which evidences the large effect of the electric contact at the electrode interfaces. This depends mainly on the structure, mechanical adaptability and material of the current collector as well as on the applied contact pressure on the corset. Current collectors at electrodes L and M are different as shown in figure 5.4. It can be hence, concluded that the current collector of the electrode L (lowest position) with the nickel knitted mesh has performed better than that of the electrode M (middle position) with the stainless steel perforated plate.

Effect of the argon pressure at the cathode side of the cell $p_c\,(Ar)$ on the OCV V^{oc}. In the 365th minute of figure 7.5 the pressure at the cathode was reduced to ~ 250 Pa as it can be observed in the graphic b). Although theoretically the pressure of argon does not have any influence on the voltage of the cell at open circuit conditions, the measurements disagree. Evacuating the cathode side of the cell had an immediate effect on the cell voltage, which went to zero as expected theoretically. Moreover, if the cathode side is floated again with argon (in the 437th minute) the cell voltage increases instantaneously to large voltage values of 1 V, which means an excessive deviation e of the measured to the calculated value (0 V).
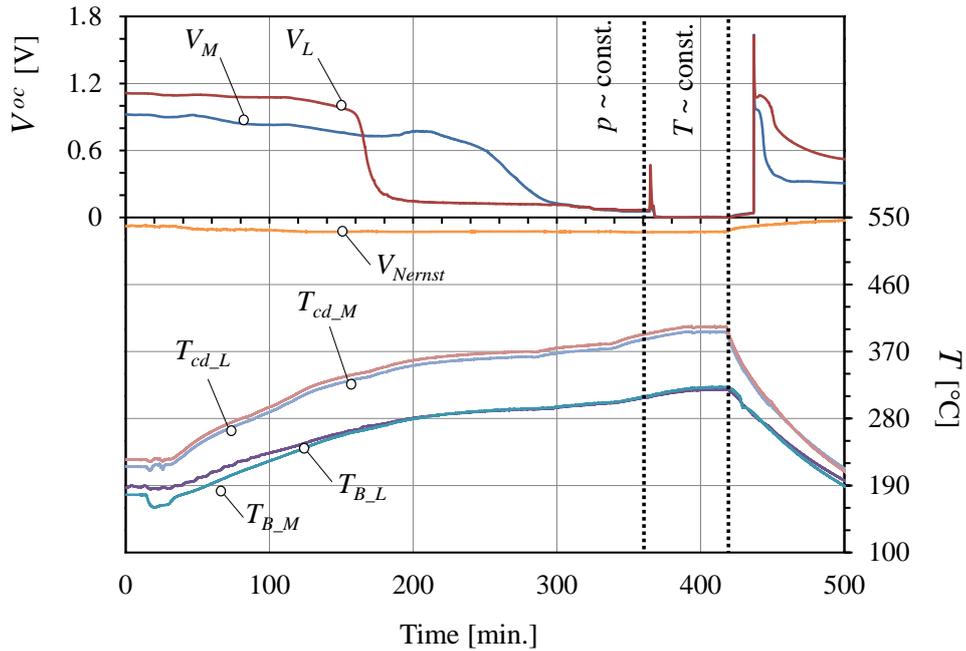
a) Effect of the cell temperature (T_B, T_{cd}) on the voltage (V_M, V_L) and on the wetting of the ceramic.
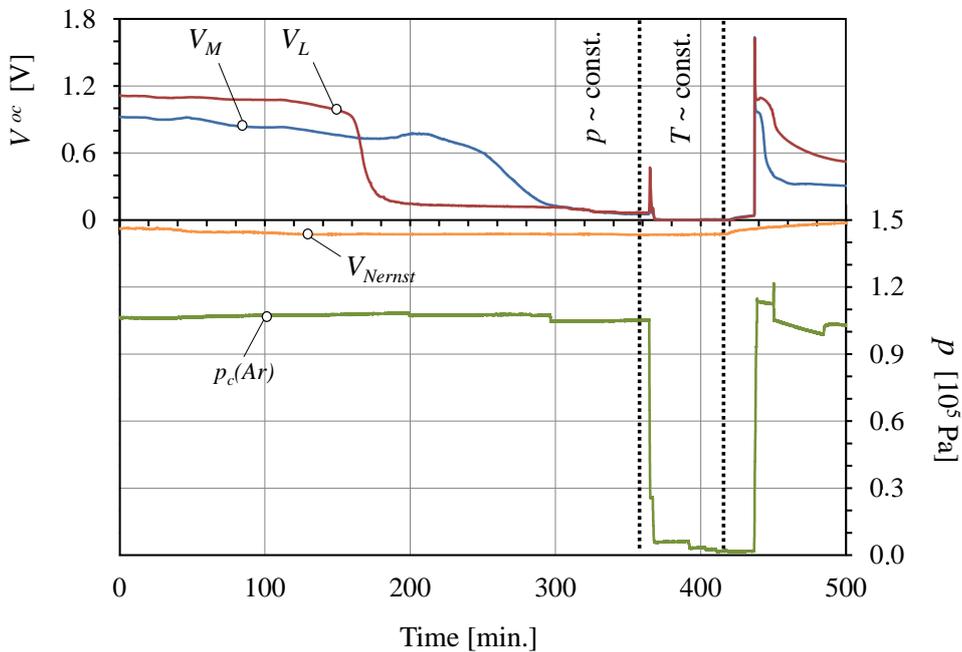
b) Effect of the argon pressure at the cathode $p_c(Ar)$ on the cell voltage (V_M, V_L).

Figure 7.5: Temporal evolution of the measured OCV at electrodes M and L (V_M, V_L) and of the calculated Nernst voltage (V_{Nernst}). The effect of the cell temperature and argon pressure at the cathode ($p_c(Ar)$) on the cell voltage are displayed in graphics a) and b).

149

Therefore, it can be concluded that a too high argon pressure increases the measured OCV of the cell, leading to a distorted result compared to the Nernst voltage. The pressure of argon may have a direct influence on the electric contact between the current collector and the BASE outer surface, which would explain the observed effect on the V^{oc}.

7.3 Characteristic curve of AMTEC

During the measuring campaign values of cell voltage, cell current, temperature and pressure of argon have been recorded. As concluded in the previous subchapter, the argon pressure has a significant influence on the cell voltage, therefore the main objectives of the pressure surveillance are two:

    i) the cathode side of the cell should be kept in underpressure and,

    ii) the argon pressure at the anode side of the cell should be higher than the saturation pressure of sodium at the given BASE temperature ($T_{Na} = 700\,°C$, $p_{Ar} > 1760\,Pa$) and also higher than the atmospheric pressure in order to avoid the entrance of air in the cell.

To exclude the influence of the electrode sputtering deposition on the BASE properties (e.g. increased brittleness), the current collector (CC) has been pressed directly onto the BASE. Hence, the electrical contact at the BASE-cathode interface is provided by the current collector, namely a nickel foam that is held to the surface of the BASE tube with a specific corset (see chapter 5). The resulting electric contact surface to the BASE is several orders of magnitude smaller than that of an equivalent sputtered cathode layer with the same surface of $\sim 45\,cm^2$. Therefore, the active surface of the electrode is also reduced by several orders. The small current production of the cell (mA) agrees with the small effective contact surface of the CC to the BASE. To avoid interferences in the current signal, the sodium level sensor has been switched off during the current measurements. The latter generates, when switched on, a current of $8\,mA$ in the cell.

Each measurement campaign covered $8 - 10$ uninterrupted hours, including the heating up, the measuring and the cooling down processes. The facility was maintained at 200 °C between measuring campaigns (during the night $> 10\,h$).

The high resistance of the electric circuit in this particular AMTEC cell (no BASE coating, high contact resistance) cannot be compensated by the low power delivered by the cell alone, therefore the high electric resistance is partially compensated by the electronic load (Electronic Load Serie ZS, Höcherl & Hackl GmbH), which generates an additional voltage. This additional voltage reduces the net electric resistance of the circuit and therefore a defined characteristic curve of the cell can be measured. If the cell would have been directly connected without electronic load, the power generated would not have been able to overcome the high resistance.

Current-voltage (I-V) measurements at $T_B = 400 - 500\,°C$. Figure 7.6 describes the characteristic curve (I-V) of the AMTEC cell at a temperature range of $T_B = 400$ - 500 °C and $T_{cd} \sim 150\,°C$. First, the BASE has been heated up from 200 °C to 300 °C in ~ 30 minutes, then it is kept at 300 °C during a development time of ~ 2.5 hours,

finally the BASE is heated up to 400 °C in ~ 15 minutes. The recording of the measurement data has been started 20 minutes after reaching 400 °C. The fluctuations of the average temperature during the measurements were $\sim \pm 3$ °C at electrode L and $\sim \pm 1$ °C at electrode M. The measured temperature fluctuations at electrode L were larger than at electrode M due to a closest location of the thermocouples to the heater wire. The recording of the measurement data at 500 °C has been started 5 minutes after reaching the 515 °C at electrode L, which generated in combination to the temperature regulation effect a large scattering of the data due to a non fully completed steady state (< 5 % temperature deviations). At electrode M data has been recorded 20 minutes after reaching 485 °C.

First observations confirm that the characteristic curve has the same behavior in both electrodes and at different temperatures, and in all cases agrees with the literature presented in this work: a rapid initial fall followed by a linear behavior. At low current densities the reaction kinetics at the electrodes are slow so that a high activation energy must be overcome. This leads to large voltage changes ΔV for small current variations ΔJ as confirmed by the experiment. The linear behavior of the voltage starts at larger currents J (depending on the BASE temperature). This behavior is caused by the predominant ohmic losses in this region. The obtained characteristic curve (I-V) does not have an apparent concentration polarization region, this is due to: i) the small measured current, and ii) the highly porous current collector used in the experiment, which does not present a resistance to sodium vapor flow.

It can also be observed that at higher BASE temperatures, both the electric current and cell performance increase, in accordance to the literature. Small voltage measurements in the range of ~ 10 mV were measured at the highest current densities. Electrode L showed during the entire measuring campaign an OCV ~ 15 - 20 % lower than the theoretical value. Electrode M, however, showed a much better agreement with the theory at a deviation of $e \sim 2$ % at $T_B = 400$ °C and a deviation of $e \sim 10$ % at $T_B = 500$ °C. As explained in the previous subchapter, this higher deviation at 500 °C is likely originated by a disagreement between the measured and the actual BASE temperature. The latter attributed to a large temperature gradient in the cell $T_B - T_{cd} = 366$ °C for electrode L and $T_B - T_{cd} = 320$ °C for electrode M.

Current-voltage (I-V) measurements at $T_B = 500$ - 600 °C. Figure 7.7 illustrates the measured characteristic curve (I-V) of the AMTEC cell at a temperature range of $T_B = 500$ - 600 °C and $T_{cd} \sim 160$ °C for all three electrodes (L, M, K). The cell has been heated up from 200 to 600 °C in ~ 6 hours and the measurement data has been recorded 20 minutes after reaching the 600 °C. The fluctuations of the average temperature during the measurements at 600 °C were large (up to ± 10 °C) due to the coarse

Figure 7.6: Measured characteristic curve (I-V) of the AMTEC test cell and cell performance for electrodes L and M at average temperatures $T_B = 400$ - 500 °C and $T_{cd} \sim 150$ °C.
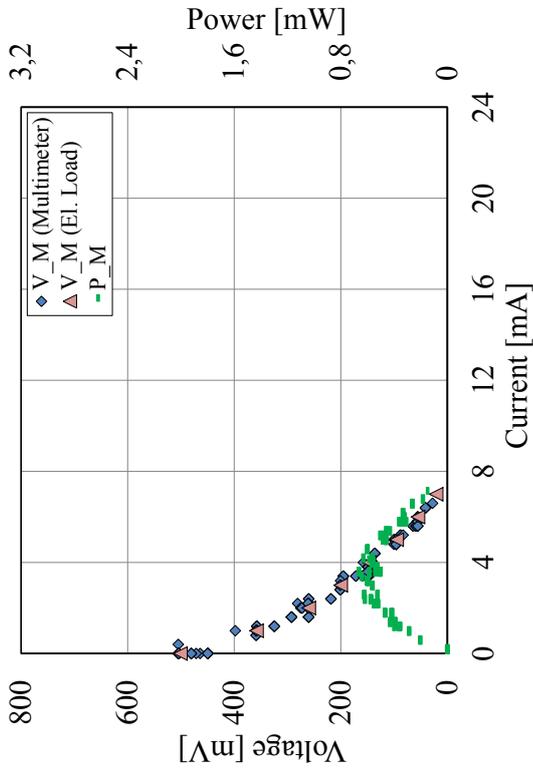
a) Electrode L, $T_B = 420$ °C, $T_{cd} = 135$ °C
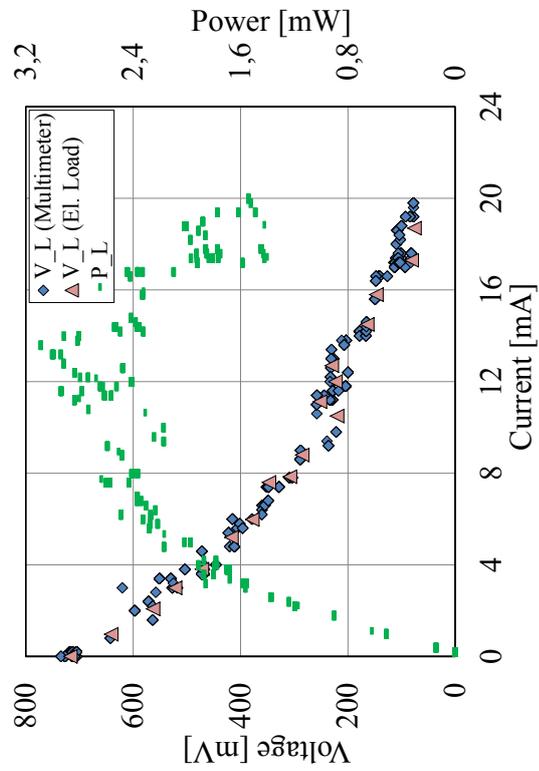
b) Electrode M, $T_B = 406$ °C, $T_{cd} = 153$ °C
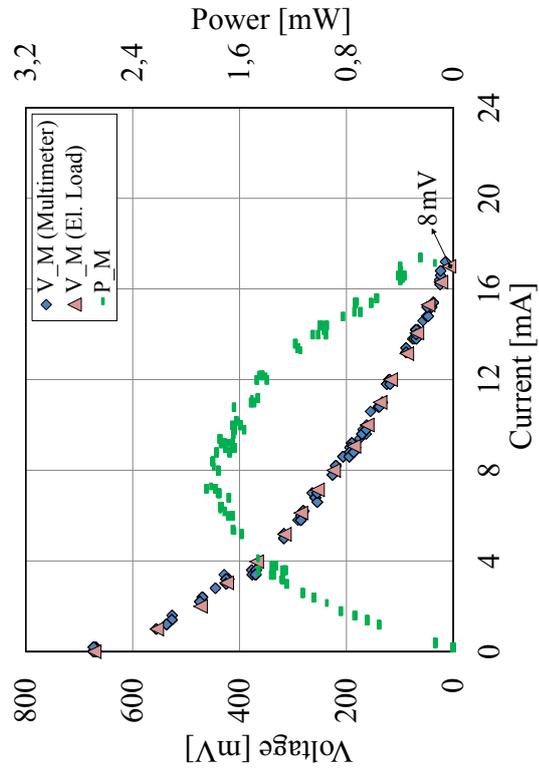
c) Electrode L, $T_B = 516$ °C, $T_{cd} = 150$ °C
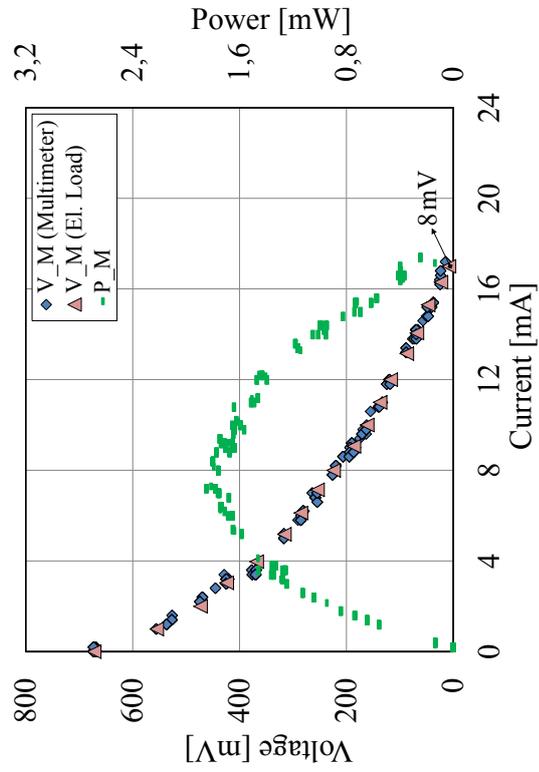
d) Electrode M, $T_B = 487$ °C, $T_{cd} = 168$ °C
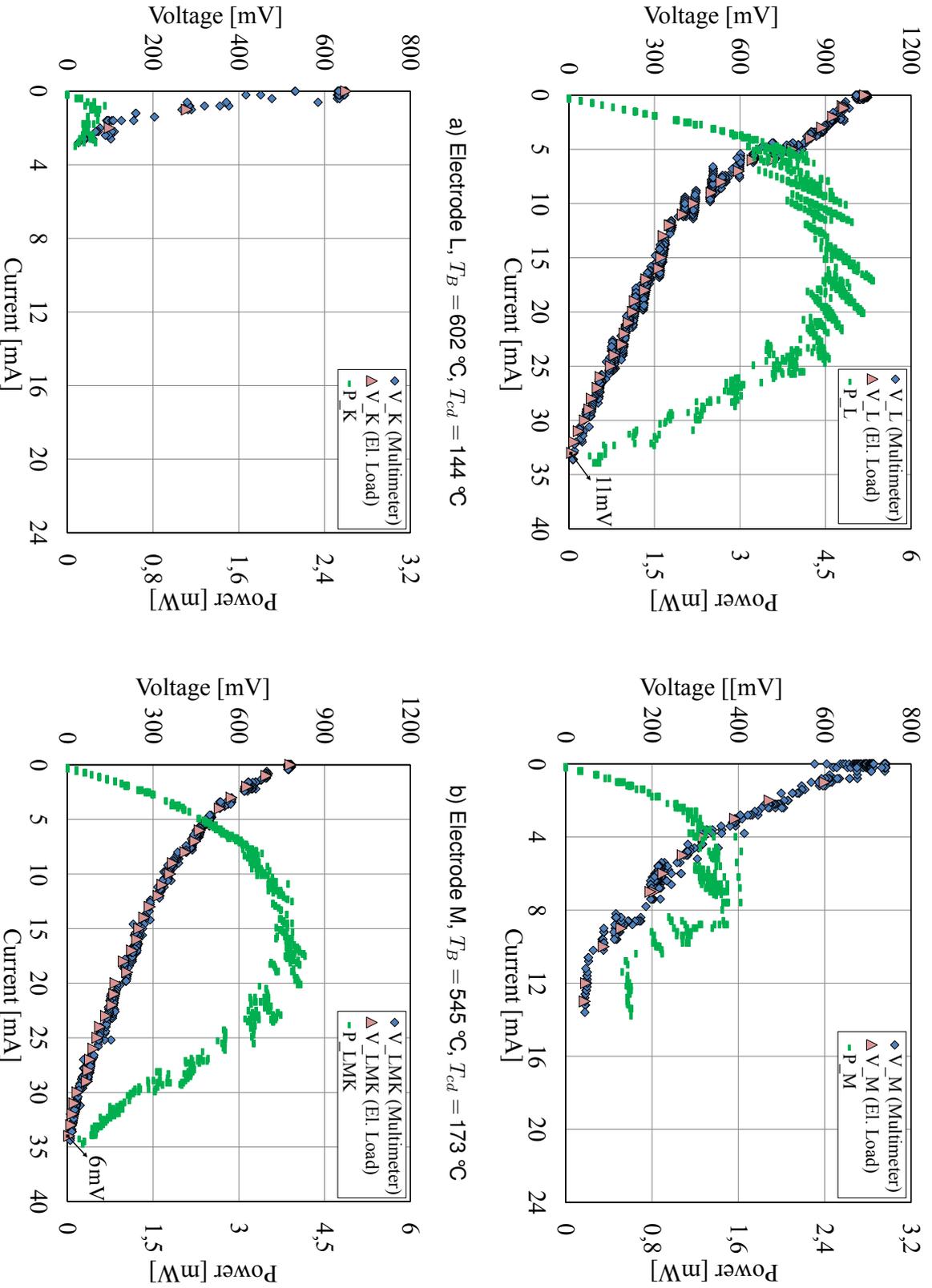
Figure 7.7: Measured characteristic curve (I-V) of the AMTEC test cell and cell performance for electrodes L, M and K at temperatures $T_B = 500$ - 600 °C and $T_{cd} \sim 160$ °C.

a) Electrode L, $T_B = 602$ °C, $T_{cd} = 144$ °C

b) Electrode M, $T_B = 545$ °C, $T_{cd} = 173$ °C

c) Electrode K, $T_B = 525$ °C, $T_{cd} = 176$ °C

d) Electrode L+M+K, $T_B = 554$ °C, $T_{cd} = 169$ °C

regulation of the temperature at high heater power levels, which explains the large scattering of the measured characteristic curve.

The data presented is recorded at a deviation of the OCV of $e_L \sim 7\,\%$, $e_M \sim 15\,\%$ and $e_K \sim 19\,\%$ at electrodes L, M and K, respectively. The maximum power of the cell rises to $\sim 5\,$mW and the maximum cell current is 36 mA. Electrodes M and K show in graphics b) and c) a lower performance and cell current than in figure 7.6 graphics c) and d), although the BASE temperature was slightly lower. Graphic d) of figure 7.7 was recorded while all three electrodes were connected to the electric circuit. The total power of the cell is, however, as high as the power of the single electrode L. It was found that there is a strong internal electric connection between the electrodes, which may take place at the anode, where all three electrodes are electrically connected. When only one of the electrodes is operating, the amount of electrons accumulated at the anode is the sum of all three electrodes, therefore it can occur that electrons coming from other electrodes are used to recombine the ions of the single connected electrode increasing as result the current of the single electrode.

Current-voltage (I-V) measurements at $T_B = 700\,°$C. Figure 7.8 summarizes the performance measurements of the cell at temperatures up to $T_B = 700\,°$C for electrodes L and M. The heating up process from $200 - 700\,°$C has been accomplished in ~ 6.5 hours. Measurement data has been recorded ~ 15 minutes after reaching the 700 °C. The fluctuations during the measurements on the average temperature at 700 °C were smaller than $\pm 5\,°$C. The maximum measured power of the cell rises to $\sim 7\,$mW and the maximum current is 52 mA. Electrode L generated at $T_B = 600\,°$C (figure 7.8 graphic a)) a lower performance than during the previous measurement campaign (figure 7.7 graphic a)) . However, electrode M shows a similar cell performance at $T_B = 550\,°$C (figure 7.8 graphic b)) than at the previous measurement campaign (figure 7.7 graphic b)) . During the measurement campaign summarized in figure 7.8 the Nernst equation and the OCV were in good agreement $e < 10\,\%$.

Effect of the current collector on the I-V measurements. In particular, electrode K generated in all measurement campaigns significantly lower performance. In figure 7.7 graphic c) the maximum measured cell power at electrode K is $> 75\,\%$ lower than that that of electrode M (graphic b)). This can be attributed to a poor electric contact of the current collector (e.g. through an insufficient pressing force of the corset towards the BASE outer surface). During the measurement campaign the measured OCV at $T_B \leq 400\,°$C (not represented in figure 7.7) was $e > 100\,\%$ larger than the Nernst voltage, even after ~ 5 hours of operation at $T_B > 300\,°$C. This cannot only be explained due to a poor wetting effect of the ceramic and/or impurities in the liquid sodium anode; but
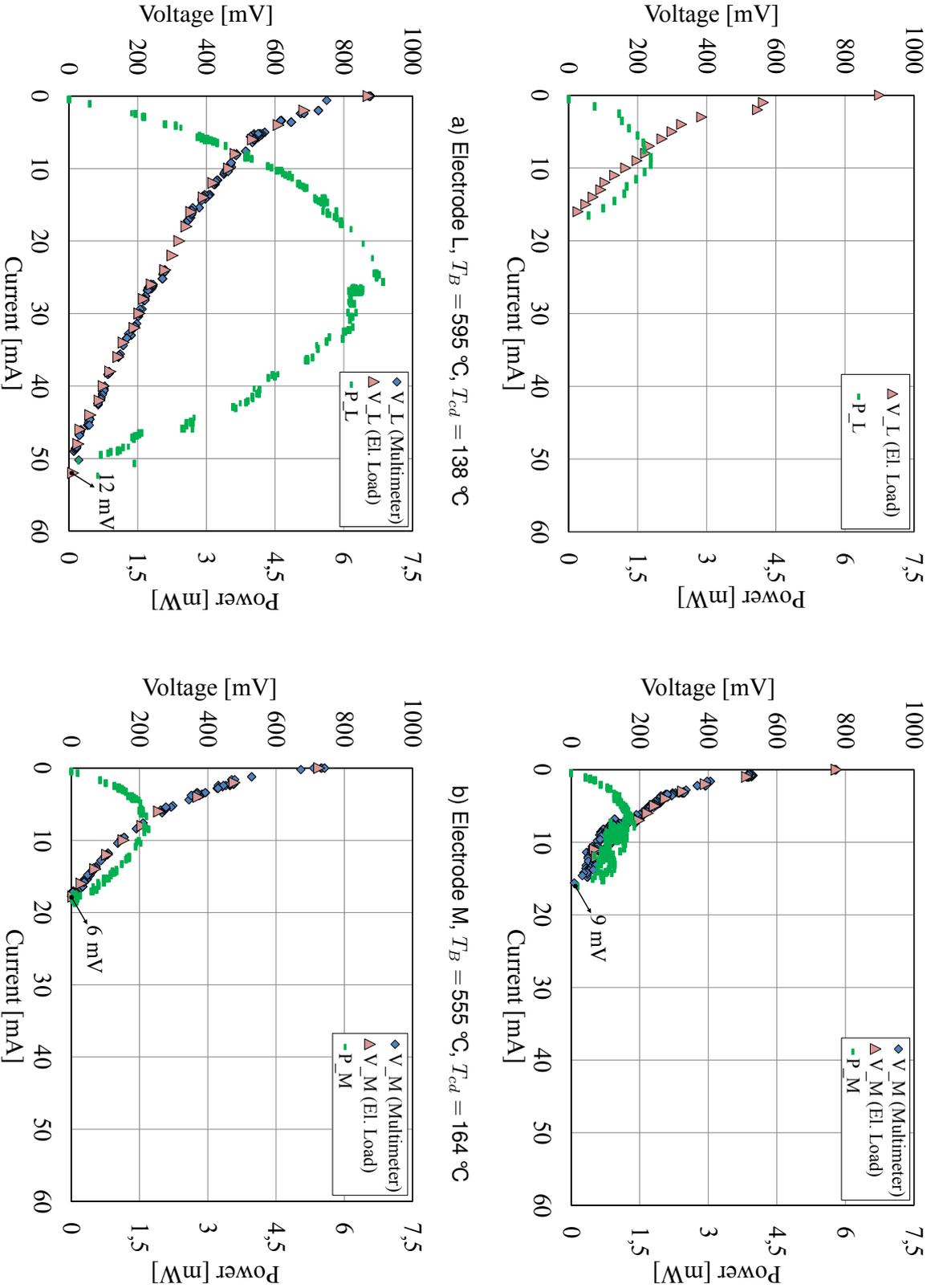
Figure 7.8: Measured characteristic curve of the AMTEC test cell and cell performance in terms of the cell current for electrodes L, M and K at temperatures $T_B = 600 - 700\ °C$ and $T_{cd} = 150 - 250\ °C$.

also due to an insufficient electric contact of the current collector to BASE surface.

Power reduction of the cell.   After each measurement campaign a power reduction of the cell was observed. Figure 7.9 illustrates the maximum measured cell power at cathodes L and M as function of the BASE temperature T_B. Circles represent the measurements at electrode L while triangles at electrode M. Different colors have been used to distinguish the measurement campaigns (MC), which have been perform at different days. It is expected that the cell power increases with the temperature, as observed at electrode L. However, electrode M keeps a rather constant cell power at temperatures > 500 °C. This may have been originated by an inefficient electric contact at the cathode M given by the CC assembly and/or by the degradation of the BASE and of the electrode (nickel foam) as reported in the literature (see chapter 3). The different CC structures of L (low) and M (middle) positions (see figure 5.4) show different behaviors. Based on the significantly higher cell power obtained with cathode L (> 70 % higher than with cathode M at 700 °C), it can be concluded that the CC structure with the nickel knitted mesh performs considerably better than the stainless steel perforated plate and is, therefore, recommended for further tests due to its increased surface adaptability. Between measurement campaigns MC2 and MC3 a power reduction at cathode L of ~ 65 % is also observed in figure 7.9 at 600 °C, which was "recovered" at 650 °C. This behavior of the CC L should be investigated after disassembling of the test cell.
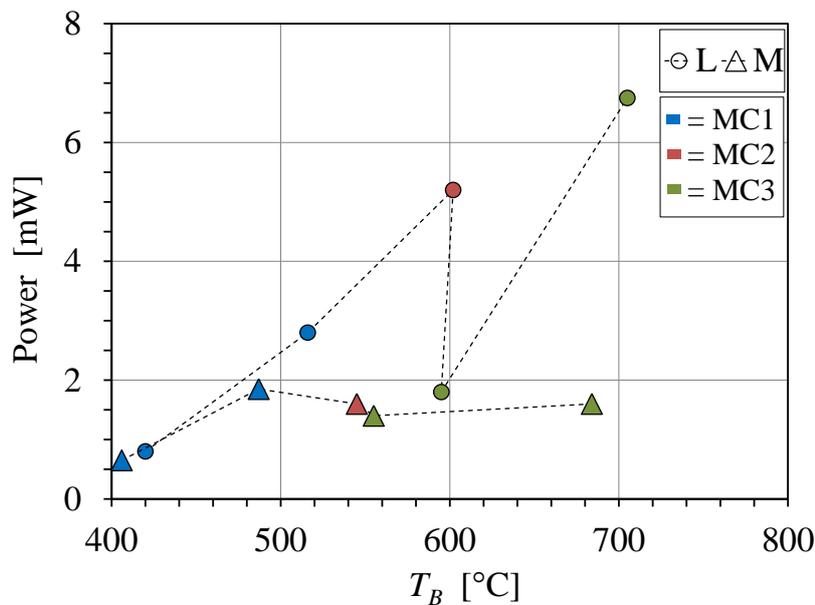
Figure 7.9: Maximum measured cell power at electrodes L and M as function of the BASE temperature T_B contrasted for three different measurement campaigns (MC).

Repeatability of the measurements. The cylindrical active contact area depends strongly on the design and assembly of the CC (pressing force applied), on the geometric tolerances and on the thermal expansion of the materials between the measurement campaigns (thermal cycling). The larger thermal expansion coefficient of the CC compared to that of the BASE reduces the electric contact with increasing temperature and thus the cell performance. It is considered as one of the main responsible for the non repeatability of the measurements.

Data reported in figures 7.6 and 7.7 have been recorded in two- different measurement campaigns; the facility was cooled down to 200 °C between campaigns. A comparison between both measurement campaigns given in figure 7.9 suggests that the AMTEC test cell does not provide a good repeatability. The repeatability is also affected by a limited wetting of the BASE inner surface at lower temperatures.

Scattering of the measurements. In figure 7.6 electrode L (graphic c)) has a rather scattered and slightly unstable data in comparison to electrode M (graphic d)). The measured fluctuations of cell power, voltage and current are represented in figure 7.10 in terms of time and are compared to the fluctuations of the measured BASE temperature T_B. The performance fluctuations in the cell may have been caused by:

– Temperature fluctuations ($< 4\%$).

– Electrical resistance fluctuations of the electronic load. Since the electronic load is designed to work at high electric current values (up to 100 A), during the measurement campaign it worked at the lowest current limit (in mA). This leads to an increased electrical resistance fluctuations.

– Not fully developed wetting of the ceramic due to an insufficient development time (< 4 hours).

– Poor and/or unstable electric contact of the current collector.

The low precision of the recorded power at electrode L in figure 7.7 graphic a) is also influenced by the fluctuations of the measured signals (I-V) and of the temperature at the BASE. Figure 7.11 illustrates the temporal evolution of the fluctuations of the measured cell power P_L and average BASE temperature T_{B-L} at electrode L.

As it can be observed the fluctuations follow a similar behavior for the temperature and the cell power. This confirms the relevant effect of the temperature on the cell power as explained in chapters 2 and 4. The power regulator of the BASE-heater is a power switching device that switches on/of the at power line zero-cross in 3 AC cycles. If 50 % of the total power output is desired, then during the first 3 AC cycles the heat power is equal to the maximum power, and during the next 3 AC cylces the heat power

a) Electrode L, characteristic curve

b) Electrode L, power

c) Electrode L, voltage

d) Electrode L, current
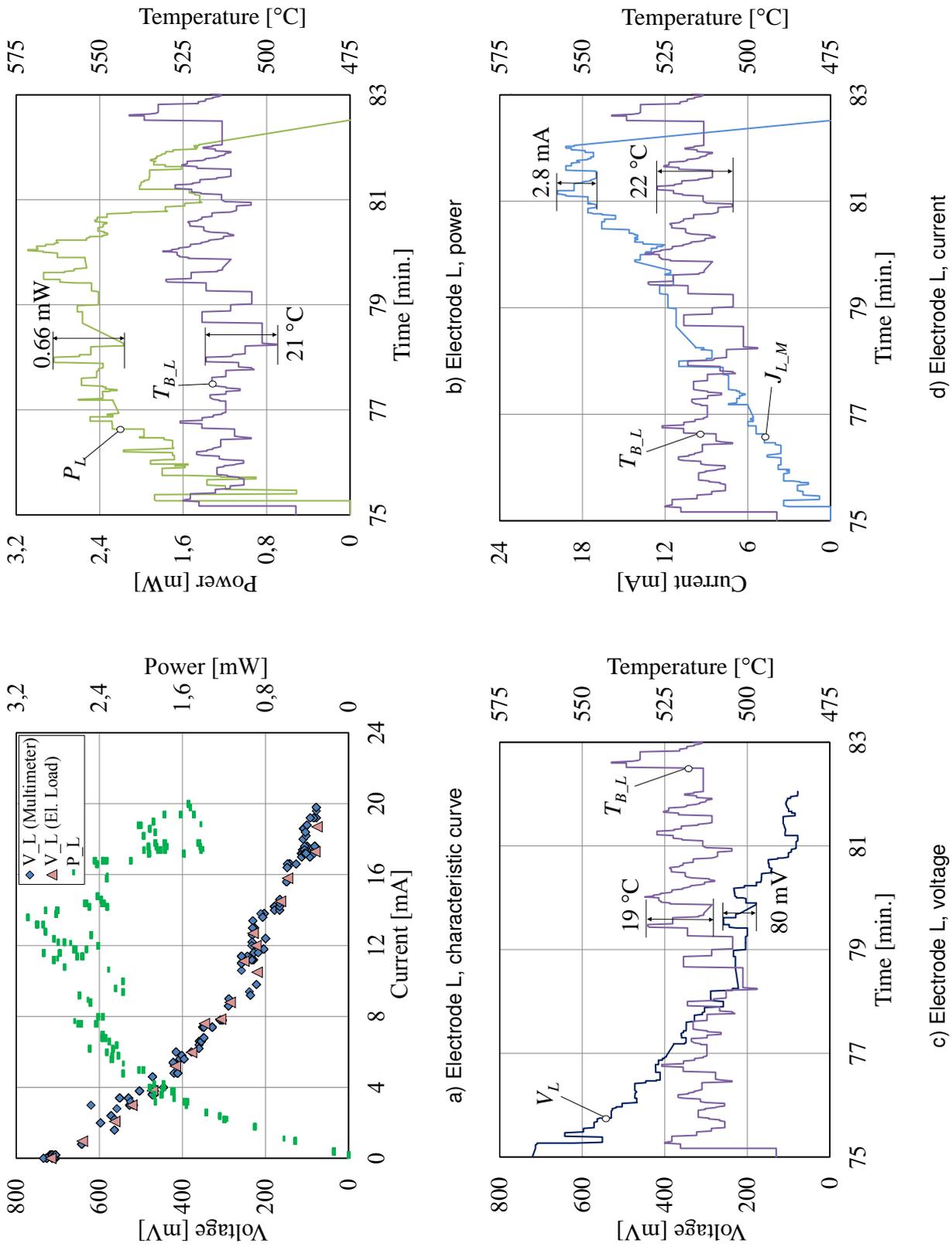
Figure 7.10: Temporal evolution of the measured BASE temperature T_B, cell power (b), voltage (c) and current (d) during the measurement of the characteristic curve (I-V) at electrode L (a). The average temperatures are $T_B = 514\ °C$, $T_B = 514\ °C$, $T_{cd} = 150\ °C$.

is zero. As a result, the measured BASE temperature through the liquid sodium imitates the effect of the heater power regulation, which is reflected in temperature fluctuations.
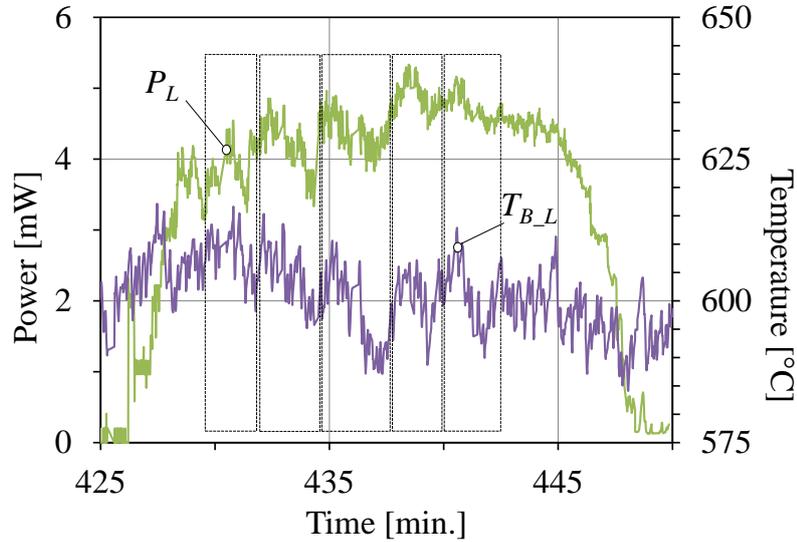
Figure 7.11: Temporal evolution of the measured cell power and BASE temperature fluctuations at electrode L. The average temperatures of the condenser is $T_{cd} = 144\,°C$.

Figure 7.12 shows the temporal evolution of the measured BASE temperature fluctuations at electrode L. T_{B-L} (Heater on) measured with the BASE-heater switched on reflects large fluctuations coming from the power regulation device, while the T_{B-L} (Heater off) shows much smaller fluctuations. This confirms that the observed fluctuations on the measured temperature are mainly originated through the power regulator of the BASE-heater. For a finer temperature control, the power regulator of the heater has to be optimized.

To obtain the internal resistance of the cell the equation (4.26) is used, which fits the measurement data to obtain the 3 unknown: J_{sat}^{ex}, K_j and R_{cell}. This model assumes the presence of a sputtered cathode layer and therefore cannot be applied in this work. The resistance of the cell includes i) the resistance of the current collector and the current feedthrough, which was measured and presented in chapter 6.3, ii) the resistance of the BASE, which can be obtained from figure 2.18 and iii) the contact resistance between the ceramic and anode/cathode can only be measured during operation and depends strongly on the temperature of the cell due to the different thermal expansion coefficients.

ATEFA was operated uninterrupted during 2 weeks without failure and temperatures up to 700 °C were reached, including several temperature cycles from 200 °C (over night) to working temperatures. It was demonstrated that the designed AMTEC cell is able to generate electric power even without electrode sputtered layer and that the characteristic curve of the cell agrees with the literature. The changes in cell power
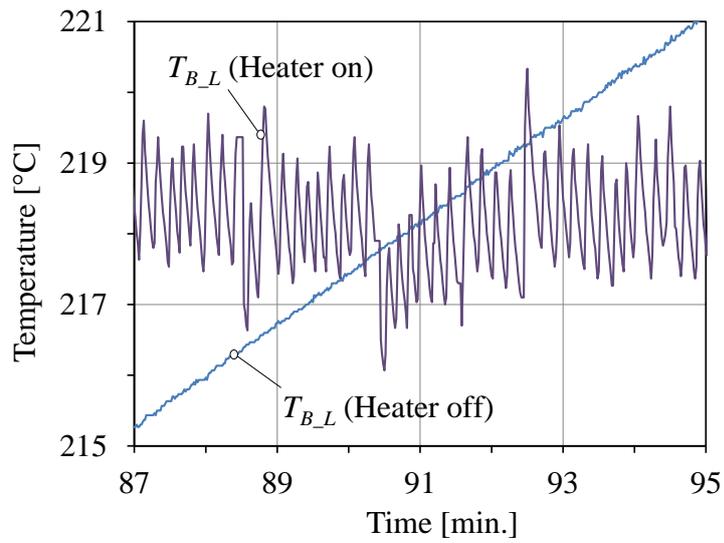
Figure 7.12: Temporal evolution of the measured BASE temperature fluctuations at electrode L with/without BASE-heater.

and OCV with temperature, pressure and time are also in a good agreement with the literature. If the recommended improvements and modifications are realized, the cell should fulfill the requirements for the further development towards AMTEC 2.0.

8 Summary and outlook

ATEFA and the AMTEC test cell, developed, constructed and set into operation as part of this work, have been operated uninterrupted during 2 weeks and short term tests have been successfully performed in a temperature range of $400 - 700\,°C$ and up to $0.05\,MPa$. A damage in the main heater of the cell lead to the termination of the experimental campaign. To exclude the influence of the magnetron sputtering process on the BASE properties (e.g. increased brittleness), the AMTEC cell module has been tested without sputtered cathode layer. ATEFA and AMTEC test cell designs have been experimentally validated and the cell behavior has been analyzed according to the AMTEC system: temperature, pressure, electrode and current collector.

Considering a short operation time, the main cell losses in AMTEC are the polarization losses, which take place in the BASE/cathode/current collector system and depend strongly on the morphology of the cathode layer and of the current collector; and the heat radiation losses for a coaxial configuration of the cell, which can be reduced by installing a remote condenser. The optimum parameters of an electrode layer (porosity, thickness and grain size) depend on the material of the layer and can only be experimentally determined at specific operating conditions. Through a detailed literature review it was observed that despite the extensive literature available regarding the performance of AMTEC cells, most results were analyzed based on temperature and electrode properties and neglected the effect of the electrode-current collector system. An optimized current collector structure can increase up to 50 - 100 % the cell performance and therefore its effect must be considered when comparing different cell results.

Based on this issue, a preliminary study of the current collector (CC) structure was performed [116] focused mainly on analyzing the impact of the CC structure on the active surface of the electrode. A large stiffness of the CC structure has shown (e.g. Mo) to be a disadvantage, since the stiffness given by the BASE combined with the stiffness of the CC results in a reduced electrical contact. In this sense, results indicate that knitted mesh structures seem very promising for AMTEC cells, as they can compensate the stiffness of a material (e.g. Mo, Ni) by the malleability of the knitted mesh and thus reach an enhanced electric contact.

The challenging operating conditions of AMTEC devices characterized by very high temperatures (up to $800\,°C$) and corrosive medium (sodium) led to various technological developments that have been addressed previous to the cell assembly: the development of a porous, electrically conductive, high-temperature resistant and stable coating layer on the BASE surface utilizing the magnetron sputtering technique and the development of a stable high-temperature resistant ceramic to metal brazing.

The developed BASE-Nb brazing consisted of a commercial Ni base soldering paste that was mixed with 16 wt% Nb and 4 wt% Ti powders. The gap size of the brazing was $\sim 500\,\mu$m appropriate for the calculated relative low shear stress at the joint. A He leak tightness of $< 10^{-5}$ mbarl/s was achieved at the best ceramic-Nb joint. The developed joint was succesfully tested in ATEFA uninterrupted during two weeks and up to 700 °C without failure.

Mo, TiN and TiC AMTEC electrodes have been considered for the coating of the BASE elements. A d.c. magnetron sputtering process was used to deposit the electrode compounds on the BASE substrate. A microstructural and elemental analysis of several sputtered samples were performed using respectively SEM and EDX methods to examine the morphology of the electrodes [176]. Mo and TiC sputtered layers showed a homogeneous grain distribution and the presence of porous channels between grains; the latter is the basis for a good transport of sodium vapor during the cell operation. A partial detachment of the TiC coating was also observed. An analysis of the detachment process suggests to be caused by the vaporization of gases (e.g. water or CO_2) from the ceramic surface, driven by high local temperatures (> 200 °C) originated during the sputtering process. A considerable amount of Na was also found at the surface of the coating revealing a diffusion from the ceramic. This effect shows consistency with the literature concerning the hydration of the ceramic. The accumulation of sodium on the TiC surface proves the permeability of the TiC layer, which is essential for a proper function of the AMTEC cell.

During the measurement campaign the changes in cell current, voltage, and power with temperature and pressure have been recorded and are in a good agreement with the literature. The measured OCV varied betweeen $501 - 1037$ mV at $400 - 700$ °C and was compared with the theoretical voltage using the Nernst equation. The agreement between theoretical and measured OCV varied strongly with the wettability of the ceramic (up to $e > 100$ %). Under optimum wetting conditions, deviations of the OCV were as good as $e < 3.5$ %. It was observed that the exposure time to liquid sodium required in the tests for a good wetting of the ceramic can be accelerated by i) increasing the sodium temperature over 300 °C and ii) closing the electric circuit of the cell (electrowetting).

The small current production of the cell (up to 52 mA at 700 °C) agrees with the small effective contact surface of the CC to BASE. The main responsible for the observed non repeatability of the measurements is attributed to the CC. On one hand, the CC structure has a great influence on the cell power: the knitted mesh performed > 70 % better than the perforated plate at 700 °C; on the other hand, an insufficient pressing force of the CC corset towards the BASE outer surface can reduce significantly the cell power: > 75 % power reduction is reported between cathodes M and K at ~ 530 °C.

It was identified that the pressure of argon at the cathode side has a considerable influence on the OCV and should, hence, not be neglected. At an Ar-pressure of $\sim$ $1 \cdot 10^5$ Pa the measured OCV deviated as much as 1 V from the Nernst voltage. Small pressure values in the order of several hundred pascals minimized this error to $< 5\,\%$. The maximum measured power of the AMTEC cell without electrode sputtered layer rises to ~ 7 mW at 700 °C.

This doctoral thesis serves as a starting point in the development of optimized AMTEC cells and promotes new high-temperature materials and fabrication methods to be applied for an optimized AMTEC 2.0 stacking design with a planar BASE. A cylindrical form of the BASE, used historically in AMTEC cells, becomes a drawback when obtaining a good and homogeneous electric contact at the cathode-CC side. A planar BASE would improve considerably the electric contact, reducing thereby significantly the cell losses. Moreover it should help to reduce the costs, volume and weight of the cell, by reducing considerably the sodium amount-electrode surface ratio and BASE manufacturing costs, and increasing the power/volume and power/weight ratios.

To corroborate the reported observations regarding the porous sputtered cathode, this work must be followed by a detailed study of the magnetron sputtering process and further analysis of the chemical stability of the ceramic electrolyte, which seems to influence considerably the quality of the electrode deposition (e.g. the adhesion to the BASE surface). It is, therefore, recommended to further optimize the handling process of the BASE in order to achieve an increased chemical stability of the BASE and, thus, of the sputtering process too.

Moreover, further experimental tests should be performed under AMTEC conditions to proceed performance optimizations on the electrode morphology as well as current collector structure and materials. During the experiments, the entire system: BASE-electrode-current collector should be considered.

Regarding long term experimental research on AMTEC cells, the degradation effect is on focus, which takes place mainly in the BASE and the cathode layer. Such tests will be performed in the SOLTEC-3 facility to be set into operation in 2018.

References

[1] V. Heinzel, F. Huber, W. Peppler, and H. Will. Technological tests with respect to the use of beta alumina in alkali-metal-thermo-electric converters (AMTEC). *Key Engineering Materials*, 59 & 60: 381 – 394, 1991.

[2] V. Heinzel, F. Huber, W. Peppler, and H. Will. Development of an AMTEC, a converter of thermal to electrical energy. *Materials Science Forum*, 76: 261 – 264, 1991.

[3] W. Hering, R. Stieglitz, and T. Wetzel. Application of liquid metals for solar energy systems. *EPJ Web of Conferences*, 33 (03003), 2012.

[4] M. Strotjohann. Quantifizierung eines detaillierten Spiegeldesigns für KASOLA. Bachelor's thesis, Karlsruhe Insitute of Technology (KIT), 2015.

[5] N. Diez de los Rios Ramos. CFD-Untersuchungen der Kühlung eines Solar-Absorberrohres mit ungleichmäßiger Wärmeflussverteilung in Umfangsrichtung. Master's thesis, Karlsruhe Institute of Technology (KIT), 2012.

[6] W. Hering, A. Jianu, and M. Lux. KASOLA - Anlagenbeschreibung und Sicherheitsvorkehrungen. Technical report, No. INR 01/13 - NUKLEAR 3454, Karlsruhe Insitute of Technology (KIT), 2013.

[7] N. Diez de los Rios Ramos, A. Onea, S. Scherrer, A. Weisenburger, and W. Hering. Direct energy conversion of heat to elelectricity using AMTEC. *Proceedings of the 5th International Youth Conference on Energy (IYCE)*, ISBN 978-1-4673-7171-1, 2015.

[8] J. P. Reason. *A comparative study of nuclear technology and direct energy conversion methods for space power systems*. PhD thesis, Naval Postgraduate School Monterey, 1997.

[9] H. Yuan, D. C. Riley, Z. X. Shen, P. Pianetta, N. A. Melosh, and R. T. Howe. Back-gated graphene anode for more efficient thermionic energy converters. *Nano energy*, 32: 67 – 72, 2017.

[10] H. Takao, K. Kobayashi, and T. Ito. Ideal efficiency of photon-enhanced thermionic emission energy converter driven by blackbody radiation. *Japanese Journal of Applied Physics*, 55 (018003): 1 – 3, 2016.

[11] J. W. Schwede, I. Bargatin, D. C. Riley, B. E. Hardin, S. J. Rosenthal, Y. Sun, F. Schmitt, P. Pianetta, R. T. Howe, Z. X. Shen, and N. A. Melosh. Photon-enhanced thermionic emission for solar concentrator systems. *Nature Materials*, 9: 762 – 767, 2010.

[12] S. N. Khatami and Z. Aksamija. Lattice thermal conductivity of the binary and ternary Group-IV Alloy Si-Sn, Ge-Sn, and Si-Ge-Sn. *Physical Review Applied*, 6 (014015): 1 – 11, 2016.

[13] S. Twaha, J. Zhu, Y. Yan, and B. Li. A comprehensive review of thermoelectric technology: Materials, applications, model and performance improvement. *Renewable and Susutainable Energy Reviews*, 65: 698 – 726, 2016.

[14] J. Tervo, A. Manninen, R. Ilola, and H. Hänninen. State-of-the-art of thermo-electric materials processing, properties and applications. *VTT Working Papers*, 2009.

[15] M. Boaro and A. S. Aricò, editors. *Advances in medium and high temperature Solid Oxide Fuel Cell technology*. CISM International Centre for Mechanical Sciences, Curses and Lectures. Springer, ISBN 978-3-319-46146-5, 2017.

[16] S. Sharma, K. K. Jain, and A. Sharma. Solar cells: in research and applications - a review. *Materials Sciences and Applications*, 6: 1145 – 1155, 2015.

[17] R. W Miles, K. M. Hynes, and I. Forbes. Photovoltaic solar cells: An overview of state-of-the-art cell development and environmental issues. *Progress in Crystal Growth and Characterization of Materials*, 51 (1 - 3): 1 – 42, 2005.

[18] R. Ajith Krishnan and B. S. Jinshah. Magnetohydrodynamic power generation. *International Journal of Scientific and Research Publications*, 3 (6), ISSN 2250-3153, 2013.

[19] K. Tanaka, T. Masuda, A. Negishi, T. Honda, Y. Hori, and T. Homma. Performance characteristics and thermal design of alkali metal thermoelectric conversion system. *Proceedings of the 25th Intersociety (IECEC)*, 2: 402 – 406, 1990.

[20] K. F. Freudenstein. Effects of sodium fires on structures and materials. Practical experience with sodium leakage accidents. Technical report, No. IWGFR–67, International Atomic Energy Agency (IAEA), 1989.

[21] K. Tanaka. Concept design of solar thermal receiver using alkali metal thermal to electric converter (AMTEC). *Current Applied Physics*, 10: 254 – 256, 2010.

[22] S. Y. Wu, L. Xiao, Y. Cao, and Y. R. Li. A parabolic dish / AMTEC solar thermal power system and its performance evaluation. *Applied Energy*, 87: 452 – 462, 2010.

[23] J. H. Boo, S. M. Kim, and Y. H. Kang. Experimental study on a sodium loop-type heat pipe for thermal transport from a high-temperature solar receiver. *Energy Procedia*, 69: 608 – 617, 2015.

[24] I. Rubinstein, editor. *Physical electrochemistry - principles, methods and applications*. Dekker, ISBN 0-8247-9452-4, 1995.

[25] Chr. M. A. Brett and A. M. O. Brett. *Electrochemistry: principles, methods and applications*. Oxford University Press, ISBN 0-19-855389-7, 1998.

[26] P. H. Rieger. *Electrochemistry*. Chapman & Hall, ISBN 978-94-010-4298-7, 1994.

[27] R. D. Armstrong and B. R. Horrocks. The double layer structure at the metal-solid electrolyte interface. *Solid State Ionics*, 94: 181 – 187, 1997.

[28] V. N. Chebotin, I. D. Remez, L. M. Solovieva, and S. V. Karpachev. Electrical double layer in solid electrolytes - Theory: oxide electrolytes. *Electrochimica Acta*, 29 (10): 1381 – 1388, 1984.

[29] M. Landstorfer, C. Guhlke, and W. Dreyer. Theory and structure of the metal-electrolyte interface incorporating adsorption and solvation effects. *Electrochimica Acta*, 201: 187 – 219, 2016.

[30] J. Garche, editor. *Encyclopedia of electrochemical power sources*. Elsevier, ISBN 978-0-444-52745-5, 2009.

[31] Electropaedia. Direct conversion of heat energy to electrical energy (2). Alkali metal thermal electric converter (AMTEC), accessed the 23.02.2018. http://www.mpoweruk.com/amtec.htm.

[32] T. Cole. Thermoelectric energy conversion with solid electrolytes. *Science*, 221 (4614): 915 – 920, 1983.

[33] J. M. Tournier, M. S. El-Genk, M. Schuller, and P. Hausgen. An analytical model for liquid-anode and vapor-anode AMTEC converters. *AIP Conference Proceedings*, 387 (3): 1543 – 1552, 1997.

[34] E. H. Kennard. *Kinetic theory of gases*. McGraw-Hill Book Company, Inc., PPN 01702465X, 1938.

[35] M. L. Underwood, R. M. Williams, M. A. Ryan, B. Jeffries-Nakamura, and D. O'Connor. An AMTEC vapor-vapor, series connected cell. *AIP Conference Proceedings*, 246: 1331– 1337, 1992.

[36] Scigiene Corporation. Infrared thermometer emissivity tables, accessed the 2015.11.13. http://www.scigiene.com/Infrared-Thermometer-Emissivity-tables.

[37] P. G Barnett, P. J. Gentry, J. D. Jackson, and D. K. W. Tong. Emissivity measurements of liquid sodium and some sodium contaminated steel surfaces. Technical report, No. IWGFR–57, International Atomic Energy Agency (IAEA), 1985.

[38] ATI Nb1Zr Alloy (Type 3 & 4). Technical data sheet, Allegheny Technologies Incorporated, 2012.

[39] J. F. Ivanenok III, R. K. Sievers, and W. W. Schultz. Modeling of remote condensing AMTEC cells. *AIP Conference Proceedings*, 301 (1): 1501 – 1506, 1994.

[40] A. Kato, H. Nakata, and K. Tsuchida. Characteristics of ceramic electrode for AMTEC, II. Structure of electrode and power density. *Proceedings of the 28th Intersociety (IECEC)*, 1: 1.819 – 1.822, 1993.

[41] Ionotec. Properties of Ionotec beta"-aluminas, accessed the 21.02.2018. http://www.ionotec.com/conductive-ceramics.html.

[42] J. H. Kennedy. *Solid electrolytes*. Springer-Verlag, ISBN 978-3-662-31264-3, 1977.

[43] T. Takahashi, editor. *High conductivity solid ionic conductors. Recent trends and applications*. World Scientific Publishing Co., ISBN 978-9971507503, 1989.

[44] J. M. Newsam and B. C. Tofield. Non-stoichiometry in beta aluminas. *Solid State Ionics*, 5: 59 – 64, 1981.

[45] D. P. Birnie. On the structural integrity of the spinel block in the ß"-alumina structure. *Acta Crystallographica*, 68: 118 – 122, 2012.

[46] Y. Sheng, P. Sarkar, and P. S. Nicholson. The mechanical and electrical properties of ZrO_2-Naß"-Al_2O_3 composites. *Journal of Materials Science*, 23: 958 – 967, 1988.

[47] H. Togawa, K. Tsuchida, and A. Kato. Interaction between ß"-alumina and liquid sodium at 700 °C. *Journal of Materials Science Letters*, 10: 96 – 100, 1990.

[48] X. Lu, J. P. Lemmon, V. Sprenkle, and Z. Yang. Sodium-beta alumina batteries: Status and challenges. *Journal of the Minerals, Metals and Materials Society (JOM)*, 62 (9): 31 – 36, 2010.

[49] A. V. Virkar, G. R. Miller, and R. S. Gordon. Resistivity-microstructure relations in lithia-stabilized polycrystalline ß"-alumina. *Journal of American Ceramic Society*, 61: 250 – 252, 1978.

[50] V. Heinzel, H. Will, F. Huber, H. Peppler, A. van Zyl, and W. F. Chu. Besprechung über ß"-aluminat am 26.11.1990. Technical report, No. IRE4-1077-90, Kernforschungszentrum Karlsruhe, 1990.

[51] S. J. Visco, M. Liu, F. Lin, P. Kimes, and L. C. De Jonghe. Properties and morphology of doped polycristalline Na-ß"-alumina electrolytes. *Solid State Ionics*, 62: 185 – 191, 1993.

[52] J. Wang, X. P. Jiang, X. L. Wei, H. Yang, and X. D. Shen. Synthesis of Na-ß"-Al_2O_3 electrolytes by microwave sintering precursors derived from the sol-gel method. *Journal of Alloys and Compounds*, 497: 295 – 299, 2010.

[53] A. V. Virkar, J. F. Jue, and K. Z. Fung. Patent, No. 6117807. Alkali-metal-ß- and ß"-alumina and gallate polycrystalline ceramics and fabrication by a vapor phase method, 2000.

[54] M. Steinbrück, V. Heinzel, F. Huber, G. Ochs, H. Peppler, and H. Will. Amtec ionenleitfähigkeit von kommerziellen na-ß"-al_2o_3 festelektrolyten. Technical report, No. IRS4-1170-93, Kernforschungszentrum Karlsruhe, 1993.

[55] R. O. Ansell. Review the chemical and electrochemical stability of beta-alumina. *Journal of materials science*, 21: 365 – 379, 1986.

[56] F. G. Will. Effect of water on beta alumina conductivity. *Journal of Electrochemical Society*, 123: 834 – 836, 1976.

[57] R. K. Sievers. Patent, No. 5,089,054. Flat plate alkali metal thermoelectric converter module, 1992.

[58] EaglePicher and Pacific Northwest National Laboratory. Planar Na-beta batteries development for renewable integration and grid applications, accessed the 21.02.2018. http://www.sandia.gov/ess/docs/pr_conferences/2011/3-SPRENKLE_2011_OE_Na_Battery_Review_final.pdf.

[59] A. Onea, N. Diez de los Rios Ramos, W. Hering, J. L. Palacios, and R. Stieglitz. AMTEC clusters for power generation in a concentrated solar power plant. *Magnetohydrodynamics*, 51 (3): 249 – 261, 2015.

[60] P. Rubiolo. Novel, integrated reactor/ power conversion system (LMR-AMTEC). Technical report, No. STD-ES-03-04, Westinghouse Electric Company LLC, 2003.

[61] K. Wasa, editor. *Handbook of sputter deposition technology: fundamentals and applications for functional thin films, nanomaterials and MEMS*. Elsevier, ISBN 978-128-370-478-6, 2012.

[62] I. L. Shabalin. *Ultra-high temperature materials I: carbon (graphene/graphite) and refractory metals*. Springer, ISBN 978-940-077-587-9, 2014.

[63] R. Syre. Niobium, molybdenum, tantalum and tungsten. Technical report, AGAR-Dograph 50, North Atlantic Treaty Organization. Advisory Group for Aeronautical Research and Development, 1961.

[64] G. S. Upadhyaya. *Metal science: past, present and future*. Materials science foundation. Trans Tech Publ., ISBN 978-3-03785-997-1, 2013.

[65] D. L. Perry, editor. *Handbook of inorganic compounds*. CRC Press, ISBN 978-1439814611, 1995.

[66] J. E. Sundgren, B. O. Johansson, S. E. Karlsson, and H. T. G. Hentzell. Mechanisms of reactive sputtering of titanium nitride and titanium carbide II : Morphology and structure. *Thin Solid Films*, 105: 367 – 384, 1983.

[67] X. Ch. Li, J. Stampfl, and F. B. Prinz. Mechanical and thermal expansion behavior of laser deposited metal matrix composites of Invar and TiC. *Materials Science and Engineering A*, 282 (1 - 2): 86 – 90, 2000.

[68] Ch. J. Engberg and E. H. Zehms. Thermal expansion of Al_2O_3, BeO, MgO, B_4C, SiC, and TiC above 1000 °C. *Journal of the American Ceramic Society*, 42 : 300 – 305, 1959.

[69] A. D. McLeod, J. S. Haggerty, and D. R. Sadoway. Electrical resistivities of monocrystalline and polycrystalline TiB_2. *Journal of the American Ceramic Society*, 67 (11): 705 – 708, 1984.

[70] R. G. Munro. Material properties of titanium diboride. *Journal of Research of the National Institute of Standards and Technology*, 105 (5): 709 – 720, 2000.

[71] The PGM Database. Platinum properties, acessed the 27.02.2018. http://www.pgmdatabase.com/jmpgm/.

[72] Midwest Tungsten Service. Tungsten properties, acessed the 27.02.2018. https://www.tungsten.com/materials/tungsten/.

[73] A. Nigro, G. Nobile, M. G. Rubino, and R. Vaglio. Electrical resistivity of polycrystalline niobium nitride films. *Physical Review B*, 37 (8): 3970 – 3972, 1988.

[74] Werkstoffblatt Nr. 1101, Nickel 99.2 - alloy 200 and LC-Nickel 99.2 - alloy 201. Technical data sheet, ThyssenKrupp VDM, 1990 (Revision 2003).

[75] M. D. Williams, L. T. Jackson, D. O. Kippenhan, K. N. Leung, M. K. West, and C. K. Crawford. Lanthanum hexaboride (LaB_6) resisitvity measurement. *Applied Physics Letters*, 50: 1844 – 1845, 1987.

[76] Sindlhauser Materials. LaB_6 ceramics and cathodes, Acessed the 27.02.2018 http://www.sindlhauser.de/en/LaB6_ceramics_and_cathodes.html.

[77] M. D. Williams, K. N. Leung, and P. Purgalis. Lanthanum hexaboride (LaB_6). Coefficient of thermal expansion. *Applied Physics Letters*, LBL-27907, 1989.

[78] Stainless Steel 316/316L. Technical data sheet, AK Steel Corporation, 2007.

[79] C. Y. Ho and T. K. Chu. Electrical resistivity and thermal conductivity of nine selected AISI stainless steels. Technical report, CINDAS No. 45, American iron and steel institute, 1977.

[80] Stainless Steel 1.4571 - 316Ti. Technical data sheet, Aalco Metals Ltd., 2017.

[81] N. Diez de los Rios Ramos, W. Hering, A. Weisenburger, M. Stüber, A. Onea, M. Lux, S. Ulrich, and R. Stieglitz. Design and construction of the ATEFA facility for experimental investigations of AMTEC test modules. *IOP Conference Series: Material Science and Engineering*, 228 (012014), 2017.

[82] K. Tsuchida, T. Nagata, H. Nakata, and A. Kato. LaB_6 and TiB_2 electrodes for the alkali metal thermoelectric converter. *Journal of Material Science Letters*, 33: 755 – 762, 1998.

[83] R. M. Williams, B. Jeffries-Nakamura, M. L. Underwood, C. P. Bankston, and J. T. Kummer. Kinetics and transport at AMTEC electrodes II. Temperature dependence of the interfacial impedance of Na/ porous Mo/ Na-beta" alumina. *Journal of Electrochemical Society*, 137 (6): 1716 – 1723, 1990.

[84] S. Y. Wu, L. Xiao, and Y. D. Cao. A review on advances in alkali metal thermal to electric converters (AMTECs). *International Journal of Energy Research*, 33: 868 – 892, 2009.

[85] R. Knödler, K. Reiss, and B. Westhoven. Characterization of porous alkali-metal thermoelectric converter electrodes operating at 800 ℃. *Journal of Material Science Letters*, 11: 343 – 345, 1992.

[86] R. Knödler, H. P. Bossmann, A. Kranzmann, and F. Harbach. Performance of single cells of an alkali metal thermoelectric converter. *Journal of Electrochemical Society*, 139: 3029 – 3034, 1992.

[87] M. L. Underwood, R. M. Williams, B. Jeffries-Nakamura, C. P. Bankston, and T. Cole. Progress in AMTEC electrode experiments and modeling. *Proceedings of the 23rd Intersociety (IECEC)*, 1: 227 – 33, 1988.

[88] T. Hunt. Test results on a kilowatt-scale sodium heat engine. *Proceedings of the 25th Intersociety (IECEC)*, 1: 420 – 425, 1990.

[89] Q. Fang and R. Knödler. Porous TiB$_2$ electrodes for the alkali metal thermoelectric converter. *Journal of Material Science*, 27: 6725 – 6729, 1992.

[90] R. W. Fletcher and J. W. Schwank. Recent developments in mixed ionic and electronic conducting electrodes for the alkali metal thermal electric converter (AMTEC). *AIP Conference Proceedings*, 654 (1): 722 – 729, 2003.

[91] B. L. Wheeler, R. M. Williams, B. Jeffries-Nakamura, J. L. Lamb, M. E. Loveland, C. P. Bankston, and T. Cole. Performance and impedance studies of thin, porous molybdenum and tungsten electrodes for the alkali metal thermoelectric converter. *Journal of Applied Electrochemistry*, 18: 410 – 416, 1988.

[92] M. A. Ryan, B. Jeffries-Nakamura, R. M. Williams, M. L. Underwood, D. O'Connor, and S. Kikkert. Directly deposited current collecting grids for AMTEC electrodes. *Proceedings of the 26th Intersociety (IECEC)*, 5: 463 – 468, 1991.

[93] R. M. Williams, B. Jeffries-Nakamura, M. L. Underwood, B. L. Wheeler, M. E. Loveland, S. J. Kikkert, J. L. Lamb, T. Cole, J. T. Kummer, and C. P. Bankston. High power density performance of WPt and WRh electrodes in the alkali metal thermoelectric converter. *Journal of Electrical Society*, 136: 893 – 894, 1989.

[94] R. M. Williams, M. A. Ryan, B. Jeffries-Nakamura, M. L. Underwood, D. O'Connor, and S. Kikkert. AMTEC cell testing, optimization of Rhodium/ Tungsten electrodes, and tests of other components. In *Space nuclear power systems, Proceedings of the 8th Symposium*, pages 464 – 471, 1991.

[95] R. M. Williams, G. Nagasubramanian, S. K. Khanna, C. P. Bankston, A. P. Thakoor, and T. Cole. The role of oxygen in porous molybdenum electrodes for the alkali metal thermoelectric converter. *Journal of the Electrochemical Society*, 133 (8): 1587 – 1595, 1986.

[96] A. V. Virkar, L. Viswanathan, and D. R. Biswas. On the deterioration of ß"-alumina ceramics under electrolytic conditions. *Journal of materials science*, 15: 302 – 308, 1980.

[97] L. Viswanathan and A. V. Virkar. Wetting characteristics of sodium on ß"-alumina and on nasicon. *Journal of materials science*, 17: 753 – 759, 1982.

[98] Y Hu, Z. Wen, X. Wu, and Y. Lu. Nickel nanowire network coating to alleviate interfacial polarization for Na-beta battery applications. *Journal of Power Sources*, 240: 789 – 795, 2013.

[99] O. Asakami, K. Tsuchida, and A. Kato. Materials for electrode of alkali metal thermoelectric converter (AMTEC) (II). *Journal of Materials Science Letters*, 9: 892 – 894, 1990.

[100] T. Hashimoto, K. Shibata, K. Tsuchida, and A. Kato. Screen-printed electrode for alkali-metal thermoelectric converter. *Journal of Materials Science Letters*, 11: 745 – 748, 1992.

[101] A. Kato, K. Tsuchida, T. Hashimoto, H. Nakata, and T. Nagata. Characteristics of ceramic electrode for AMTEC. *Proceedings of the 27th Intersociety (IECEC)*, 3 (929006): 3.1 – 3.6, 1992.

[102] M. A. Ryan, R. M. Williams, C. Saipetch, A. Kisor, D. O'Connor, M. Underwood, and B. Jeffries-Nakamura. Developments in AMTEC devices, components and performance. *AIP Conference Proceedings*, 301: 1498 – 1500, 1994.

[103] M. A. Ryan, R. M. Williams, L. Lara, B. G. Fiebig, R. H. Cortez, A. K. Kisor, V. B. Shields, and M. L. Homer. Advances in electrode materials for AMTEC. *AIP Conference Proceedings*, 552: 1088 – 1093, 2001.

[104] S. D. Kim, S. Y. Kim, J. H. H. Joo, and S. K. Woo. Microstructure and electrical conductivity of Mo/TiN composite powder for alkali metal thermal to electric converter electrodes. *Ceramics International*, 40: 3847 – 3853, 2014.

[105] Indium Corporation. Chemical vapor deposition vs. physical vapor deposition. Application note, www.indium.com, 2008.

[106] L. R. Pederson, P. Singh, and X.-D. Zhou. Application of vacuum deposition method to solid oxide fuel cells. *Vacuum*, 80: 1066 – 1083, 2006.

[107] R. Radhakrishnan, A. V. Virkar, S. C. Singhal, G. C. Dunham, and O. A. Marina. Design, fabrication and characterization of a miniaturized series-connected potentiometric oxygen sensor. *Sensors and Actuators B*, 105: 312 – 321, 2005.

[108] J. H. Park and T. S. Sudarshan, editors. *Chemical Vapor Deposition*. The Materials Information Society, ISBN 0-87170-731-4, 2001.

[109] F. Löffler. Functional metal-based coatings on ceramic substrates. *Surface and Coatings Technology*, 132: 222 – 227, 2000.

[110] H. Hofmann and J. Spindler. *Verfahren in der Beschichtungs- und Oberflächentechnik : Grundlagen, Vorbehandlung, Oberflächenreaktionen, Schichtabscheidung, Strukturierung, Prüfung*. Fachbuchverlag Leipzig im Carl-Hanser-Verlag, ISBN 978-3-446-42378-7, 2010.

[111] K. Seshan, editor. *Handbook of thin film deposition - processes and techniques*. Noyes Publ., ISBN 0-8155-1442-5, 2002.

[112] F. Huber. AMTEC Schnelltestzelle, Versuch Nr. AS09. Reduzierte Wandstärke. Technical report, No. IRE4-1115-91, Kernforschungszentrum Karlsruhe, 1991.

[113] F. Huber. AMTEC Schnelltestzelle, Versuch Nr. AS11 und AS12. Änderung des Stromabgriffs. Technical report, No. IRE4-1116-91, Kernforschungszentrum Karlsruhe, 1991.

[114] F. Huber and G. Ochs. AMTEC Schnelltestzelle Versuch Nr. AS17. Technical report, No. IRE4-1119-91, Kernforschungszentrum Karlsruhe, 1991.

[115] F. Huber and G. Ochs. AMTEC-Schnelltestzelle. Versuch Nr. AS21-24. Kleiner Stromabgriff. Technical report, No. IRE4-1130-92, Kernforschungszentrum Karlsruhe, 1992.

[116] L. Biergans. Experimentelle Untersuchung von Stromsammlern einer AMTEC-Zelle unter idealisierten Bedingungen. Bachelor's thesis, Karlsruhe Institute of Technology (KIT), 2016.

[117] M. Kornely, A. Leonide, A. Weber, and E. Ivers-Tiffée. Performance limiting factors in anode-supported cells originating from metallic interconnector design. *Journal of Power Sources*, 196: 7209 – 7216, 2011.

[118] J. K. Fink and L. Leibowitz. Thermodynamic and transport properties of sodium liquid and vapor. Technical report, No. ANL/RE-95/2, Argonne National Laboratory, 1995.

[119] V. Sobolev. Database of thermo-physical properties of liquid metal coolants for GEN-IV. Technical report, No. SCK-CEN BLG 1069, Studiecentrum voor Kernenergie, 2011.

[120] O. J. Foust, editor. *Sodium-NaK engineering handbook*, volume I. Gordon and Breach, ISBN 0-677-03020-4, 1972.

[121] J. M. Tournier and M. S. El-Genk. Performance analysis of Pluto/ Express multitube AMTEC cells. *Energy Conversion and Management*, 40 (2): 139 − 173, 1999.

[122] J. M. Merril, M. J. Schuller, R. Sievers, C. Borkowski, L. Huang, and M. S. El-Genk. Vacuum testing of high effciency multi-base tube AMTEC cells. *Proceedings of the 32nd Intersociety (IECEC)*, 2: 1184 − 1189, 1997.

[123] J. F. Mondt and R. K. Sievers. Alkali metal thermal to electric converter (AMTEC), Technology development for potential deep space scientific missions. *Conference paper. Fith Space Congress - Horizons Unlimited*, ID 20060034650, 1992.

[124] M. D. Bennett. Patent, No. 0048487 A1. Solar AMTEC power system, 2011.

[125] J. T. Kummer, A. Arbor, and N. Weber. Paten, No. 3458356. Thermo-electric generator, 1966.

[126] T. K. Hunt. Solar thermal/ electric conversion using the sodium heat engine. In *Proceedings: Workshop on Solar Applications of Energy Conversion Technology*, SERI/CP–252-2714, 1985.

[127] M. Schuller, B. Fiebig, P. Hudson, and I. Kakwan. Performance measurements of advanced amtec electrodes. *AIP Conference Proceedings*, 504: 1371 − 1376, 2000.

[128] H. Peppler, B. Westhoven, H. Wendt, F. Harbach, R. Knödler, H. P. Boßmann, V. Schüle, and A. Kranzmann. Abhängigkeit der Leistungsdichte von der Dicke der TiN Elektrodenschich. Technical report, No. CRH 42/91, ABB, 1991.

[129] T. Masuda, A. Negishi, K. Tanaka, T. Honda, and T. Fujii. Experimental and design study on alkali metal thermoelectric converter for aerospace power. *Proceedings of the European Space Power Conference*, 1: 431 − 435, 1991.

[130] J. M. Tournier, M. S. El-Genk, and L. Huang. Experimental investigations, modeling and analyses of high-temperature devices for space applications. Technical Report TR-1108, Institute for Space and Nuclear Power Studies, University of New Mexico, January 1999.

[131] M. A. K. Lodhi, P. Vijayaraghavan, and A. Daloglu. An overview of advanced space/ terrestrial power generation device: AMTEC. *Journal of Power Sources*, 103: 25 − 33, 2001.

[132] R. D. Armstrong, T. Dickinson, and J. Turner. The breakdown of ß-alumina ceramic electrolyte. *Electrochimica Acta*, 19: 187 − 192, 1974.

[133] R. H. Richman and G. J. Tennenhouse. A model for degradation of ceramic electrolytes in Na-S-batteries. *Journal of the American Ceramic Society*, 58: 63 − 67, 1975.

[134] L. C. De Jonghe, L. Feldman, and A. Beuchele. Slow degradation and electron conduction in sodium/ beta-aluminas. *Journal of Materials Science*, 16: 780 − 786, 1981.

[135] P. S. Nicholson. A supersaturation model for the degradation of sodium ß/ ß"-aluminas. *Journal of Materials Science*, 18: 1597 − 1603, 1983.

[136] M. A. K. Lodhi, P. Vijayaraghavan, and A. Daloglu. Simulation and analysis of time-dependent degradation behavior of AMTEC. *Journal of Power Sources*, 96: 343 − 351, 2001.

[137] M. A. Ryan, A. Kisor, and R. M. Williams. Lifetimes of thin film AMTEC electrodes. In *Energy Conversion Engineering Conference, Proceedings of the 29th Intersociety (IECEC)*, number A94-31838, pages 877 − 881, 1994.

[138] M. A. K. Lodhi and J. B. Briggs. Temperature effect on lifetimes of AMTEC electrodes. *Journal of Power Sources*, 168: 537 − 545, 2007.

[139] T. K. Hunt and J. R. Rasmussen. Fractional watt AMTEC converter. *AIP Conference Proceedings*, 813: 567 − 572, 2006.

[140] M. A. Ryan, V. B. Shields, R. H. Cortez, L. Lara, M. L. Homer, and R. M. Williams. Lifetimes of AMTEC electrodes: molybdenum, rhodium-tungsten, and titanium nitride. In *AIP Conference Proceedings*, volume 504, pages 1377 − 1382, 2000.

[141] R. M. Williams, C. P. Bankston, S. K. Khanna, and T. Cole. Voltammetric studies of porous molybdenum electrodes for the alkali metal thermoelectric converter. *Journal of the Electrochemical Society*, 133: 2253 − 2257, 1986.

[142] H. P. Boßmann, Q. Fang, R. Knödler, and F. Harbach. Test cells for the development of the alkali metal thermoelectric converter. *Proceedings of the 26th Intersociety (IECEC)*, 5: 481 – 486, 1991.

[143] M. A. Ryan, B. Jeffries-Nakamura, R. M. Williams, M. L. Underwood, D. O'Connor, and S. Kikert. Advances in materials and current collecting networks for AMTEC electrodes. *Proceedings of the 27th Intersociety (IECEC)*, 3 (929007): 3.7 – 3.12, 1992.

[144] H. Nakata, T. Nagata, K. Tsuchida, and A. Kato. Ceramic electrodes for an alkali metal thermo-electric converter (AMTEC). *Journal of Applied Electrochemistry*, 23: 1251 – 1258, 1993.

[145] Q. Fang and H. Wendt. Performance and thermodynamic properties of Na-Sn and Na-Pb molten alloy electrodes for alkali metal thermoelectric converter (AMTEC). *Journal of Applied Electrochemistry*, 26: 343 – 352, 1996.

[146] M. S. El-Genk and J. M. Tournier. Recent advances in vapor-anode, multi-tube, alkali metal thermal-to-electric conversion cells for space power. In *Proceedings of the 5th European Space Power Conference*, pages 257 – 264, 1998.

[147] S. Matsuoka. Ultrasonic welding of ceramic/metal. *Journal of Materials Processing Technology*, 47: 185 – 196, 1994.

[148] A. K. Goreev, V. A. Burdovitsin, A. S. Klimov, and E. M. Oks. Electron beam welding of ceramic to metal using fore-vacuum plasma electron source. *Anorganic Materials: Applied Research*, 3 (5): 446 – 449, 2012.

[149] H. Will. Festelektrolyt/ Niob-Lötverbindungen. Technical report, No. IRE4-1067-90, Kernforschungszentrum Karlsruhe, 1990.

[150] V. Heinzel and H. Will. AMTEC, Keramik/ Struktur - Lötverbindung. Technical report, No. IRE4-1093-91, Kernforschungszentrum Karlsruhe, 1991.

[151] R. M. Williams, A. K. Kisor, M. L. Homer, K. Manatt, V. B. Shields, and M. A. Ryan. Reactivity of thin metal films on sodium beta" alumina ceramic in high temperature, low pressure sodium vapor. *AIP Conference Proceedings*, 522: 1100 – 1106, 2001.

[152] S. Kim, J. H. Joo, S. D. Kim, and S. K. Woo. Evaluation of CaO-Al_2O_3 adhesive bonding properties ß"-Al_2O_3 solid electrolyte sealing for alkali metal thermal electric converter. *Ceramics International*, 39: 9223 – 9227, 2013.

[153] L. C. De Jonghe. Transport number gradients and solid electrolyte degradation. *Journal of Electrochemical Society*, 129 (4): 752 – 755, 1982.

[154] K. Kuribayashi and P. S. Nicholson. The deterioration of sodium ion conductors under applied stress. *Journal of Materials Science*, 18: 1590 – 1596, 1983.

[155] R. N. Singh and N. Lewis. Role of electrolyte-sodium interface behavior to the degradation of a sodium-sulfur cell. *Solid State Ionics*, 9: 159 – 164, 1983.

[156] A. V. Virkar. The role of superimposed stresses on the degradation of solid electrolytes. *Journal of Materials Science*, 21: 859 – 865, 1986.

[157] A. V. Virkar and L. Viswanathan. A three-dimensional approach to the electrolytic degradation of solid electrolytes. *Journal of Material Science*, 18: 1202 – 1212, 1983.

[158] T. K. Hunt, J. Pantolin, R. K. Sievers, J. T. Kummer, and R. F. Novak. Engineering developments for sodium heat engine systems. *Proceedings of the 26th Intersociety (IECEC)*, 2: 455 – 460, 1991.

[159] M. Steinbrück, V. Heinzel, F. Huber, and W. Peppler. Investigations of beta-alumina solid electrolytes for application in AMTEC cells. *Proceedings of the 28th Intersociety (IECEC)*, 1: 1.799 – 1.808, 1993.

[160] M. Fritz, M. R. Barbosa, G. Staikov, W. J. Lorenz, M. Steinbrück, and R. Knödler. Electronic conductivity of Na ß"-alumina ceramics at high temperatures. *Solid State Ionics*, 62: 273 – 277, 1993.

[161] M. A. K. Lodhi, P. Vijayaraghavan, and A. Daloglu. Time-dependent BASE performance and power degradation in AMTEC. *Journal of Power Sources*, 93: 41 – 49, 2001.

[162] J. M. Tournier and M. S. El-Genk. Sodium Vapor Pressure Losses in a Multitube, Alkali-Metal Thermal-to-Electric Converter. *Journal of Thermophysics and Heat Transfer*, 13 (1): 117 – 125, 1999.

[163] A. Schock, H. Noravian, and Ch. Or. Coupled thermal, electrical, and fluid flow analyses of AMTEC converters, with illustrative application to OSC's cell design. *Proceedings of the 32nd Intersociety (IECEC)*, 2: 1156 – 1164, 1997.

[164] A. Schock, H. Noravian, and V. Kumar. Design, analyses, and fabrication procedure of AMTEC cell, test assembly, and radioisotope power system for outer-planet missions. *Acta Astronautica*, 50 (8): 471 – 510, 2002.

[165] H. Schindler. Analyse des AMTEC-Prozesses Bezüglich der Prozess- und aus-führungsbedingten Verluste und deren Anwendung auf experimentelle Daten. Diplomarbeit, Kernforschungszentrum Kalrsruhe, 1993.

[166] R. M. Williams, M. E. Loveland, B. Jeffries-Nakamura, M. L. Underwood, C. P. Bankston, H. Leduc, and J. T. Kummer. Kinetics and transport at AMTEC electrodes I - The interfacial impedance model. *Journal of Electrochemical Society*, 137 (6): 1709 – 1716, 1990.

[167] J. Aktaa. Analyse der Umwandlungswirkungsgrade von AMTEC-Systemen unter verschiedenen Randbedingungen. Diplomarbeit, Kernforschungszentrum Karlsruhe, 1989.

[168] Pfeiffer Vacuum. Mean free path, acessed the 28.02.2018. https://www.pfeiffer-vacuum.com/en/know-how/introduction-to-vacuum-technology/fundamentals/mean-free-path/.

[169] J. M. Tournier and M. S. El-Genk. An electric model of a vapour anode, multitube alkali-metal thermal-to-electric converter. *Journal of Applied Electrochemistry*, 29: 1263 – 1275, 1999.

[170] J. L. Palacios Encalada. Numerical investiation of the structural and thermal behavior of an AMTEC experimental cell developed for concentrated solar power systems. Master's thesis, Karlsruhe Institute of Technology (KIT), 2014.

[171] E. Lugscheider and W. Tillmann. Methods for brazing ceramic and metal-ceramic joints. *Materials & Manufacturing Processes*, 8: 219 – 238, 1993.

[172] M. F. Arenas, V. L. Acoff, and R. G. Reddy. Physical properties of selected brazing filler metals. *Science and Technology of Welding and Joining*, 9 (5): 423 – 429, 2004.

[173] S. Venkatesu, P. K. Chaurasia, S. Murugan, and S. Venugopal. Development of high-temperature nicrobrazed joints using induction heating in an argon gas environment. *Trans Indian Inst Met*, 69: 1417 – 1422, 2016.

[174] V. Schüle. AMTEC: Bericht über die Diffusion von Ti, Cu und Ni ß"-Al$_2$O$_3$. Technical report, No. CRH 57/ 91, ABB, 1991.

[175] K.-P. Müller. *Praktische Oberflächentechnik: Vorbehandeln - Beschichten - Prüfen.* Vieweg, ISBN 3-528-36562-5, 2003.

[176] M. Bologa. Analyse des mit TiC beschichteten Festelektrolyten einer AMTEC-Zelle. Master's thesis, Karlsruhe Institute of Technology (KIT), 2017.

[177] B. Dunn. Effect of air exposure on the resistivity of sodium beta and beta" aluminas. *Journal of the American Ceramic Society*, 64 (3): 125 – 128, 1981.

[178] F. M. Smits. Measurement of sheet resisitivities with the four-point probe. *Bell System Technical Journal*, pages 711 – 718, 1957.

[179] K. Tanaka, A. Negishi, and T. Masuda. Structure of current collector and flow characteristics of sodium vapor for the alkali metal thermoelectric converter. *Proceedings of the 27th Intersociety (IECEC)*, 929008, 1992.

[180] P. Browning and P. E. Potter. *Handbook of thermodynamic and transport properties of alkali metals*. Blackwell Scientific Publications, ISBN 0-632-01447-4, 1985.

[181] *VDI-Wärmeatlas: Berechnungsunterlagen für Druckverlust, Wärme- und Stoffübertragung*. Springer, ISBN 978-3-540-25504-8, 2006.

Appendix A: Uncertainty of Nernst equation

The application of the Nernst equation to compare the theoretical values with the measured data requires the consideration of the uncertainties in the temperature and saturated pressure of sodium. Therefore, this appendix calculates the propagated uncertainty of the Nernst equation:

$$V_{Nernst}^{oc} = \frac{R_g T_B}{F} ln \left[p_{sat}\left(T_B\right) / p_c^{oc} \right] \qquad . \tag{A.1}$$

To calculate the pressure at the cathode the following equation of Cole (1983) is considered [32]:

$$p_c^{oc} = p_{sat}\left(T_{cd}\right) \sqrt{\frac{T_B}{T_{cd}}} \qquad . \tag{A.2}$$

The fitted equation for the vapor pressure of saturated sodium from Browning and Potter [180] is used:

$$p_{sat}\left(T\right) = exp\left[11.9463 - 12633.73/T - 0,4672 lnT\right] \qquad , \tag{A.3}$$

which has different uncertainty ranges depending on the sodium temperature as summarized in table A.1.

Temp. Range [K]	Uncertainty [%]
$400 - 600$	$9 - 25$
$600 - 864$	$4 - 6$
$864 - 1500$	3
$1500 - 2000$	4
$2000 - 2500$	5

Table A.1: Uncertainty of equation from Browning and Potter [180] for sodium vapor pressure at different temperatures ($400 - 2500\,$K).

It is well known that the propagated uncertainty u_f of a function $f\left(x, y, z, ...\right)$ of the physical variables $x, y, z, ...$ which have uncertainties u_x, u_y, u_z, ... is derived from the following equation:

$$u_f^2 = u_x^2 \left(\frac{\partial f}{\partial x}\right)^2 + u_y^2 \left(\frac{\partial f}{\partial y}\right)^2 + u_z^2 \left(\frac{\partial f}{\partial z}\right)^2 + \ldots \qquad . \tag{A.4}$$

First the propagated uncertainty of p_c^{oc} will be calculated as follows:

$$u_{p_c^{oc}}^2 = u_{p_{sat}(T_{cd})}^2 \left(\frac{\partial f}{\partial p_{sat}\left(T_{cd}\right)}\right)^2 + u_{T_B}^2 \left(\frac{\partial f}{\partial T_B}\right)^2 + u_{T_{cd}}^2 \left(\frac{\partial f}{\partial T_{cd}}\right)^2 \qquad , \tag{A.5}$$

which is equal to:

$$
u^2_{p^{oc}_c} = u^2_{p_{sat}(T_{cd})} \left(\sqrt{\frac{T_B}{T_{cd}}} \right)^2 + u^2_{T_B} \left(\frac{p_{sat}(T_{cd})}{2\sqrt{T_{cd}T_B}} \right)^2 + u^2_{T_{cd}} \left(-\frac{p_{sat}(T_{cd})\sqrt{T_B}}{2\sqrt[1,5]{T_{cd}}} \right)^2 \qquad . \quad \text{(A.6)}
$$

Considering the Nernst equation as a function of the temperature at the BASE, temperature at the condenser and the saturated pressure of sodium at the BASE the propagated uncertainty of the Nernst equation $u_{V^{oc}_{Nernst}}$ can be calculated as follows:

$$
u^2_{V^{oc}_{Nernst}} = u^2_{T_B} \left(\frac{\partial f}{\partial T_B} \right)^2 + u^2_{p_{sat}(T_B)} \left(\frac{\partial f}{\partial p_{sat}(T_B)} \right)^2 + u^2_{p^{oc}_c} \left(\frac{\partial f}{\partial p^{oc}_c} \right)^2 \qquad , \quad \text{(A.7)}
$$

which is equal to:

$$
u^2_{V^{oc}_{Nernst}} = u^2_{T_B} \left(\frac{R}{F} ln \frac{p_{sat}(T_B)}{p^{oc}_c} \right)^2 + u^2_{p_{sat}(T_B)} \left(\frac{RT_B}{Fp_{sat}(T_B)} \right)^2 + u^2_{p^{oc}_c} \left(-\frac{RT_B}{Fp^{oc}_c} \right)^2 \qquad . \quad \text{(A.8)}
$$

Introducing in the last equation the values of the known parameters, one can obtain the uncertainty of the Nernst equation, which for instance at $T_B = 501 \pm 2$ °C and $T_{cd} = 166 \pm 3$ °C is equal to $V^{oc}_{Nernst} = 794 \pm 15$ mV, equivalent to an uncertainty of 2 %.

Appendix B: ATEFA facility description

Trace heating system

Sodium is kept molten at $\geq 150\,°C$ in tanks and piping during operation thanks to a trace heating system; the maximum temperature of $800\,°C$ is only reached inside the BASE tube and therefore confined in a small volume ($\sim 0.17\,l$). Exceptionally, during the filling process, the complete sodium system is heated up to $\sim 300\,°C$ to ensure a good wetting. Moreover the temperature gradient between the BASE tube and the Na-feeding pipe at the inlet of the cell is kept below $150\,°C$ in order to avoid a thermal shock, which may break the BASE tube. Also a large temperature gradient in the axial direction of the BASE tube may cause a break of the BASE and is therefore monitored by the heating system not to exceed a temperature gradient of $150\,°C$.

A description of the system and the installed electric power is given in table B.1. The heat losses in ATEFA are small due to the small volume of sodium and low temperature ($< 250\,°C$) and therefore, the required electric power for the trace heating system in ATEFA is small too (except for the BASE). To obtain a homogeneous temperature all over the cell it is important in order to avoid local solidification of sodium, however this task becomes difficult due to the complex structure of the AMTEC test cell (different diameters and wall thicknesses and large amount of feedthroughs). For this reason, the criteria followed to determine the power to be installed was based on the geometry rather than on the heat losses. Therefore, the installed power is most of the cases (central flange, lower flange etc.) significantly larger than the required power to cover the heat losses. The estimated total power consumption of the facility is of $\sim 1500\,W$ based on the correlations of [181] for heat transfer in insulated pipes with free or forced convection and under consideration of radiation losses. Some of the heaters were connected in series or parallel to the power source, depending on their power consumption and operating temperature. The effective electric power is controlled by power regulators, which are connected to the control system of the facility (see chapter 5.2).

Miniature heaters have depending on their length and thickness a specific voltage limit. This needs to be considered when selecting the power supply and control system. Three possibilities were observed for the power control through: phase angle, zero cross or a variable transformer. The advantages and disadvantages of each technology are summarized in table B.2.

The reduced available space in the experimental facility lead to discard variable transformers due to their large sizes. Furthermore a transformer with automatic control can become extremely expensive in comparison to phase-angle or burst-fired regulators.

Heater	Component		Max. temp. [°C]	Max. installed power [W]
Hz1	AMTEC cell	BASE (anode)	800	765
Hz2		Upper flange	250	57
Hz3		Inlet pipe		50
Hz4		Valve AR-VI-08		80
Hz5		Central flange		333
Hz6		Lower flange		404
Hz7		Condenser		169
HN1 + HN2	Tank NA-ST-01		250	163
HN3	Piping 1 (Na-inlet)			998**
HN4	Piping 2 (Na-outlet)			912**
HN5 + HN6	Tank NA-ST-02			163
HN7	Valve NA-VI-01			59
HN8	Valve NA-VI-02			59
			4212	Total [W] (installed)
			∼ 1500	Total [W] (estimated)

Table B.1: Review of the heaters assembled in ATEFA. The maximum installed power was obtained considering the maximum installed voltage. *For the particular case of HN3 and HN4 the heaters are connected to a 230 V source, therefore the installed maximum power is considerably higher than the estimated value (67 and 129 W respectively); the final power is however monitored and reduced before reaching the heaters with a power regulator device.

Power regulator	Main advantages	Disadvantages
Phase-angle	- Very fine resolution - Fast responding - Adequate for resistive and inductive loads	- Higher harmonic distortion - Radio-frequency interference (RFI)
Burst-fired (zero cross)	- Very low harmonics - Very low RFI - Economic	- Not recommended for motors - Resolution depends on cycle time
Variable transformer	- Output voltage regulation - No harmonics / RFI	- Very large devices - Very expensive (automatic regulation)

Table B.2: Overview on power regulator devices.

Phase-angle controllers have a very fine resolution and fast responding, however they generate high harmonic distortion and radio-frequency interference, which can dismiss the sensor measurements in the facility. This is produced when closing and opening the electrical circuit at high voltages. For that reason, zero cross devices were preferred. In particular, zero cross regulators with variable time-base control can be easily controlled through an input signal (e.g. 4 - 20 mA) given by the automation system

or PC. However the resolution is affected by the looped-cycle time of the zero cross regulator.

A transformer was used to reduce the maximum voltage applied to the heaters and an accurate automatic control of the supplied electric power was done combining a PID (Proportional-Integral-Derivative) controller and a zero cross device (Watlow type DIN-A-MITE-A), which has a variable time-base control with looped cycle (minimum 3 cycles on or off). A phase gating dimmer (Dimmtronic M1000/5.3 from EPV Electronics) was used for controlling the cooling power of the ventilator in the condenser.

Figure B.1 shows an infra-red-photograpy picture made with the thermographic camera during a test of the heating system without thermal insulation. Two spots in the cell, the lower part of the cell and the flange, seem to have a lower temperature than the rest of the structure, however thermocouples located directly on that position showed a higher temperature than the measured by the camera. This is due to the modified emissivity at of those regions, which have a more polished surface, that modified the heat radiation effect captured by the camera. Feedthroughs at the upper flange are not actively heated and are, therefore, colder than the rest of the cell. The metallic wall of the facility containment located behind the cell produces a mirror effect reflecting the heat radiation of the cell. The design of the heating system in the cell provides up to 300 °C in the ceramic even in case of a failure of the main heater, thanks to the indirect heating system installed on the outer wall of the condenser.
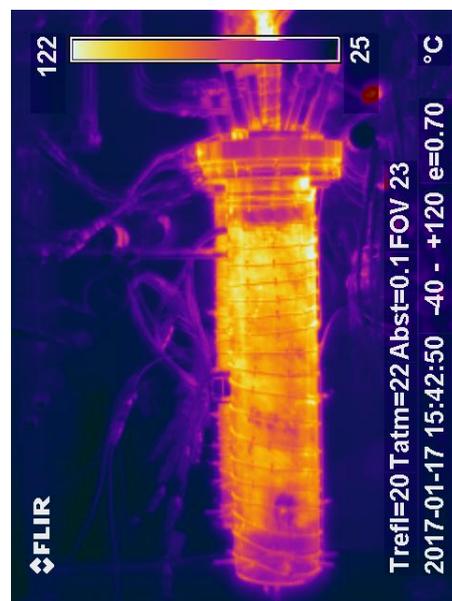
Figure B.1: Infra-red picture of the AMTEC cell made with the thermographic camera during heater tests. Total applied power 235 W, ambient temperature 25 °C.

Mineral wool of 30 mm thickness was used as thermal insulation in the sodium system. Additional insulation was installed on the walls of the facility containment made

of calcium silicate, Promasil 950-KS. These calcium silicate plates located between the walls of the ATEFA facility have multifunction: isolate thermally the sodium side from the laboratory and make the ATEFA doors robust and lightweight.

Operation procedure

The operation procedure of ATEFA is divided in three main stages: i) *cell empty,* ii) *maintenance* and iii) *cell full (operating)*. The main characteristics of each stage are described in table B.3 and figure B.2 shows the main steps of the process control system of ATEFA.

Stage	Cell empty	Maintenance	Cell full (Operating)
Tanks	Contain cold sodium $(T_{Na} \sim 30 \,°C)$	Contain hot sodium $(T_{Na} > 100 \,°C)$	Contain hot sodium $(T_{Na} > 100 \,°C)$
Fill-status cell and piping	Empty	Empty $(T_{Na} = 150 \,°C)$	Contain hot sodium $(T_{Na} = 250 \text{ - } 800 \,°C)$

Table B.3: Overview of the main stages in the operational procedure of ATEFA.

In *cell empty* stage the facility is cold, depressurized and empty. During *maintenance* the facility is still empty, however, sodium is molten in the tanks. Here transition processes take place like pressure test and cleaning of the facility from moisture and air rests. *Cell full* stage represents the ATEFA facility under operating conditions: a pressurized, full and hot facility. Here the filling of the cell with sodium, the adjustment of the pressure and temperature in the cell or the recording of measurements take place.

1. *Cell empty.* Cell and tanks can be disassembled from the facility since sodium is at room temperature and the facility depressurized.

2. *Maintenance*. First of all a verification of enough available sodium in the facility is done. This can be carried out by weighing the tank. Once the cell and both tanks are connected to the facility and the doors of the facility are closed, a cold inspection is performed (*pressure test*). Once the facility is leak tight the *cleaning* process is followed. This transition includes an evacuation of the facility at 150 °C, which allows the vaporization of water from the inner walls of the system.

3. *Cell full.* The filling of the cell with hot sodium at 250 °C (*Na - fill cell*) is first proceeded, followed by the *adjustment* of temperature and pressure in the cell. Finally the *electrical circuit* can be closed and recording of *measurements* started.
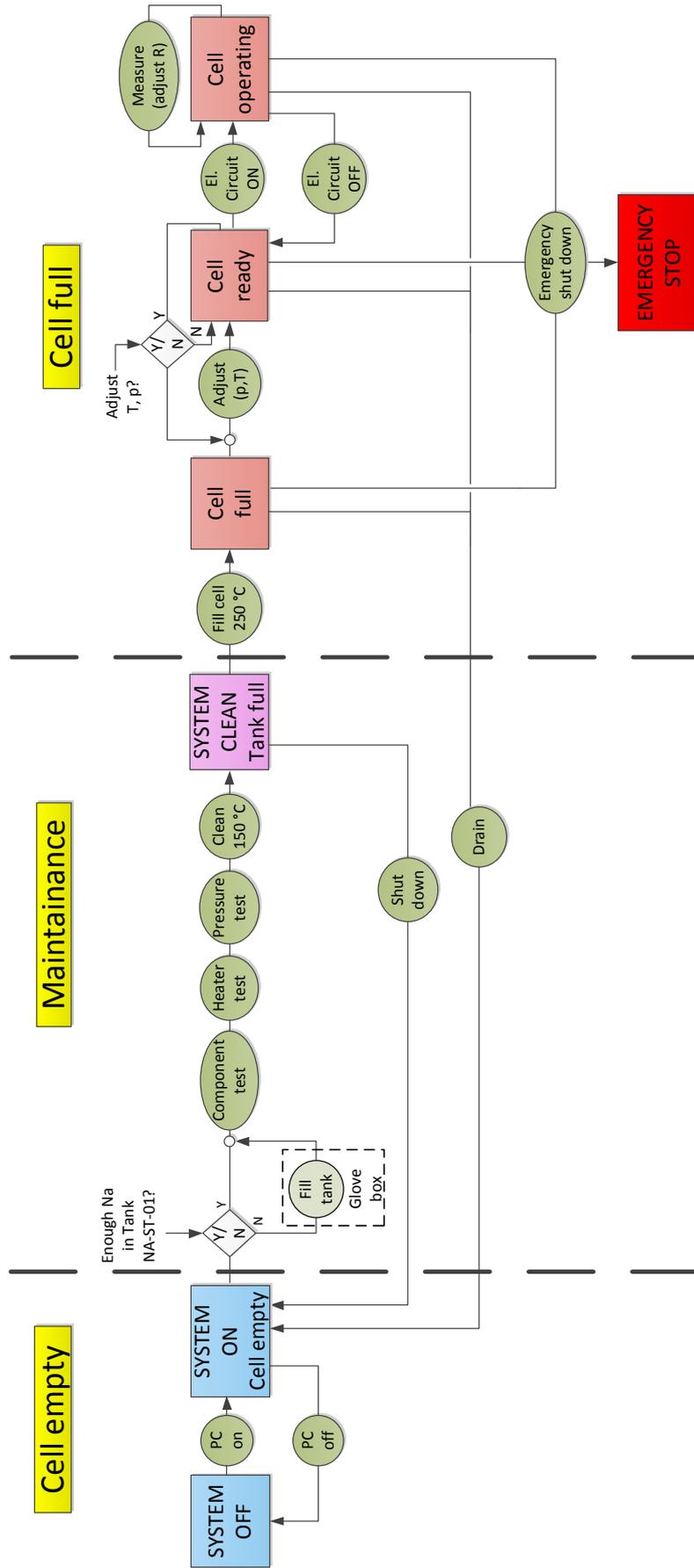
Figure B.2: Operating description of the ATEFA facility. Boxes symbolize states and green circles represent transition procedures between the states.

Filling process. In order to fill up the BASE tube with Na a pressure difference between cell and tank is required. Assuming an inner diameter of the ceramic $D_B = 28$ mm and that the minimum volume of sodium to be pumped needs to fully cover the electrical heater and the anodic current lead: $H_{Na}^{min} = 97$ mm (see figure B.3), the minimum sodium amount to be pumped in the cell is $Vol_{Na}^{min} \sim \pi D_B^2 H_{Na}^{min}/4 = 5.97 \times 10^{-5}$ m^3. On the other hand, maximum volume of sodium in the BASE should not exceed the height of the last electrode: $H_{Na}^{max} = 218$ mm, $Vol_{Na}^{max} \sim \pi D_B^2 H_{Na}^{max}/4 = 1.34 \times 10^{-4}$ m^3. Above the last electrode liquid sodium would contact the Nb-brazing and the electrical isolation of the anode would disappear.
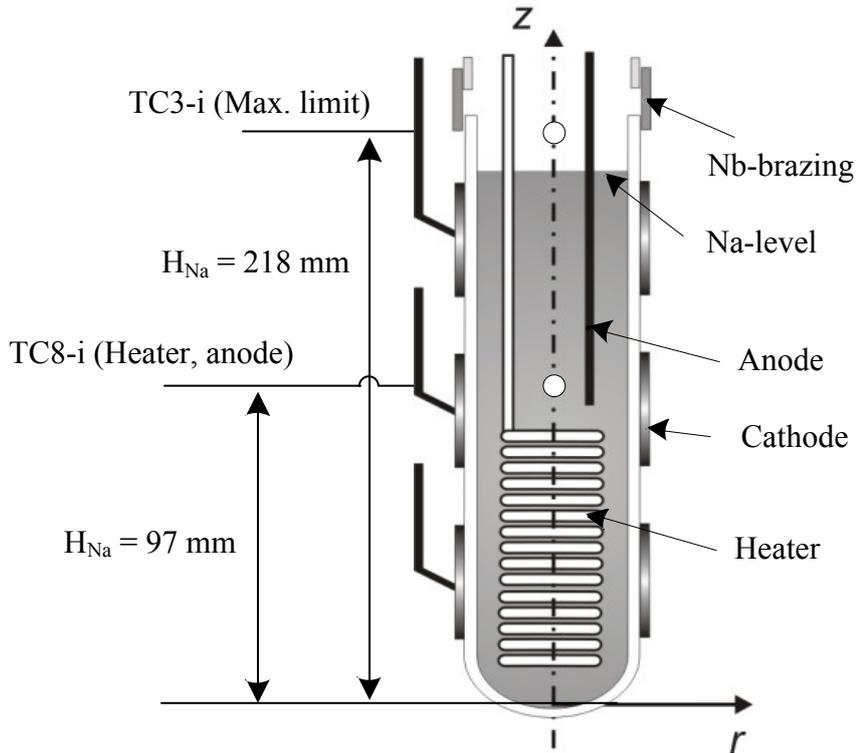
Figure B.3: Sketch of the BASE tube indicating two measurement points of the Na-level: minimum Na-level (TC8-i) covers the heater and contacts the anode, and maximum Na-level (TC3-i) allowed prevents electrical short circuit as well as over-flooding.

The storage tank has an internal diameter of $D_{Tank} = 131.7$ mm a width of $L_{Tank} = 315$ mm. If the amount and the temperature of sodium and argon in the system (tank+piping+cell) remain constant, the expression for ideal gases can be used to obtain the relation between volume and pressure at the different states:

$$p\,Vol = constant \qquad . \tag{B.9}$$

Pumping liquid sodium from the tank NA-ST-01 to the cell requires also the consideration of a hydrostatic pressure, which appears due to the height difference between

cell and tank. The hydrostatic pressure can be calculated as follows:

$$p_{hyd} = H \varrho \, g \qquad , \tag{B.10}$$

$$p_{Tank} = p_{Cell} + p_{hyd} \qquad , \tag{B.11}$$

where H denotes the height difference between the tank (filled state) and the cell, ϱ is the specific density of sodium and g is the gravity constant. If $\varrho(150\,°C) = 914\,\text{kg/m}^3$ and $H = 1.6\,\text{m}$, then $p_{hyd} = 0.143\,\text{bar}$. During calculations, it was observed that if the initial pressure of the cell is $> 1.05\,\text{bar}$, the maximum pressure allowed in the tank ($p_{Tank} > 1.5\,\text{bar}$) is reached before the cell is completely full. Thus, the filling process must be performed in two or more steps: first fill up the cell with sodium until $\sim 1.3\,\text{bar}$ in cell are reached. Then close valves NA-VI-01 and open valve AR-VO-03 to release excessive argon from the cell ($p_{Cell} = 1.05\,\text{bar}$), this is the intermediate state. Finally, the filling process can be finished. In the calculations not only the volume from tank and cell were taken into account but also the piping that communicates both parts.

As soon as the tests have been finished, the facility can be *drained*. First of all, electrical circuit is switched off, then the in facility is cooled down to 200 °C and the overpressure in tank NA-ST-01 eliminated. Then, AMTEC cell is drained by means of using the pressure difference between cell and tank, pushing simultaneously the liquid sodium to both tanks.

Draining process. In the facility the total amount of sodium of ~ 0.28 liters is divided between cell ~ 17 liter and piping system ~ 0.11 liter. Due to the small cross section of the sodium piping system (4 mm inner diameter), the effect of capillary forces in the piping needs to be considered. Therefore, the draining process is supported not only through the gravity forces but also through a pressure gradient generated between the cell and the sodium tanks. The sodium valves (NA-VI-01, -02) determine the draining speed of the facility owing to their small aperture. Assuming a pressure difference between cell and tank of 0.3 bar (generated by an underpressure in the tanks), a sodium density of $830\,\text{kg/m}^3$ and the flow coefficient of the valve given by the manufacturer $c_v = 1$, the sodium mass flow rate through the valve is therefore $\dot{m} = 0.671\,\text{m}^3\text{/h}$. Consequently the calculated time to drain the total amount of sodium is ~ 2 seconds. This rapid draining is favorably to a safe operation of the facility.

When the facility is empty, the trace heating system is switched off, sodium solidifies and over/underpressure is eliminated.

Emergency shut down. The facility is supplied with an emergency stop button. When the button is pressed, power supply switches off immediately and solenoid outlet valves (AR-VO-01, -02, -03) located at the argon system open by power disconnection. A consequent automatic depressurization the facility occurs and the heating system as well as any electric devices are automatically switched off. Additionally, the metallic containment of the sodium system is flooded with argon through the open solenoid valves.

During the experimental operation, several subroutines are executed independently from the state or transition. This are subroutines in charge of a secure working of the facility:

– Supervision of temperature in sodium system. Warning if temperature drops below 150 °C. If temperature exceed the maximum allowed temperature in the facility the power supply of the respective heater are switched off.

– The power control system of the heater in the BASE tube does not allow a temperature gradient higher than 150 °C, to avoid a thermal shock and thereby preventing a damage of the ceramic.

– Supervision of pressure in the sodium system. If the pressure exceeds the specified maximum allowed temperature then the outlet valves (AR-VO-02 and AR-VO-03) open automatically to release the excess pressure. Opening of the outlet valves is only allowed in case of overpressure, to avoid air ingress in the facility.

– Warning in case of a ceramic break. The vacuum sensor in the cell records a rapid pressure increase indicating a ceramic failure.

– Automatic protection of the vacuum sensor by monitoring the solenoid valve AR-VI-06. The valve closes when the maximum pressure permitted by the sensor is reached.

In case of a ceramic break and a simultaneously open mass flow controller, the latter is automatically closed to avoid an uncontrolled loss of sodium from the primary tank NA-ST-01. Thanks to the pressure difference across the BASE tube, molten sodium is automatically "pushed" into the collecting tank NA-ST-02. The temperature of the containment box is measured and must not exceed 80 °C to ensure sodium solidification in case of a leakage and to avoid cabling damage. The monitoring of the facility during commissioning (pressure test, cleaning), filling up the cell, adjustment of pressure and temperature and drainage is done combining manual and automatic actions; in any case the manual steps are surveyed by the control system to limit possible mistakes by the operator. In steady state conditions only PC-based (automatic) control is required.

Safety provisions

Working with molten sodium at high temperatures requires special attention during design, construction and operation the ATEFA. The most important safety features considered are summarized here.

– Small amount of sodium in the facility of $\sim 0.3\,l$ (without tanks).

– Limited pressure to $\sim 0.17\,$MPa ensured by three safety valves and three outlet valves.

– Highest temperature of 800 °C located only in the ceramic electrolyte. The rest of the sodium system is maintained at a temperature of ~ 200 °C.

– In case of a ceramic rupture sodium is collected in the condenser containment and secondary tank.

– Fast draining of sodium into the tanks in ~ 2 seconds.

– Several metallic filters were installed in the Ar-piping at the connecting zones with the Na-system to protect pressure gauges and the vacuum pump from molten sodium and to act as a barrier for sodium to avoid entering the Ar-system.

– Isolation of the sodium system by enclosing it in a metallic containment. It retains liquid sodium inside the containment in case of a leakage and acts as a physical barrier between the sodium system and the operators.

– Argon outlet valves release the overpressure in the containment of the sodium system and are used to float the facility in case of a sodium leakage, to extinguish a possible subsequent fire.

– A metallic catch pan is located on the bottom of the facility containment under the tanks to collect liquid sodium in case of a leakage.

– Emergency stop button.

– Ventilation system in the laboratory: for aerosol/smoke and argon suction. The latter activated through an oxygen sensor.

– Dry sand and fire blankets are available in the laboratory to stop fire from small leakages

Appendix C: Laboratory infrastructure

Sodium melting device

The sodium is delivered in solid ingots of around 1 kg with a protective oxide layer. Thus, filling the tanks of ATEFA and SOLTEC facilities with sodium requires first a cleaning and melting process. The glovebox is used for this purpose and a sodium melting device has been constructed and coupled to the structure of the glovebox. It consists of a glass containment of 2 liters that is placed on top of a heater plate and is connected through a 8 mm pipe with the sodium tank. First the sodium ingots are melted inside the glass and heated up to 250 °C to ensure a good wetting of the piping system. Sodium oxide rests are accumulated on the free surface of the melt. Then an underpressure is generated in the tank while a valve near to the tank is closed. After opening the valve, the pressure gradient between glovebox and tank helps filling it with molten sodium from the lower part of the glass (clean sodium). A level sensor in the tank indicates a full state of the tank. For safety reasons the glass containment is fixed to a static structure and a metallic tub is placed underneath the heater plate. The sodium tank is placed outside the glovebox on top of a second metallic tub. Figure C.1 shows the sodium melting system. Inside the glove box a second valve is used to drain the pipe after the filling process.

Laboratory ventilation system

The AMTEC laboratory has been provided with a ventilation system consisting of three main loops. At floor level an argon suction system has been installed, which is monitored by an oxygen sensor that activates the ventilation system for argon and gives both acoustic and visual warning signals in the laboratory in case of emergency. At the top of the laboratory a second ventilation system has been installed for aerosol suction. The latter is activated only after the sodium fire has been extinguished to prevent intensifying the fire. Therefore, the activation button is located outside the laboratory and is used before entering the laboratory after a sodium fire. The third ventilation loop is foreseen for ATEFA and SOLTEC-3 cooling systems. Figure C.2 shows the upper view of the ventilation system located on top of the laboratory ceiling.
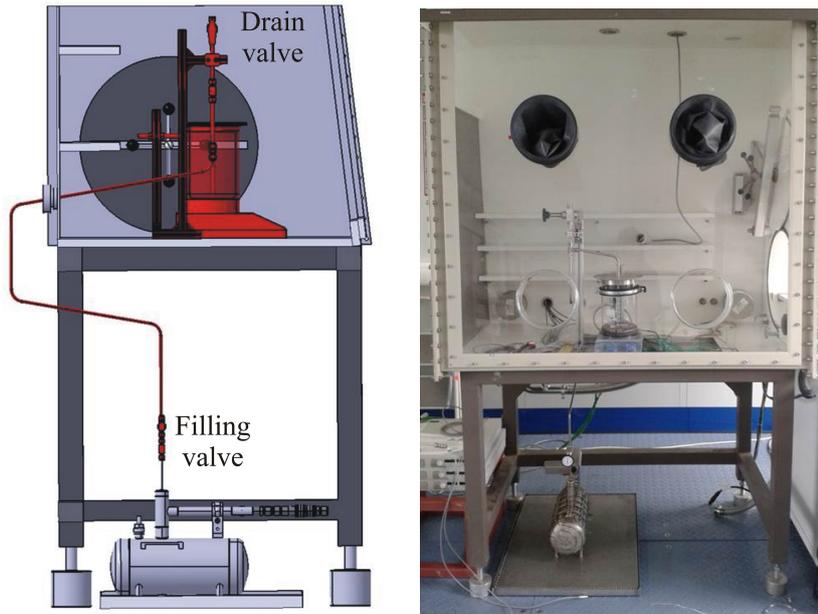
Figure C.1: Sketch and picture of the sodium melting system. The picture (right side) illustrates the system before assembling of thermal isolation.
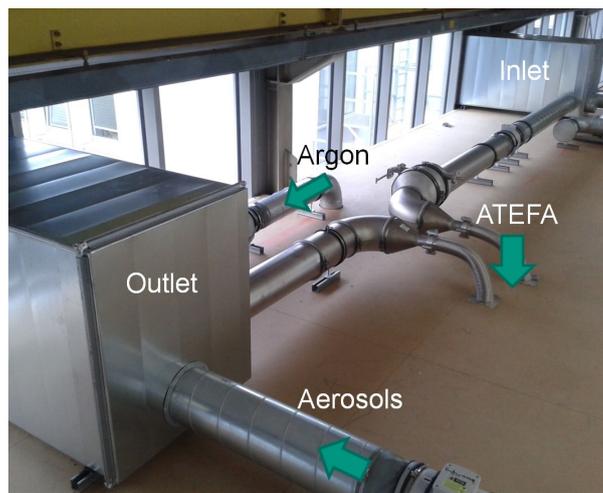
Figure C.2: Upper view of the ventilation system, located on top of the laboratory ceiling.

Cold air comes through the right window and is used to cool the AMTEC condenser in ATEFA. The left outlet window is used to release hot air , argon and aerosols from all three loops. Non-return valves are used to ensure the correct direction of the flow. The mass flow rate of cooling air in ATEFA is controlled using a PID regulator included in the LabView ATEFA control system.

List of Figures

List of Tables